

Engineered Structural Fibres as Replacement for Traditional Reinforcements for Concrete

By

Mohammad Hajsadeghi

The thesis is submitted in accordance with the requirements of the

UNIVERSITY OF LIVERPOOL

School of Engineering

for the degree of Doctor of Philosophy

May 2018

Supervisors: Prof. Chee Seong Chin, Dr. Stephen W. Jones

This copy of the thesis has been supplied on condition that anyone who consults it is understood to recognise that its copyright rests with its author and that no quotation from the thesis and no information derived from it may be published without proper acknowledgement.

UNIVERSITY OF LIVERPOOL

School of Engineering Sciences

CERTIFICATE OF EXAMINATION

Supervisors

Examiners

Prof. Chee Seong Chin

Prof. Jian Yang

Dr. Stephen W. Jones

Dr. Isaac Galobardes

The thesis by

Mohammad Hajsadeghi

entitled:

**Engineered Structural Fibres as Replacement for
Traditional Reinforcements for Concrete**

is accepted in partial fulfilment of the requirements for the degree of

Doctor of Philosophy

Date

Chair of the Thesis Examination Board

ABSTRACT

Fiber Reinforced Concrete (FRC) has been gaining more attention as an effective way to improve the performance of concrete which is used in various types of civil engineering applications. The addition of fibres into concrete enhances the load carrying capacity and ductility of the structural members and controls crack propagation, increases energy absorption, and alters the mode of failure. However, unfavourable performance and benefit-cost ratios of most fibres commercially available hinder the large employment of such reinforcement especially for structural applications.

In this research, a new generation of structural steel fibres was developed for applications in Reinforced Concrete (RC) structures using a validated three-dimensional non-linear Finite Element (FE) model. The model was employed as a virtual laboratory unit to investigate the pullout performance of steel fibres from the concrete matrix with various geometrical and material properties. Based on the comprehensive FE analyses, a type of fibre with a spirally deformed shape is selected and optimised through numerical and experimental investigations. Findings of extensive numerical and experimental pullout tests show that the fibre possesses slip-hardening response (until complete withdrawal) in normal concrete which indicates that the fibre effectively contributes to the performance of structural members especially where wide cracks are expected.

Further experimental investigations were performed to evaluate the compressive and flexural behaviour of normal concrete incorporating the newly designed fibre. A closed form solution was used for the load-deflection response of the concrete specimens under bending to back-calculate the material's behaviour in compression and tension. It was shown that with the employment of the new fibre, hardening behaviour under bending can be achieved. The obtained constitutive material behaviour can be employed as preliminary input for numerical and analytical investigations of concrete members.

To quantify the structural performance of the newly designed steel fibres, two sets of RC beams (flexure-critical and shear-critical sections) with various fibre dosages were tested. The test results have revealed that the fibre could be employed as partial/full replacement for conventional reinforcement in RC structures. The shear and flexural design procedures for RC beams with the new fibres have also been developed.

DEDICATION

To my loving parents

who first showed me the taste of learning

and my beautiful wife

for her unconditional love, support, encouragement, and patience

ACKNOWLEDGEMENT

Firstly, I would like to express my sincere gratitude and appreciation to my primary supervisor Prof. Chee Seong Chin for his continuous support and motivation, and for sharing his knowledge and experience with me throughout my Ph.D. project. His guidance helped me throughout the project and writing of this thesis. I could not have imagined having a better supervisor for the project. Besides, I am greatly indebted to my co-supervisor Dr. Stephen W. Jones for his support during my research project and proof-reading of the thesis.

I would like also to take this opportunity to acknowledge the rest of my thesis committee, Prof. Jian Yang and Dr. Isaac Galobardes for their incredibly valuable comments and amazing feedback which incited me to widen my research from various perspectives.

I wish to convey a deep sense of gratitude to my great parents for whom words cannot express how grateful I am. I greatly appreciate your faith in me and allowing me to be as ambitious as I wanted. I would like also to thank my brother and sister for being my closest friends in my entire life.

My deepest appreciation is extended to my beloved wife Maryam for her support, patience, and unwavering love. You have been on this journey with me, enduring the triumphs and the challenges with the utmost care, respect and love. You are not just my partner, you are my life.

Finally, I want to thank all of those people who, previously, were my teachers and who helped me begin this long journey. Their names are numerous to mention, but many of them inspired me to continue learning and sharing with others.

TABLE OF CONTENTS

CERTIFICATE OF EXAMINATION	-----	ii
ABSTRACT	-----	Iii
DEDICATION	-----	iv
ACKNOWLEDGEMENTS	-----	v
TABLE OF CONTENTS	-----	vi
LIST OF FIGURES	-----	x
LIST OF TABLES	-----	xv
LIST OF EQUATIONS	-----	xvii
LIST OF APPENDICES	-----	xviii
LIST OF ABBREVIATIONS	-----	xix
LIST OF NOTATIONS	-----	xx
CHAPTER 1 - INTRODUCTION	-----	1
1.1. Background	-----	1
1.2. Objectives and Scope of the Thesis	-----	3
1.3. Layout of the Thesis	-----	5
CHAPTER 2 - LITERATURE SURVEY	-----	7
2.1. Introduction	-----	7
2.2. Fibre Types and Classification of FRC	-----	8
2.3. Steel Fibre Reinforced Concrete (SFRC)	-----	11
2.3.1. SFRC Properties	-----	11
2.3.1.1. Fibre Volume Content	-----	11
2.3.1.2. Fibre Aspect Ratio	-----	13
2.3.1.3. Fibre Geometry (Length and Shape)	-----	13
2.3.1.4. Fibre Orientation	-----	14
2.3.1.5. Fibre and Matrix Material	-----	15
2.3.1.6. Fibre Surface and Matrix Composition	-----	15
2.3.2. Applications	-----	16

2.3.3. Experimental Investigations	18
2.3.3.1. Material Testing	18
2.3.3.1.1. Fibre Pullout	18
2.3.3.1.2. Flexure Test	20
2.3.3.1.3. Direct Tension Test	21
2.3.3.1.4. Compression Test	22
2.3.3.2. Structural Testing	23
2.3.3.2.1. Beam Tests	24
2.3.4. Numerical Modelling	25
2.3.5. Analytical and Empirical Studies	27
2.4. Summary	31
CHAPTER 3 - DEVELOPMENT OF A NEW STEEL FIBRE	33
3.1. Introduction	33
3.2. Finite Element Model of Pullout	33
3.2.1. Fibre and Matrix Materials	34
3.2.2. Fibre-Matrix Interface	35
3.3. Validation of the Numerical Model	41
3.3.1. Straight Fibre	41
3.3.2. Hooked-end Fibre	45
3.3.3. Crimped Fibre	49
3.3.4. Twisted Fibre	51
3.4. Fibre Development	54
3.4.1. Experimental Pullout Test	58
3.4.2. FE Model Re-Validation	63
3.4.3. Parametric Study	64
3.4.4. Pullout Load Prediction	71
3.4.5. Fibre Design	72
3.4.6. Fibre Production	73
3.5. Summary	76

CHAPTER 4 - FRC MATERIAL TESTING	77
4.1. Introduction	77
4.2. Material Properties	78
4.2.1. Concrete	78
4.2.1.1. Aggregates	79
4.2.1.2. Fibres	81
4.3. Concrete Mixing, Casting, and Curing	82
4.4. Experimental Parameters	85
4.5. Workability Assessment	85
4.6. Material Testing	86
4.6.1 Compression Test	86
4.6.2. Flexure Test	88
4.6.2.1. Test Instrumentation and Procedure	88
4.7. Experimental Results	90
4.7.1. Compressive Strengths	90
4.7.2. Flexural Characteristics	93
4.7.3. Results Analysis	100
4.8. Constitutive Models	102
4.8.1. Load-Deflection Formulation	102
4.8.2. Simulation Procedure	110
4.8.3. Material Behaviour (Tension and Compression)	111
4.9. Summary	121
CHAPTER 5 - STRUCTURAL TESTING	122
5.1. Introduction	122
5.2. Testing Programme	123
5.2.1. Reinforcement Properties	124
5.2.2. Shear Resistance Contribution of New Fibre	126
5.2.2.1. Empirical Shear Design Equation	137
5.2.3. Flexural Contribution of New Fibre	138

5.2.4. Fibres Performance Comparison	141
5.3. Summary	147
CHAPTER 6 - DESIGN OF REINFORCED CONCRETE BEAMS WITH THE NEW FIBRE	148
6.1. Introduction	148
6.2. Analysis of Section	149
6.3. Design Example for Beams with the New Steel Fibre	151
6.4. Summary	157
CHAPTER 7 - CONCLUSIONS AND RECOMMENDATIONS	158
7.1. Conclusions	158
7.2. Recommendations for Future Work	160
REFERENCES	162~171
APPENDICES	172~192

LIST OF FIGURES

Fig. 2.1. Various types of steel fibre grouped according to their bond characteristics.	9
Fig. 2.2. FRC classifications.	10
Fig. 2.3. Effect of fibre volume content on the SFRC performance (Shah and Rangan 1971)	12
Fig. 2.4. SFRC compressive stress-strain curve (Fanella and Naaman 1985).	13
Fig. 2.5. Crack propagation mechanism of long and short fibres (Brandt 2008).	14
Fig. 2.6. Brass-coated steel fibre surface and its damage during pullout from UHPC (Wille and Naaman 2013).	16
Fig. 2.7. Traditional applications of SFRC.	17
Fig. 2.8. Pullout test setups.	19
Fig. 2.9. Flexure test setup (ASTM C1609/C1609M - 12 2012).	20
Fig. 2.10. Direct tensile test setup.	22
Fig. 3.1. Properties of the fibre-matrix interface.	36
Fig. 3.2. Penalty method formulation.	37
Fig. 3.3. Contact and target elements with corresponding bodies, i.e. contact and target bodies.	38
Fig. 3.4. Location of contact detection.	39
Fig. 3.5. Applying initial contact pressure on the contact surface, i.e. steel fibre surface.	40
Fig. 3.6. Finite element model of the straight fibre.	42
Fig. 3.7. Experimental and numerical load-slip curves of the straight fibre.	42
Fig. 3.8. The fibre-matrix interface of the straight fibre during pullout process.	43

LIST OF FIGURES (CONTINUED)

Fig. 3.9. The von Mises stress contours (in MPa) of the straight fibre at (a) slip = 0.02 mm, i.e. debonding; (b) slip = 2 mm.	44
Fig. 3.10. Normalised von Mises stress versus slip of the straight fibre.	44
Fig. 3.11. Dimensions of the hooked-end steel fibre (in mm).	45
Fig. 3.12. Finite element model of the hooked-end fibre.	46
Fig. 3.13. Experimental and numerical load-slip curves of the hooked-end fibre.	46
Fig. 3.14. The von Mises stress contours (in MPa) of the hooked-end fibre.	47
Fig. 3.15. Average interfacial shear stress versus slip for the hooked-end fibre.	47
Fig. 3.16. Pullout mechanism after straightening of the end hook, slip = 16.5 mm.	48
Fig. 3.17. Normalised von Mises stress versus displacement of the hooked-end fibre.	49
Fig. 3.18. Geometrical properties of the crimped steel fibre (in mm).	49
Fig. 3.19. Experimental and numerical load-slip curves of the crimped fibre.	50
Fig. 3.20. The von Mises stress contour (in MPa) of the crimped fibre at slip = 0.3 mm.	50
Fig. 3.21. Normalised von Mises stress versus displacement of the crimped fibre.	51
Fig. 3.22. Dynamic coefficient of friction - slip relationship for the twisted fibre.	52
Fig. 3.23. Experimental and numerical load-slip curves of the twisted fibre.	52
Fig. 3.24. Average interfacial shear stress versus slip for the twisted fibre.	53
Fig. 3.25. The von Mises stress contours (in MPa) of the twisted fibre at slips correspond to (a) debonding load, (b) peak load, and (c) the complete pullout.	53
Fig. 3.26. Normalised von Mises stress versus displacement at five levels of the twisted fibre.	54

LIST OF FIGURES (CONTINUED)

Fig. 3.27. Dimensions of the new steel fibres (in mm), fibre length (L_f) = 50 mm.	55
Fig. 3.28. Pullout response of the new steel fibres and the hooked-end fibre.	56
Fig. 3.29. The von Mises stress contour (in MPa) of the new steel fibres (not in scale).	57
Fig. 3.30. Dimensions of the mould designed for double-sided pullout specimens.	59
Fig. 3.31. Dimensions of the clamp of double-sided pullout testing.	60
Fig. 3.32. 3D representation of (a) pullout specimens' mould and (b) pullout clamps.	61
Fig. 3.33. Individual and average pullout responses of SD-5-2-0.9-50.	62
Fig. 3.34. Average pullout responses of spirally deformed steel fibres.	62
Fig. 3.35. Average pullout responses of spirally deformed steel fibres.	64
Fig. 3.36. Average pullout responses of the typical spirally deformed steel fibres.	65
Fig. 3.37. The dissipated pullout energy of the typical steel fibres.	66
Fig. 3.38. Fibre efficiency versus geometry index.	71
Fig. 3.39. Pullout load-slip curves of SD-9-1.45-0.4-40 and SD-9-1.55-0.4-40.	73
Fig. 3.40. Fibre production.	74 ~ 75
Fig. 3.41. Samples of fibre SD-9-1.45-0.4-40.	76
Fig. 4.1. Grading of aggregates.	79
Fig. 4.2. Steel fibres used for material testing (dimensions are in mm).	82
Fig. 4.3. Concrete mixing.	83

LIST OF FIGURES (CONTINUED)

Fig. 4.4. Completed mixes.	86
Fig. 4.5. Compression testing machine.	87
Fig. 4.6. Concrete cylinder grinding.	88
Fig. 4.7. Flexure test (ASTM C1609/C1609M - 12 2012).	89
Fig. 4.8. Variation of compressive strengths.	91
Fig. 4.9. Cube and cylinder strengths of concrete and their relationship.	92
Fig. 4.10. Fibrous concrete prism under flexural testing.	93
Fig. 4.11 (Continued). Individual and average flexural responses of SFRC containing 0.2% of the new fibre (ASTM C1609/C1609M - 12 2012).	94 ~ 97
Fig. 4.12. Schematic load vs. deflection curve of SFRC with the new fibre.	98
Fig. 4.13. Individual and average flexural responses of SFRC containing 0.5% of the commercially available fibres (ASTM C1609/C1609M - 12 2012).	98 ~ 99
Fig. 4.14. SFRC specimens with different steel fibres under flexure.	99
Fig. 4.15. Effect of the new fibre volume content on the flexural characteristics.	101
Fig. 4.16. Relationship of cylinder strength of concrete and modulus of rupture.	102
Fig. 4.17. Material models for FRC materials (Mobasher, Bakhshi et al. 2014).	103
Fig. 4.18. Strain and stress diagrams at pre-cracking and post-cracking stages.	105
Fig. 4.19. Bending test.	108
Fig. 4.20. Predicted constitutive models from load-deflection curves fitting.	112 ~ 120
Fig. 4.21. Effect of fibre volume content on the post-peak tensile stress.	121

LIST OF FIGURES (CONTINUED)

Fig. 5.1. Universal Testing Machine (300 kN) with the beam testing setup.	123
Fig. 5.2. Coupon testing setup.	124
Fig. 5.3. Average coupon testing results of steel reinforcement bars.	125
Fig. 5.4. Shear-critical SFRC beams testing.	127
Fig. 5.5. Response of shear-critical RC beams, $\rho = 0.55\%$ and $a/d = 1.5$.	128 ~ 131
Fig. 5.6. Failure of shear-critical non-fibrous RC beams.	133
Fig. 5.7. Failure of shear-critical RC beams with the newly-designed fibre.	134 ~ 135
Fig. 5.8. Contribution of the experiment parameters on the shear strength of SFRC beams.	136
Fig. 5.9. Flexure-critical SFRC beams testing.	139
Fig. 5.10. Response of flexure-critical RC beams.	140
Fig. 5.11. Failure of flexure-critical RC beams with the newly-designed fibre.	141
Fig. 5.12. Response of shear-critical RC beams with commercially available steel fibres.	142
Fig. 5.13. Failure of shear-critical RC beams with commercially available fibres.	144
Fig. 5.14. Response of flexure-critical RC beams with commercially available steel fibres.	145
Fig. 5.14. Failure of flexure-critical RC beams.	146
Fig. 6.1. Stress block of RC section with steel fibre.	150
Fig. 6.2. Dimensions of the RC beam for three different design schemes.	151
Fig. 6.3. Reinforcement schemes.	156

LIST OF TABLES

Table 2.1	29 ~
Analytical and empirical models for prediction of the shear strength of FRC.	31
Table 3.1	41
Geometrical and material properties of the straight steel fibre, (Naaman and Najm 1991).	
Table 3.2	42
Contact parameters for the FE models.	
Table 3.3	56
Comparison of pullout response of the new fibres with the hooked-end fibre.	
Table 3.4	58
Specifications of the considered spirally deformed steel fibres.	
Table 3.5	63
The calibrated contact parameters for spirally deformed steel fibres.	
Table 3.6	65
Specifications of the steel fibres for the parametric study.	
Table 3.7	67 ~
Pullout results of the steel fibres for the parametric study.	70
Table 3.8	72
Fibre design procedure.	
Table 4.1	78
Concrete mix design.	
Table 4.2	80
Specific gravity and water absorption of fine aggregate.	
Table 4.3	80
Specific gravity and water absorption of coarse aggregate.	
Table 4.4	81
Moisture content of fine and coarse aggregates.	
Table 4.5	81
Correction of required ingredients for concrete with $f_m = 35$ MPa.	
Table 4.6	85
Experiment parameters of material testing.	
Table 4.7	85
Slump cone test results.	
Table 4.8	90
Compression tests results.	
Table 4.9	99
Flexural tests results.	

LIST OF TABLES (CONTINUED)

Table 4.10	
Governing equations for calculating k , M' and ϕ' for each stage specified by strains at the bottom and top fibres.	107
Table 4.11	
The parameters used for simulating the load-deflection response of SFRC.	111
Table 5.1	
Coupon test results of reinforcing bars.	125
Table 5.2	
Number and specifications of the shear-critical beams with the new fibre.	126
Table 5.3	
Shear-critical beams results.	132
Table 5.4	
Number and specifications of the flexure-critical beams with the new fibre.	139
Table 5.5	
Number and specifications of the beams with commercially available fibres.	142
Table 5.6	
Results summary of the shear-critical beams with commercially available fibres.	143
Table 5.7	
Results summary of the flexure-critical beams with commercially available fibres.	146
Table 6.1	
Tensile contribution of fibrous concrete to the flexural performance of RC beams.	150
Table 6.2	
Steel weight used for the RC beam design.	155

LIST OF EQUATIONS

(3.1)	Calculating mean tensile stress of concrete	34
(3.2)	Calculating modulus of elasticity of concrete	34
(3.3)	Uniaxial stress-strain relationship of the cementitious matrices in compression according to MacGregor (1992)	35
(3.4)	Ultimate compressive strain of concrete according to MacGregor (1992)	35
(3.5)	Young's modulus of concrete according to MacGregor (1992)	35
(3.6)	Equivalent frictional shear stress	35
(3.7)	Friction decay (Hallquist 1998)	36
(3.8)	Normal component of contact force (Bathe 1996)	37
(3.9)	Tangential component of contact force (Bathe 1996)	37
(3.10)	Contact status (sticking or sliding)	38
(3.11)	Finite element formulation of contact problems	38
(3.12)	Geometry index of the newly-designed steel fibre	71
(3.13)	Fibre efficiency of the newly-designed steel fibre	71
(3.14)	Mean absolute error (MAE)	72
(4.1)	Moisture content of the aggregates	80
(4.2)	Required aggregates for the mix design based on the current moisture	80
(4.3)	Modification of required water for the mix design considering the aggregates moisture condition	81
(4.4)	Strength correlation between cubic and cylinder concrete specimens	92
(4.5)	Correlation between suddenly-decayed load (P_{f2}) to the peak elastic load (P_{f1}) ratio and fibre volume content (V_f)	100
(4.6)	Correlation between peak post-cracking load (P_{f3}) to the peak elastic load (P_{f1}) ratio and fibre volume content (V_f)	100
(4.7)	Modulus of rupture (f_r)	102
(4.8)	Normalised parameters used in the load-deflection formulation	104
(4.9)	Normalised strains and their correlation with the neutral axis depth ratio (k)	104
(4.10)	Compressive and tensile stresses in the load-deflection formulation	104
(4.11)	Normalised internal bending moment in the load-deflection formulation	106
(4.12)	Normalised internal curvature moment in the load-deflection formulation	106
(4.13)	Critical normalised post-peak tensile stress (μ_{crit})	106
(4.14)	Deflection at first cracking moment (δ_{cr}) for three-point loading	109
(4.15)	Deflection at ultimate moment (δ_u) for three-point loading ($\mu_{crit} > \mu_{crit}$)	109
(4.16)	Deflection at ultimate moment (δ_u) for three-point loading ($\mu_{crit} < \mu_{crit}$)	109
(4.17)	Deflection at first cracking moment (δ_{cr}) for four-point loading	109
(4.18)	Deflection at ultimate moment (δ_u) for four-point loading ($\mu_{crit} > \mu_{crit}$)	109

LIST OF EQUATIONS (CONTINUED)

(4.19)	Deflection at ultimate moment (δ_u) for four-point loading ($\mu_{crit} < \mu_{crit}$)	109
(4.20)	Total load P_i at a given point i in the load-deflection formulation	110
(5.1)	General form of empirical shear design equation for fibrous beams	137
(5.2)	General form of empirical shear design equation for beams	137
(5.3)	Empirical shear design equation for fibrous beams	138
(5.4)	Empirical shear design equation for beams	138
(6.1)	Reinforced (rebar and fibre) section equilibrium	149
(6.2)	Compressive and tensile internal forces of reinforced section	149
(6.3)	Moment of resistance of the section	149

LIST OF APPENDICES

Appendix 3.1	173 ~
A Parametric Code in APDL for Spirally deformed Steel Fibres	186
Appendix 4.1	187 ~
Concrete Mix Design	187
Appendix 4.2	189 ~
Risk Assessment, Job Description: General Considerations	190
Appendix 4.3	191
Risk Assessment, Job Description: Concrete Mixing And Casting, And Cylinder Grinding	
Appendix 4.4	192
Risk Assessment, Job Description: Operating Testing Equipment	

LIST OF ABBREVIATIONS

APDL	ANSYS Parametric Design Language
2D	Two-dimensional
3D	Three-dimensional
FE	Finite Element
FEM	Finite Element Method
FRC	Fibre Reinforced Concrete
GA	Genetic Algorithm
GUI	Graphical User Interface
LVDT	Linear Variable Differential Transformer
NLFEM	Non-linear Finite Element Method
RC	Reinforced Concrete
SFRC	Steel Fibre Reinforced Concrete
HPC	High-Performance Concrete
UHPC	Ultra-High Performance Concrete
UTM	Universal Testing Machine

LIST OF NOTATIONS

a	Shear span, mm;
A_f	Fibre cross-sectional area, mm ² ;
A_s	Cross-sectional area of tension reinforcement, mm ² ;
A_{sw}	Cross-sectional area of the two legs of shear links, mm ² ;
A'_s	Cross-sectional area of compression reinforcement, mm ² ;
b	Width of rectangular beam sections, mm;
c	Contact cohesion, MPa;
d	Effective depth, mm;
d_b	Steel bar diameter, mm;
d_c	Decay coefficient;
d_f	Fibre diameter (wire diameter), mm;
d'	Depth of compression reinforcement, mm;
E	Young's modulus of concrete (fibrous concrete) in Tension, GPa;
E_c	Young's modulus of concrete, GPa;
E_{cr}	Post-cracking modulus of concrete in Tension, GPa;
E_f	Fibre efficiency;
$E_{f, FE}$	Fibre efficiency obtained from finite element simulation;
$E_{f, Pre.}$	Fibre efficiency calculated from the proposed empirical equation;
E_s	Young's modulus of steel, GPa;
E_t	Total dissipated pullout energy, N.mm;
f_c	The specified characteristic cylinder strength of concrete, MPa;
$f_{cd} (f_{ck} / \gamma_c)$	Design cylinder strength of concrete, MPa;
$f_{ck} \text{ (or } \hat{f}_c)$	Cylinder strength of concrete from experiment, MPa;
$f_{ck, cube}$	Cube strength of concrete from experiment, MPa;
f_{ctm}	Mean tensile stress of concrete, MPa;
$f_{ctm,pc}$	Mean post-cracking tensile stress of concrete, MPa;
f_m	Target mean cylinder strength of concrete for concrete mix design, MPa;
f_n	Normal component of contact force;
$f_r \text{ (or } f_f)$	Modulus of rupture, MPa;
f_t	Tangential component of contact force;
f_u	Ultimate stress of steel, MPa;
f_y	Yield stress of steel, MPa;
$f_{yd} (f_y / \gamma_s)$	Design stress of steel, MPa;
f_X^D	Residual strength at net deflection of L/X ;
F	Force vector;
F_{cc}	Compressive force in concrete, kN;

LIST OF NOTATIONS (CONTINUED)

F_f	Fibre factor;
F_{st}	Tensile force in steel, kN;
g_n	Penetration along the normal direction;
g_t	Penetration along the tangential direction;
I_{ge}	Fibre geometry index;
k	Neutral axis depth ratio;
k_n	Normal penalty stiffness, N/mm;
k_t	Tangential penalty stiffness, N/mm;
K_b	Stiffness matrix of the contacting bodies;
K_c	Contact stiffness matrix;
l_f	Fibre length, mm;
l_{em}	Embedded length, mm;
L	Clear span of beams;
L_d	Pullout load decay;
L_p	Plastic length for crack localisation in beams;
M	Bending moment;
M_{cr}	Moment at first cracking, kN.m;
M_i	Moment at stage i , kN.m;
$M_{int.}$	Moment of resistance of the section, kN.m;
M_u	Ultimate moment carrying capacity, kN.m;
M'_i	Normalised moment at stage i with moment at first cracking (M_i / M_{cr});
P	Load;
P_{max}	Maximum pullout load, N;
P_s	Pitch of spring (or spirally deformed fibre);
S	Spacing of shear links, mm;
T^D_X	Toughness (area under the load vs. net deflection curve 0 to L/X);
u	Displacement vector;
v_{fc}	Shear strength of an FRC beam without stirrups;
V_{Ed}	Maximum shear force, kN;
V_f	Fibre volume content;
$V_{Rd,c}$	Shear capacity of concrete, kN;
$V_{Rd,max}$	Maximum design value of shear which can be resisted by the concrete strut, kN;
x	Neutral axis depth, mm;
z	Lever arm, mm;
α	Normalised transition strain with first cracking strain ($\epsilon_{trm} / \epsilon_{cr}$);
β	Normalised tensile strain at the bottom fibre with first cracking strain ($\epsilon_{tbot} / \epsilon_{cr}$);

LIST OF NOTATIONS (CONTINUED)

β_{tu}	Normalised ultimate tensile strain with first cracking strain ($\varepsilon_{tu} / \varepsilon_{cr}$);
γ	Ratio of Young's modulus of concrete in compression to tension (E_c / E);
γ_c	Partial safety factor for concrete;
γ_s	Partial safety factor for steel;
δ	Net deflection;
δ_{cr}	Deflection at first cracking moment;
δ_u	Deflection at ultimate moment;
ε	Normal strain;
ε_{cr}	First cracking tensile strain;
ε_{ctop}	Compressive strain at the top fibre;
ε_{cu}	Ultimate compressive strain of concrete (or fibrous concrete);
ε_{cy}	Compressive yield strain of concrete (or fibrous concrete);
ε_{st}	Tensile strain of steel;
ε_{tbot}	Tensile strain at the bottom fibre;
ε_{trn}	Transition strain;
ε_{tu}	Ultimate tensile strain of fibrous concrete;
ε_u	Ultimate strain of steel;
ε_y	Yield strain of steel;
η	Ratio of post-cracking modulus to Young's modulus of concrete in tension (E_{cr} / E);
θ	Angle of diagonal concrete strut;
λ	Normalised compressive strain at the top fibre with first cracking strain ($\varepsilon_{ctop} / \varepsilon_{cr}$);
λ_{cu}	Normalised ultimate compressive strain with first cracking strain ($\varepsilon_{cu} / \varepsilon_{cr}$);
μ	Normalised post-peak tensile stress (in the constant stress region);
μ_{crit}	Critical normalised post-peak tensile stress;
μ_d	Dynamic coefficient of friction;
μ_f	Frictional coefficient;
μ_s	Static coefficient of friction;
v	Slip rate, mm;
ν_c	Poisson's ratio of the concrete;
ν_s	Poisson's ratio of the steel;
ρ	Longitudinal reinforcement ratio;
ρ_c	Normal contact pressure;
ρ_f	Fibre bond factor;
ρ_s	Tension reinforcement ratio (A_s / bd);
ρ'_s	Compression reinforcement ratio (A'_s / bd);
σ	Normal stress;

LIST OF NOTATIONS (CONTINUED)

σ_c	Compressive stress, MPa;
σ_{cr}	Cracking tensile stress, MPa;
σ_{cst}	Post-cracking stress in the constant stress region;
σ_{ctop}	Compressive strain at the top fibre;
σ_{cy}	Compressive yield stress of concrete (or fibrous concrete);
σ_{st}	Tensile stress of steel, MPa;
σ_t	Tensile stress, MPa;
σ_{tbot}	Tensile stress at the bottom fibre;
τ	Average fibre-matrix interfacial bond stress;
τ_e	Equivalent shear stress, MPa;
τ_{max}	Maximum shear stress, MPa;
ϕ	Curvature;
ϕ_{cr}	Curvature at first cracking;
ϕ_i	Curvature at stage i ;
ϕ_u	Ultimate curvature;
ϕ'_i	Normalised curvature at stage i with curvature at first cracking (ϕ_i / ϕ_{cr});
ω	Normalised compressive yield strain with first cracking tensile strain ($\varepsilon_{cy} / \varepsilon_{cr}$);

CHAPTER 1

INTRODUCTION

1.1. BACKGROUND

Concrete is a durable construction material which can be formed into varying shapes and sizes ranging from a simple rectangular column to a slender curved dome. The relatively low tensile strength and ductility, and poor resistance to crack opening and propagation, i.e. brittleness, are the main disadvantages of concrete. Once cracking is initiated, concrete drastically loses its load carrying capacity in tension. This limitation to practical applications of plain concrete is overcome by the inclusion of steel reinforcing bars which have higher tensile strength and ductility. They are usually embedded in the concrete, known as Reinforced Concrete (RC). In other words, this composite material is made to simultaneously utilise the compressive strength of concrete and tensile strength of steel. Due to relative advantages of reinforced concrete such as low cost, material availability, easy maintenance, and good resistance to fire, it is widely used in various types of structures around the world. Along with the advantages, reinforced concrete also possesses some disadvantages mainly attributed to the low tensile strength of the concrete which could result in the concrete cracking and consequently deterioration of reinforced concrete structures (Naaman and Najm 1991, Mosley, Bungey et al. 2007).

On the other hand, discontinuous and short fibres which are randomly distributed within the concrete could be employed to improve tensile strength of the concrete. The idea of using discrete fibres to reinforce brittle construction materials has been in practice for many centuries. For instance, ancient Egyptians used straw to improve the post-cracked behaviour of sun-dried mud bricks for huts (Mansour, Srebric et al. 2007, Brandt 2008). However, no significant development for discrete fibre reinforcement technology was achieved until the early 1960s. The reports from Romualdi and Batson (1963) followed by Romualdi and Mandel (1964) initiated a modern era in research and development of this technology where the feasibility of improving the tensile strength of concrete using steel fibres was demonstrated. In the following decades, extensive research was conducted to expand on this finding. There are varying fibre materials such as steel, carbon, glass, plastic, polypropylene, and nylon, however, steel is the most suitable for structural applications (Brandt 2008).

Findings of the investigations are indicative of the significant effect of the fibres on the brittle response of the concrete material. After micro-cracks initiate, the fibres contribution starts as crack growth arrestors, which leads to an increase in the ultimate strength of concrete (Shah and Rangan 1971). If the combined performance of the fibres and the matrix is appropriate, there is a better control of the micro-cracks' opening leading to a delay in the formation of macro-cracks which increases the post-cracked toughness and ductility of the concrete (Batson 1976, Vandewalle 1999). Hence, a significant improvement in crack control is achieved in the concrete, with a reduction in width and spacing of the cracks (Grzybowski and Shah 1990, Banthia, Azabi et al. 1993). The smaller crack widths would promote an improvement in the long-term serviceability of the structures by reducing the permeability of the chemicals and water which can have deleterious effects. This beneficial property of the fibres can be utilised to enhance durability and serviceability of RC structures and enable them to sustain for the service lives as originally designed (Wang, Backer et al. 1987).

Fibre Reinforced Concrete (FRC) provides advantages over the use of conventional reinforced concrete for non-structural applications such as cost saving, distributing localised stresses, and reducing crack widths and surface permeability. In other words, fibres are a viable alternative to the secondary reinforcement such as shrinkage and

temperature reinforcement. FRC can be used in highway/airport runway overlays and industrial floors, thin-sheet materials, nuclear reactor shielding, pile caps, and tunnel wall linings (!!! INVALID CITATION !!! (Wang, Backer et al. 1987, Bernard 2002, ACI Committee 544 2014)). Moreover, there are limited structural applications of FRC, Steel Fibre Reinforced Concrete (SFRC) in particular, such as in precast structural elements (Ferrara and Meda 2006) and footings (Curiger 1995), and for seismic applications and repairs (Mechtcherine 2013). It is shown that the addition of steel fibres, not only could replace the minimum amount of stirrups in RC structures, but also can be used to reduce the need for transverse shear reinforcing bars while improving the overall ductility and controlling crack growth (Sharma 1986, Narayanan and Darwish 1988, Ashour, Hasanain et al. 1992, Li, Ward et al. 1992, Shin, Oh et al. 1994, Khuntia, Stojadinovic et al. 1999, Kwak, Eberhard et al. 2002, Shahnewaz and Shahria Alam 2014). However, the large structural application of SFRC is hindered by the inadequate development of relevant design standards (Richardson and Landless 2009) which are needed to build the confidence of practitioners in the employment of the material (Noghabai 2000, Lee, Cho et al. 2013). This is likely attributable to the benefit-cost ratio of the commercially available steel fibres. Most types of steel fibres on the market at the volume contents generally used in practice do not have favourable structural performance and those which relatively have are expensive and demand restrictive requirements on the concrete matrix properties (Wille and Naaman 2012, Wille and Naaman 2013).

In this research, a newly-designed steel fibre is developed in order to increase the structural efficiency of the steel fibre as a replacement for conventional reinforcement.

1.2. OBJECTIVES AND SCOPE OF THE THESIS

The main significance of this research is to develop a new generation of steel fibre which possesses appropriate structural performance compared with the existing steel fibres on the market.

There are three main objectives in this research project:

1. To develop a new shape of steel fibre with high-performance behaviour, i.e. slip hardening response, in normal concrete.
2. To investigate the performance of the new fibre in enhancing the compressive and flexural characteristics of normal concrete
3. To examine the structural contribution of the new fibre to the shear and flexural performance of Reinforced Concrete (RC) members (beams) and subsequently propose design equations and procedures.

To fulfil the abovementioned objectives, a research programme comprising numerical simulations and experimental tests is undertaken. A three-dimensional Finite Element (FE) model for fibre pullout process is presented where its accuracy is achieved using a comparison of the numerical results with experimental data. Using the model, a series of numerical simulations is performed to examine pullout performance of varying new steel fibres from a concrete matrix where based on the preliminary performance of the fibres, one configuration concept is selected for further studies. Experimental pullout tests of fibres with the new configuration and varying geometrical parameters are conducted for the further enhancement of the numerical model. In order to optimise the fibre pullout efficiency, parametric studies are conducted on the new fibre shape and material where practical aspects are considered.

To evaluate material properties of normal concrete with the fibre, a series of material testing including compression and flexure tests are performed on the specimens with various fibre volume contents and concrete strengths. In addition, an analytical method is employed to back-calculate the material behaviours of fibrous concrete in compression and tension from the load-deflection response of the specimens under bending. The material behaviour results are employed for the structural analysis of SFRC members.

Subsequently, in order to study the structural contribution of the newly-designed steel fibre to the shear and flexural behaviour of RC members, two categories of beams, i.e. flexure-critical and shear-critical, are designed, cast, and tested. Fibre volume content,

concrete strength, longitudinal reinforcement ratio, and shear span to effective depth are considered as the experiment parameters.

1.3. LAYOUT OF THE THESIS

This research project comprises a series of non-linear finite element analyses, experimental tests, and analytical methods to develop a high-performing steel fibre for normal concrete which possesses effective contribution to the structural performance of RC members. This thesis is divided into seven chapters as below:

Chapter 1 provides a brief overview of FRC as well as objectives and contents of this research study.

Chapter 2 presents a review of FRC technology and classification. The chapter also encompasses a summary of SFRC properties and applications, and research available to date in the material evaluation and structural applications which include experimental works, analytical studies, and finite element simulations.

Chapter 3 reveals a non-linear FE model for steel fibre pullout from cementitious matrices which is employed as a virtual laboratory unit to simulate pullout mechanism of different new preliminary steel fibres from concrete. Given the pullout performance, one fibre is selected for further investigations. A repetitive procedure consists of experimental pullout tests and FE simulations are performed to optimise the material and geometrical properties of the fibre.

Chapter 4 covers the material testing of FRC with the newly developed steel fibre (including compression and flexure tests) to evaluate the effectiveness of the fibre in enhancing material properties of concrete. The specimens' dimensions, mixing and casting procedures, workability observations, material properties, and test instrumentation and setups are provided. Experimental results are presented and comparisons of the findings in terms of fibre volume content and compressive strength of concrete are discussed. The flexural test results are utilised to back calculate material properties of the FRC in compression and tension, i.e. constitutive models, to reach some preliminary conclusions about the structural performance of the new steel fibre.

Chapter 5 discusses the results of the structural testing in which the fibre contribution to shear and flexural capacities is investigated. To achieve this, two sets of RC beams both with the newly-designed steel fibre including flexure-critical and shear-critical specimens, with varying fibre volume contents are constructed and tested. The compression test and third-point loading test are included in the experimental programme. For the first set, i.e. flexure-critical specimens, the compressive strength of concrete and fibre volume content are considered as the experiment parameters. For the second set (shear-critical beams) in addition to those of the first set, shear span-effective depth and longitudinal reinforcement ratios are considered for the experiment parameters. The specimens' specifications, material properties, and test setups are provided in this chapter.

Chapter 6 presents the shear and flexural design procedures of RC beams with the new fibre. An empirical shear equation for the SFRC beams is proposed where an optimisation algorithm is utilised over the shear-critical specimens' results to find the equation with the best. Using capacity values of flexure-critical specimens, fibre contribution (stress block of fibrous concrete) in bending is back-calculated which can be employed for the flexural design of FRC beams.

Chapter 7 summarises the main conclusions drawn from this research. Some recommendations are provided for future investigations.

CHAPTER 2

LITERATURE SURVEY

2.1. INTRODUCTION

Employment of steel reinforcing bars makes concrete a suitable composite material for various structural and non-structural applications. Such bars, however, reinforce concrete against tension only locally where the cracks in reinforced concrete (RC) members can freely initiate and propagate until encountering a rebar. The need for multi-directional and closely spaced reinforcement for concrete led to the introduction of Fibre Reinforced Concrete (FRC). FRC is a cement-based composite material reinforced with discrete, usually randomly distributed, fibres. Fibre reinforcement mainly enhances the post-cracking properties of concrete and leads to a more ductile material behaviour. The increased ductility is due to the ability of fibres to transfer tensile stresses across the cracked sections, potentially leading to a reduction in crack widths. However, the fibres available on the market (with the practical fibre dosages and normal matrix compositions) have a marginal contribution to the bearing capacity of FRC members. Due to the fibres' performance, the overall internal force transferred by the fibres through the cracked sections (bridging contribution of fibres) is generally less than the internal force transferred through the section before cracking.

There is a wide range of research ongoing with emphasis on the fibres' applications and development (in terms of material and geometry) to advance applications of the fibres in practice.

2.2. FIBRE TYPES AND CLASSIFICATION OF FRC

Based on the material, fibres applied for construction purposes can be categorised into four major groups:

- Steel fibres with varying shapes (deformed and undeformed) and dimensions (micro and macro fibres);
- Glass fibres, mainly used in cement matrices as alkali-resistant (AR) fibres;
- Synthetic fibres made with different materials such as polypropylene, polyethylene, polyolefin, and polyvinyl alcohol (PVA);
- Carbon, pitch and polyacrylonitrile (PAN) fibres.

The susceptibility of glass fibres to environmental conditions, i.e. durability issues, the high cost of carbon-based fibres, and low modulus of elasticity and interfacial bond of synthetic fibres make such materials less attractive for practical applications. Relative advantages of steel to the other materials, for example, higher Young's modulus and tensile strength, make it the most common and important fibre material for structural purposes (Brandt 2008).

In the early days of Steel Fibre Reinforced Concrete (SFRC), the fibres were mostly undeformed (Banthia and Trottier 1994). The crack bridging performance of such fibres directly depends on the physical and chemical adhesions between the fibres and the surrounding matrix (the physiochemical bond) which are predominantly determined by the properties of the fibre-matrix interface and matrix packing density (Wille and Naaman 2012). Findings of numerous studies indicate that mechanical anchorage in the deformed fibres effectively improves pullout resistance (Naaman and Najm 1991, Banthia and Trottier 1994, Carnovale 2013). The mechanical bond properties are determined by the physical geometry of the fibre and the transverse tensile stress resistance of the matrix. The mechanical anchorage could be achieved by having deformation at the fibre ends, such as with hooked-end fibres or deformation along the fibre length, such as in crimped or twisted fibres (Wille and Naaman 2012). Typical steel fibres are shown in **Fig. 2.1**.

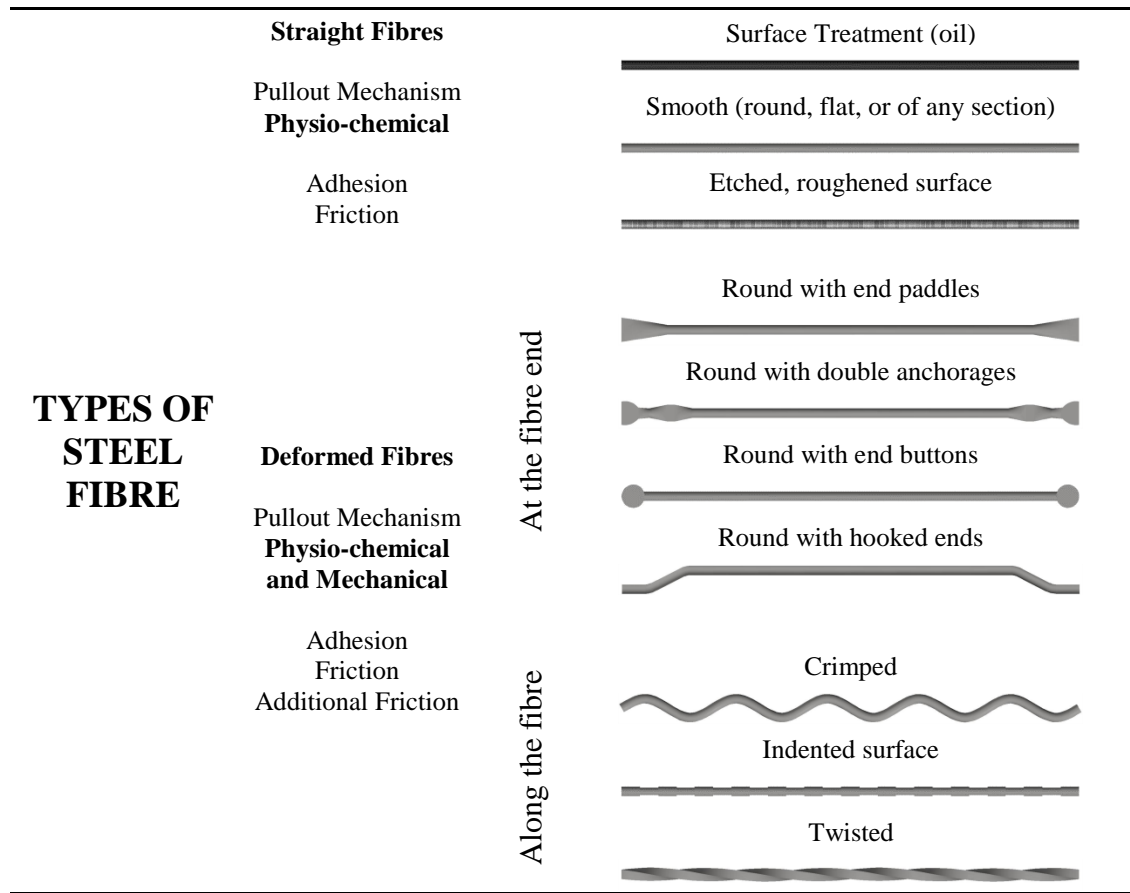


Fig. 2.1. Various types of steel fibre grouped according to their bond characteristics.

A general and simple classification of FRC composites is illustrated in **Fig. 2.2** which is based on the material response after first cracking under direct tensile loadings and bending moments (Naaman and Reinhardt 2003). The key distinguishing characteristic is that whether the post-cracking response of the composite under direct tension is strain-hardening or strain-softening, and within the latter category under bending, whether it is deflection-hardening or deflection-softening. If the resultant force transferred through the fibres, bridging a cracked section is greater than (or equal to) the tensile force at the section before the cracking, it is known as strain-hardening behaviour. For the members under flexure, after the first cracking if with the increase in mid-span deflection, the load increases, it is considered as deflection-hardening behaviour.

The strain-hardening composite material is deemed to have better mechanical performance than a strain-softening one. Results of previous research indicate that the

employment of strain-hardening FRC composites can significantly improve the seismic performance of concrete structures subjected to cyclic loadings as well as their impact and blast resistance (Naaman and Reinhardt 2006). A tension strain-softening composite can show either deflection-hardening or deflection-softening response. Composites with deflection-hardening behaviour are suitable for structural applications where bending prevails, while deflection-softening materials encompass a wide range of applications starting at the lower end by the control of plastic shrinkage cracking of concrete, to the higher end where they are used in slabs-on-grade (e.g. industrial floors), runways, and road pavements.

Most types of steel fibres on the market do not give hardening behaviour when they are used with normal concrete at practical fibre content ratios and those which have such as twisted steel fibre are relatively expensive and demand restrictive requirements on the concrete composition (Wille and Naaman 2012, Wille and Naaman 2013).

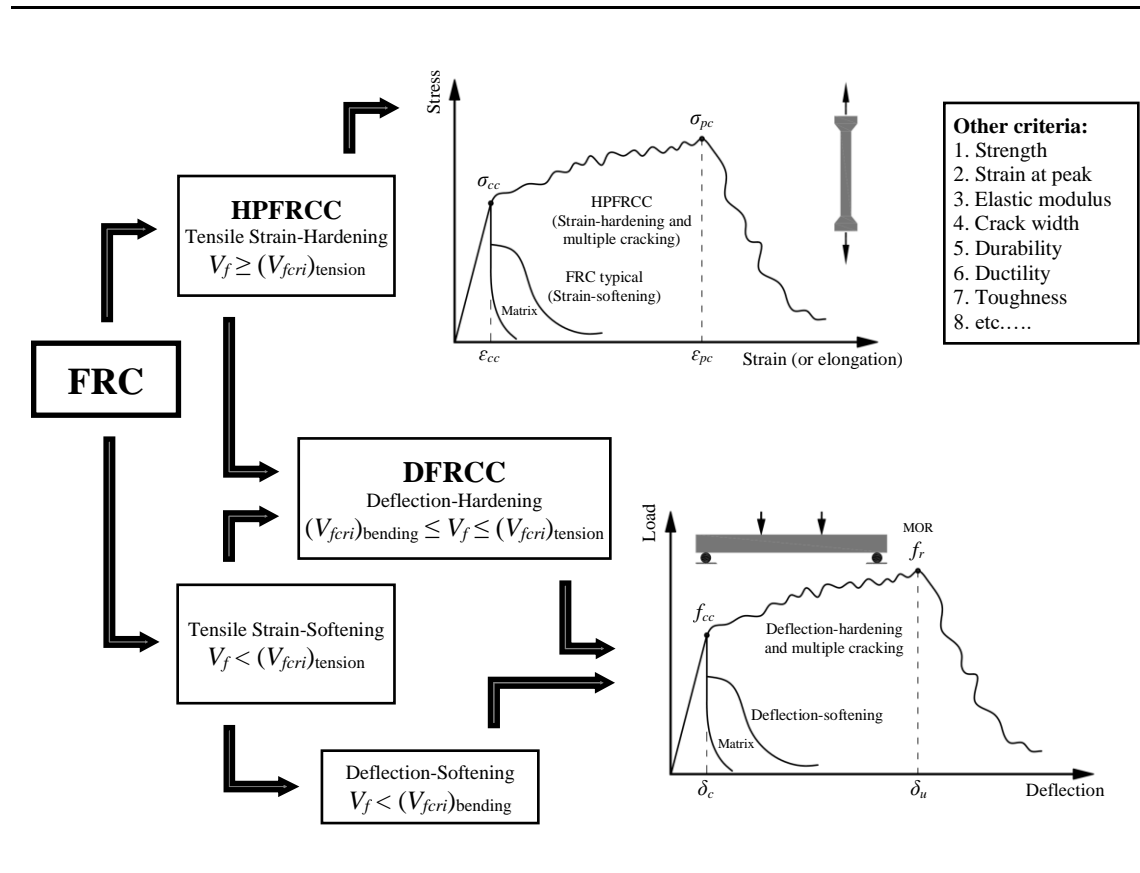


Fig. 2.2. FRC classifications.

2.3. STEEL FIBRE REINFORCED CONCRETE (SFRC)

The idea of steel fibre being employed to strengthen concrete was first suggested by Porter in 1910, but no significant progress was achieved in its development until 1963, when Romualdi and Batson (1963) conducted extensive experimental investigations on Steel Fibre Reinforced Concrete (SFRC) in the United States and published the first scientific research paper on the subject (Naaman 1985).

SFRC is a mixture of conventional hydraulic cement, fine and coarse aggregates, water, and steel fibres. Commercially available steel fibres have varying geometry (aspect ratio, cross-section, and shape) and material properties which are sufficiently small to be easily, evenly, and randomly distributed within the fresh concrete mix using conventional mixing procedures. Superplasticizers (chemical admixtures) may also be added to the concrete mix to enhance the workability of SFRC (Behbahani 2011).

2.3.1. SFRC PROPERTIES

The crack bridging mechanism of steel fibres leads to a delay in the cracks propagation and consequently enhancement of post-cracking behaviour and energy absorption capacity of the structures. However, the level of SFRC performance is influenced by a number of variables.

2.3.1.1. FIBRE VOLUME CONTENT

Fibre volume content is one of the key parameters affecting the behaviour of SFRC. As the number of fibres increases, the probability of more fibres bridging any possible cracks increases. Findings of extensive direct/in-direct tension and shear tests, indicate that the increase in the fibre dosage leads to improvements of toughness, ductility, and strength (Shah and Rangan 1971, Khaloo and Kim 1997). It was shown that toughness (the area under the load-deflection diagram) and ductility are improved significantly with an increase in the fibre content; however, strength is just marginally improved. As seen in **Fig. 2.3(a)**, the concrete uniaxial tensile toughness is improved from 1.8 times to 2.7 times that of the plain concrete by increasing the fibre content from 0.5% to 1.0%; however, the concrete uniaxial tensile strength is only increased from 1.1 times to 1.3

times that of the plain concrete. The level of improvement is higher in flexure tests (see **Fig. 2.3(b)**).

High fibre volume contents could result in a strain-hardening response, a favourable performance where the maximum tensile strength of the concrete is higher than the first cracking strength (Naaman 1987), however, the exact amount of fibres required to achieve strain-hardening behaviour depends on other properties of the fibre and the matrix (Setkit 2012).

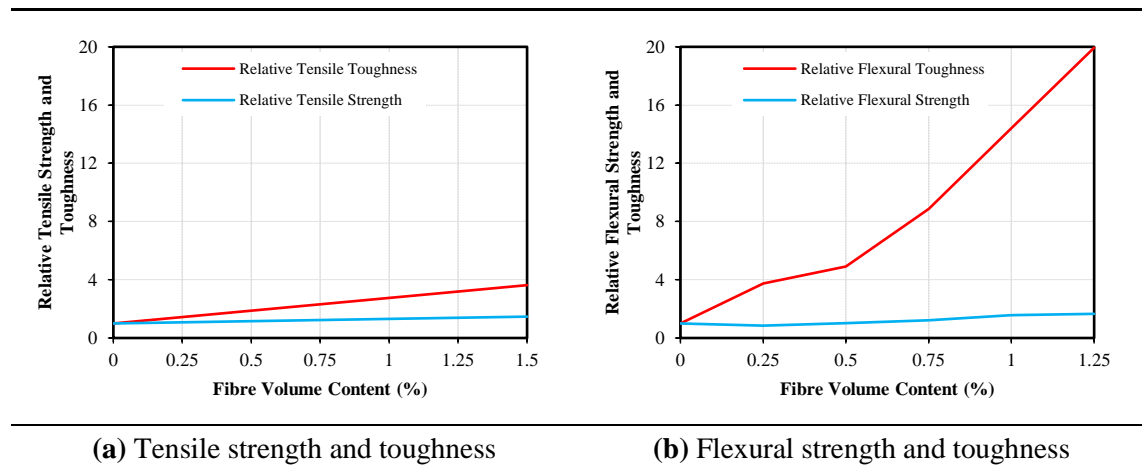


Fig. 2.3. Effect of fibre volume content on the SFRC performance (Shah and Rangan 1971).

As seen in **Fig. 2.4(a)**, increasing the fibre content enhances the compressive post-peak response of concrete (Fanella and Naaman 1985) with a lowering of the rate of strength decay. Fibre volume increase has a slight effect on the other characteristics of concrete such as modulus of elasticity and peak load (Luo 2014).

Despite the advantages associated with increases in the fibre dosage, limits should be considered on the maximum fibre amount due to workability and bundling issues. Increasing of the fibre content decreases the mixture workability since the fibres reduce the paste volume fraction available for the free movement of coarse and fine aggregates. On the other hand, increasing the fibre content could result in balling of the fibres in the mixes. Producing SFRC with high fibre dosages often demands special mixing and placing procedures (Zollo 1997).

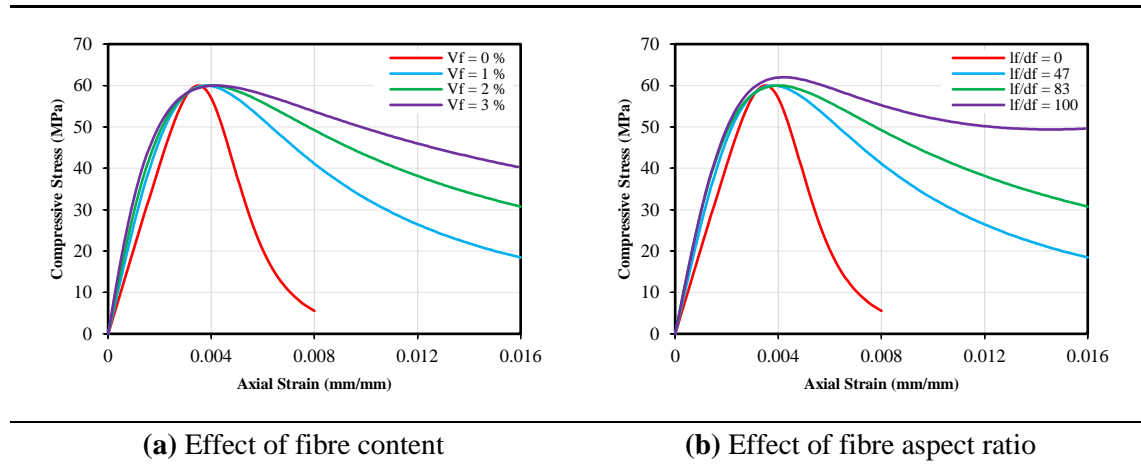


Fig. 2.4. SFRC compressive stress-strain curve (Fanella and Naaman 1985).

2.3.1.2. FIBRE ASPECT RATIO

The ratio of length to diameter of the fibre, i.e. fibre aspect ratio, has an important effect on the overall performance of the fibres. With the same fibre content, a higher aspect ratio results in improvement of the overall fibre-matrix interface which leads to an improved bond between the fibres and the matrix (Naaman 2003).

Findings of flexure and direct tension tests carried out by Shah and Rangan (1971) indicate that fibres with higher aspect ratio (same diameter but various lengths) significantly increase toughness, even though it has a marginal effect on the strength. As can be seen in **Fig. 2.4(b)**, fibrous concrete cylinders with higher fibre aspect ratios show better post-peak responses resulting in significant increases in toughness and ductility (Fanella and Naaman 1985).

2.3.1.3. FIBRE GEOMETRY (LENGTH AND SHAPE)

Fibre length has a key role on the SFRC behaviour. With the same fibre aspect ratio, shorter/smaller fibres result in a considerable larger number of fibres required to achieve the same fibre volume content. This larger amount of fibres improves the crack bridging mechanism and stress transfer across the cracks (particularly at the early stage of cracking) and consequently leads to higher peak loads. However, short embedment length of fine fibres causes relatively higher decay rates in the post-peak characteristics of SFRC compared with the long fibres. Therefore, long fibres have a higher

contribution to the overall performance of the structures at the ultimate state where large deformations are expected (see **Fig. 2.5**).

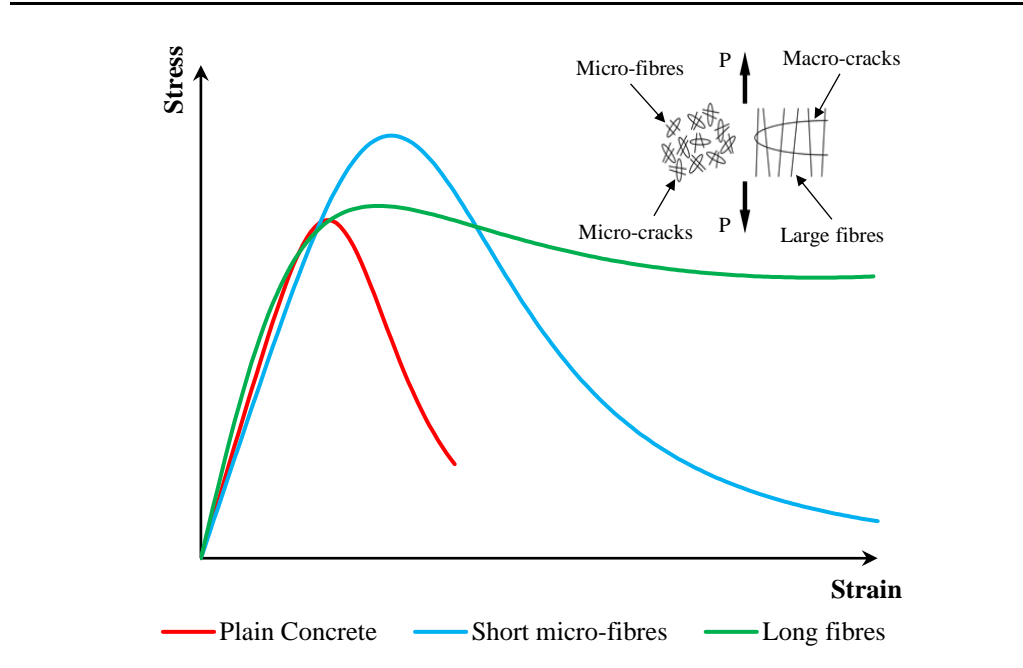


Fig. 2.5. Crack propagation mechanism of long and short fibres (Brandt 2008).

The properties of SFRC material is mainly governed by the fibre-matrix interfacial bond characteristics. Findings of numerous experimental tests are indicative of the major role of mechanical anchorage in the bond between the deformed steel fibres and the matrix (Wille and Naaman 2012).

2.3.1.4. FIBRE ORIENTATION

The fibre-matrix interfacial bond is affected by fibre orientation, i.e. the fibre inclination angle with respect to the crack opening direction (Shah and Rangan 1971). Banthia and Trottier (1994) carried out an experimental programme to investigate the effect of fibre inclination angle of deformed steel fibres (hooked-end, crimped, and flat-end) on the pullout characteristics. It was concluded that the fibres aligned in the loading direction demonstrate the most efficient pullout response compared with the non-perpendicular fibres. Lee, Kang et al. (2010) conducted a series of pullout tests on straight steel fibres embedded in ultra-high strength cementitious matrices with various inclinations. The

results indicate that the largest peak load is achieved at the inclination angle ranges from 30° to 45°. In addition, with the increase in the inclination, the embedment length decreases which consequently affects the effectiveness of the fibres, i.e. energy absorption capacity.

The orientation of fibres is affected by the rheological properties of the mix, the geometry of the formwork, the casting procedure, and the type of vibration (Álvarez 2013).

2.3.1.5. FIBRE AND MATRIX MATERIAL

The complete fibre pullout from concrete is the most favourable failure mechanism of SFRC which results in the largest dissipated pullout energy in comparison with the fibre fracture and matrix damage which are brittle failures (Banthia and Trottier 1994).

Depending on the fibre geometry, the material strength of the fibre and matrix should be optimised to ensure the complete withdrawal of the fibre could be achieved.

2.3.1.6. FIBRE SURFACE AND MATRIX COMPOSITION

The crack bridging performance of a steel fibre directly depends on the physiochemical bond (the physical and chemical adhesions between the fibre and the surrounding matrix) and its mechanical anchorage. While the chemical adhesion and the mechanical anchorage respectively depend on the chemical characteristics of the materials and the fibre shape, the physical bond relies upon the collaborative contribution of the fibre surface and matrix. Just after the full debonding and initiation of slippage, depending on the fibre coating characteristics and matrix composition, the fibre surface experiences continuous damage, scratching, and delamination which leads to a gradual increase in the physical interface bond (Wille and Naaman 2012, Wille and Naaman 2013); however, in most cases the interface bond improvement is negligible.

There are examples of commercially available steel fibres such as brass-coated straight and twisted fibres which are engineered in terms of surface coating and geometry for compatibility with high/ultra-high performance concretes (HPC and UHPC) to achieve higher rates of increase in the fibre-matrix interface friction which could result in a hardening pullout response (Naaman 2003, Lin and Quek 2007).

Microscopic images of the surface of a brass-coated steel fibre before pullout and after pullout from UPHC are shown in **Fig. 2.6** which are indicative of extensive damage to the fibre surface due to the pullout process.

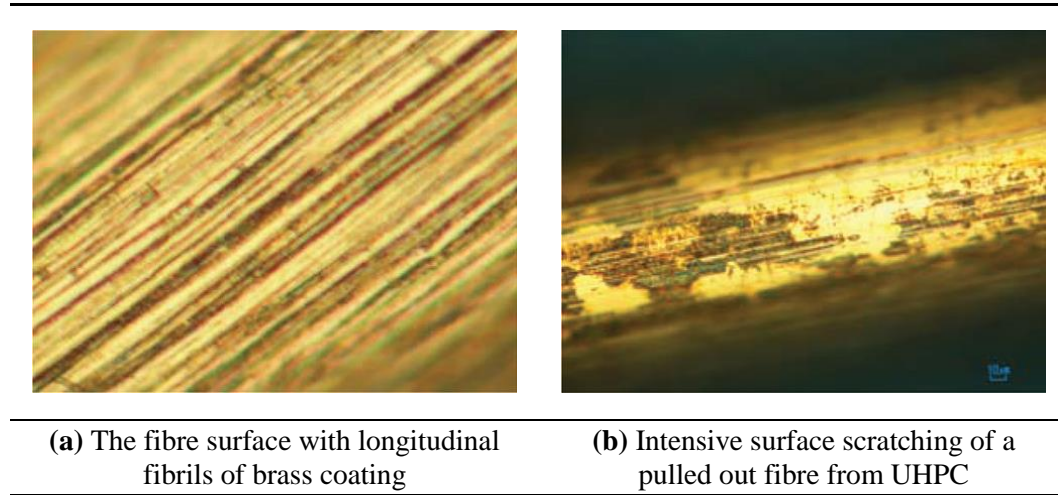


Fig. 2.6. Brass-coated steel fibre surface and its damage during pullout from UHPC (Wille and Naaman 2013).

2.3.2. APPLICATIONS

Concrete permeability plays a profound role in the degradation of Reinforced Concrete (RC) members as a result of sulphate attack, freeze-thaw cycling, alkali-silica reaction, the chlorite attack, carbonation, and corrosion of embedded reinforcing bars (Banthia, Bindiganavile et al. 2012). Therefore, the durability of RC elements is influenced by the rate at which water may seep into the matrix. The crack bridging mechanism of fibres could be exploited to improve concrete crack resistance and consequently reduce the permeability of concrete. SFRC is widely used in the construction industry as a replacement for secondary reinforcement to provide requirements of serviceability and durability designs. There is a wide range of non-structural applications for steel fibres such as in precast elements, blast resistant structures, ground floor slabs, thin shell, walls, pipes, and manholes, tunnel lining and slope stabilisation, dams and hydraulic structures, runway, aircraft parking aprons, and pavements. Examples of SFRC applications are shown in **Fig. 2.7** (Zollo 1997, Brandt 2008).

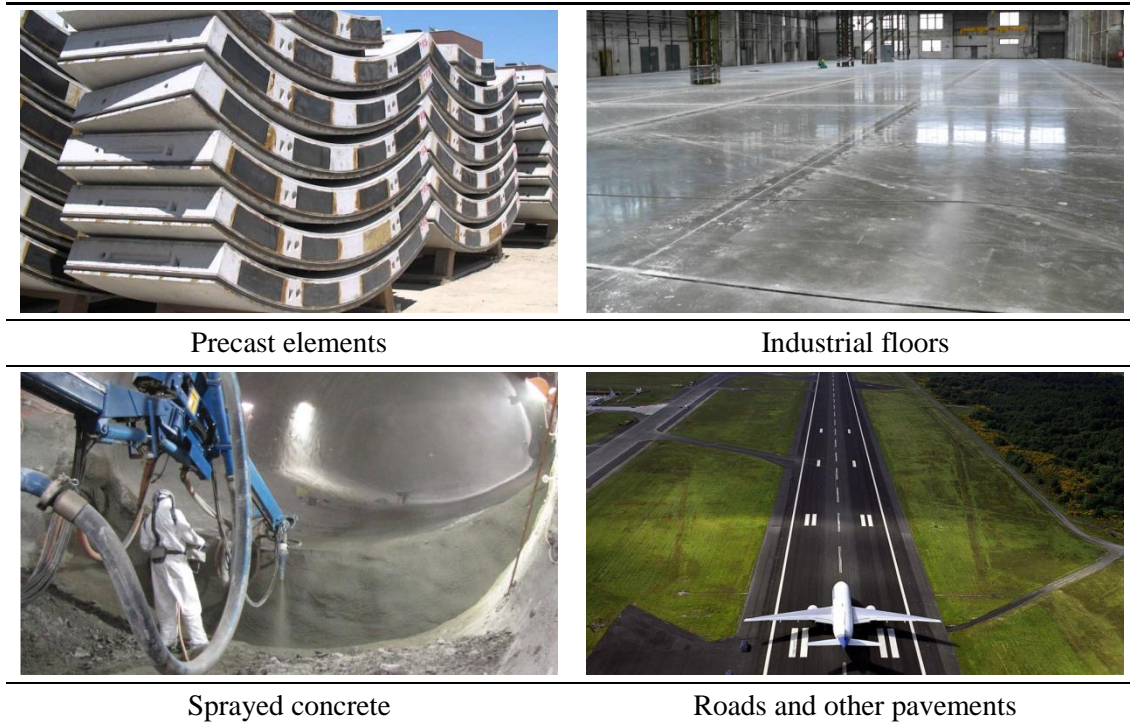


Fig. 2.7. Traditional applications of SFRC (Brandt 2008).

It is shown that deformed steel fibres could replace the minimum amount of stirrups in RC structures to provide adequate reserve shear strength (ACI 318-08 2008). Furthermore, findings of numerous investigations indicate that steel fibres possess a potential role in the shear capacity of RC members and they can be employed as a partial/full replacement for shear links (Narayanan and Darwish 1988, Noghabai 2000, Kwak, Eberhard et al. 2002). However, the unfavourable structural performance of commercially available steel fibres hindered SFRC adoption as a structural alternative to conventional reinforcement and its use is generally confined to the improvement of cracking control (Shahnewaz and Shahria Alam 2014). Commercially available steel fibres for normal concrete such as hooked-end and crimped fibres possess slip-softening behaviour (after the peak load at the early stage of the pullout, as the slip increases, the pullout load decreases). It implies that at the ultimate capacity of structures where excessive deformations and wide cracks are expected, the overall structural contribution of the fibres to the load bearing capacity of SFRC members is negligible.

2.3.3. EXPERIMENTAL INVESTIGATIONS

Since the introduction of steel fibres in concrete, numerous experimental investigations have been conducted to study the effects of such fibres interacting with concrete. The investigations are classified into material and structural testing.

2.3.3.1. MATERIAL TESTING

Properties evaluation of SFRC is necessary for the material to be employed effectively and economically in practice. There are various standards and testing methods for the evaluation of properties of SFRC. However, there is no agreement on which standard/method is the best for a specific structural application. This could be a major reason hindering the introduction of SFRC into structural design guidelines and codes (Chao, Cho et al. 2011).

This section discusses four major material evaluation methods (fibre pullout test, flexure test, direct tension test, and compression test) where a literature survey on each method is also presented.

2.3.3.1.1. *Fibre Pullout*

The mechanical behaviour of SFRC is mainly governed by the fibre-matrix interfacial bond characteristics. Such characteristics are best described by a bond-shear-stress-slip relationship; however, the direct experimental determination of such a relationship has not yet been possible. Therefore, a load versus slip response which can be obtained from the fibre pullout test is employed to study the characteristics of the fibre-matrix interface (Naaman, Namur et al. 1991 a, Kim, Naaman et al. 2009).

There is no standard method for this type of test; however, there are two different test setups used by researchers, i.e. single-sided and double-sided setups. In a single-sided pullout test, one side of the fibre with the intended angle of inclination and embedment length is placed in concrete and the other side is gripped to apply pullout load. In contrast, in the double-sided setup, the whole length of the fibre with the intended inclination angle is placed within two separate concrete blocks with consideration of intended embedment lengths for each side of the fibre (see **Fig. 2.8**). The deformation (elastic/plastic) at the free end of the fibre in the single-sided pullout test might affect the accuracy of the results; however, due to the difficulties involved in casting the

specimens for double-sided tests, it is not common (Chin and Xiao 2012, Wille and Naaman 2012).

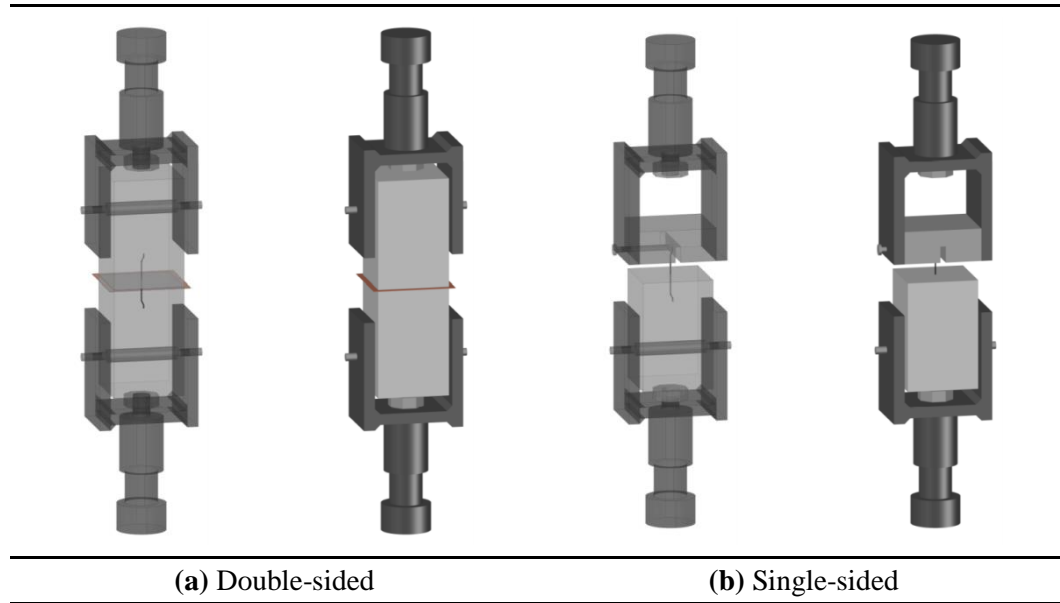


Fig. 2.8. Pullout test setups.

Numerous investigations have been performed to study the fibre-matrix pullout behaviour in which the most investigated parameters are fibres geometry and type, strength and composition of the matrix, surface treatment (coating) of fibres, the orientation of fibres, and loading rate.

Naaman and Najm (1991) performed pullout tests to study the influence of fibre shape (hooked-end and straight fibres) on the pullout response where other experiment parameters remained unchanged. It was shown that the mechanical anchorage enhances the bond-slip characteristics, i.e. maximum pullout load and total dissipated pullout energy. A comprehensive study was conducted by Chin and Xiao (2012) to investigate the effect of fibre geometry on the pullout response of steel fibres. The investigated fibres were corrugated, flat-end, hooked-end, crimped, and double-anchored. It was concluded that the pullout peak load and the pullout toughness are correlated to the size, amount, intensity, or degree of deformation if complete fibre pullout occurs.

The premature failure of the fibre pullout process, i.e. matrix splitting or fibre fracture, in general, is expected in cementitious matrices with higher strengths (Banthia and

Trottier 1994). Depending on the collaborative contribution of the fibre surface (coating) and the matrix, the physiochemical bond at the interface could increase which enhances the pullout response (Wille and Naaman 2012, Wille and Naaman 2013).

It is shown that the inclination angle has a different influence on the pullout response. Regarding straight steel fibres, the largest peak load is achieved when they are inclined with respect to the loading direction (at angle ranges from 30° to 45°); however, deformed steel fibres show optimal performance when they are aligned in the loading direction (Banthia and Trottier 1994, Lee, Kang et al. 2010).

The rate of loading affects the fibre-matrix interfacial bond; as the loading rate increases, the bond increases. However, at high loading rates, the possibility of fibre fracture is higher (Boshoff, Mechtcherine et al. 2009, Abu-Lebdeh, Hamoush et al. 2010).

2.3.3.1.2. Flexure Test

The flexural performance of SFRC material can be evaluated using parameters derived from the load-deflection curve obtained by testing a simply supported beam under three- or four-point bending (Banthia and Trottier 1995).

The most widely used standard for flexure test is ASTM C1609/C1609M - 12 (2012). In this test method, a rectangular yoke, which surrounds the specimen and is clamped to it at mid-depth directly over the supports, is employed to measure the net deflection (see Fig. 2.9).

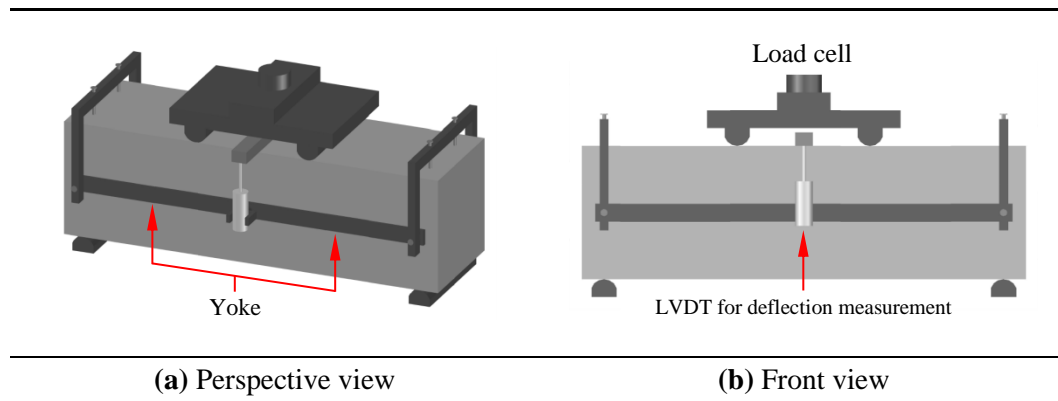


Fig. 2.9. Flexure test setup (ASTM C1609/C1609M - 12 2012).

Two displacement transducers such as LVDTs are mounted on the yoke at mid-span, one on each side, to measure the beam deflection through contact with brackets attached to the top of the specimen. The net deflection is the average of the measurements.

There are extensive experimental studies on the flexural characteristics of SFRC where fibre volume content (V_f), fibre aspect ratio (l_f/d_f), fibre shape, and matrix strength (f_{ck}) are the most investigated experiment parameters (see **Sections 2.3.1.1 to 2.3.1.3** and **Sections 2.3.1.5 to 2.3.1.6**).

2.3.3.1.3. Direct Tension Test

The direct tension test can identify the key properties of FRC including strain-hardening or strain-softening, modulus of elasticity, and stress-strain relationship under tension, which is the constitutive behaviour of FRC (Chao, Cho et al. 2011). However, there is no standard method for such a test mainly because it is difficult to provide a proper gripping arrangement to avoid specimen cracking at the end grips. Generally, specimens in dog-bone geometry are employed to ensure cracking would only occur at the central portion of the specimen, within the gauge length. A pair of Linear Variable Differential Transformers (LVDTs) is mounted on both sides of the specimen to measure displacement (see **Fig. 2.10**). To mitigate the stress concentration resulting from the reduction of the cross-section area, the double dog-bone geometries could be used for this test (Wille, El-Tawil et al. 2014).

Numerous investigations have been conducted to study the behaviour of SFRC material under pure tension where fibre volume content (V_f), fibre shape, and specimen dimensions are the most investigated test parameters (Naaman 2003, Naaman 2007, Chao, Cho et al. 2011, Wille, El-Tawil et al. 2014).

The constitutive behaviour of SFRC in tension (stress-strain curve), obtained from direct tension test is useful for modelling and design of SFRC structural members. However, it is shown that such curves are highly sensitive to scale effects which makes the use of large-scale specimens necessary to get a more realistic response (Chao, Liao et al. 2007).

The fibres have negligible effects on the pre-peak response of SFRC (in compression and tension) and their main contribution initiates after cracking (post-peak response) as

crack growth arrestors. Regarding indirect tension test, i.e. Brazilian test (Armelin and Banthia 1997), after the peak load and initiation of cracking, the applied tensile stress on the cracked surfaces cannot remain uniform, therefore the result (load deflection curve and stress-strain relationship) obtained from such a test, cannot represent the post-peak behaviour of SFRC under tension.

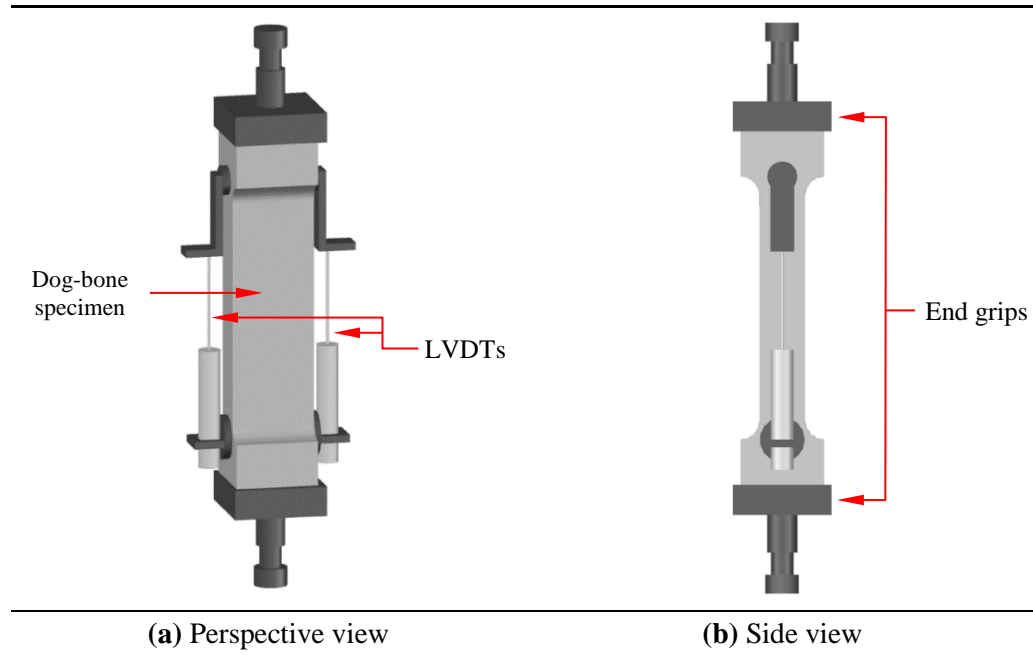


Fig. 2.10. Direct tensile test setup (Wille, El-Tawil et al. 2014).

2.3.3.1.4. Compression Tests

To evaluate the uniaxial compressive characteristics of SFRC such as compressive strength, modulus of elasticity, and stress-strain relationship, the compression test is performed on SFRC specimens. There are two types of standard test specimens, i.e. cylinder and cube, whose dimensions should conform to the requirements given in the codes (Carnovale 2013, Luo 2014).

It was shown that the inclusion of steel fibres in concrete causes a slight decrease in modulus of elasticity since the fibres parallel to the load direction act like voids within the concrete. The compressive strength of SFRC depends on the fibre type, fibre volume content, and the concrete characteristics. The crack bridging mechanism of the fibres works at both the micro- and macro-levels. At the micro-level, fibres arrest the

development of micro-cracks, leading to higher compressive strengths whereas, at the macro-level, fibres control the cracks growth and opening, enhancing the energy absorption capacity of the composite material. The capability of fibres to control the growth of micro-cracks depends mainly on the number and shape of the fibres, and the fibre-matrix interface bond characteristics. As the number of fibres increases, the probability of the fibres bridging micro-cracks increases where depending on the fibre pullout stiffness and the interface bond, the cracks development could be controlled. On the other hand, the addition of fibres especially at high fibre dosages to concrete might cause some workability and compaction issues which could result in higher voidage. The voids can act as defects where micro-cracking initiates. Therefore the influence of fibres on the compressive strength is influenced by the balance between micro-cracks bridging and additional voids caused by fibre addition. Overall, findings of extensive research on the compressive behaviour of SFRC demonstrate that the addition of steel fibres at the common fibre volume contents in practice has marginal influence on the compressive strength and it generally improves the post-peak response of SFRC (Shah and Rangan 1971, Fanella and Naaman 1985, Neves and Almeida 2005, Carnovale 2013, Luo 2014).

2.3.3.2. STRUCTURAL TESTING

The ability of steel fibres to bridge the cracks and transfer tensile stresses across the cracked sections can be employed to enhance material properties of concrete (ductility and tensile strength) to reduce the demand for conventional steel reinforcement. The major industrial incentive in the fibre employment is to cut down the production costs by partially/fully replacing the conventional reinforcement (Luo 2014, Shahnewaz and Shahria Alam 2014). There are numerous investigations on the contribution of steel fibres to the structural behaviour of RC members such as beams, slabs, shear walls, beam-column joints, and coupling beams (Filiatrault, Pineau et al. 1995, Michels, Waldmann et al. 2012, Setkit 2012, Adamantia and Gustavo 2013, Shahnewaz and Shahria Alam 2014). Less difficulties of beams testing (equipment with lower loading capacities and simpler testing setup) compared with other components e.g. columns and connections, make them the most popular testing component where the contribution of fibres to the shear and flexural performance of members can be investigated.

2.3.3.2.1. Beam Tests

The bridging effect of steel fibres can generally prevent tensile cracking localisation and produce multiple cracks. Hence, after the first cracking (either diagonal or vertical flexural) initiates, the role of steel fibres as crack growth arrestors starts which in turn improves the stiffness of SFRC beams and decreases the deflection of the beams (Aoude, Belghiti et al. 2012). The addition of steel fibres can also enhance the ductility and ultimate shear capacity of RC beams (Mansur, Ong et al. 1986, Aoude, Belghiti et al. 2012). Extensive research has been conducted to investigate the contribution of steel fibres to the behaviour of SFRC beams. The experiment parameters mainly include the compressive strength of concrete (f_{ck}), shear span-effective depth ratio (a/d), yield strength of steel (f_y), longitudinal reinforcement ratio (ρ), fibre aspect ratio (l_f/d_f), fibre volume content (V_f), and type of fibre (Shahnewaz and Shahria Alam 2014).

Findings of relevant research indicate that the effectiveness of steel fibres depends on the geometry of the beams. Results of an experimental study performed by Swamy and Bahia (1985) showed that the enhancement of shear strength varies for different types of beams; with 0.8% fibre volume content, the shear strength of T-beams increases 80% while the shear strength enhancement is just 30% for rectangular beams (Ashour, Hasanain et al. 1992, Mansour, Srebric et al. 2007). In addition, as the shear span-depth ratio decreases, the cracking and ultimate loads improve (Mansur, Ong et al. 1986, Ashour, Hasanain et al. 1992).

Parra-Montesinos (2006) performed a quantitative investigation on a compiled database of 147 SFRC beams without shear reinforcement to evaluate the contribution of deformed steel fibres to the shear resistance of RC beams. The results indicate that the minimum shear reinforcement can fully replace by deformed steel fibres with at least 0.75% fibre volume content. A series of full-scale SFRC beams including two different beam sizes with and without minimum shear reinforcement was tested by Aoude, Belghiti et al. (2012) to study the contribution of steel fibres on the overall performance of RC beams. The fibre reinforced cementitious matrix consisted of low strength concrete with hooked-end steel fibres ($l_f/d_f = 55$). The results support the employment of steel fibres as an alternative to the conventional shear reinforcement. It was shown that the load capacity of beams without shear links is significantly increased with the

addition of steel fibres, however, in some cases, a full replacement of shear reinforcement by the addition of 1% fibre cannot be achieved. In addition, the contribution of fibres to the behaviour of flexure-critical beams is negligible, i.e. the addition of fibres does not lead to an increase in the load carrying capacity. This is attributable to the significant tensile straining after longitudinal reinforcement yields; hence the limited tensile straining capacity of fibres restricts the fibres contribution to the post-yielding capacity.

2.3.4. NUMERICAL MODELLING

The fibre pullout mechanism and structural response of SFRC members using constitutive material properties are the main streams of the numerical investigations performed by researchers. The multiscale modelling of SFRC is hindered by the huge computational costs and complexities (Georgiadi-Stefanidi, Mistakidis et al. 2010).

Two-dimensional (2D) FE models for the fibre pullout mechanism were adopted by several researchers (Li and Mobasher 1998, Yang, Qin et al. 2003, Tsai, Patra et al. 2005). Li and Mobasher (1998) developed a 2D model for straight fibres in which a yield surface based on interfacial normal and shear stresses was used for the interface failure and following the interface debonding, the Coulomb frictional stress was applied at the interface. It was shown that the peak pullout load occurs under partial interfacial debonding. The effect of parameters including fibre length, interfacial shear strength, and residual stress on the fibre pullout behaviour was investigated. Tsai, Patra et al. (2005) performed the quasi-static analysis of complete fibre pullout process using the finite element method based on an updated Lagrangian formulation. A combined cohesive and Coulomb friction model was proposed to approximate the non-linearity of the interface behaviour. The parameters of the interface model are determined through comparison of the FE results with those from straight fibre pullout tests. Following the validation, the model was used to design an optimal shape of a flat-end steel fibre to maximise the pullout dissipated energy.

Georgiadi-Stefanidi, Mistakidis et al. (2010) proposed a three-dimensional (3D) FE model for the hooked-end fibre pullout from cementitious matrices. The physiochemical bond of the fibre-matrix interface was taken into account by a number of non-linear

spring elements which transfer the bond stresses through a set of equivalent point loads. Chin and Xiao (2012), also, presented a 3D numerical model to capture the complete pullout response of end deformed and fully deformed steel fibres in which the interfacial bond between the fibre and matrix was defined by the Coulomb friction model.

Numerous numerical studies have been performed to simulate the structural response of SFRC members using the constitutive models. Özcan, Bayraktar et al. (2009) developed a FE model to simulate the response of SFRC beams in which the material properties were adopted from the material testing results. Blanco, Cavalaro et al. (2014) employed the constitutive model of SFRC calculated from flexural test results to estimate the flexural response of slabs using the FE method. A parametric study was conducted to examine the effects of the constitutive model parameters on the flexural response of the slabs, and then to find the best values of the parameters which lead to the best agreement between the FE and the experimental results. It was concluded that the numerical simulations with the constitutive models based on the flexural testing overestimates the structural response of SFRC slabs.

A FE model to investigate SFRC members was proposed by Abbas, Syed Mohsin et al. (2016). Several structural members with different arrangements and loading conditions (monotonic and cyclic) were considered to assess the accuracy of the model in the prediction of SFRC members' response. First, a few SFRC small notched beams were modelled to examine the responses at the material level where good agreement between numerical results and experimental data was achieved. Then, the validated model was employed to investigate the SFRC behaviour at the structural level where different SFRC structural members including simply-supported beams, columns under both axial and lateral forces, and external and internal joints all under monotonic and cyclic loadings were considered. Despite the model simplicity, it was found that the model can reasonably predict the key aspects of the structural behaviour of the SFRC members.

Sarmiento, Hendriks et al. (2016) proposed a numerical modelling approach for FRC in which the fibre structure is discretised into volumes and two fibre parameters are assigned for each discrete volume, the dominant fibre orientation and the fibre volume content. The parameters are incorporated in a numerical model which employs a single phase material definition. The results demonstrated that the modelling approach can

accurately capture the flexural response of SFRC beams as well as the location and propagation pattern of the critical cracks.

A non-linear FE model was developed by Mohamed and Nehdi (2016) to simulate the behaviour of SFRC pipes under the three-edge-bearing test in which the Concrete Damaged Model offered by the FE software, ABAQUS was employed. The proposed model was capable of simulating the load-deformation response of SFRC pipes tested using the three-edge-bearing method.

2.3.5. ANALYTICAL AND EMPIRICAL STUDIES

The analytical studies have been mainly focused on the fibre pullout mechanism, constitutive material models and SFRC members' behaviour.

Naaman, Namur et al. (1991 b) proposed an analytical relationship between the bond shear stress and the slip at the fibre-matrix interface to predict the complete pullout response of straight fibres. The frictional behaviour of the interface was derived based on the shrink-fit and fibre-matrix misfit theories. Lee, Kang et al. (2010) presented an analytical pullout behaviour model for straight steel fibres with consideration of the fibre inclination. Chanvillard (1999) proposed a pullout model for non-straight steel fibres (hooked-end and crimped) which requires a numerical integration procedure to simulate the pullout load-slip response. Alwan, Naaman et al. (1999) developed a frictional pulley model to predict the contribution of mechanical anchorage (the end hook). Sujivorakul, Waas et al. (2000) extended the straight fibre pullout model in which a non-linear spring is considered at the end of the fibre to model the effect of the mechanical anchorage. Laranjeira, Molins et al. (2010) advanced a procedure for the pullout response of inclined hooked-end steel fibres which requires the strength properties of the fibre and matrix. Using the experimental data of fibres aligned with the load direction, the contribution of the hook and straight segments are estimated. The fibre-matrix interaction nearby the fibre exit point is estimated by consideration of the amount of spalled matrix and local friction effects. A simple model was developed by Zile and Zile (2013) to simulate the pullout response of deformed steel fibre in which the fibre geometry consists of straight and curved segments. The contribution of mechanical anchorage, i.e. fibre deformation, depends on the amount of plastic work

required for straightening the fibre during the pullout which is a function of geometrical properties and yield stress of the fibre material.

Lee, Cho et al. (2013) developed a simplified analytical model based on the Diverse Embedment Model (DEM) which accounts for random distribution and pullout behaviour of fibres to predict the ductile tensile behaviour of SFRC. In the model, it is assumed that the fibre slips only on the shorter embedded side in which to prevent overestimation of the tensile stress, coefficients for frictional bond behaviour and mechanical anchorage effect are incorporated. It was demonstrated that the model can properly predict the direct tensile and flexural behaviour of SFRC members. Blanco, Pujadas et al. (2014) presented an analytical formulation to predict the post-cracking tensile response of SFRC from the Barcelona test results in which a multilinear diagram for the stress-strain relationship is assumed.

A constitutive material behaviour was developed by Soranakom and Mobasher (2007 (a)) in which an elastic constant post-peak, i.e. a drop-down model, and elastic perfectly plastic properties are respectively assumed for the material in tension and compression. The material properties are defined by Young's modulus, first cracking strain as well as four non-dimensional parameters to describe post-peak tensile stress, compressive strength, and ultimate strain levels in tension and compression. A closed-form solution for the moment-curvature diagram of SFRC under bending is derived and normalised with respect to the corresponding values at the cracking moment. By applying the moment-area method to the moment-curvature diagram, the mid-span deflection of three- and four-point bending tests can be derived. To enable the model for simulating strain hardening materials and to improve the model's accuracy, Mobasher, Bakhshi et al. (2014) extended the tensile material behaviour to a tri-linear response.

Armelin and Banthia (1997) used strain compatibility and force equilibrium principles to predict the flexural behaviour of SFRC based on the experimental pullout load-slip relationships of single fibres at varying angles of inclination and the compressive strength of the composite. Singh (2015) suggested a flexural model based on simple principles of mechanics to determine the ultimate flexural capacity of SFRC rectangular sections and the corresponding crack widths. The proposed model considers an elastic

perfect-plastic model for compression and an elastic constant post-peak response for SFRC in tension. In the model, the random fibre orientation is taken into account.

Extensive investigations have been performed to quantify the contribution of fibres to the shear capacity of SFRC beams. There are numerous analytical and empirical models concerning the shear problem in RC beams with steel fibres. The analytical models directly incorporate the influential fibre properties in the mechanical performance of FRC including fibre aspect ratio, fibre content, a bond factor, and in some cases, fibre orientation (Mansur, Ong et al. 1986, Narayanan and Darwish 1988, Ashour, Hasanain et al. 1992, Swamy, Jones et al. 1993, Imam, Vandewalle et al. 1995, Khuntia, Stojadinovic et al. 1999). In contrast, fibre mechanical properties are indirectly taken into account in the empirical models using material strength characteristics such as modulus of rupture, splitting tensile strength, equivalent flexural strength, and residual tensile strength factors (Sharma 1986, Kwak, Eberhard et al. 2002, Dupont and Vandewalle 2003, RILEM TC 162-TDF 2003, CEB-fib Model Code for Concrete Structures 2011). A few examples of the models are summarised in **Table 2.1**.

Table 2.1

Analytical and empirical models for prediction of the shear strength of FRC.

Sharma (1986)	$v_{fc} = \frac{2}{3} f_{sp} \left(\frac{d}{a} \right)^{0.25}$ <p>f_{sp} = Split-cylinder tensile strength of concrete d/a = Effective depth-to-shear span ratio</p>
Mansur, Ong et al. (1986)	$v_{fc} = \left(0.16 \sqrt{f'_c} + 17.2 \frac{\rho V d}{M} \right) + v_b$ <p>f'_c = Cylinder compressive strength of plain concrete, MPa V/M = Ratio of the external shear to moment ρ = Longitudinal reinforcement ratio $v_b = 0.41 \tau F_f$ (accounts for the fiber pullout resistance) F_f = Fibre factor τ = Average fiber matrix interfacial bond stress</p>
Ashour, Hasanain et al. (1992)	$v_{fc} = \left(0.7 \sqrt{f'_c} + 7F \right) \frac{d}{a} + 17.2 \rho \frac{d}{a}$

Table 2.1 (Continued)

Analytical models for prediction of the shear strength of FRC.

Narayanan and Darwish (1988)	$v_{fc} = e \left[0.24 f_{spfc} + 80 \rho \frac{d}{a} \right] + v_b$ $e = \begin{cases} 2.8 d/a & a/d < 2.8 \\ e = 1 & a/d \geq 2.8 \end{cases}$ $f_{spfc} = \frac{f_{cu}}{(20 - \sqrt{F})} + 0.7 + \sqrt{F}$ $f_{cu} = \text{Cube compressive strength of fibrous concrete}$
Ashour, Hasanain et al. (1992)	$\begin{cases} v_{fc} = \left(2.11 \sqrt[3]{f_c'} \right) \left(\rho \frac{d}{a} \right)^{0.33} & a/d > 2.5 \\ v_{fc} = \left(2.11 \sqrt[3]{f_c'} \right) \left(\rho \frac{d}{a} \right)^{0.33} \times \frac{2.5}{a/d} + v_b (2.5 - a/d) & a/d \leq 2.5 \end{cases}$
Li, Ward et al. (1992)	$\begin{cases} v_{fc} = 1.25 + 4.68 \left[(f_f f_{sp})^{3/4} \left(\rho \frac{d}{a} \right)^{1/3} d^{-1/3} \right] & a/d \leq 2.5 \\ v_{fc} = 9.16 \left[f_f^{2/3} \rho^{1/3} \frac{d}{a} \right] & a/d > 2.5 \end{cases}$ $f_f = \text{Modulus of rupture}$
Swamy, Jones et al. (1993)	$v_{fc} = 0.9 \sigma_{cu} + v_c$ $\sigma_{cu} = v_b = \text{Post-cracking tensile strength of FRC}$ $\begin{cases} \sigma_{cu} = 0.41 \tau F_f & l_f < L_c \\ \sigma_{cu} = 0.41 \left(1 - \frac{\sigma_{fu}}{4\tau} \frac{d_f}{l_f} \right) \sigma_{fu} V_f & l_f < L_c \end{cases}$ $F_f = (l_f / d_f) V_f \rho_f$ $\rho_f = \text{Fibre bond factor}$ $d_f = \text{Fibre diameter}$ $l_f = \text{Fibre length}$ $L_c = \text{Critical fibre length}$ $\sigma_{fu} = \text{Fibre fracture strength}$ $v_c = \text{Concrete contribution to the shear strength}$
RILEM TC 162-TDF (2003) Dupont and Vandewalle (2003)	$v_{fc} = v_{c,RLM} + v_{f,RLM}$ $v_{c,RLM} = 0.15 \sqrt[3]{3(d/a)} k (100 \rho f_c')^{1/3}$ $k = 1 + \sqrt{200/d} \leq 2$ $v_{f,RLM} = k_1 0.5 \frac{d}{a} f_{e,3}$ $k_1 = \frac{1600 - d}{1000} \geq 1$ $f_{e,3} = \text{Equivalent flexural strength}$

Table 2.1 (Continued)

Analytical models for prediction of the shear strength of FRC.

Kwak, Eberhard et al.
(2002)

$$v_{fc} = 3.7ef_{spfc}^{2/3}(\rho\frac{d}{a})^{1/3} + 0.8v_b$$

$$v_{rd} = v_{Rd,F} + v_{Rd,s}$$

$$v_{Rd,F} = \frac{0.18}{\gamma_c} k \left[100\rho \left(1 + 7.5 \frac{f_{Ftu}}{f_{ctk}} \right) f_{ck} \right]^{1/3} + 0.15\sigma_{cp}$$

 γ_c = Partial safety factor for concrete

$$k = 1 + \sqrt{200/d} \leq 2$$

 f_{ctk} = Characteristic concrete tensile strength f_{ck} = Characteristic concrete compressive strengthCEB-fib Model Code
for Concrete
Structures (2011)

$$f_{Ftu}(w_u) = f_{Fts} - \frac{w_u}{2.5} (f_{Fts} - 0.5f_{R3} + 0.2f_{R1}) \geq 0$$

 f_{Ftu} = Ultimate residual tensile strength at 1.5mm crack width

$$f_{Fts} = 0.45f_{R,1}$$

$$f_{R,j} = \frac{3F_j L}{2bh_{sp}^2}$$

 F_j = Force corresponding to crack mouth opening at stage j σ_{cp} = Average compressive stress acting on the concrete cross section
(prestress action) $v_{Rd,s}$ = Contribution of FRC to shear strength

2.4. SUMMARY

Extensive experimental, analytical, and numerical investigations have been carried out to assess material properties of SFRC and quantify the contribution of steel fibres to the structural performance (flexural and shear) of SFRC members.

As a result of extensive experimental tests on the behaviour of RC members containing steel fibres (especially on the shear and flexural capacities of SFRC beams), codes, regulations, and technical recommendations are developed by the relevant institutes and societies (RILEM TC 162-TDF 2003, CEB-fib Model Code for Concrete Structures 2011, ACI Committee 544 2014). In spite of the presence of the codes and regulations, the large structural applications of steel fibres are hindered mainly due to the unfavourable structural performance of the commercially available steel fibres.

As mentioned earlier, this research project is targeted to develop a new generation of steel fibres which can effectively contribute to the ultimate capacity of SFRC structural members as an efficient and viable alternative to the conventional reinforcement. It is evident that the design guidelines and equations presented by the codes might not be applicable to the new fibre and hence it is required to quantify the performance of SFRC members with the new fibre.

CHAPTER 3

FIBRE DEVELOPMENT

3.1. INTRODUCTION

The fibre pullout process is a highly complex mechanism which consists of cohesion, interfacial debonding, sliding frictional contact, fibre deformation, and material plasticity (Chin and Xiao 2012). In some cases, even by consideration of simplifying assumptions, the problem complexities (the geometries and/or boundary conditions) preclude use of such methods. On the other hand, Finite Element (FE) simulation is more efficient and cost effective when compared with physical tests. Furthermore, with the current level of technology, results obtained from FE simulations could be more detailed than those of the tests. Therefore, a FE model for a steel fibre pullout from concrete with varying physical and material properties is developed to be employed as a virtual laboratory unit to investigate pullout behaviour of new steel fibres and consequently optimise the design. The complete bond-slip response of the proposed model is validated using experimental results obtained from the literature.

3.2. FINITE ELEMENT MODEL OF PULLOUT

In this section, a generic non-linear 3D finite element model is proposed to analyse the complex bond-slip behaviour of steel fibres in concrete. ANSYS is employed as a platform for all simulation tasks.

3.2.1. FIBRE AND MATRIX MATERIALS

The 8-noded solid element (SOLID185) with three degrees of freedom at each node (i.e. translations in the nodal x, y, and z directions) is used to model the steel fibres. The element has plasticity, stress stiffening, large deflection, and large strain capabilities. Cementitious matrices are modelled using the 8-noded solid brick elements (SOLID65) with cracking, crushing, and plastic deformation capabilities (ANSYS® Academic Research 2015).

The von Mises yielding criterion is adopted to simulate the plasticity of the steel fibre's material. The criterion (also known as the Maximum Distortion Energy Theory of Failure) suggests that yielding of a ductile material begins when the second deviatoric stress invariant reaches a critical value. It is part of plasticity theory that applies best to ductile materials, such as some metals.

The von Mises yielding criterion is combined with the modified Willam and Warnke failure criterion (Willam and Warnke 1975) to model the cementitious matrices. The yield and ultimate stresses (f_y and f_u) and the ultimate strain (ϵ_u) for fibres material are taken from the actual experimental specimens. The modulus of elasticity and the Poisson's ratio of the steel material (E_s and ν_s) are taken as 210 GPa and 0.3 respectively. The uniaxial tensile and compressive strengths (f_{ctm} and f_{ck}) and the modulus of elasticity (E_c) of cementitious matrices are specified according to those experimentally obtained. However, in some cases where the actual tensile strength and the modulus of elasticity are not available, they are estimated by using **Eqs. (3.1)** and **(3.2)** in accordance with Eurocode 2 (2004). The Poisson's ratio of the cementitious material (ν_c) is taken as 0.2.

$$f_{ctm} = 0.3 \times f_{ck}^{2/3} \quad (\text{MPa}) \quad (3.1)$$

$$E_c = 22 \times \left(\frac{f_{ck} + 8}{10} \right)^{0.3} \quad (\text{GPa}) \quad (3.2)$$

Eqs. (3.3) to (3.5) (MacGregor 1992) are used to define the uniaxial stress-strain relationship of the cementitious matrices in compression.

$$\sigma = \frac{E_c \varepsilon}{1 + \left(\frac{\varepsilon}{\varepsilon_{cu}} \right)^2} \quad (3.3)$$

$$\varepsilon_{cu} = \frac{2 f_{ck}}{E_c} \quad (3.4)$$

$$E_c = \frac{\sigma}{\varepsilon} \quad (3.5)$$

where σ and ε are the stress and strain at any point of the curve. The stress-strain curve requires a first point to define the linear part of the relation which must satisfy the Hooke's law (**Eq. (3.5)**). In this research, the stress equivalent to $0.3f_{ck}$ and the corresponding strain ($0.3f_{ck}/E_c$) is considered as the elastic limit.

3.2.2. FIBRE-MATRIX INTERFACE

The surface-to-surface contact is used to represent the fibre and matrix surfaces which are in contact (the fibre-matrix interface) where both contact and target surfaces would make up a “Contact Pair”. The contact and target elements have the same geometric characteristics as interconnecting fibre and cementitious matrix which are capable of simulating the deformable contact interface.

The physiochemical bond of the fibre-matrix interface is defined by the Coulomb friction model where two contacting surfaces carry shear stresses up to a certain magnitude across their interface before they start sliding relative to each other. An equivalent shear stress (τ_e) is defined as a fraction of the normal contact pressure (ρ_c) at which sliding on the surface begins, as seen in **Eq. (3.6)** and **Fig. 3.1(a)**.

$$\tau_e = \mu_f \rho_c + c; \quad \tau_e \leq \tau_{max} \quad (3.6)$$

where μ_f is the coefficient of friction and c is the contact cohesion which provides sliding resistance even with zero normal pressure (Wriggers, Vu Van et al. 1990).

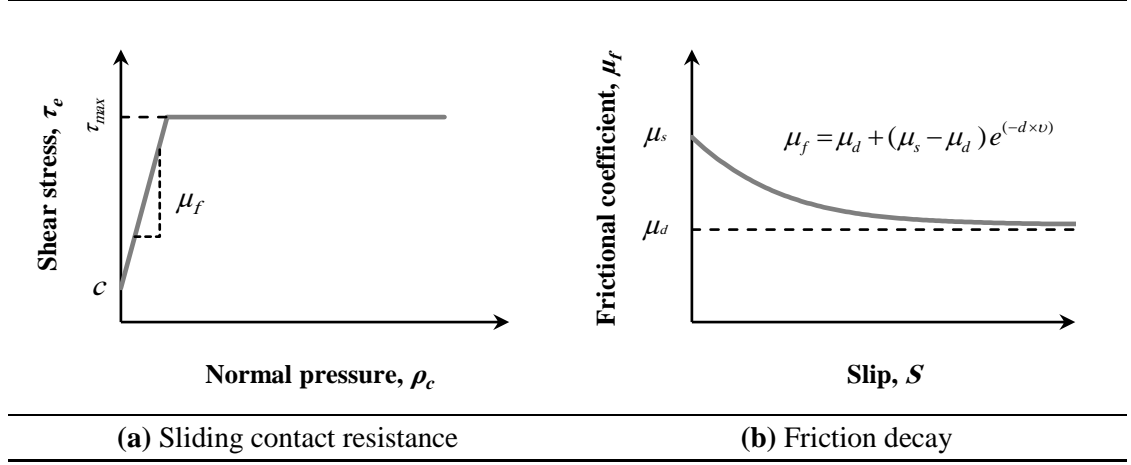


Fig. 3.1. Properties of the fibre-matrix interface.

To consider interfacial debonding between the fibre and the surrounding matrix, the friction decay is specified based on **Eq. (3.7)** (Hallquist 1998).

$$\mu_f = \mu_d + (\mu_s - \mu_d) e^{(-d_c \times v)} \quad (3.7)$$

where μ_d and μ_s are the dynamic and static coefficients of friction respectively, d_c is the decay coefficient, and v represents slip rate (see **Fig. 3.1(b)**).

During the pullout process, material failure would occur in the high-stress regions of the fibre-matrix interface. Hence, the maximum contact friction, τ_{max} , is introduced in the friction model as seen in **Fig. 3.1(a)**, so irrespective of the magnitude of the normal contact pressure, sliding occurs once the frictional stress reaches this value (ANSYS® Academic Research 2015). The sticking/sliding calculations determine when a point transitions from sticking to sliding or vice versa.

The pure penalty method is employed to establish a relationship between the contact and target elements to prevent or limit penetration, i.e. contact compatibility, where the compatibility is achieved using a fictitious spring. When contact is detected, the spring would deflect, thus creating an action, i.e. contact force, to resist the penetration. The spring stiffness is known as contact or penalty stiffness. The elements can transmit compressive normal and tangential forces but not tensile normal forces and they are free

to separate and move away from each other (Cook, Malkus et al. 1989, Bathe 1996, Gu, Murty et al. 2002, ANSYS® Academic Research 2015).

Fig. 3.2 shows a contact scenario in which a contact element is penetrated into a target element. The contact element consists of a slave node and the target element is represented by a master line connecting nodes 1 and 2. S_o and S represent the slave node before and after penetration.

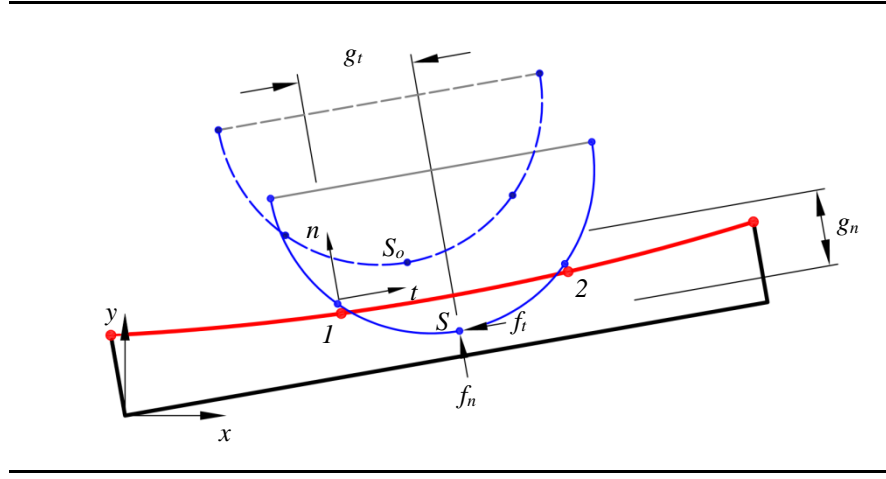


Fig. 3.2. Penalty method formulation.

The penetration is resisted by the contact force which is resolved into two components in the normal and tangential directions, i.e. f_n and f_t , and are defined by **Eqs. (3.8) and (3.9)** (Bathe 1996, ANSYS® Academic Research 2015).

$$f_n = -k_n g_n \quad (3.8)$$

$$f_t = -k_t g_t \quad (3.9)$$

where g_n and g_t are penetrations along the normal and tangential directions and k_n and k_t are penalty terms which respectively express the relationship between the contact force and the penetration along the normal and tangential directions.

Once the tangential contact force exceeds the static friction force, sliding occurs, as below.

$$\begin{aligned}
f_t &\leq \mu_s f_n \rightarrow \text{Sticking State} \\
f_t &> \mu_s f_n \rightarrow \text{Sliding State}
\end{aligned}
\tag{3.10}$$

As seen in **Fig. 3.3** and mentioned above, the contact and target elements overlay the surfaces of contacting bodies (the steel fibre and matrix) and have the same geometric characteristics as the underlying elements. Therefore, the compatibility is applied to the fibre and matrix surfaces which respectively underlay the contact and target elements.

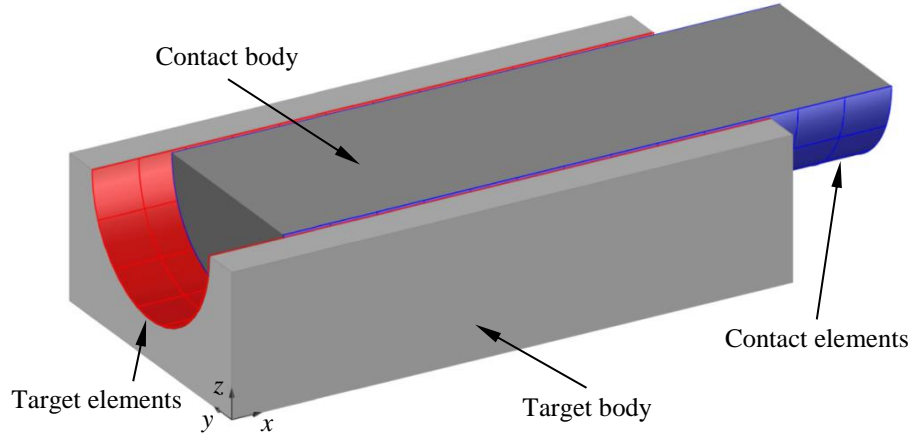


Fig. 3.3. Contact and target elements with corresponding bodies, i.e. contact and target bodies.

To derive the contact stiffness matrix, the contact surface is divided into a set of contact elements. The element represents the interaction between the surface nodes of the contact body with the corresponding element face of the target body. The contact stiffness matrix, K_c , is assembled into the stiffness matrix of the contacting bodies (K_b). The equilibrium equation for the system is expressed as **Eq. (3.11)**.

$$[K_b + K_c]u = F \tag{3.11}$$

where u and F are displacement and force vectors respectively (Bathe 1996, Gu, Murty et al. 2002).

The contact stiffness matrix depends on the contact status, whether the surfaces are touching or separated, therefore the matrix is a non-linear term (Gu, Murty et al. 2002). In this study, the contact stiffness matrix is updated at each iteration. Ideally, zero penetration is only possible with an infinite contact stiffness which is numerically impossible with penalty-based methods. However, as long as the penetration value is in the allowable interpenetration range, the results are deemed to be valid. If the penetration is larger than the allowable values, the global solution would be invalid, even though the residual forces and displacements have met the convergence criteria (ANSYS® Academic Research 2015).

In this research, asymmetric contact pair is selected for the contact modelling where the fibre and matrix surfaces are specified as contact and target surfaces respectively. Contact elements are constrained against penetration into the target surface at Gauss integration points as they generally provide more accurate results compared with nodal points (**Fig. 3.4**) (ANSYS® Academic Research 2015).

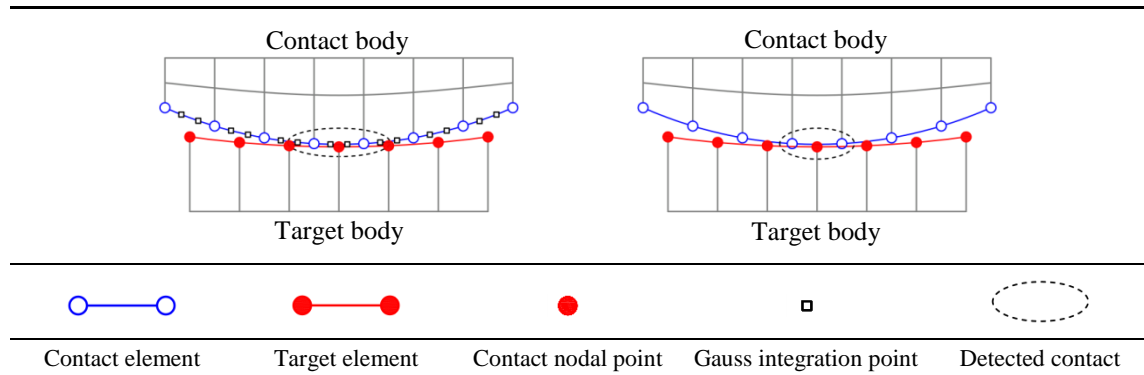


Fig. 3.4. Location of contact detection.

A spherical zone around each detection point of contact elements is used to determine far-field open and near-field open status known as the “Pinball Region”. If a node on the target surface is within this sphere, it is considered to be in near contact and its relationship to the contact detection point is monitored more closely. The computational cost of searching for contact depends on the size of the pinball region (Belytschko and Yeh 1993). The pinball region as a sphere of radius 2 times depth of the underlying elements of the contact surface is considered for all FE models.

In order to model debonding at the interface, two frictional coefficients, i.e. static and dynamic coefficients of friction, are introduced in the models. Therefore, before any slip occurs, the frictional force is calculated using the static coefficient (μ_s). After sliding happens, the interface friction is determined using **Eq. (3.7)** (see **Fig. 3.1(b)**). However according to **Eq. (3.6)**, the frictional stress, $\mu_f \rho_c$, is available just by the presence of normal contact pressure. Since at the beginning of the analysis, there is no normal pressure to activate static friction, an initial normal pressure on contact elements (the fibre surface at the interface) is required, before any slip occurs. To this end, the channel of the matrix surrounding the fibre is modelled with a diameter smaller than that of the fibre wire. Then the model is analysed with the presence of initial penetration. Since the interpenetration is detected, the contact pressure is applied on the contact surface, i.e. fibre surface at the interface (see **Fig. 3.5**), to enforce the contact compatibility. Following applying the initial pressure, the incremental load is applied at the free end of the fibre in a displacement-controlled manner to capture the bond-slip response.

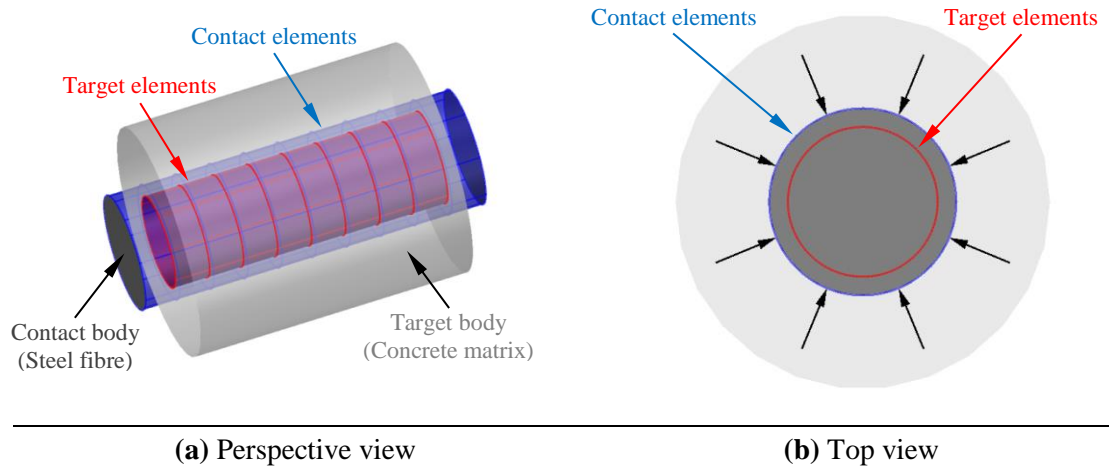


Fig. 3.5. Applying initial contact pressure on the contact surface, i.e. steel fibre surface.

3.3. VALIDATION OF THE NUMERICAL MODEL

Experimental pullout data of various steel fibres including straight, hooked-end, crimped, and twisted which were tested in the single-sided manner are employed to validate the numerical model.

In order to consider debonding in the non-linear analyses, the channel of matrices surrounding the fibres is modelled 0.1 percent of wire's diameter smaller (see **Section 3.2.2**). Taking advantage of symmetry in geometry and loading of some specimens, a fraction of the specimens with consideration of proper boundary conditions are modelled. The contact parameters including μ_s , μ_d , c , d , k_n , k_t , and τ_{max} are determined for each model in accordance with the respective experimental data.

Considering the frictional contact problem produces non-symmetric stiffnesses, the unsymmetric solution is incorporated in the Newton-Raphson method to improve the computational efficiency (Laursen and Simo 1993).

3.3.1. STRAIGHT FIBRE

Pullout testing data of a straight fibre given by Naaman and Najm (1991) are employed for the validation. The geometrical and material properties of the fibre are provided in **Table 3.1**. The cylinder compressive strength of the cementitious matrix is 60 MPa.

Table 3.1
Geometrical and material properties of the straight steel fibre, Naaman and Najm (1991).

Cross-section	Diameter (d_f)	Embedded length (l_{em})	Yield strength (f_y)	Ultimate strength (f_u)
Circular	0.48 mm	12.7 mm	450 MPa	600 MPa

Due to symmetry in geometry and loading, a quarter of the specimen is modelled, as shown in **Fig. 3.6**. The contact parameters adjusted for this model are presented in **Table 3.2**.

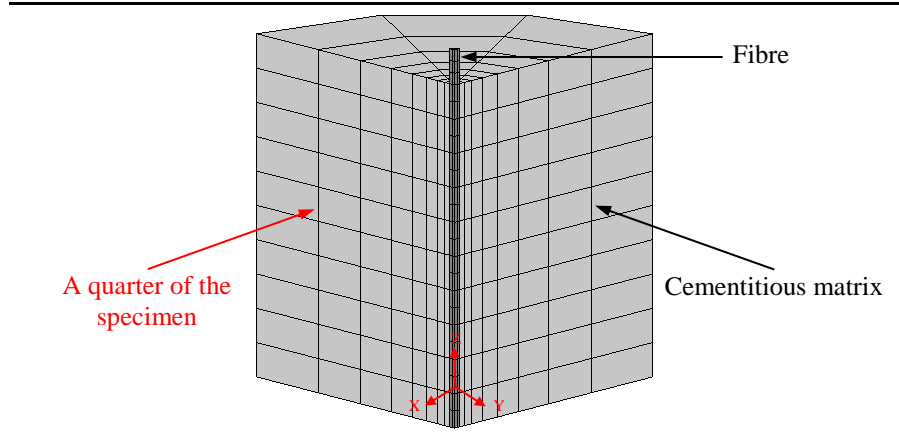


Fig. 3.6. Finite element model of the straight fibre.

Table 3.2
Contact parameters for the FE models.

Fibre type	Dynamic friction of coefficient	Static friction of coefficient	Cohesion (MPa)	Maximum contact friction (MPa)
	μ_d	μ_s	c	τ_{max}
Straight	0.0155	0.07	0.25	100
Hooked-end	0.1875	0.47	1.25	100
Crimped	0.1	0.25	1.25	100
Twisted	0.05 - 2 ^a	0.056	4	120

^a The range of frictional coefficient

Fig. 3.7 shows the comparison between the experimental and numerical bond-slip responses.

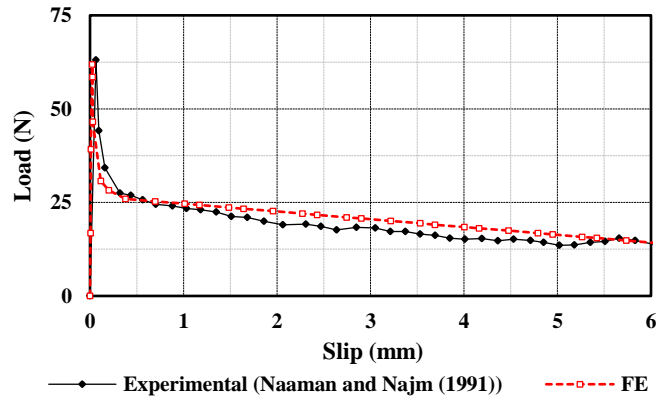


Fig. 3.7. Experimental and numerical load-slip curves of the straight fibre.

From the figure, the agreement between the experimental and numerical results is good and the model predicts the peak load as well as the pre-peak, debonding, and post-peak responses well. Average interfacial shear stresses (pullout loads divided by the corresponding fibre-matrix interface value) at various values of displacement along with the corresponding frictional contact stress (shear stress at the interface) contours are illustrated in **Fig. 3.8**. Agreement between the results is good which verifies a relatively constant shear stress at the interface after debonding (Wille and Naaman 2013).

Figs. 3.9(a) and (b) show the von Mises stress contours of the fibre at slips equal to 0.02 mm, corresponding to the maximum pullout load, and 2 mm. The normalised von Mises stress (with respect to the yield stress) at three levels along the fibre length (bottom, middle, and top of the fibre) versus slip are illustrated in **Fig. 3.10**. The results indicate that the entire length of the fibre responds similarly to the pullout process by suffering considerable stress decay after the displacement corresponding to the debonding.

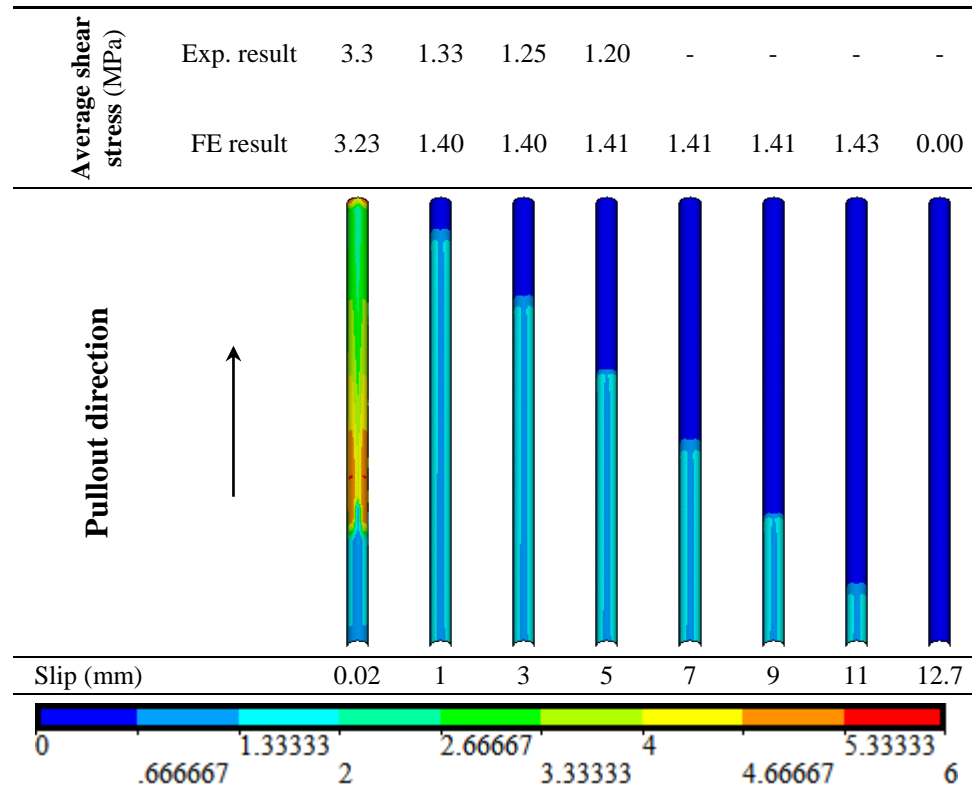


Fig. 3.8. The fibre-matrix interface of the straight fibre during pullout process.

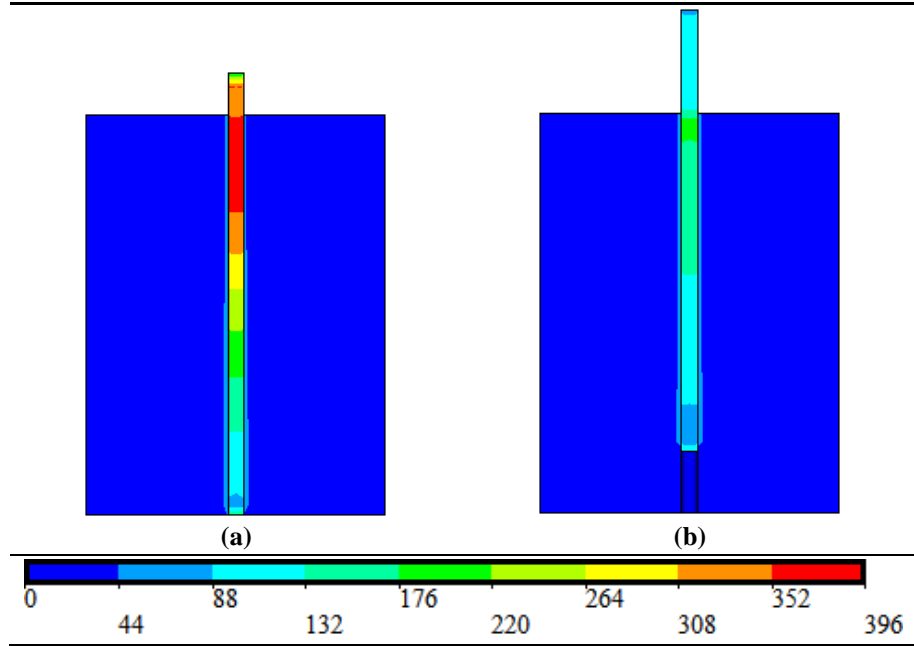


Fig. 3.9. The von Mises stress contours (in MPa) of the straight fibre at (a) slip = 0.02 mm, i.e. debonding; (b) slip = 2 mm.

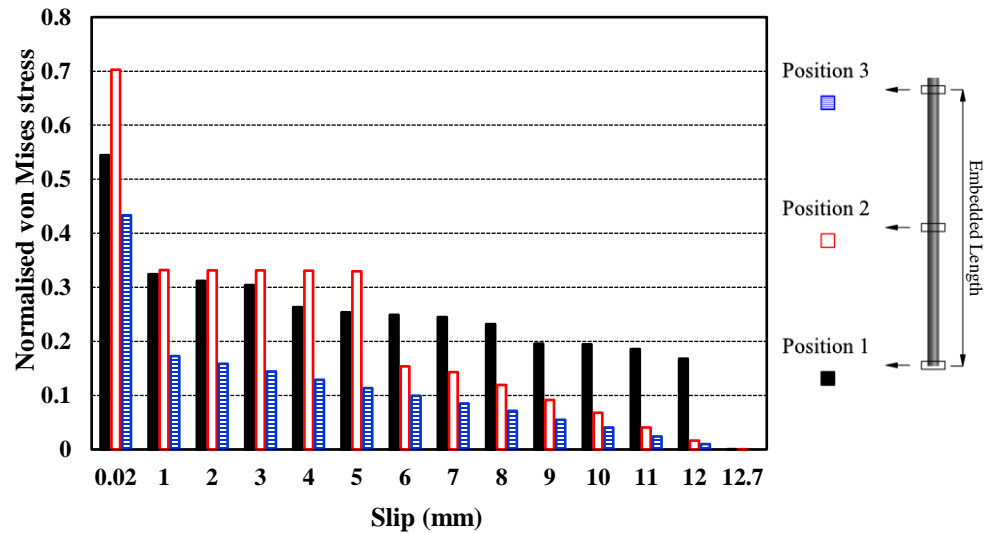


Fig. 3.10. Normalised von Mises stress versus slip of the straight fibre.

It is well known that straight steel fibres are normally characterised by linear bond-slip softening behaviour after the fibre-matrix interface debonding which implies a constant shear stress at the interface (Naaman, Namur et al. 1991 a). The bond strength of such fibres embedded in concrete is generally small and mostly frictional in nature (Naaman

2003). However, by tailoring the matrix composition and surface coating of the fibres, it is possible to achieve slip-hardening behaviour. The key feature of such performance is that when the fibre is pulled out from a cementitious matrix, its resistance increases with the slippage. As mentioned in **Section 2.3.1.6**, it is attributed to the intensive damage of the fibre surface by matrix particles during the pullout process which leads to an increase in the interface friction and consequent improvement in bond behaviour (Wille and Naaman 2012, Wille and Naaman 2013). Therefore, during pullout depending on the interface properties, matrix packing density and the fibre shape, the coefficient of friction between the fibre and matrix could increase.

3.3.2. HOOKED-END FIBRE

In this section, a hooked-end steel fibre pullout, tested by Jamee (2013) is investigated. The geometrical properties of the fibre are shown in **Fig. 3.11**.

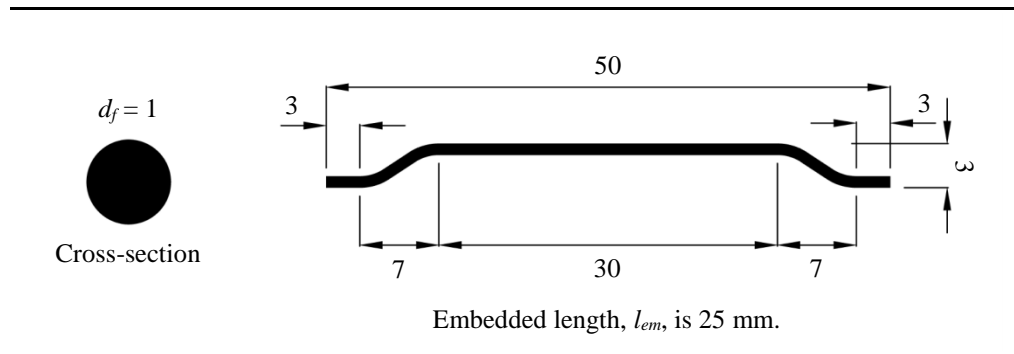


Fig. 3.11. Dimensions of the hooked-end steel fibre (in mm).

The yield and ultimate stresses of the fibre material are 650 MPa and 800 MPa, and the cylinder compressive strength and the elastic modulus of the cementitious matrix are 60 MPa and 38 GPa respectively. Using **Eq. (1)** the mean tensile strength of concrete is estimated to be 4.6 MPa.

Fig. 3.12 shows the FE model of the hooked-end fibre embedded in the matrix. The contact parameters used for this model are presented in **Table 3.2**. The bond-slip curves of the numerical model and the experimental specimen are shown in **Fig. 3.13** in which good agreement is observed; in particular, the model properly captures the two expected load drops during the pullout process.

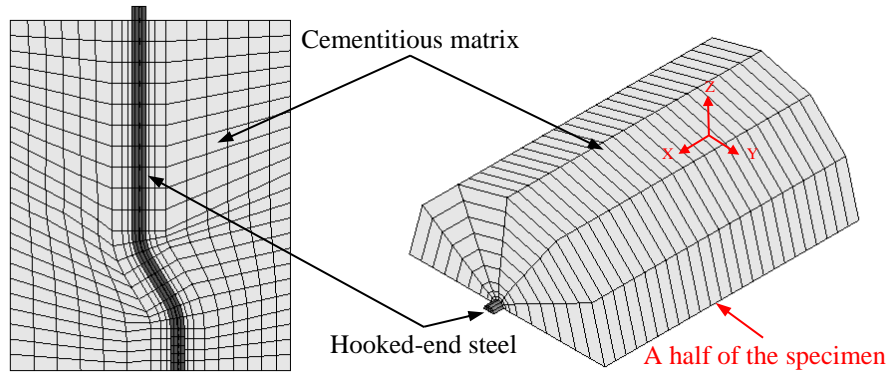


Fig. 3.12. Finite element model of the hooked-end fibre.

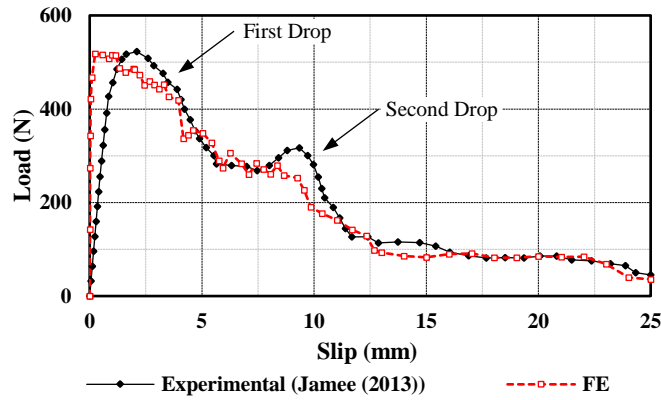


Fig. 3.13. Experimental and numerical load-slip curves of the hooked-end fibre.

The pullout behaviour of hooked-end fibres is dominated by the mechanical interlock and the plastification of the hooked end, i.e. two curved segments. As the fibre is pulled out, the curved segments are consecutively straightened and therefore their resistance against pullout is considerably decreased one after another one resulting into two consecutive drops in the pullout load, as seen in **Fig. 3.13**.

In **Fig. 3.14**, the von Mises stress contours of the fibre at slips equal 0.45 mm and 2 mm which correspond to the complete interface debonding and the initiation of the first drop in the load-slip curve (see **Fig. 3.13**) are illustrated. As can be seen in the figure, as a result of the fibre tendency to change its shape during passing through the two curved regions of the matrix, i.e. fibre straightening, plastic hinges are formed in the fibre in the vicinity of those regions.

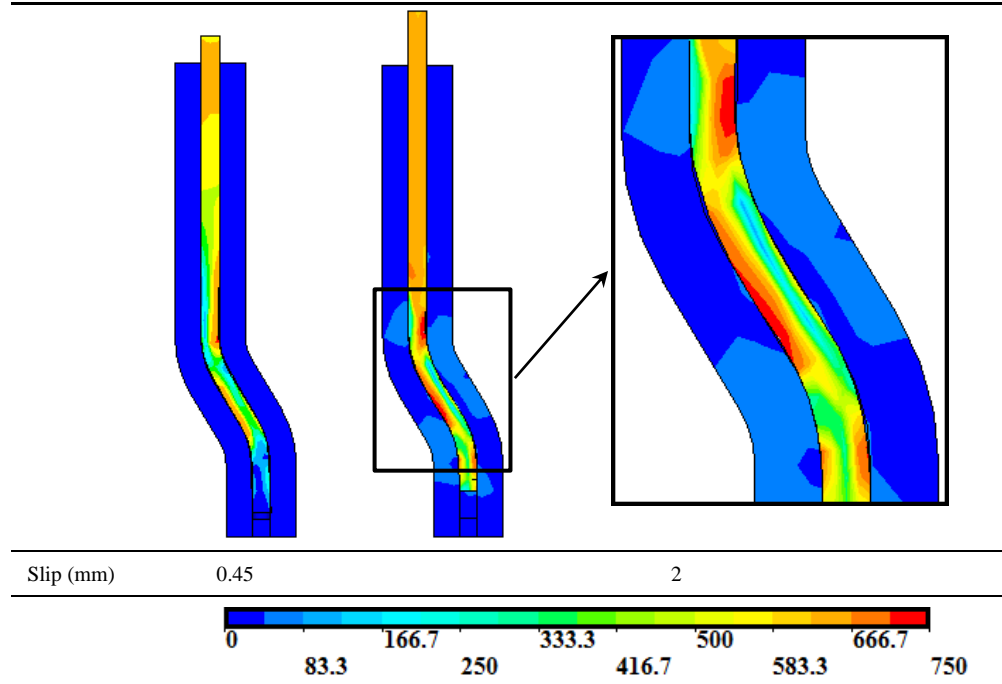


Fig. 3.14. The von Mises stress contours (in MPa) of the hooked-end fibre.

Average interfacial shear stress versus slip is shown in **Fig. 3.15**.

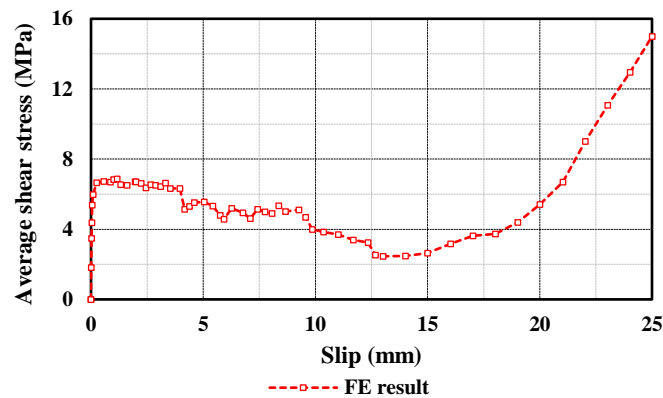


Fig. 3.15. Average interfacial shear stress versus slip for the hooked-end fibre.

The graph consists of three distinctive parts, a steep initial ascending portion, followed by a smoothly descending branch up to the slip equals 12.5 mm and then an ascending branch up to the complete pullout. As observed in **Fig. 3.13**, after slip around 12.5 mm, even though the interface is decreasing, there is only marginal load decay which leads to the continuous increase of the average interfacial shear stress after this slip, as seen in

Fig. 3.15. It might be mainly attributed to the existing permanent deformation at the fibre end after straightening, where the fibre experiences higher levels of frictional contact stress compared with the other interface areas (see **Figs. 3.16(a)** and **(b)**).

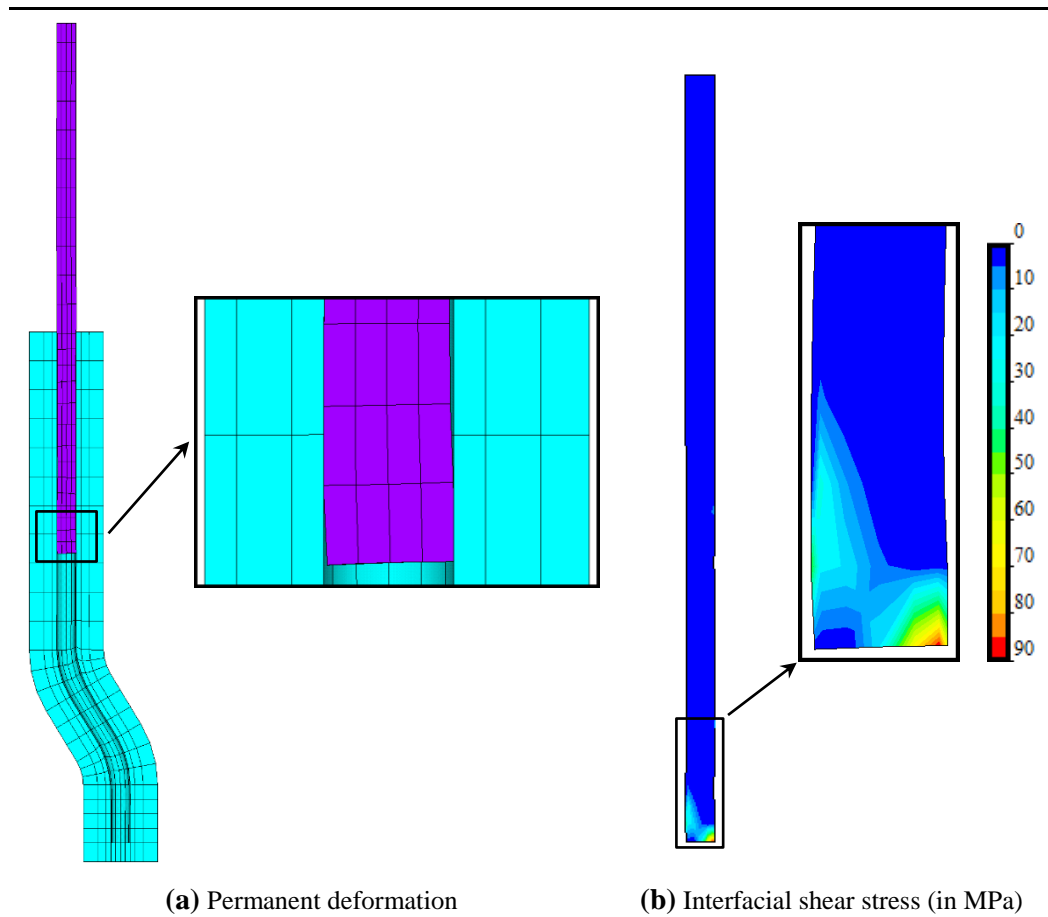


Fig. 3.16. Pullout mechanism after straightening of the end hook, slip = 16.5 mm.

The normalised von Mises stress at three cross-sections located at the bottom and top of the fibre as well as the middle of the end hook are plotted versus displacement in **Fig. 3.17**. Regarding the bottom level, as it is observed, there are two peak points, each one followed by a trough point, as a result of the straightening, and then relatively high levels of stress compared with the two other regions. These levels of stress are indicative of the dominant contribution of the shape of the fibre end to the pullout load (see **Fig. 3.16(b)**).

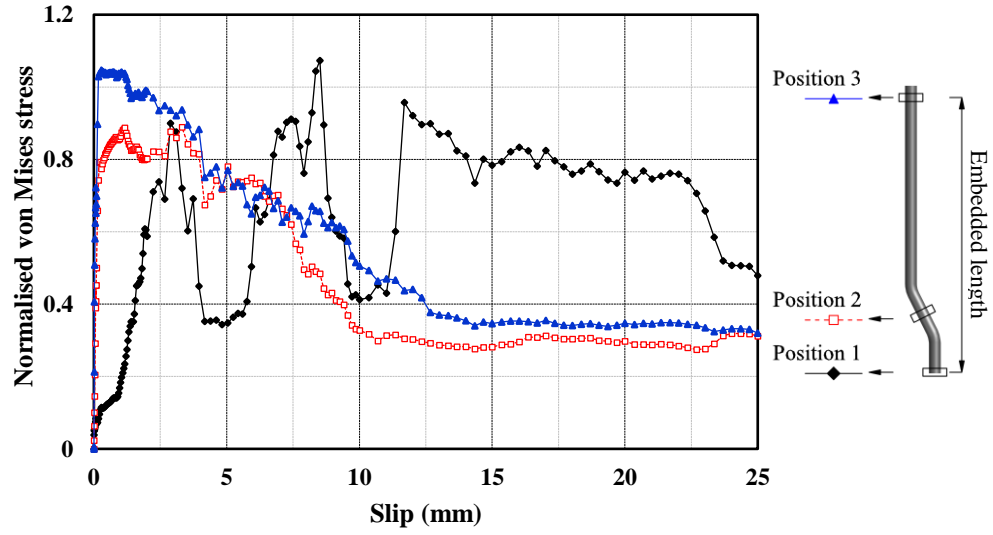


Fig. 3.17. Normalised von Mises stress versus displacement of the hooked-end fibre.

3.3.3. CRIMPED FIBRE

Pullout testing data of a crimped steel fibre with an embedded length of 15 mm (Zile and Zile 2013) are employed for further validation. The geometrical properties of the fibre are shown in **Fig. 3.18**.

The yield and ultimate stresses of the fibre material are 1450 MPa and 1800 MPa, respectively and the cylinder compressive strength of the cementitious matrix is 39 MPa. The mean tensile strength and Young's modulus of the matrix are assumed to be 3.5 MPa and 35 GPa, respectively. The adjusted contact parameters for the model are provided in **Table 3.2**.

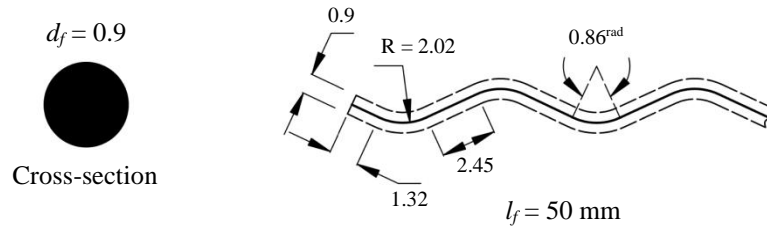


Fig. 3.18. Geometrical properties of the crimped steel fibre (in mm).

Fig. 3.19 shows the comparison of the experimental and numerical bond-slip curves where good agreement is found and the model can reasonably predict the bond-slip behaviour of the fibre throughout the pullout process.

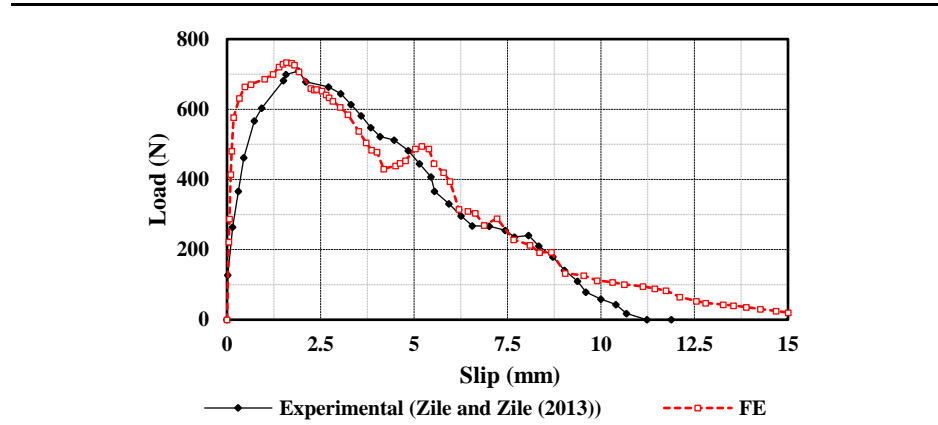


Fig. 3.19. Experimental and numerical load-slip curves of the crimped fibre.

Fig. 3.20 shows the von Mises stress contour of the fibre at a slip equal to 0.3 mm, which corresponds to the complete interface debonding.

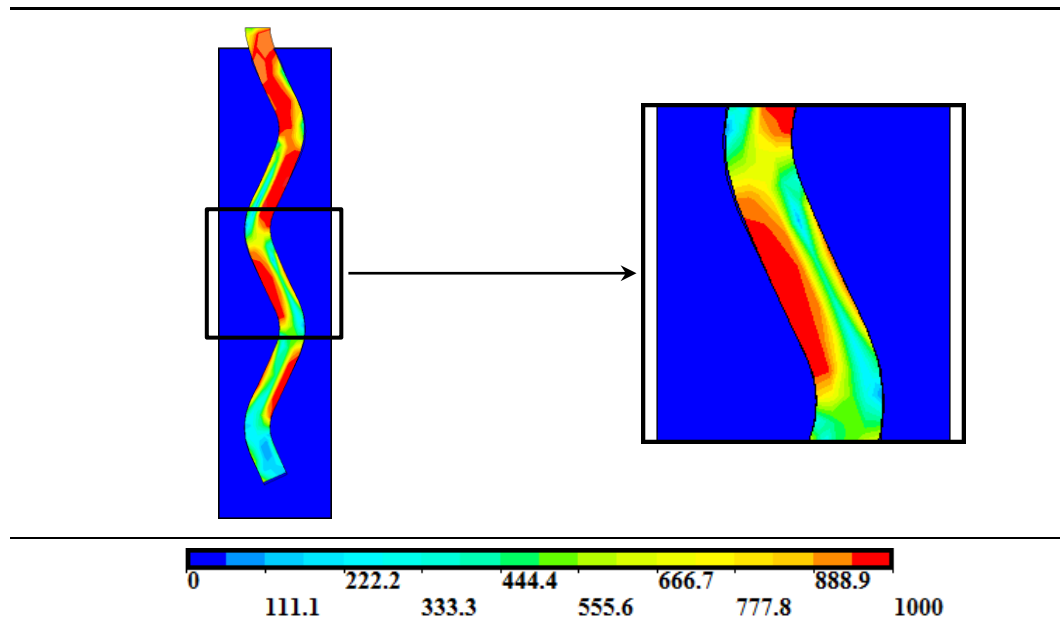


Fig. 3.20. The von Mises stress contour (in MPa) of the crimped fibre at slip = 0.3 mm.

The normalised von Mises stress with respect to the yield stress at three levels, bottom, middle and top of the fibre versus displacement is shown in **Fig. 3.21**. The results indicate that during pullout the embedded length of the fibre is subjected to repetitive bending and straightening, which result in improving the interface friction and consequently an increase in the pullout load.

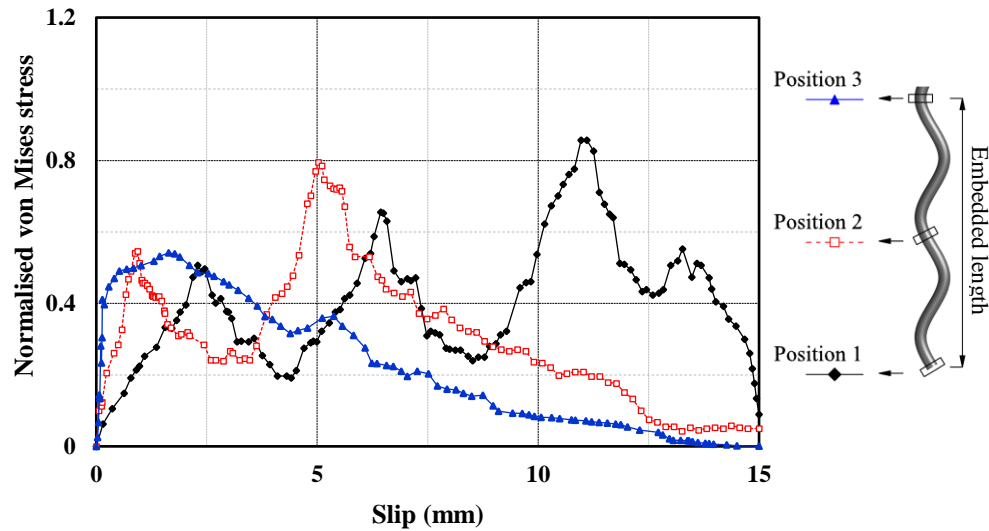


Fig. 3.21. Normalised von Mises stress versus displacement of the crimped fibre.

3.3.4. TWISTED FIBRE

The pullout performance of steel fibres directly depends on the physiochemical bond and mechanical anchorage. Twisted steel fibres (Torex) are engineered in terms of geometrical and material properties for compatibility with High-Performance Concrete (HPC) and Ultra-High Performance Concrete (UHPC) to achieve hardening behaviour (see **Sections 2.3.1.6** and **3.3.1**) (Naaman 2003).

In this section, as the final step for validation of the proposed numerical model, a rectangular twisted fibre embedded in UHPC tested by Wille and Naaman (2012) is employed in which the fibre shows strain-hardening behaviour. The total and embedded lengths of the fibre are 13 mm and 6.5 mm, respectively and the cross-sectional dimensions are 0.24 mm by 0.3 mm. Moreover, the fibre pitch, i.e. the length of one full

(360-degree) twist around the fibre axis, is 8 mm. The yield and ultimate stresses of the fibre material are 3100 MPa and 3400 MPa, respectively and the cylinder compressive strength of the matrix is 100 MPa. Since the actual values of the mean tensile strength and Young's modulus of the matrix were not reported, they are estimated to be 6.5 MPa and 44 GPa.

The contact parameters for the model are provided in **Table 3.2**. The dynamic coefficient of friction is assumed to be linearly correlated to the fibre slip, as shown in **Fig. 3.22**. In **Fig. 3.23** and **Fig. 3.24**, the experimental and numerical pullout load and interfacial shear stress curves, both versus slip are provided where reasonable correlations are achieved.

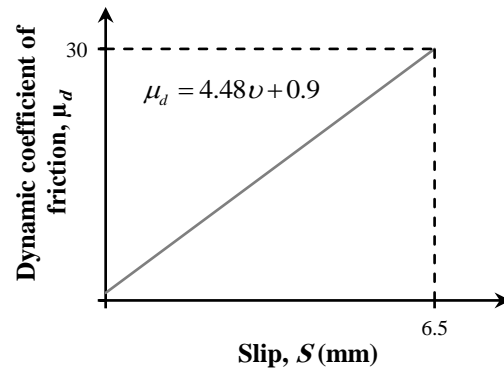


Fig. 3.22. Dynamic coefficient of friction - slip relationship for the twisted fibre.

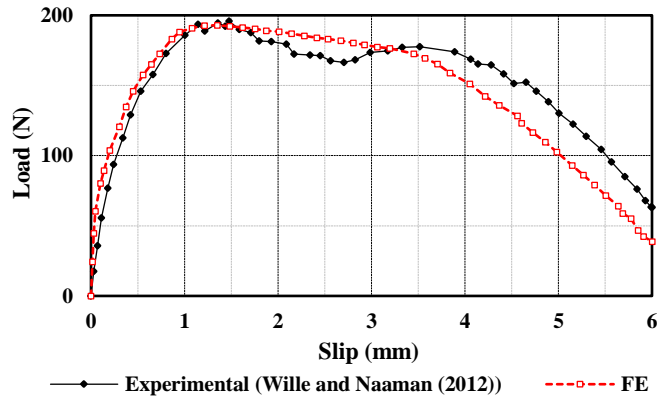


Fig. 3.23. Experimental and numerical load-slip curves of the twisted fibre.

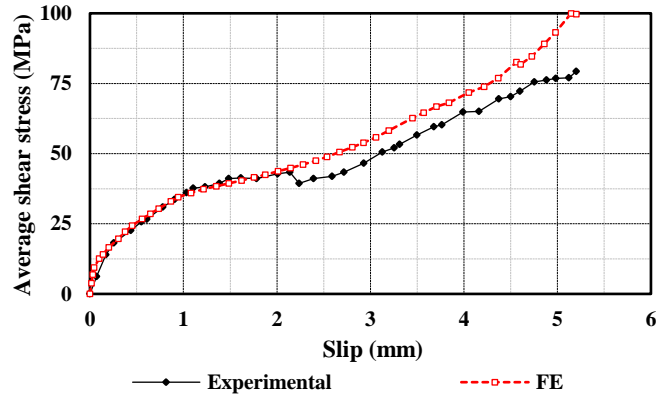


Fig. 3.24. Average interfacial shear stress versus slip for the twisted fibre.

Fig. 3.25 shows the von Mises stress contours of the fibre at slips equal 0.015 mm, 1.35 mm, and 6 mm which respectively correspond to the debonding load, the peak load, and the complete pullout from the matrix.

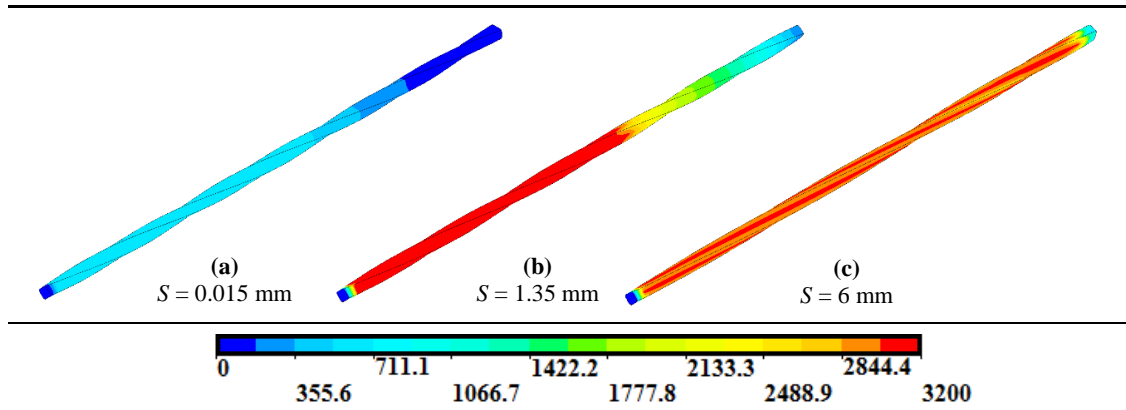


Fig. 3.25. The von Mises stress contours (in MPa) of the twisted fibre at slips correspond to (a) debonding load, (b) peak load, and (c) the complete pullout.

In addition, the normalised von Mises stress at five levels along the fibre length, 0.5 mm, 2 mm, 3 mm, 4 mm, and 6 mm from the bottom of the fibre is plotted versus displacement in **Fig. 3.26**.

The results are indicative of the effectiveness of the twist along the fibre as the mechanical anchorage which leads to higher performance and favourable stress distribution along the fibre.

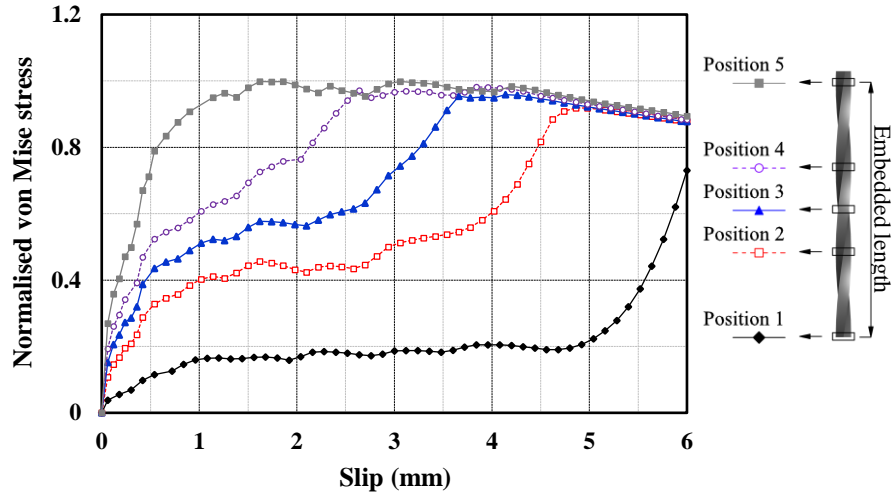


Fig. 3.26. Normalised von Mises stress versus displacement at five levels of the twisted fibre.

3.4. FIBRE DEVELOPMENT

As the first step for the development of a new fibre, numerous fibres with various new configurations (shapes) are considered. To investigate the fibres pullout performance, the validated FE pullout model is employed which is more time- and cost-efficient than the physical pullout test. The FE simulations are performed on a DELL™ WORKSTATION T7500 machines (2×X5690@3.47 GHz and 48 GB RAM). The hooked-end fibre validated in **Section 3.3.2** is used as the basis of the geometrical, material, and the fibre-matrix interface properties of the new fibres. For example, the diameter and length of all the fibres, i.e. d_f and l_f , are 1 mm and 50 mm, and the initial yield and ultimate stresses of the fibres material (f_y and f_u) are 650 MPa and 800 MPa, respectively. Depending on the mechanical anchorage of the new fibres, a few consecutive simulations are performed to optimise the mechanical properties of the fibre's material (f_y and f_u) and avoid the fibre's fracture.

In order to compare the effectiveness of the fibre's shape irrespective of the level of the fibre's deformity, the normalised pullout load with respect to the steel wire's tensile strength versus slip curves of the new fibres are assessed. The considered criteria are the normalised peak pullout load, i.e. fibre efficiency ($E_f = P_{max} / (A_f f_u)$) and the pullout load decay (L_d), i.e. the ratio of the pullout load corresponding to the slip of 25 mm to

the peak pullout load. Since the main objective of this project is to develop a new fibre with the slip-hardening response, the parameter L_d plays the major role in the comparison process. The study of pullout characteristics of quite a few fibres with various hook geometries imply that the slip-hardening response cannot be achieved using such geometries (NF-1 and NF-2 are typical fibres with hook mechanical anchorages as seen in **Fig. 3.27**). Considering the favourable performance of crimped and twisted fibres which respectively possess high peak pullout load and slip-hardening response, it is deemed that the spiral configuration which is somehow a combination of crimp and twist geometries could lead to the desired performance (NF-3 in **Fig. 3.27**). The optimised yield and ultimate stresses of the fibre's material for NF-1, NF-2, and NF-3 are found to be 1600 MPa and 2000 MPa, 1000 MPa and 1250 MPa, and 600 MPa and 750 MPa respectively. The normalised pullout load versus slip curves of the new fibres as well as the hooked-end fibre are illustrated in **Fig. 3.28**. The normalised peak pullout load (E_f) and the pullout load decay (L_d), as well as their differences relative to those of the hooked-end fibre, are provided in **Table 3.3**. The von Mises stress distribution of the new fibres at varying slips are shown in **Fig. 3.29**.

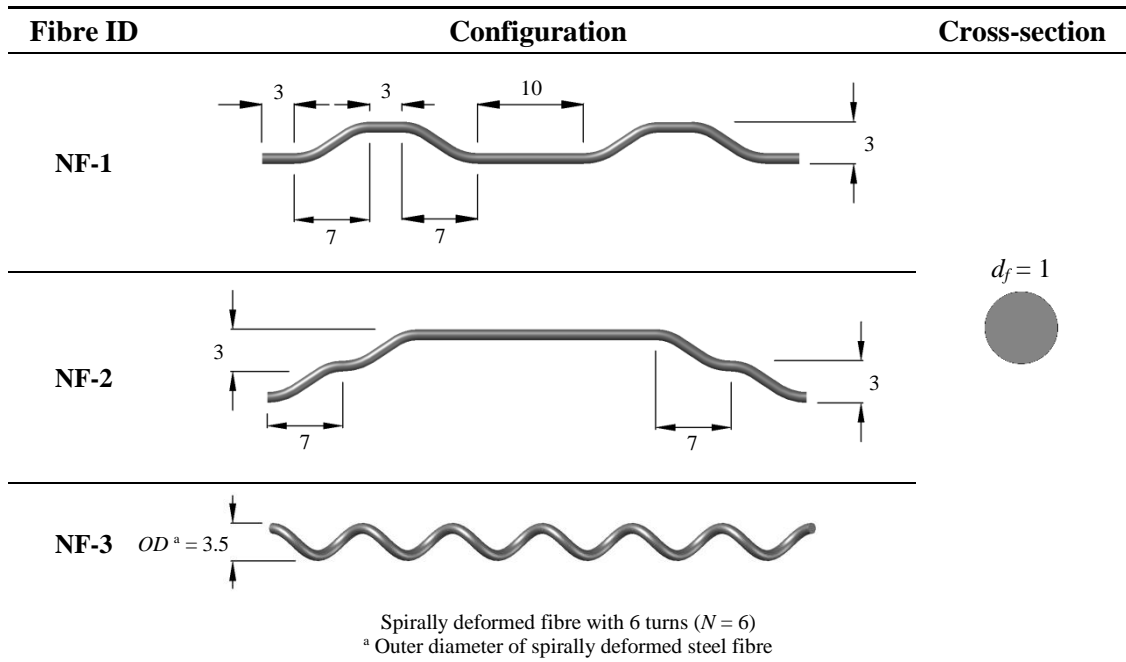


Fig. 3.27. Dimensions of the new steel fibres (in mm), fibre length (L_f) = 50 mm.

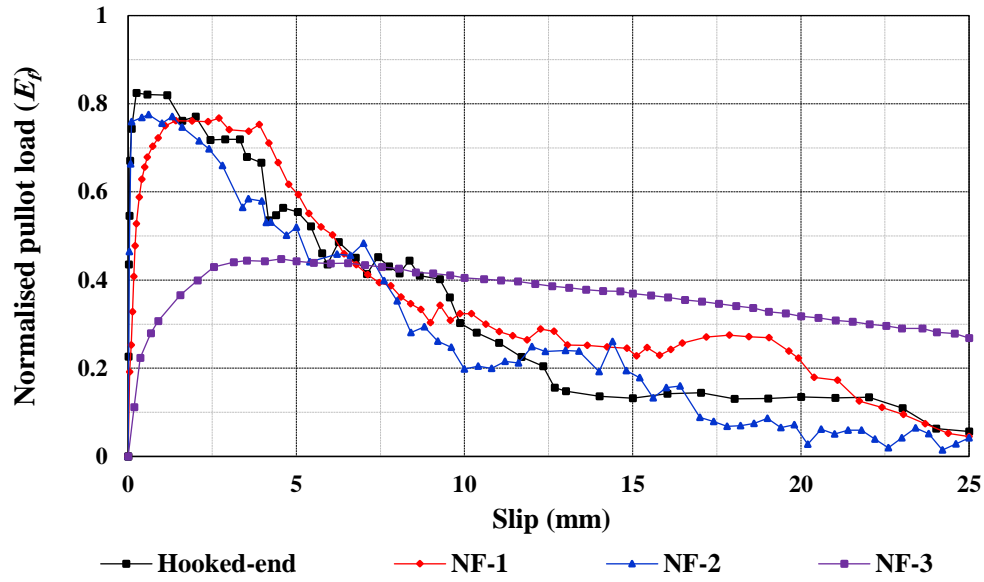


Fig. 3.28. Pullout response of the new steel fibres and the hooked-end fibre.

Table 3.3

Comparison of pullout response of the new fibres with the hooked-end fibre.

Fibre type	E_f	Difference (%)	L_d	Difference (%)
Hooked-end	0.82	-	0.07	-
NF-1	0.77	-6.10	0.06	-13.93
NF-2	0.77	-6.10	0.06	-18.81
NF-3	0.45	-45.12	0.60	786.96

From the results, it is evident that NF-1 and NF-2, i.e. modified hooked-end fibres, have relatively higher efficiencies compared with NF-3, however, they suffer from significant pullout load decay following the peak load. It should be noted that in real scenarios, the cracks might initiate at any point along the fibre and the fibre generally slips on the shorter embedded side. This could highly affect the pullout performance of steel fibres especially those which are fully deformed such as crimped and twisted. The study of the stress distributions over the spirally deformed fibre indicates that during the pullout process the regions nearby the exit point experiences considerably higher level of stress compared with the other regions. It implies that the pullout response of such fibres is less influenced by the variation of embedded length compared with the other fully deformed steel fibres such as NF-1, NF-2, and crimped (see **Figs. 3.20** and **3.29**).

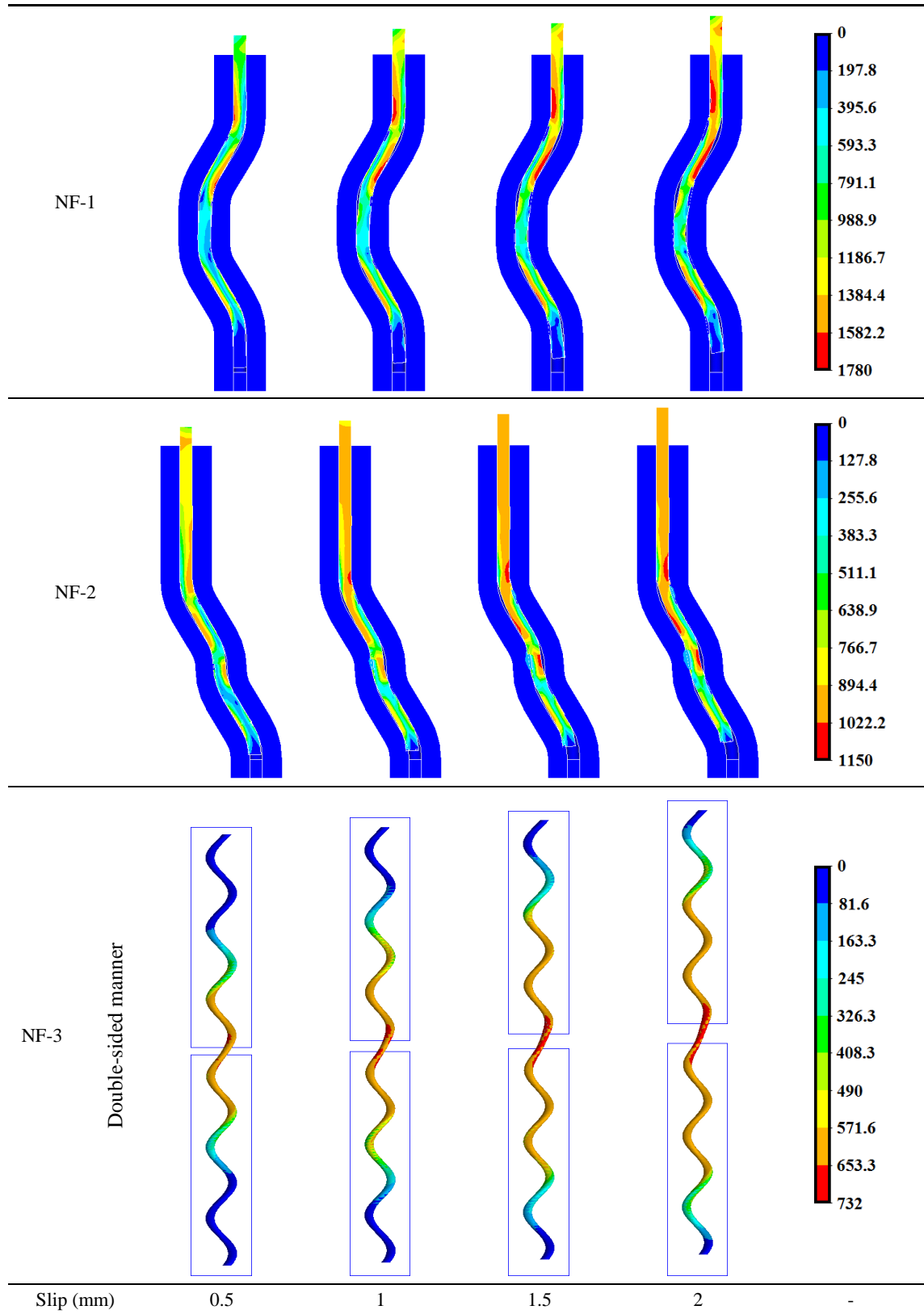


Fig. 3.29. The von Mises stress contour (in MPa) of the new steel fibres (not in scale).

In addition to the fibres pullout characteristics (E_f and l_d), the feasibility of fibre production and corresponding costs as well as fibre geometry and mixing issues e.g. balling are considered to select one shape concept for further investigations.

Overall, the spiral configuration is selected as the most favourable and practical geometry for mechanical anchorage.

3.4.1. EXPERIMENTAL PULLOUT TEST

In order to re-validate the numerical pullout model and further adjust its non-linear parameters to enhance the simulations prediction, a set of experimental pullout tests were conducted on four different spirally deformed steel fibres. Steel wires with two different diameters ($d_f = 0.55$ and 0.9 mm) are deformed to the desirable shapes using basic tools including a drill, steel nails, and pliers to produce the fibres. The ultimate strength (f_u) of the wires with a diameter of 0.55 mm and 0.9 mm are 1000 MPa and 1600 MPa, respectively. The specifications of the considered fibres are summarised in **Table 3.4** in which N = number of turns, OD = outer diameter of the fibre, d_f = wire diameter (fibre diameter), and l_f = length of the fibre (see **Fig. 3.27**).

As it is seen in the table, the fibres are labelled such that the geometrical properties of the fibres can be identified by the label. For instance, the label “SD-4-2-0.9-50” indicates that the fibre is spirally deformed, with 4 turns, outer diameter of 2 mm, wire diameter of 0.9 mm, and it is 50 mm in length. To cast the specimens for the fibre pullout test in a double-sided manner, a wooden mould is designed as seen **Fig. 3.30**.

Table 3.4
Specifications of the considered spirally deformed steel fibres.

Label SD - N - OD - d_f - l_f	N	OD (mm)	d_f (mm)	l_f (mm)
SD-5-2-0.55-50	5	2	0.55	50
SD-10-1-0.55-50	10	1	0.55	50
SD-4-2-0.9-50	4	2	0.9	50
SD-5-2-0.9-50	5	2	0.9	50

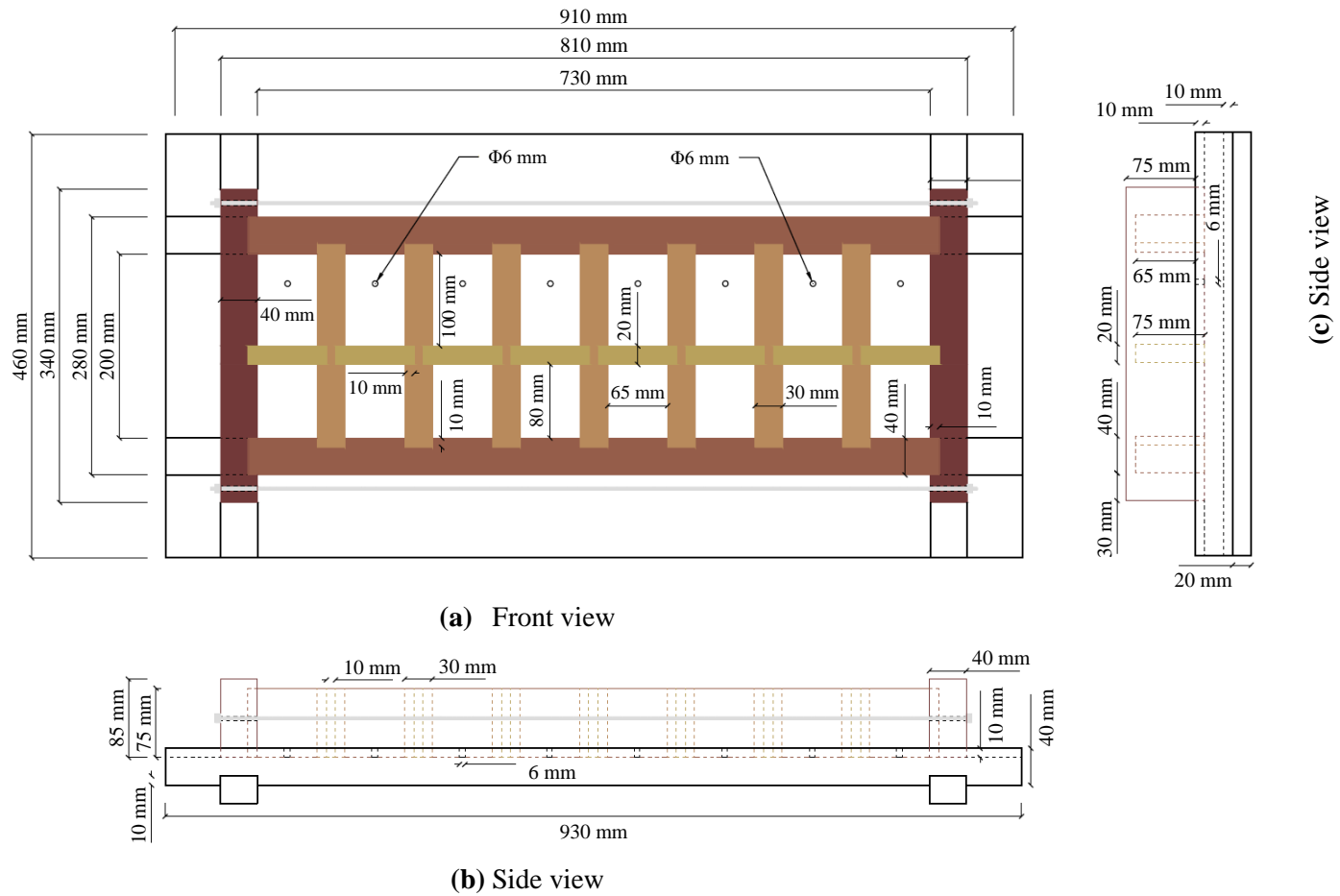


Fig. 3. 30. Dimensions of the mould designed for double-sided pullout specimens.

As seen in **Fig. 3.30**, the mould can be used to cast eight identical specimens. The double-sided fibre pullout specimens consist of two separate concrete blocks each with dimensions of 65 mm \times 65 mm \times 100 mm which are touching each other. The fibres are perpendicularly aligned to the concrete blocks interfaces, i.e. the crack surfaces, and the embedded lengths of the fibres in the concrete blocks are equal. It should be mentioned that one side of the specimens is cast and once the block is hardened, a plastic separator is placed on the top of the block and then the other part is cast. During the concrete casting, steel tubes are placed into the concrete blocks to provide a proper arrangement for the test specimens to be gripped to the pullout testing clamps (see **Fig. 2.8(a)**). Considering the specimens' dimensions, a clamp is designed (as seen in **Fig. 3.31**) which can be gripped to the electro-hydraulic servo Universal Testing Machine (100 kN). A pair of the clamps is fabricated to grip both sides of the specimens.

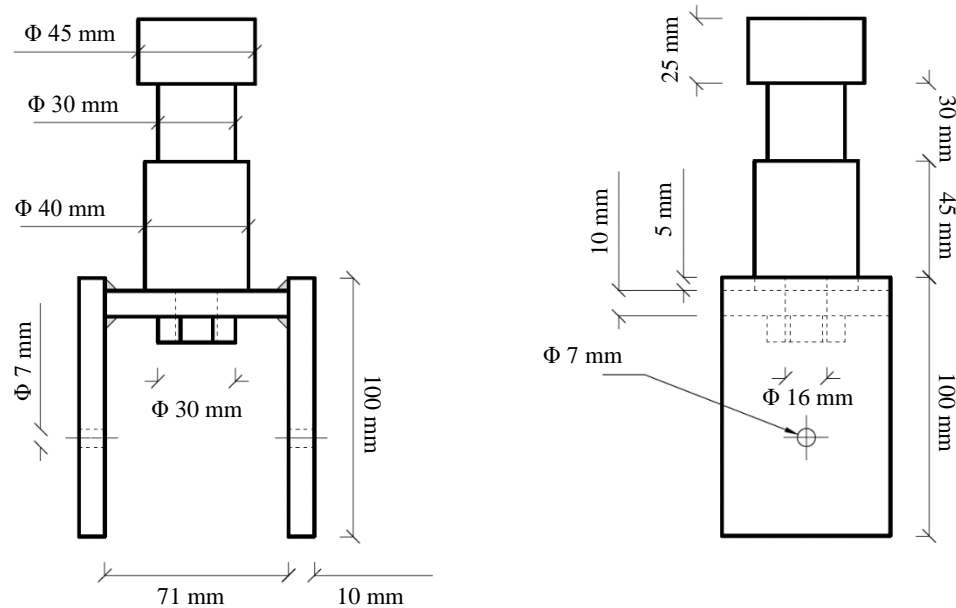


Fig. 3.31. Dimensions of the clamp of double-sided pullout testing.

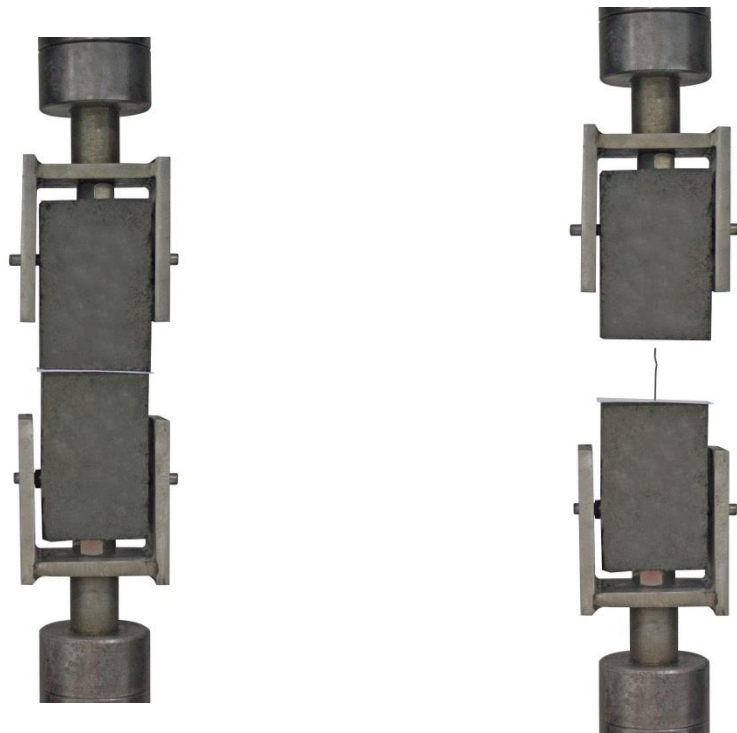
The mould and the steel clamps of the fibre pullout test are shown in **Fig. 3.32**. For each fibre, eight specimens are tested where the average result is considered as the pullout

response of the fibre. The pullout response of eight “SD-5-2-0.9-50” fibres and the corresponding average pullout response are shown in **Fig. 3.33**.

The concrete strength of the specimens is $f_{ck} = 35.4 \pm 2.9$ MPa ($f_m = 35$ MPa). The mix proportions and design procedure are provided in **Section 4.2.1**.



(a) Pullout specimens' mould



Embedded fibre

Pulled out fibre

(b) Pullout clamps

Fig. 3.32. Fibre pullout test.

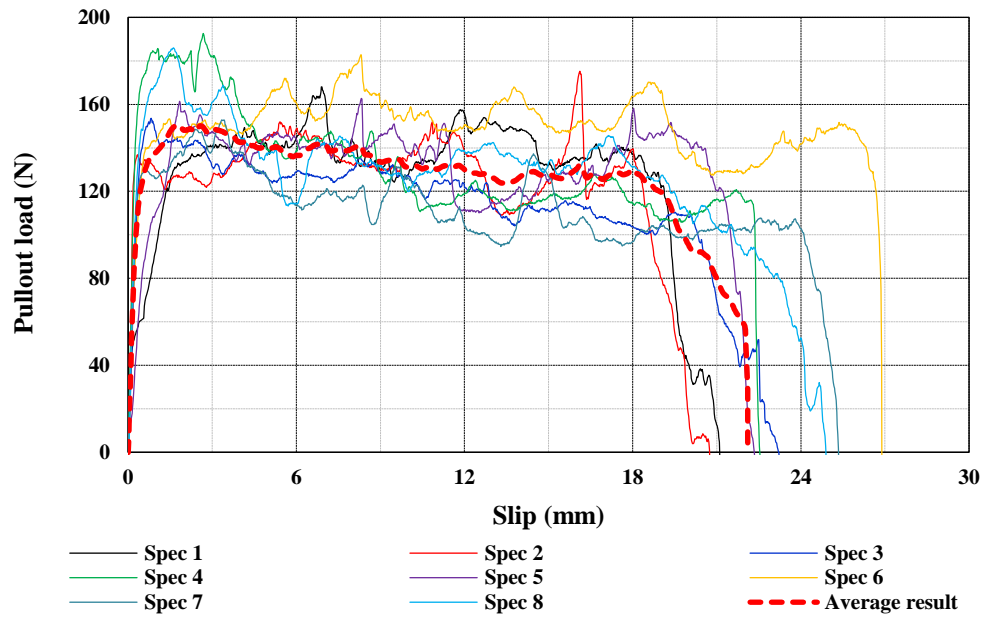


Fig. 3.33. Individual and average pullout responses of SD-5-2-0.9-50.

The average pullout response of the spirally deformed steel fibres is shown in **Fig. 3.34**.

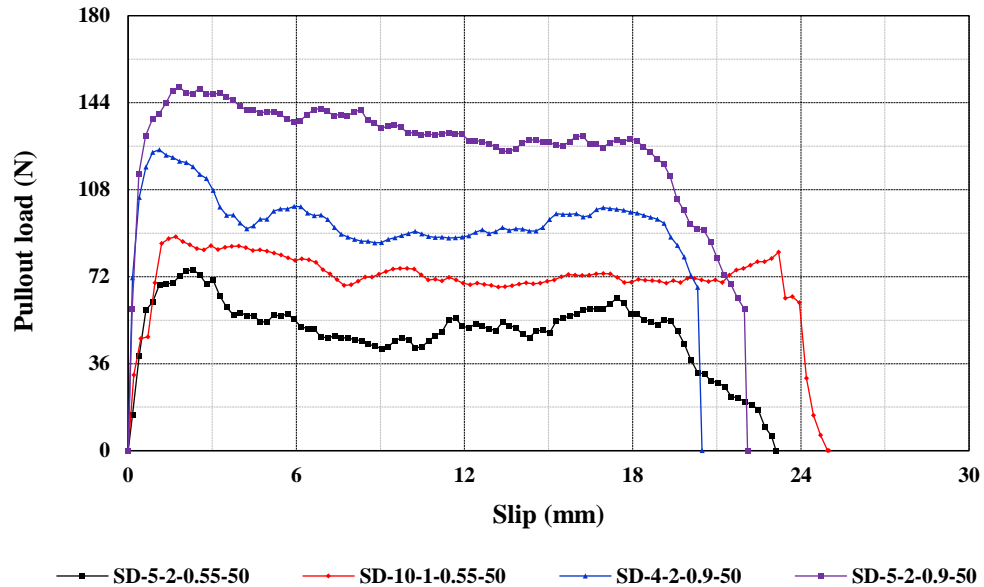


Fig. 3.34. Average pullout responses of spirally deformed steel fibres.

As can be seen in the figure, spirally deformed steel fibres show slip-hardening pullout response in normal concrete which implies the superior post-peak pullout behaviour compared with the commercially available steel fibres. Moreover, the geometrical parameters of the fibres (N , OD , d_f , and l_f) affect the pullout behaviour.

3.4.2. FE MODEL RE-VALIDATION

The characteristics of the matrix such as strength and density affect the pullout behaviour of steel fibres. The non-linear parameters of the fibre-matrix interface were determined based on the experimental data in the literature (see **Section 3.3.2**). Hence, the calibration of the interface parameters is necessary to enhance the accuracy of the numerical model in predicting the pullout behaviour of the spirally deformed steel fibres for the material which are used for the material and structural testing.

A few consecutive pullout simulations are performed for each fibre to calibrate the interface parameters which result in the best agreement between the experimental pullout response and the numerical results. The average values of the calibrated parameters of the spirally deformed steel fibres (see **Table 3.4**) are presented in **Table 3.5**.

Table 3.5
The calibrated contact parameters for spirally deformed steel fibres.

Fibre type	Dynamic friction of coefficient	Static friction of coefficient	Cohesion (MPa)	Maximum contact friction (MPa)
	μ_d	μ_s	c	τ_{max}
Spirally deformed	0.18	0.45	1.2	100

The numerical pullout load-slip curves of the fibres, as well as their experimental counterparts, are shown in **Fig. 3.35**. As seen, the FE model can properly predict the pullout response of spirally deformed steel fibres; hence, it can be used as a virtual laboratory unit to optimise the material and geometrical properties of such fibres.

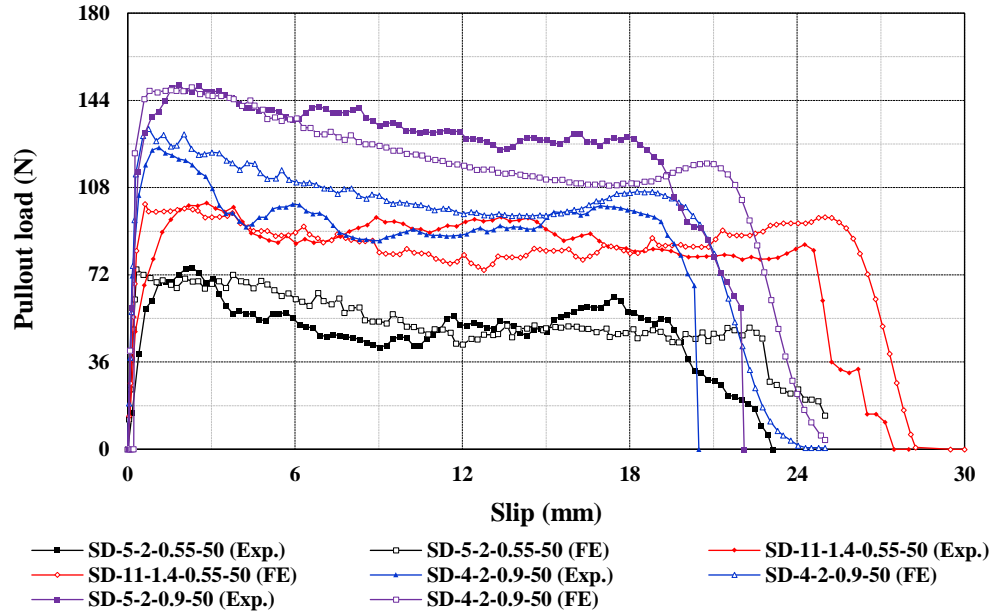


Fig. 3.35. Average pullout responses of spirally deformed steel fibres.

3.4.3. PARAMETRIC STUDY

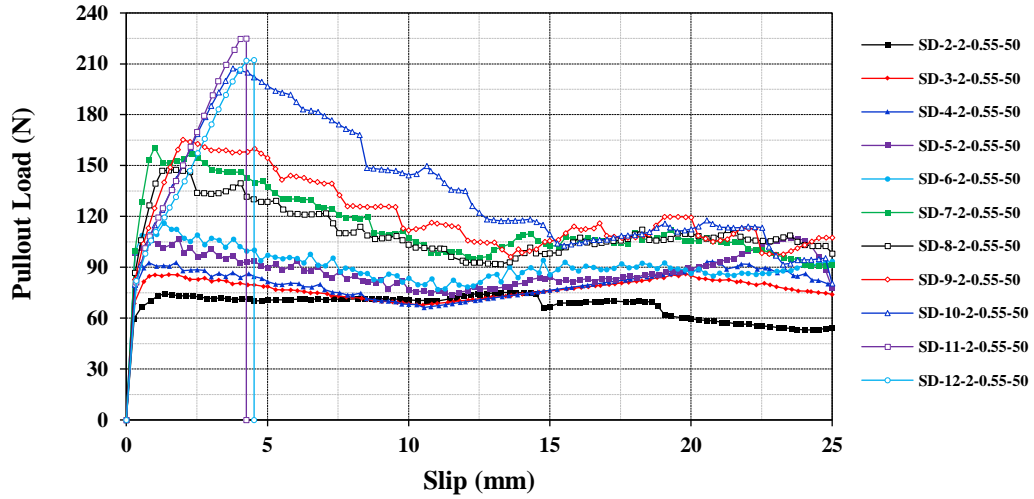
A parametric study is performed on the geometrical properties of the spirally deformed steel fibres to examine the effects of N , OD , d_f , and l_f on the pullout performance. Moreover, to consider the effect of fibre material properties on the pullout characteristics, two different steel materials with yield and ultimate strengths of 800 MPa and 1000 MPa, and 1200 MPa and 1500 MPa are incorporated into the study. The specifications of the models are summarised in **Table 3.6**. Amongst all the possible combinations (in total 1344 fibres), 340 fibres are selected such that the effect of the geometrical parameters variation are properly covered. A parametric code in APDL (ANSYS Parametric Design Language) is developed to reduce the modelling time using GUI (Graphical User Interface) which is presented in **Appendix 3.1**.

Table 3.6

Specifications of the steel fibres for the parametric study.

Label	N	OD (mm)	d_f (mm)	l_f (mm)
SD - N - OD - d_f - l_f	2, 3, 4, 5, 6, 7, 8, 10, 11, 12	1, 1.5, 2, 2.5 3, 3.5, 4	0.4, 0.45, 0.5, 0.55	40, 45, 50

For instance, the pullout load-slip curves of typical steel fibres with varying numbers of turns (N) are shown in **Fig. 3.36** where the other geometrical parameters (OD , d_f , and l_f) are kept constant. As seen, as N increases, the peak pullout load increases, however, for N greater than 10, fibres fracture which results in a significant decrease in the dissipated pullout energy.

**Fig. 3.36.** Average pullout responses of the typical spirally deformed steel fibres.

The dissipated pullout energy (E_t) of the fibres is provided in **Fig. 3.37**. In the figure, the solid and hatched bars respectively indicate that the corresponding fibres are completely withdrawn or fractured. The effects of variations of N on the pullout energy are shown in the figure (with bars in black) in which the OD , d_f , and l_f are kept constant. Moreover, the effects of variations of OD on the pullout energy are shown with bars in red and blue. From the figure, it is evident that with the increase in the number of turns (N) or outer diameter (OD), the pullout energy increases. However, with the increase in the

parameters (N and/or OD) the possibility of fibre fracture increases which results in a drastic reduction in the pullout energy.

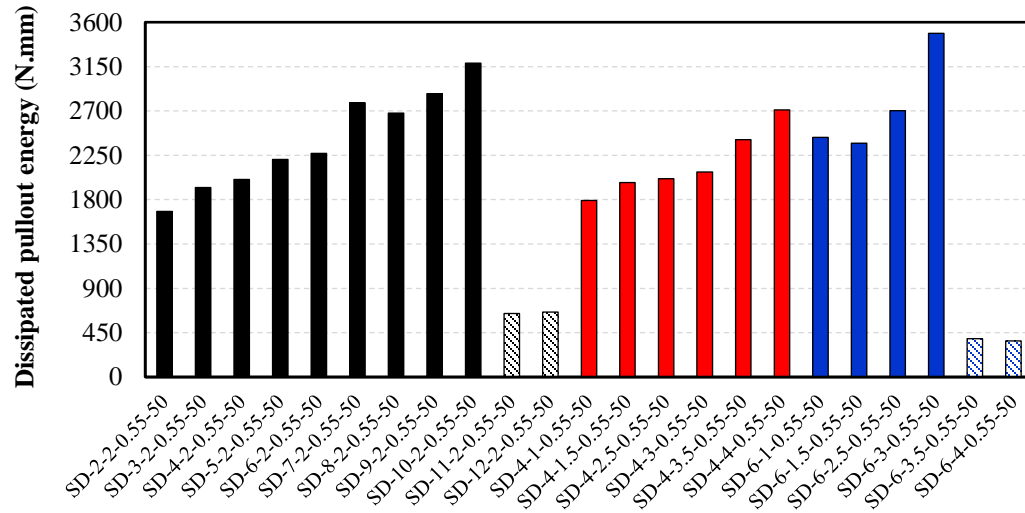


Fig. 3.37. The dissipated pullout energy of the typical steel fibres.

The pullout results of the investigated spirally deformed steel fibres including pullout load, dissipated pullout energy, and fibre efficiency are summarised in **Table 3.7**. As seen, each fibre is examined with two different steel materials. The bold values demonstrate that the corresponding fibres fracture during the pullout process.

Table 3.7
Pullout results of the steel fibres for the parametric study.

Label	$f_y = 800 \text{ MPa}$ and $f_u = 1000 \text{ MPa}$			$f_y = 1200 \text{ MPa}$ and $f_u = 1500 \text{ MPa}$		
	Pullout energy (N.mm)	Load (N)	Efficiency %	Pullout energy (N.mm)	Load (N)	Efficiency %
SD-2-2-0.55-50	963.92	53.36	0.22	1680.29	75.24	0.21
SD-3-2-0.55-50	1147.21	63.47	0.27	1922.74	86.18	0.24
SD-4-2-0.55-50	1312.17	67.87	0.29	2004.54	93.43	0.26
SD-5-2-0.55-50	1445.91	74.5	0.31	2207.73	107.43	0.30
SD-6-2-0.55-50	1563.73	87.17	0.37	2269.16	116.09	0.33
SD-7-2-0.55-50	1722.82	96.35	0.41	2781.56	160.69	0.45
SD-8-2-0.55-50	1935.38	112.61	0.47	2677.63	147.59	0.41
SD-9-2-0.55-50	328.99	134.23	0.57	2874.80	165.19	0.46
SD-10-2-0.55-50	289.16	129.17	0.54	3184.76	207.38	0.59
SD-11-2-0.55-50	320.89	133.21	0.56	644.66	224.98	0.64
SD-12-2-0.55-50	301.14	132.19	0.56	659.06	212.20	0.60
SD-4-1-0.55-50	1113.9	60.55	0.25	1790.08	79.46	0.23
SD-4-1-0.55-50	1113.9	60.55	0.25	1790.08	79.46	0.23
SD-4-1.5-0.55-50	1251.28	70.6	0.3	1972.14	88.65	0.25
SD-4-2.5-0.55-50	1347.76	70.32	0.3	2011.13	101.25	0.29
SD-4-3-0.55-50	1473.67	76.68	0.32	2079.65	109.58	0.31
SD-4-3.5-0.55-50	1653.72	85.78	0.36	2407.93	117.10	0.33
SD-4-4-0.55-50	1870.28	96.51	0.41	2710.15	137.88	0.39
SD-6-1-0.55-50	1647.42	73.2	0.31	2431.60	104.99	0.30
SD-6-1.5-0.55-50	1538.95	83.08	0.35	2372.40	112.73	0.31
SD-6-2.5-0.55-50	1895.92	103.87	0.44	2702.60	145.01	0.41
SD-6-3-0.55-50	235.58	131.59	0.55	3487.06	185.96	0.53
SD-6-3.5-0.55-50	240.73	117.24	0.49	388.98	221.51	0.63
SD-6-4-0.55-50	258.78	126.03	0.53	366.38	199.23	0.56
SD-2-2-0.5-50	831.79	46.03	0.23	1284.56	60.85	0.21
SD-3-2-0.5-50	970.69	51.78	0.26	1484.66	69.60	0.24
SD-4-2-0.5-50	1103.82	57.76	0.29	1672.83	90.65	0.31
SD-5-2-0.5-50	1231.44	68.52	0.35	1846.06	91.86	0.31
SD-6-2-0.5-50	1354.3	82.08	0.42	2021.45	113.10	0.39
SD-7-2-0.5-50	1581.97	91.02	0.46	2260.61	125.15	0.43
SD-8-2-0.5-50	1878.21	112.23	0.57	2590.14	152.14	0.51
SD-9-2-0.5-50	216.51	111.58	0.57	3045.89	193.19	0.65
SD-10-2-0.5-50	249.38	104.04	0.53	462.55	193.98	0.66
SD-4-1-0.5-50	931.59	49.33	0.25	1597.16	75.30	0.25
SD-4-1.5-0.5-50	1045.94	56.56	0.29	1643.50	75.30	0.25
SD-4-2.5-0.5-50	1156.29	62.97	0.32	1698.88	84.45	0.29
SD-4-3-0.5-50	1282.72	68.38	0.35	1845.15	94.19	0.33
SD-4-3.5-0.5-50	1470.77	75.31	0.38	2113.98	105.18	0.36
SD-4-4-0.5-50	1704.9	86.66	0.44	2395.89	116.38	0.40
SD-6-1-0.5-50	1359.03	61.16	0.31	2054.86	90.79	0.31
SD-6-1.5-0.5-50	1280.79	64.68	0.33	1924.48	90.36	0.31
SD-6-2.5-0.5-50	1769.46	100.04	0.51	2537.89	137.88	0.46
SD-6-3-0.5-50	171.45	108.83	0.55	3376.10	184.13	0.63
SD-6-3.5-0.5-50	177.26	95.87	0.49	261.86	182.93	0.63
SD-6-4-0.5-50	182.78	86.78	0.44	187.20	165.81	0.56

Table 3.7 (Continued)

Pullout results of the steel fibres for the parametric study.

Label	$f_y = 800 \text{ MPa}$ and $f_u = 1000 \text{ MPa}$			$f_y = 1200 \text{ MPa}$ and $f_u = 1500 \text{ MPa}$		
	Pullout energy (N.mm)	Load (N)	Efficiency %	Pullout energy (N.mm)	Load (N)	Efficiency %
SD-2-2-0.45-50	711.5	40.06	0.25	973.40	52.51	0.23
SD-3-2-0.45-50	810.64	43.63	0.27	1264.46	60.96	0.25
SD-4-2-0.45-50	926.43	50.59	0.32	1386.79	70.89	0.30
SD-5-2-0.45-50	1035.23	60.63	0.38	1512.05	81.04	0.34
SD-6-2-0.45-50	1205.09	72.32	0.45	1693.94	99.36	0.41
SD-7-2-0.45-50	1486.6	88.24	0.55	2004.29	112.90	0.48
SD-8-2-0.45-50	152.39	93.59	0.59	2412.44	150.30	0.63
SD-9-2-0.45-50	163.29	89.92	0.57	389.45	169.96	0.71
SD-10-2-0.45-50	166.71	84.5	0.53	299.64	157.66	0.66
SD-4-1-0.45-50	770.02	41.28	0.26	1296.85	60.70	0.25
SD-4-1.5-0.45-50	872.67	45.75	0.29	1384.45	73.56	0.31
SD-4-2.5-0.45-50	973.99	55.48	0.35	1410.50	75.64	0.31
SD-4-3-0.45-50	1132.54	60.8	0.38	1611.50	83.36	0.35
SD-4-3.5-0.45-50	1316.44	67.33	0.42	1862.18	93.76	0.39
SD-4-4-0.45-50	1513.1	77.51	0.49	2175.94	103.10	0.44
SD-6-1-0.45-50	1028.79	58.43	0.37	1637.86	75.98	0.31
SD-6-1.5-0.45-50	1071.92	57.14	0.36	1631.81	80.56	0.34
SD-6-2.5-0.45-50	119.41	81.6	0.51	2204.68	127.53	0.54
SD-6-3-0.45-50	128.47	85.66	0.54	241.73	161.45	0.68
SD-6-3.5-0.45-50	135.69	77.54	0.49	248.66	146.51	0.61
SD-6-4-0.45-50	154.54	86.78	0.55	227.20	152.50	0.64
SD-2-2-0.4-50	595.58	33.87	0.27	811.49	44.63	0.24
SD-3-2-0.4-50	663.88	36.96	0.29	965.69	52.63	0.28
SD-4-2-0.4-50	761.3	43.29	0.34	1100.19	58.41	0.31
SD-5-2-0.4-50	879.12	51.85	0.41	1253.38	70.08	0.38
SD-6-2-0.4-50	1083.56	63.11	0.5	1498.50	88.23	0.46
SD-7-2-0.4-50	107.73	80.57	0.64	1905.70	115.24	0.61
SD-8-2-0.4-50	107.76	74.99	0.6	171.94	138.34	0.74
SD-9-2-0.4-50	115.61	69.26	0.55	182.83	130.78	0.70
SD-10-2-0.4-50	116.62	66.66	0.53	212.71	123.86	0.66
SD-4-1-0.4-50	631.71	35.23	0.28	976.86	49.10	0.26
SD-4-1.5-0.4-50	708.29	39.71	0.32	1038.64	56.39	0.30
SD-4-2.5-0.4-50	814.67	49.37	0.39	1149.66	64.88	0.35
SD-4-3-0.4-50	983.94	52.86	0.42	1343.63	70.09	0.38
SD-4-3.5-0.4-50	1162.5	58.61	0.47	1574.69	78.89	0.41
SD-4-4-0.4-50	1332.81	69.78	0.56	1794.28	91.48	0.49
SD-6-1-0.4-50	805.59	42.63	0.34	1300.23	59.80	0.31
SD-6-1.5-0.4-50	884.47	51.89	0.41	1304.91	69.21	0.36
SD-6-2.5-0.4-50	104.62	75.95	0.6	2005.54	111.34	0.59
SD-6-3-0.4-50	89.54	67.78	0.54	136.50	127.78	0.68
SD-6-3.5-0.4-50	78.19	61.86	0.49	150.41	113.93	0.60
SD-6-4-0.4-50	84.55	55.06	0.44	128.93	120.69	0.64

Table 3.7 (Continued)

Pullout results of the steel fibres for the parametric study.

Label	$f_y = 800 \text{ MPa}$ and $f_u = 1000 \text{ MPa}$			$f_y = 1200 \text{ MPa}$ and $f_u = 1500 \text{ MPa}$		
	Pullout energy (N.mm)	Load (N)	Efficiency %	Pullout energy (N.mm)	Load (N)	Efficiency %
SD-2-2-0.5-45	728.22	42.46	0.22	1241.34	58.95	0.20
SD-3-2-0.5-45	869.18	51.75	0.26	1414.64	65.33	0.23
SD-4-2-0.5-45	1000.86	54.92	0.28	1511.95	86.81	0.30
SD-5-2-0.5-45	1143.52	64.21	0.33	1741.69	88.14	0.30
SD-6-2-0.5-45	1295.75	71.62	0.36	1959.98	108.00	0.36
SD-7-2-0.5-45	1483.68	83.08	0.42	2189.98	117.28	0.40
SD-8-2-0.5-45	271.29	111.47	0.57	2550.11	141.39	0.48
SD-9-2-0.5-45	218.14	103.64	0.53	3017.40	190.79	0.65
SD-10-2-0.5-45	243.69	98.91	0.5	402.41	168.76	0.58
SD-4-1-0.5-45	845.83	48.06	0.24	1635.23	76.79	0.26
SD-4-1.5-0.5-45	927.14	57.06	0.29	1586.18	73.29	0.25
SD-4-2.5-0.5-45	1070.32	60.8	0.31	1626.28	82.76	0.28
SD-4-3-0.5-45	1253.76	52.2	0.27	1856.16	90.89	0.31
SD-4-3.5-0.5-45	1477.04	71.47	0.36	2232.51	127.24	0.44
SD-4-4-0.5-45	1761.35	94.69	0.48	2596.08	149.96	0.51
SD-6-1-0.5-45	1277.21	58.78	0.3	2023.69	89.94	0.30
SD-6-1.5-0.5-45	1151.49	60.81	0.31	2057.50	104.86	0.35
SD-6-2.5-0.5-45	1831.8	94.83	0.48	2543.01	132.21	0.45
SD-6-3-0.5-45	166.82	101.11	0.51	155.08	189.88	0.65
SD-6-3.5-0.5-45	145.18	90.85	0.46	206.34	166.00	0.56
SD-6-4-0.5-45	133.99	81.38	0.41	162.33	159.96	0.54
SD-2-2-0.4-45	513.05	31.61	0.25	886.80	41.26	0.23
SD-3-2-0.4-45	571.61	34.58	0.28	848.58	52.18	0.28
SD-4-2-0.4-45	680.82	41.65	0.33	989.05	56.04	0.30
SD-5-2-0.4-45	833.32	48.61	0.39	1160.58	66.03	0.35
SD-6-2-0.4-45	1068.63	62.05	0.49	1456.59	83.19	0.44
SD-7-2-0.4-45	417.68	74.28	0.59	1901.59	117.34	0.63
SD-8-2-0.4-45	429.85	68.85	0.55	182.24	131.40	0.70
SD-9-2-0.4-45	444.85	66.65	0.53	194.70	123.90	0.66
SD-10-2-0.4-45	446.77	62.05	0.49	176.69	119.85	0.64
SD-4-1-0.4-45	557.89	32.74	0.26	796.28	46.80	0.25
SD-4-1.5-0.4-45	613.08	36.51	0.29	920.10	56.35	0.30
SD-4-2.5-0.4-45	793.73	46.96	0.37	1101.03	62.74	0.34
SD-4-3-0.4-45	962.35	50.1	0.4	1356.16	68.36	0.36
SD-4-3.5-0.4-45	1142.17	57.76	0.46	1662.48	92.34	0.49
SD-4-4-0.4-45	167.08	66.97	0.53	1944.48	110.60	0.59
SD-6-1-0.4-45	716.01	43.66	0.35	1261.35	59.14	0.31
SD-6-1.5-0.4-45	803.32	47.9	0.38	1189.25	65.60	0.35
SD-6-2.5-0.4-45	92.03	71.15	0.57	2093.76	117.98	0.63
SD-6-3-0.4-45	92.39	63.44	0.5	165.06	133.63	0.71
SD-6-3.5-0.4-45	80.58	57.36	0.46	156.13	147.03	0.78
SD-6-4-0.4-45	79.35	52.3	0.42	162.39	133.15	0.71

Table 3.7 (Continued)

Pullout results of the steel fibres for the parametric study.

Label	$f_y = 800 \text{ MPa}$ and $f_u = 1000 \text{ MPa}$			$f_y = 1200 \text{ MPa}$ and $f_u = 1500 \text{ MPa}$		
	Pullout energy (N.mm)	Load (N)	Efficiency %	Pullout energy (N.mm)	Load (N)	Efficiency %
SD-2-2-0.5-40	897.85	42.04	0.21	1290.19	62.30	0.21
SD-3-2-0.5-40	740.34	51.66	0.26	1377.38	64.25	0.21
SD-4-2-0.5-40	872.13	51.81	0.26	1617.10	77.35	0.26
SD-5-2-0.5-40	1035.23	58.98	0.3	1546.43	83.04	0.29
SD-6-2-0.5-40	1199.16	66.96	0.34	1770.85	96.93	0.33
SD-7-2-0.5-40	1503.82	80.08	0.41	2155.48	110.89	0.38
SD-8-2-0.5-40	236.35	105.23	0.54	2656.33	153.14	0.53
SD-9-2-0.5-40	265.49	97.25	0.5	327.83	164.71	0.56
SD-10-2-0.5-40	207.9	90.68	0.46	291.66	144.45	0.49
SD-4-1-0.5-40	1035.95	51.4	0.26	1752.06	84.74	0.29
SD-4-1.5-0.5-40	824.8	58.82	0.3	1568.18	76.21	0.26
SD-4-2.5-0.5-40	1013.68	58.28	0.3	1488.96	79.78	0.28
SD-4-3-0.5-40	1255.58	91.73	0.47	1905.06	92.38	0.31
SD-4-3.5-0.5-40	1522.18	89.54	0.46	2210.58	121.94	0.41
SD-4-4-0.5-40	1655.88	88.51	0.45	2574.89	131.90	0.45
SD-6-1-0.5-40	1226.32	56.24	0.29	2004.21	87.45	0.30
SD-6-1.5-0.5-40	1050.25	59.02	0.3	1847.29	90.93	0.31
SD-6-2.5-0.5-40	1850.15	96.26	0.49	2660.59	147.50	0.50
SD-6-3-0.5-40	144.23	91.73	0.47	144.43	148.75	0.50
SD-6-3.5-0.5-40	129.75	83.52	0.43	174.59	143.16	0.49
SD-6-4-0.5-40	119.36	76.53	0.39	139.94	143.91	0.49
SD-2-2-0.4-40	438.6	29.29	0.23	838.79	41.46	0.23
SD-3-2-0.4-40	493.83	33.1	0.26	932.28	45.31	0.24
SD-4-2-0.4-40	608.35	38.82	0.31	895.11	53.05	0.29
SD-5-2-0.4-40	765.2	47.31	0.38	1099.60	65.40	0.35
SD-6-2-0.4-40	1054.31	62.61	0.5	1443.93	81.04	0.43
SD-7-2-0.4-40	98.35	68.83	0.55	1995.78	114.36	0.61
SD-8-2-0.4-40	108.41	64.15	0.51	233.39	114.34	0.61
SD-9-2-0.4-40	109.93	60.25	0.48	258.94	126.18	0.68
SD-10-2-0.4-40	102.58	57.11	0.45	306.33	140.65	0.75
SD-4-1-0.4-40	497.16	33.54	0.27	1026.38	45.03	0.24
SD-4-1.5-0.4-40	539.6	35.1	0.28	815.43	56.96	0.30
SD-4-2.5-0.4-40	755.7	43.79	0.35	1137.41	58.29	0.31
SD-4-3-0.4-40	914.11	51.22	0.41	1486.83	82.98	0.44
SD-4-3.5-0.4-40	1104	57.23	0.46	1806.60	107.04	0.56
SD-4-4-0.4-40	79.29	63.03	0.5	2008.69	120.45	0.64
SD-6-1-0.4-40	825.55	44.96	0.36	1214.33	57.39	0.30
SD-6-1.5-0.4-40	707.33	45	0.36	1201.53	62.96	0.34
SD-6-2.5-0.4-40	96.37	67.1	0.53	123.33	126.50	0.68
SD-6-3-0.4-40	87.27	58.45	0.47	149.78	125.26	0.66
SD-6-3.5-0.4-40	85.18	57.05	0.45	117.78	120.55	0.64
SD-6-4-0.4-40	92.89	62.77	0.5	125.84	122.91	0.65

3.4.4. PULLOUT LOAD PREDICTION

The fibre efficiency (E_f) versus geometry index (I_{ge}) of the fibres is plotted in **Fig. 3.38**. The geometry index is defined by **Eq. 3.12**.

$$I_{ge} = \frac{OD \times N}{d_f \times l_f} \quad (3.12)$$

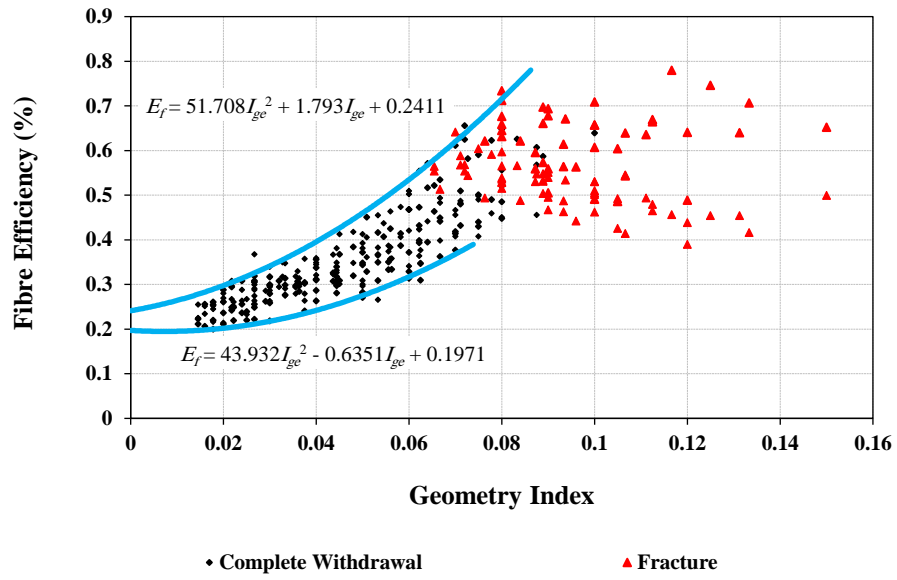


Fig. 3.38. Fibre efficiency versus geometry index.

As seen in the figure, with the increase in the geometry index, the fibre efficiency enhances, however, the probability of fibre fracture increases. Moreover, it can be estimated that fibres with $I_{ge} \geq 0.08$ fracture during the pullout process.

A metaheuristic inspired by the process of natural selection known as the Genetic algorithm (GA) (Goldberg 1989) is employed with a primary population size of 800 to propose an empirical equation to estimate the fibre efficiency in which material and geometrical properties are considered as the inputs.

$$E_{f,pre.} = 0.065l_f^{-0.08} f_u^{0.0187} N^{0.694} OD^{0.465} d_f^{-0.617} \quad (3.13)$$

To assess the accuracy of the proposed equation, the mean absolute error (MAE), is calculated using **Eq. 3.14**.

$$MAE = \frac{1}{n} |E_{f,FE} - E_{f,Pre.}| \times 100 \quad (3.14)$$

The error over the available database (see **Table 3.7**) is 10.1%.

3.4.5. FIBRE DESIGN

In this section, a spirally deformed steel fibre is designed for the material and structural testing programme. The design procedure of the spirally deformed steel fibres is summarised as follows:

1. Fibre geometry index (I_{ge}), wire diameter (d_f), fibre length (l_f), and ultimate tensile strength (f_u) of steel are selected.
2. Using **Eq. 3.12**, and assuming the value of either OD or N , the other parameter is calculated.
3. Fibre efficiency (E_f) is calculated by **Eq. 3.13**.

The fibre geometry index (I_{ge}) is considered to be 0.08 (see **Fig. 3.38**). Considering steel wires available on the market, intended application of the fibre, i.e. structural purposes, and also mixing issues, fibre diameter (d_f) and fibre length (l_f) are selected to be 0.4 mm and 40 mm which result in the fibre aspect ratio of 100 (see **Sections 2.3.1.2** and **2.3.1.3**). The ultimate tensile strength of the steel wire is 1500 MPa. In **Table 3.8**, the design steps of the fibre are provided.

Table 3.8
Fibre design procedure.

Step	1				2		3	
Parameter	I_{ge} (-)	d_f (mm)	l_f (mm)	f_u (MPa)	$OD \times N$ (mm)	N (-)	OD (mm)	$E_{f, Pre.}$ (-)
	0.8	0.4	40	1500	12.8	9	1.42	0.54

The calculated value for the outer diameter in step (2) is rounded to 1.45 mm. Therefore the peak pullout load of the fibre, i.e. SD-9-1.45-0.4-40, is:

$$P_{max} = E_{f,pre.} \times A_f f_u = 0.54 \times 0.25 \times \pi \times 0.4^2 \times 1500 = 102 \text{ N}$$

To check the predicted peak pullout load obtained from **Eq. 3.13**, a FE pullout simulation is performed for fibre SD-9-1.45-0.4-40 whose load-slip curve is shown in **Fig. 3.39**. The peak pullout load from the simulation is 108 N, which indicates the acceptable accuracy of the empirical equation (**Eq. 3.13**). Moreover, the outer diameter of the fibre (*OD*) is slightly increased (from 1.45 mm to 1.55 mm) to investigate the effect of a slight increase in the fibre geometry index (from 0.815 to 0.872) on the fibre pullout performance. As seen in **Fig. 3.39**, even with the small increase in *OD*, the fibre fractures, therefore, SD-9-1.45-0.4-40 is considered as an optimum shape.

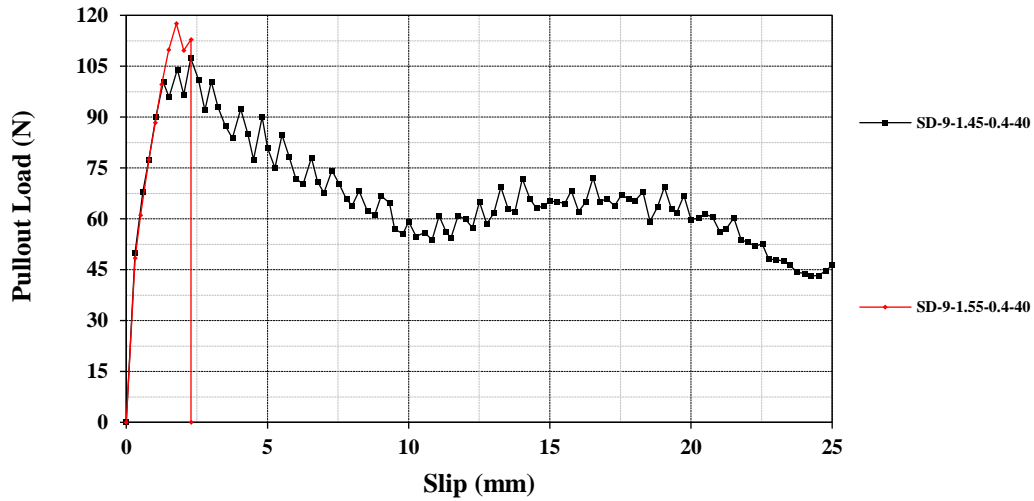


Fig. 3.39. Pullout load-slip curves of SD-9-1.45-0.4-40 and SD-9-1.55-0.4-40.

3.4.6. FIBRE PRODUCTION

To produce the designed fibre (SD-9-1.45-0.4-40) in large quantity for material and structural testing, a production line is established comprising three phases as follows:

1. Spring production:

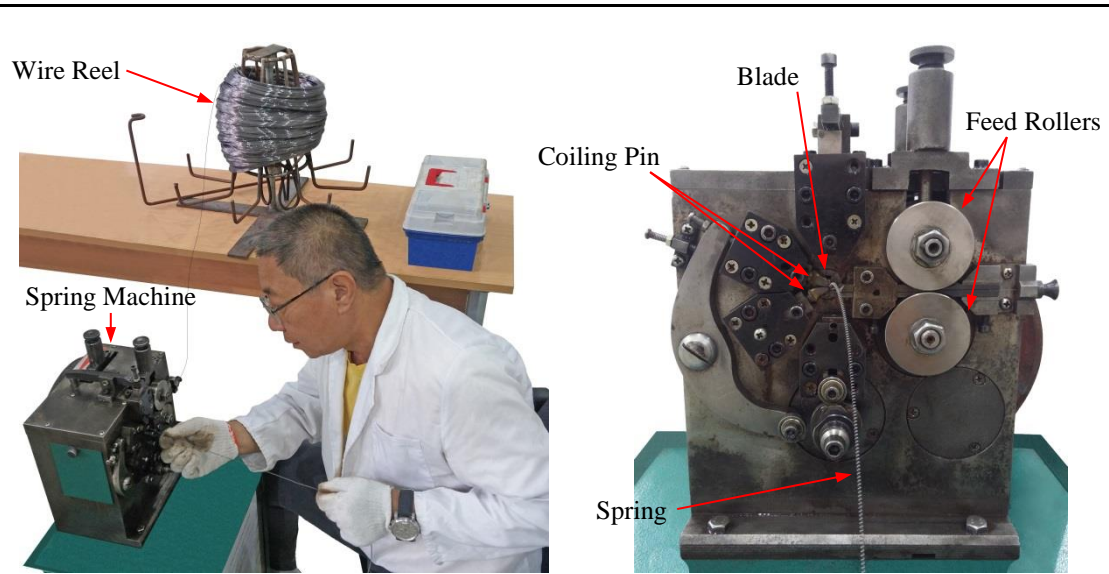
As the first step, the steel wire with $d_f = 0.4$ mm and $f_u = 1500$ MPa, is deformed to springs with length, outer diameter, and pitch of 100 cm, 2 mm, and 1.875 mm, respectively (see **Fig. 3.40(a)**).

2. Spring stretching:

To decrease the outer diameter and also increase the pitch of the springs to the intended values, i.e. $OD = 1.45$ mm and $P_s = 4.45$ mm, they are stretched. It is worthy to mention, a trial and error procedure for phase 1 and 2 is performed to determine the geometrical properties (outer diameter and pitch) and the stretch length of the springs in order to achieve the intended shape (see **Fig. 3.40(b)**).

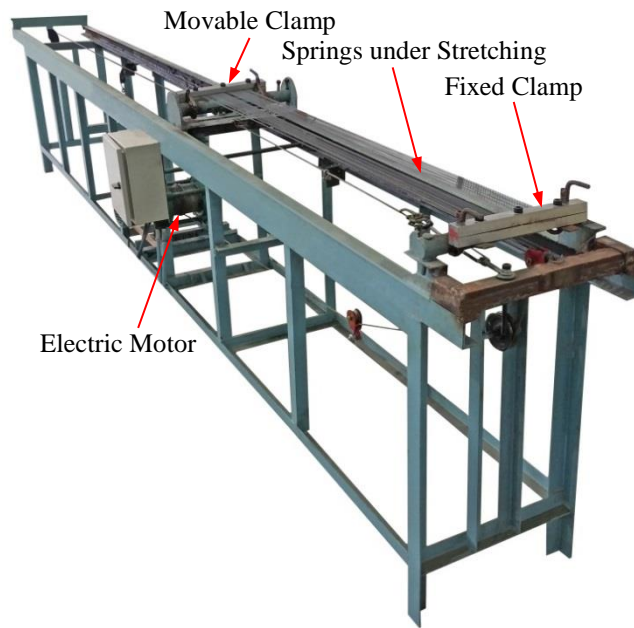
3. Cutting stretched springs

The stretched springs are cut into the intended length, i.e. 40 mm, as seen in **Fig. 3.40(c)**.

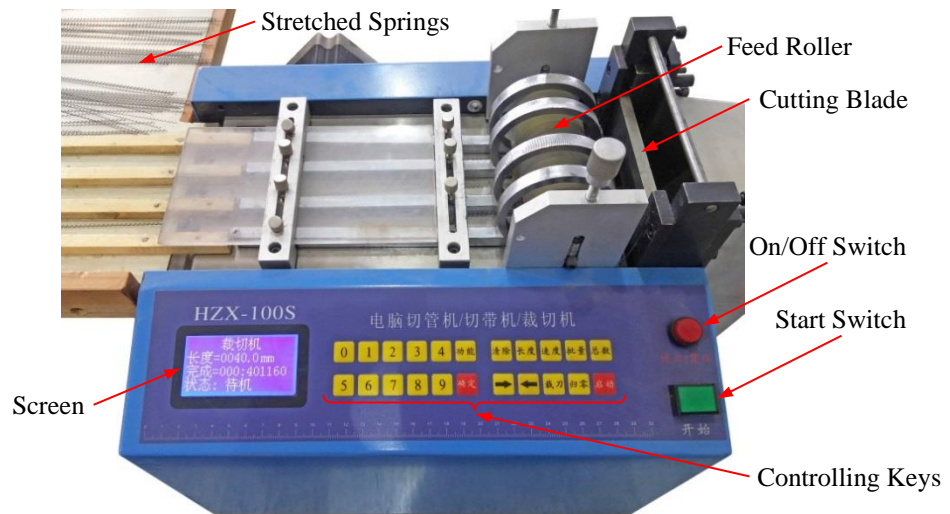


(a) Phase 1: Spring production

Fig. 3.40. Fibre production.



(b) Phase 2: Spring stretching



(c) Phase 3: Cutting stretched springs

Fig. 3.40 (Continued). Fibre production.

After a few days of trial and error, the chain of fibre production (consisting three consecutive stages) was optimised to enhance the bottlenecks of the process chain, then it was possible to produce 4 kg of the new fibre in one working day.

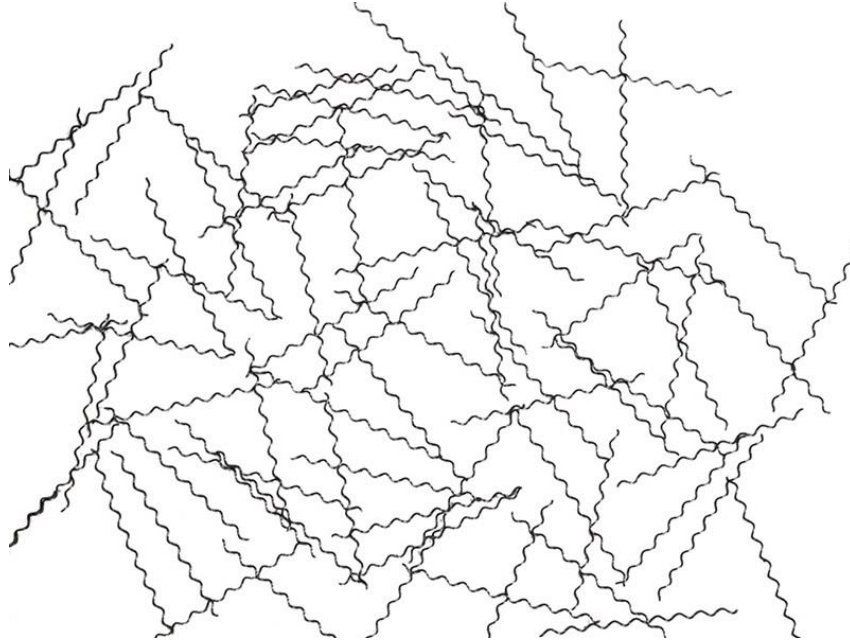


Fig. 3.41. Samples of fibre SD-9-1.45-0.4-40.

3.5. SUMMARY

Fibre pullout simulations are performed on fibres with new geometrical concepts. Given the preliminary fibres' performance (post-peak response and peak pullout load), the spirally deformed configuration is selected as the most favourable shape for further studies. Comprehensive pullout simulations are performed to determine the effects of variations of the fibre geometrical and material properties on the fibre pullout performance where the accuracy of the numerical simulations is verified through comparison of the numerical results with experimental data. Using the pullout database, the fibre is optimised (SD-9-1.45-0.4-40) which possesses slip-hardening response (in normal concrete) and suitable fibre efficiency. Moreover, an empirical equation is proposed to predict the fibre efficiency for a given geometry.

A production line is designed and established to produce the newly-designed steel fibre in large quantity for the following material and structural testing.

CHAPTER 4

MATERIAL TESTING

4.1. INTRODUCTION

The evaluation of SFRC's material properties is important for this composite to be employed effectively and economically in practice. The structural performance of such material mainly depends on its stress-strain characterisation under tension, i.e. constitutive properties. This chapter investigates the material behaviour of fibre reinforced concrete with the newly-designed steel fibre (SD-9-1.45-0.4-40) to characterise the SFRC. The study consists of compression and flexural tests where parameters including concrete strength and fibre volume content are considered. As a reference for the performance comparison of the new fibre with the most common steel fibres on the market, hooked-end and crimped fibres are also included in the experimental phase.

As mentioned in **Section 2.3.3.1.3**, there is no standard direct tension test for fibrous concrete mainly because it is difficult to provide a proper gripping arrangement to avoid specimen cracking at grips and induced bending. On the other hand, bending tests are a widely used test method for the evaluation of the flexural performance of SFRC (Chao, Cho et al. 2011). As an alternative, closed-form formulations are used to back-calculate the constitutive model of FRC. In these methods, an iterative procedure is performed to best fit the load-deflection curve calculated using assumed constitutive material models (in compression and tension) to its experimental counterpart from flexural testing, i.e.

curve fitting. In this chapter, constitutive models in compression and tension proposed by Mobasher, Bakhshi et al. (2014) are used to derive material behaviour of concrete with the newly-designed fibre (SD-9-1.45-0.4-40).

Furthermore, the constitutive material behaviour is required as a basic input for Finite Element and Analytical modelling of SFRC members including the new fibre.

4.2. MATERIAL PROPERTIES

4.2.1. CONCRETE

Two different concrete mix designs are used in this research programme for both plain and fibrous concrete. The 28-day target cylinder strengths of concrete are 35 MPa and 45 MPa where the Building Research Establishment (1997) procedure is selected for the mix design. To increase the workability of fibrous concrete and also considering the consistency issue, superplasticizer with the amount of 1 percent of the cement content is added to the both types of the mixture, i.e. fibrous and non-fibrous. For the material and structural testing, the required materials including fine and coarse aggregates, cement, reinforcing bars, steel fibre, and superplasticizer are calculated and ordered (or produced) to make sure the material consistency over the programme. The 42.5 type Portland cement (GB 175 2007) is used which are packed into the plastic barrels with sealed caps to avoid moisture absorption.

To verify the achievability of the intended strengths, a few trial batches are made to adjust the mix proportions. The dry composition per cubic metre of mixes is presented in **Table 4.1**. The mix designs procedure is provided in **Appendix 4.1**. The required water-cement ratio to achieve the target strengths are respectively 0.538 and 0.445 for concrete with strengths of 35 MPa and 45 MPa.

Table 4.1
Concrete mix design.

Target strength (MPa)	Cement (kg)	Water (kg)	Superplasticizer ¹ (kg)	Fine aggregate ² (kg)	Coarse aggregate ² (kg)
$f_m = 35$	350.0	188.3	3.5	880	988
$f_m = 45$	423.1	188.3	42.5	802	993

¹ Sika ViscoCrete® 1200 series

² Saturated Surface-Dry (SSD) condition

4.2.1.1. AGGREGATES

To decrease the risk of fibre balling, a type of coarse aggregate which is 95 percent finer than 10 mm is used. The fine and coarse aggregates conform to the requirements given in BS EN 12620 (2013). The sieve analyses of the aggregates are provided in **Fig. 4.1**.

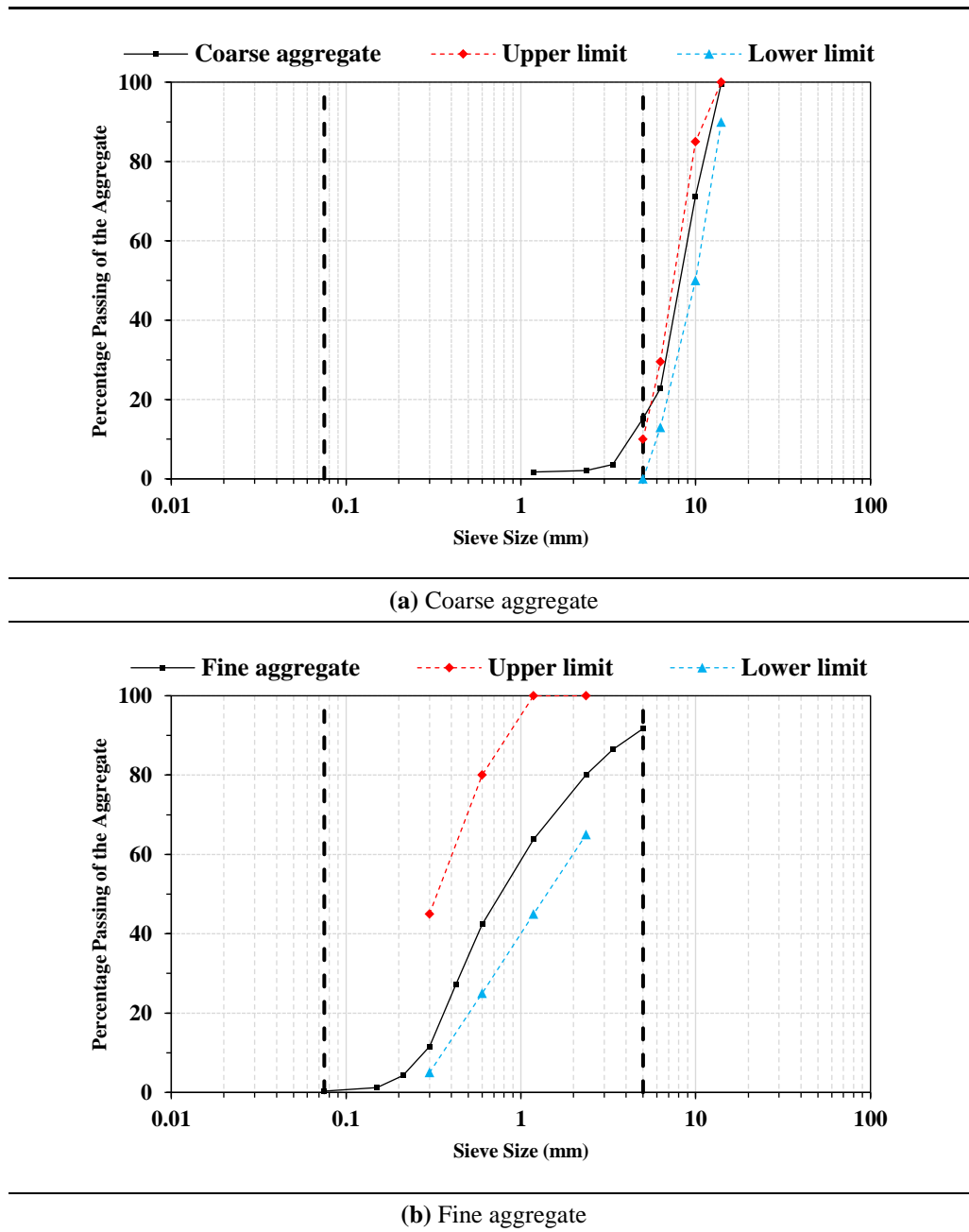


Fig. 4.1. Grading of aggregates.

The specific gravity of the fine and coarse aggregates used for the mix design are determined according to ASTM C128 - 15 (2015) and ASTM C127 - 15 (2015) which are provided in **Table 4.2** and **Table 4.3** The aggregates were stored in polythene sacks in the Structures laboratory prior to mixing.

Table 4.2

Specific gravity and water absorption of fine aggregate.

Item	Weight (g)	$G_{bulk SSD}^1$	Absorption (V) (%)
Pycnometer filled with water (B)	367.48	$\frac{W_{SSD}}{(B + W_{SSD} - C)}$	$\left[\frac{(W_{SSD} - A)}{A} \right] \times 100$
SSD specimen (W_{SSD})	250.00		
Pycnometer, specimen, and water (C)	520.81		
Oven-dry specimen in air (W_{OD})	245.80		
		2.59	1.71

¹ Bulk saturated surface-dry (SSD) specific gravity

Table 4.3

Specific gravity and water absorption of coarse aggregate.

Item	Weight (g)	$G_{bulk SSD}^1$	Absorption (V) (%)
Oven-dry specimen in air (W_{OD})	1981.14	$\frac{W_{SSD}}{(W_{SSD} - C)}$	$\left[\frac{(W_{SSD} - W_{OD})}{W_{OD}} \right] \times 100$
SSD specimen (W_{SSD})	2000		
Saturated SSD specimen in water (C)	1261.8		
		2.71	0.95

¹ Bulk saturated surface-dry (SSD) specific gravity

The measurements of the required water and aggregates in the mix designs are based on the Saturated Surface-Dry (SSD) condition of the aggregates. Therefore, the moisture content of the aggregates (fine and coarse) is calculated using **Eq. 4.1** before mixing of each concrete batch to correct the required quantity of water and aggregates using **Eqs. (4.2)** and **(4.3)** (ASTM C566 - 13 2013).

$$U = (W_{stock} - W_{OD}) / W_{OD} \times 100 \quad (4.1)$$

$$W_{stock} = W_{SSD} \times \frac{(1 + U / 100)}{(1 + V / 100)} \quad (4.2)$$

$$Water_{req.} = Water_{design} + (W_{SSD} - W_{stock})_{fine\ and\ coarse} \quad (4.3)$$

For instance, the moisture content of the first concrete batch with $f_m = 35$ MPa is provided in **Table 4.4**. Since the moisture content varies over the aggregate's sacks depth, three samples are taken from different levels of each sack where the average moisture content is considered for the moisture correction. The corrected quantity of water and aggregates is provided in **Table 4.5**.

Table 4.4
Moisture content of fine and coarse aggregates.

Type	Sample ID	W_{stock}^1 (gr)	W_{OD}^2 (gr)	U^3 (%)	Average (%)
Fine	1	248.3	245.8	1.01	1.27
	2	251.3	247.9	1.35	
	3	250.5	246.9	1.44	
Coarse	1	251.5	244.6	2.74	3.18
	2	249.3	241.3	3.21	
	3	248.4	239.5	3.58	

¹ Weight in stock

Table 4.5
Correction of required ingredients for concrete with $f_m = 35$ MPa.

Aggregate	Water (kg)	Fine aggregate (kg)	Coarse aggregate (kg)
SSD condition	188.3	880	988
Stored in sacks	174.1	996	984

4.2.1.2. FIBRES

Spirally deformed steel fibre, i.e. SD-9-1.45-0.4-40, designed in **Section 3.4.5** is used for the material testing. The fibre material strength is 1500 MPa. To compare the effectiveness of the new fibre compared with its counterparts available on the market, two types of steel fibre, i.e. hooked-end and crimped, are incorporated into the study.

The ultimate strength (f_u) of the hooked-end and crimped fibres material are 1000 MPa and 1500 MPa, respectively. The fibre material is assumed to have a density of 7850 kg/m³ for calculating the required amount of fibres for the various volume fractions.

The geometrical properties of the fibres are shown in **Fig. 4.2**.

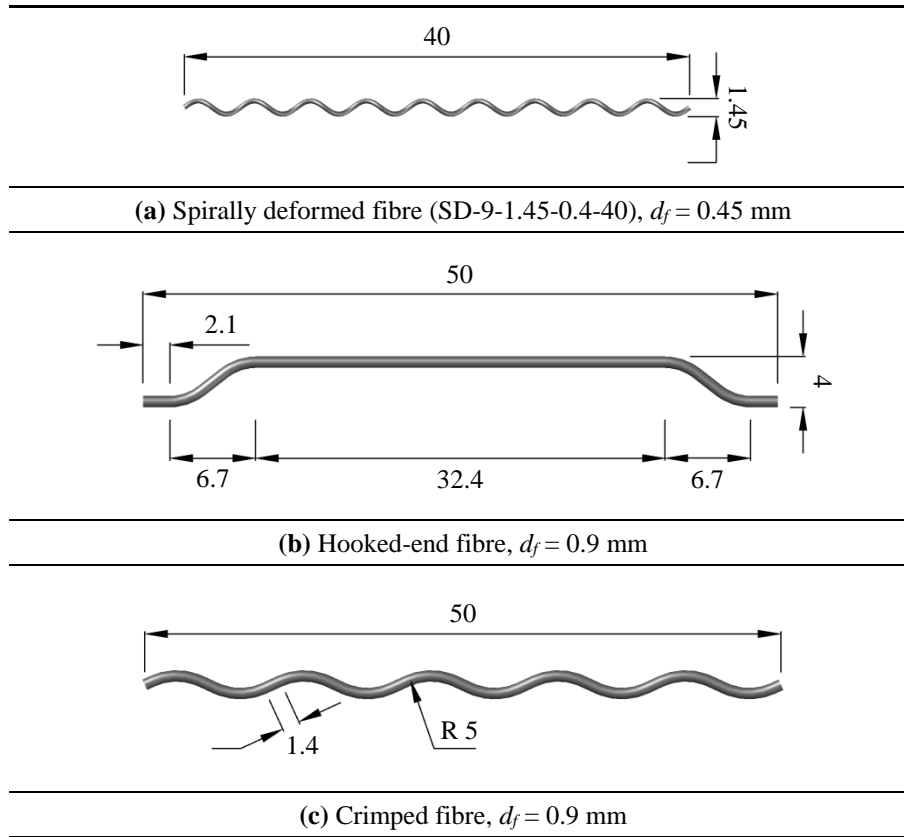


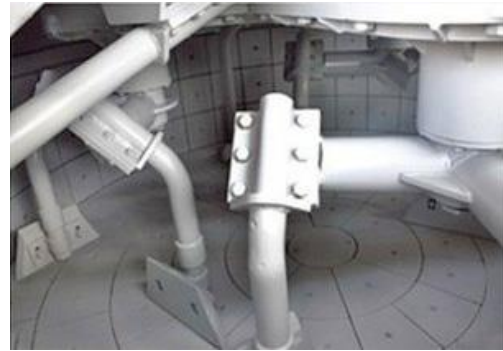
Fig. 4.2. Steel fibres used for material testing (dimensions are in mm).

4.3. CONCRETE MIXING, CASTING, AND CURING

A centrifugal concrete mixer with a capacity of 500 litres is used for the mixing of both types of concrete, i.e. plain and fibrous (see **Fig. 4.3**). Such a large mixer is needed since the structural and material testing specimens are cast at the same time. The regulations presented in **Appendices 4.2** and **4.3** are strictly followed during the general tasks and concrete mixing in the laboratory.



(a) Mixer (capacity: 500 litre)



(b) Mixer drum



(c) Slump test



(d) Bucket dumper (capacity: 150 litre)



(e) Vibration table



(f) Curing tank (capacity: 2000 litres)

Fig. 4.3. Concrete mixing.

The mixing and casting procedure is summarised as follows:

1. All parts of the mixer including the drum and chute are cleaned and rinsed with water. Excess water is drained out of the mixer drum.
2. Fine and coarse aggregates are added to the mixer and they are dry-mixed for 1 minute.
3. Cement is added to the mixer and the mixing process continues for 2 minutes.
4. One-third of the required superplasticizer and two-thirds of the water are gradually added to the mix and the mixing continues for another 2 minutes.
5. The remaining quantities of the superplasticizer and water are gradually added to the mix and the mixer is run for another minute.
6. For SFRC mixes, all of the fibres are gradually sprinkled into the drum while the beater blades are rotating. The sprinkling process takes approximately 12 minutes per 10 kg for the new fibre (spirally deformed fibre) and 2 minutes per 10 kg for the hooked-end and crimped fibres. Because the new fibre has a much smaller diameter than the other two ones (around half) which means for a constant volume fraction, the new fibre is considerably more than the others.
7. Following the fibre addition, the mixing process continues for another 3 minutes to ensure a uniform distribution of fibres within the concrete.
8. Once the concrete mixing is completed, the slump test is performed to ensure the concrete is workable (ASTM C143/C143M - 15a 2015).
9. The concrete moulds are placed on the vibration table. The table is 1 m by 2 m with a capacity of 400 kg which can provide a vibrational frequency between 10 and 100 Hz.
10. The concrete is then discharged into a bucket dumper (see **Fig. 4.3**) and using an overhead crane in the Structures laboratory, shovels and trowels are to cast the specimens while the vibration table is running with a frequency of 50 Hz.

Following the casting, the mixer and all tools are cleaned and rinsed with water. A few hours after the casting, one final pass with trowels is performed to remove any slight imperfections and, in the case of SFRC, remove any fibres protruding out from the finished surfaces of the specimens. The specimens are covered with a plastic cover and

left to set for one day. A day after the concrete casting, the specimens are demoulded and put into the temperature-controlled water tanks (see **Fig. 4.3**) for 28 days. The curing temperature is set to be 23°C according to ASTM C192/C192M - 16a (2016).

4.4. EXPERIMENTAL PARAMETERS

Compression and flexure tests are performed to evaluate the contribution of the new fibre to the concrete behaviour. The fibre volume content (V_f), concrete strength (f_m) and fibre type are considered as the experiment parameters which are listed in **Table 4.6**.

Table 4.6
Experiment parameters of material testing.

f_m (MPa)	V_f (%)	Fibre type
35, 45	0.2, 0.35, 0.5, 0.65	Newly-designed
35	0.5	Hooked-end, Crimped

4.5. WORKABILITY ASSESSMENT

The concrete workability is assessed using the slump cone test. The slump results of all concrete batches with their corresponding ID are listed in **Table 4.7**.

Table 4.7
Slump cone test results.

Concrete Type	Mix ID	V_f (%)	f_m (MPa)	Slump (mm)
Plain	P-35	-	35	198
	P-45	-	45	136
Fibrous	N-0.2-35	0.2	35	168
	N-0.2-45		45	112
	N-0.35-35	0.35	35	139
	N-0.35-45		45	91
	N-0.5-35	0.5	35	99
	N-0.5-45		45	63
	N-0.65-35	0.65	35	79
	Hooked-end	0.5	35	121
	Crimped	0.5	35	77

The mixes are labelled such that the specifications of each mix can be identified from the mix ID. For instance, the label “P-35” represents the plain concrete (non-fibrous concrete) with target mean cylinder strength of 35 MPa; also the label “N-0.5-45” indicates that the mix is fibrous with the new fibre at the fibre content of 0.5% whose target strength is 45 MPa. Examples of completed mixes are shown in **Fig. 4.4**.

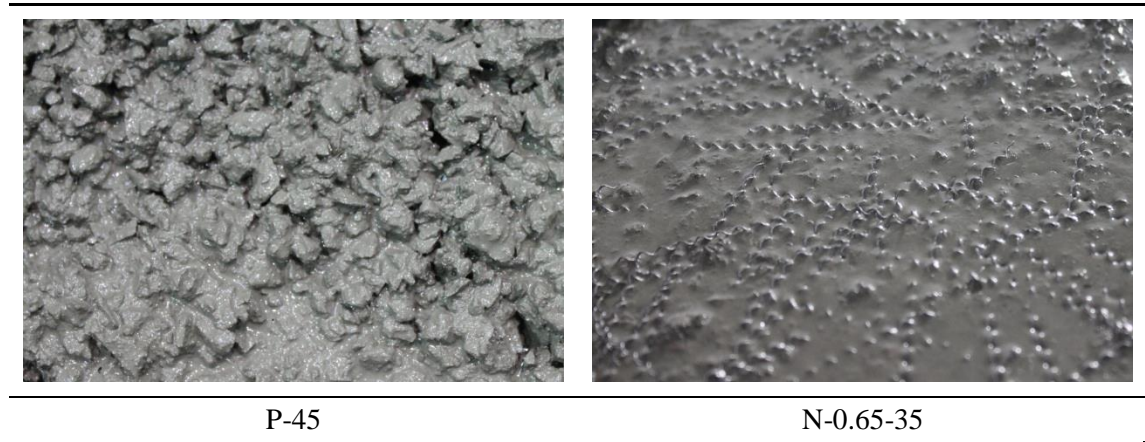


Fig. 4.4. Completed mixes.

4.6. MATERIAL EXPERIMENTAL TESTS

The material tests performed in this project is outlined in this section.

4.6.1. COMPRESSION TEST

The compression tests are performed to assess the compressive strengths of concrete (plain and fibrous) and propose a correlation between cylinder and cube strengths of concrete.

The compression test is conducted using a displacement-controlled compression testing machine (see **Fig. 4.5**) with the capacity of 3000 kN on cylinder (diameter of 150 mm and height of 300 mm) and cube (each side 150 mm) specimens. The loading rate of the specimens is 0.6 MPa/s. The test procedure and specimens' dimensions conform to BS EN 12390-3 (2009) and BS EN 12390-1 (2012). For each concrete batch, the test consists of three cylinders and three cubes.



Fig. 4.5. Compression testing machine.

The finished surface of the cylinders (as one of the intended load-bearing surfaces) is ground to remove the end's weak paste and ensure that both surfaces are parallel to each other. Due to the higher strength of fibre material (steel) than conventional concrete, a diamond grinding disk is used for the specimens, as seen in **Fig. 4.6**.



Fig. 4.6. Concrete cylinder grinding.

4.6.2. FLEXURE TEST

ASTM C1609/C1609M - 12 (2012) is adopted to conduct the four-point loading flexure tests in order to characterise the flexural performance of SFRC including modulus of rupture (f_r), residual flexural strengths, and toughness. The specimens' dimensions are 150 mm \times 150 mm \times 550 mm. The flexure tests comprise three specimens for each batch of concrete. The specimens are cast at the same time with their corresponding cylinder and cube specimens.

The test is performed using a closed-loop control Universal Testing Machine (UTM) controlled by displacement transducers with the capacity of 300 kN.

4.6.2.1. TEST INSTRUMENTATION AND PROCEDURE

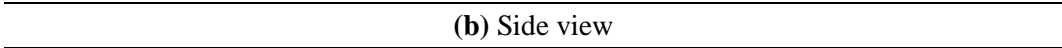
The loading arrangement and instrumentation setup of the flexure test can be seen in **Fig. 4.7**. As required in the standard, the clear span between the supports is 450 mm and the distance between the four loading points are 150 mm (quarter-point loading).

A rectangular jig which surrounds the specimen and is clamped to it at mid-depth directly over the supports, i.e. yoke, is employed to measure the net mid-span deflection as seen in **Fig. 4.7**. Two Linear Variable Differential Transducers (LVDTs) with a total stroke of ± 15 mm and precision of ± 0.001 mm are mounted on the LVDT slots of the yoke to measure the mid-span deflections on each vertical face of the specimens. The average value is considered as the mid-span net deflection of the specimens.

The locations of the supports and the loading points are marked on all four sides of the specimens. This is done by finding the average centre of the specimens using a ruler and then marking off the supports 225 mm each way from the centre and the loading points 75 mm each way from the centre. The mid-depth is also marked so that the yoke could be fixed to the right position. To test the specimens, they are turned on their side with respect to the position as cast before placing on the supports such that the finished face is the side face of the tested specimen.

The testing machine is set so that the net deflection of the specimen increases at the constant rate of 0.1 mm/min. For net deflection beyond 0.6 mm, the loading rate increases to 0.3 mm/min with the increment of 0.05 mm/min. During the test, the testing data including load and displacement from the UTM and deflection from two LVDTs

The diagram shows the front view of the experimental setup. A composite beam is supported by two roller supports at the base. A yoke is positioned above the beam, with a central LVDT (Linear Variable Differential Transformer) measuring its vertical displacement. The yoke is connected to a loading mechanism, which includes a central loading roller and two side loading rollers. The dimensions of the setup are indicated: the total width of the base is 550 mm, the width of the yoke is 450 mm, and the height of the yoke is 150 mm. Labels include 'Loading rollers', 'Yoke', 'Roller support', and 'LVDT'.



89

4.7. EXPERIMENTAL RESULTS

The test results of material testing including compressive strengths and flexural characteristics of SFRC are presented in this section. It is mentioned that the Health and Safety regulations outlined in **Appendices 4.1, 4.3, and 4.4** are strictly followed.

4.7.1. COMPRESSIVE STRENGTHS

The average results of the compression tests of the cylinder and cube concrete specimens at the 28th day after casting are summarised in **Table 4.8** in which the variation of each test set is also provided.

Table 4.8
Compression tests results.

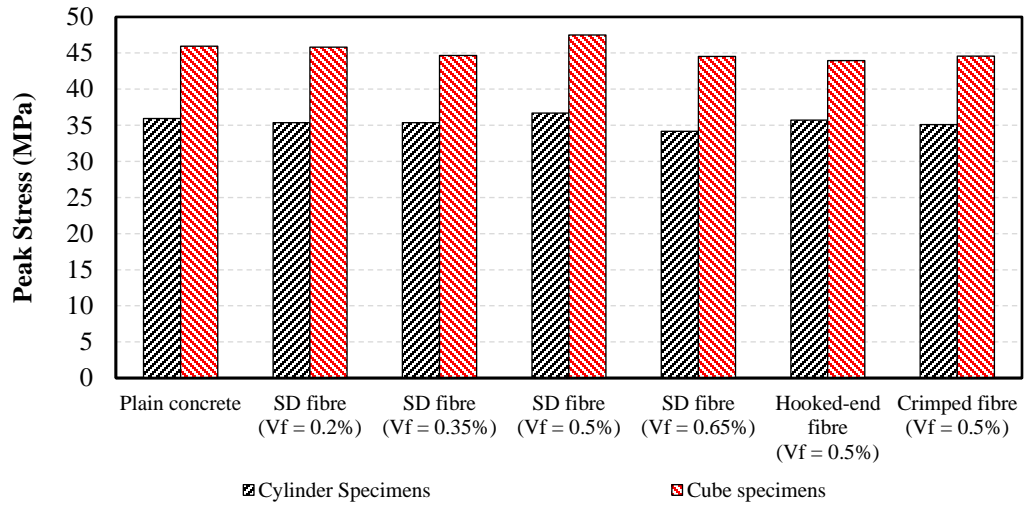
Mix ID	f_{ck}^1 (MPa)	$f_{ck, cube}^{1,2}$ (MPa)
P-35	35.9±1.9	45.9±1.8
P-45	46.0±2.2	55.9±2.4
N-0.2-35	35.3±2.1	45.8±2.3
N-0.2-45	46.5±1.6	55.6±2.5
N-0.35-35	35.4±0.7	44.7±0.3
N-0.35-45	46.0±1.7	55.2±3.4
N-0.5-35	36.7±0.8	47.5±1.6
N-0.5-45	47.3±0.6	58.2±1.0
N-0.65-35	34.2±1.1	44.5±0.6
H-0.5-35	35.7±0.5	43.9±0.5
C-0.5-35	35.1±1.0	44.6±0.4

¹ Average of three specimens

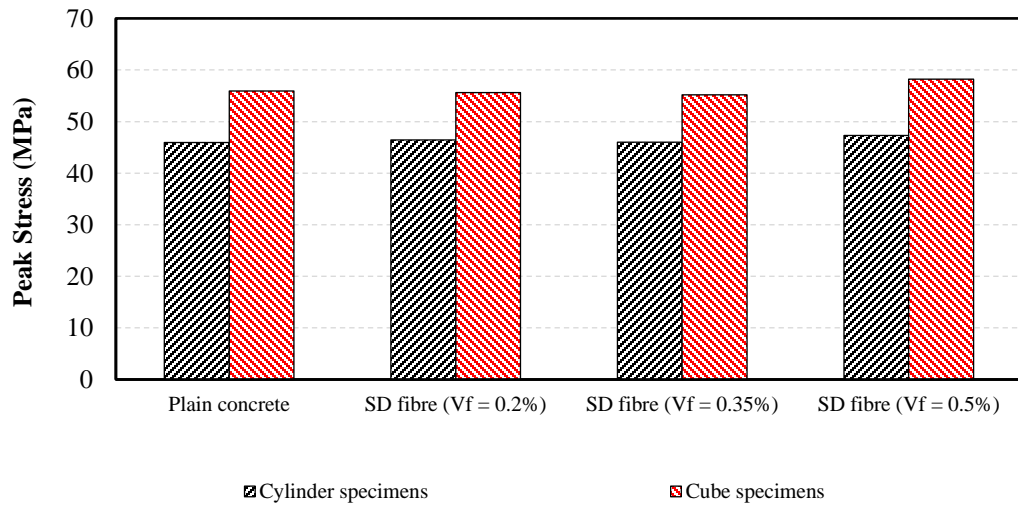
² Characteristic cube strength of concrete

As seen in the table, the mix designs used in this project yield compressive strengths close to the corresponding target values.

The variation of compressive strengths for the varying mixes with different fibre contents is shown in **Fig. 4.8**. As anticipated, the inclusion of fibres does not influence the compressive peak stress. However, since the concrete batches were made separately, the variation in the peak stresses is reasonable due to small differences in the moisture content of the aggregates, and mixing and casting process.



(a) $f_m = 35$ MPa



(b) $f_m = 45$ MPa

Fig. 4.8. Variation of compressive stress.

The strengths of cylinder concrete specimens versus the corresponding cube strengths of concrete are plotted in **Fig 4.9**.

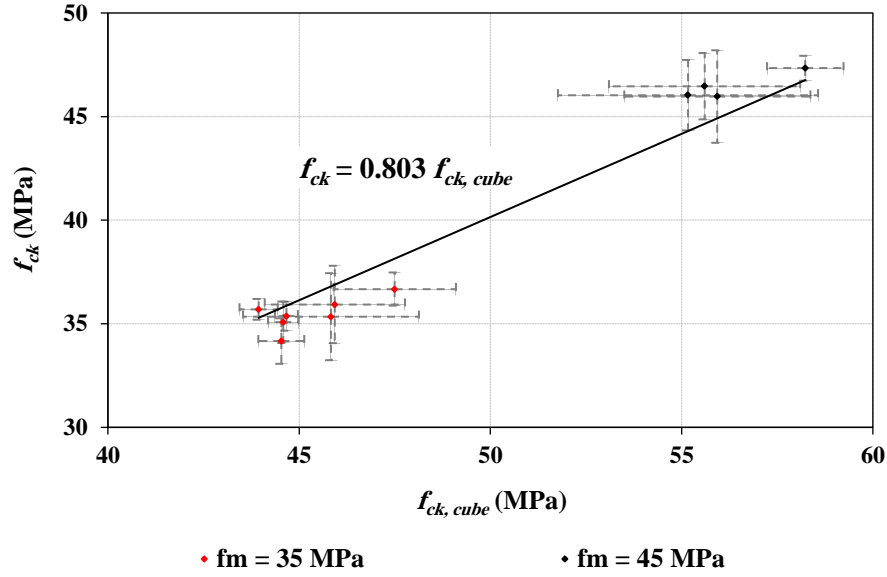


Fig. 4.9. Cube and cylinder strengths of concrete and their relationship.

A linear regression analysis is performed on the database to derive a relationship between two types of strengths, as seen in **Eq. (4.4)**.

$$f_{ck} = 0.803 f_{ck, cube} \quad (4.4)$$

This equation is in good agreement with the proposed equation by CEN Eurocode 2 (2004) where the coefficient is 0.84.

4.7.2. FLEXURAL CHARACTERISTICS

In this section, the flexure tests results conducted in accordance with ASTM C1609/C1609M - 12 (2012) are presented. For each batch of concrete, three specimens are prepared and tested at the 28th day after casting where the average results are considered as the SFRC behaviours.

In **Fig. 4.10**, a concrete prism reinforced with steel fibres under flexural testing is shown.

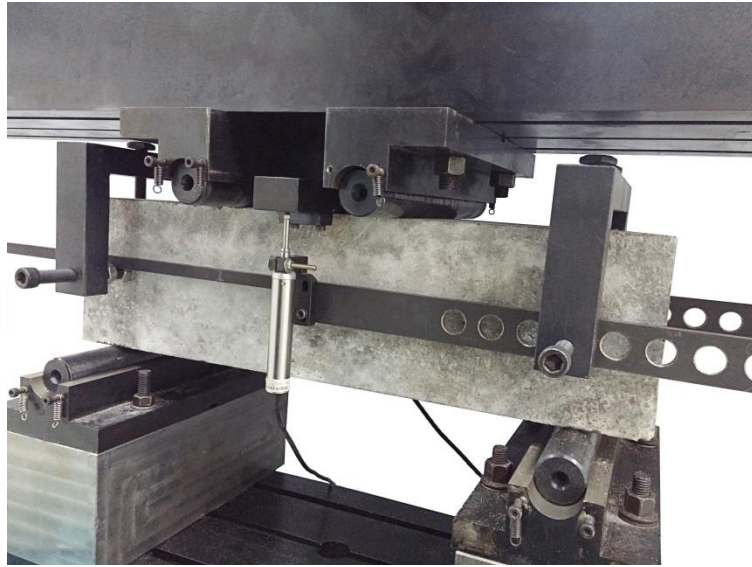
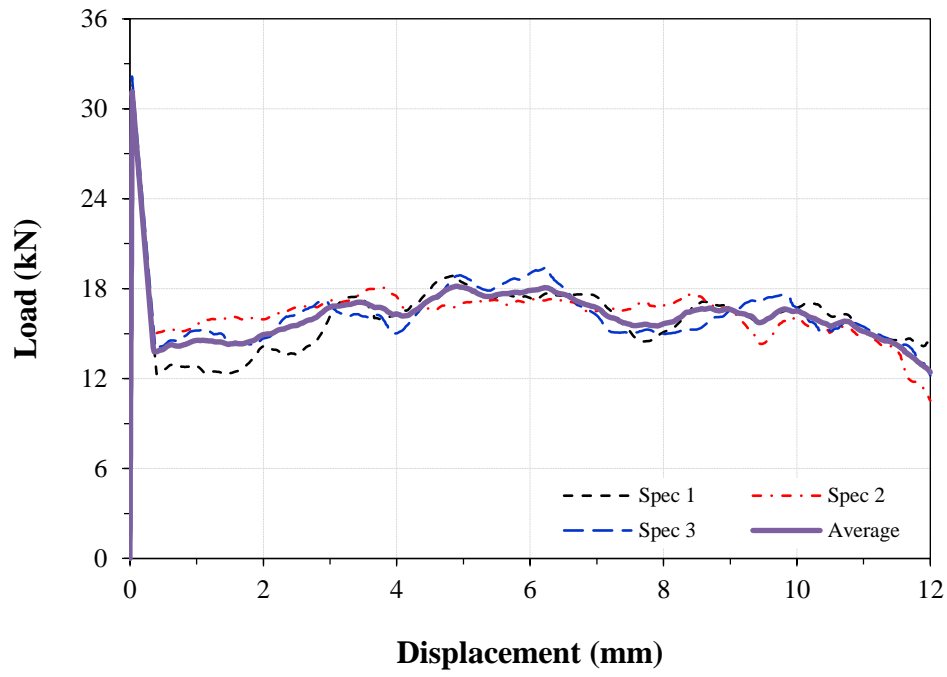
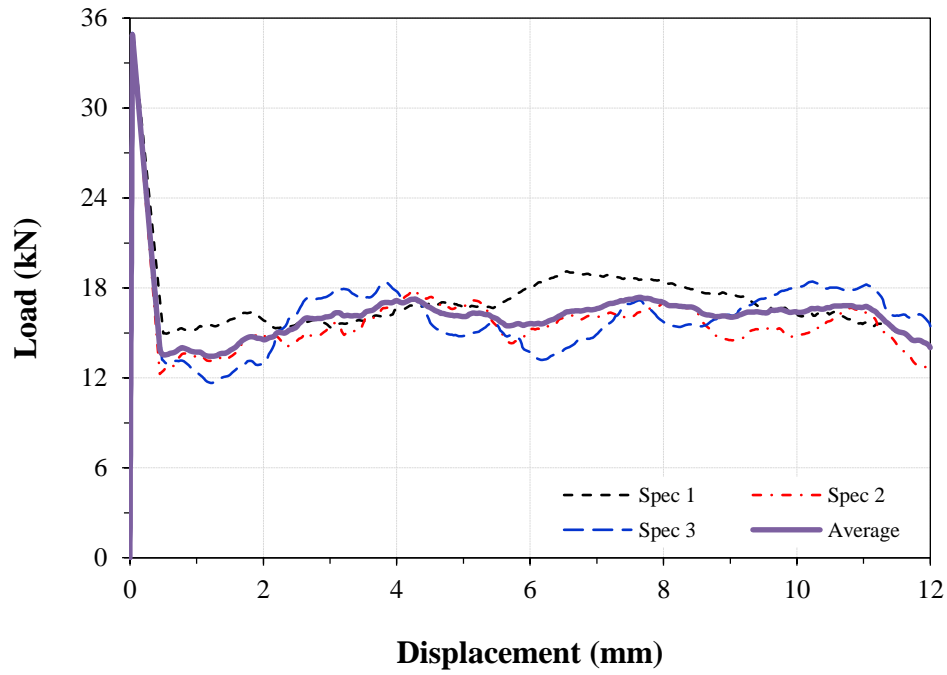


Fig. 4.10. Fibrous concrete prism under flexural testing.

The load-deflection curves of the SFRC specimens with the new fibre under four-point bending are shown in **Fig. 4. 11**.

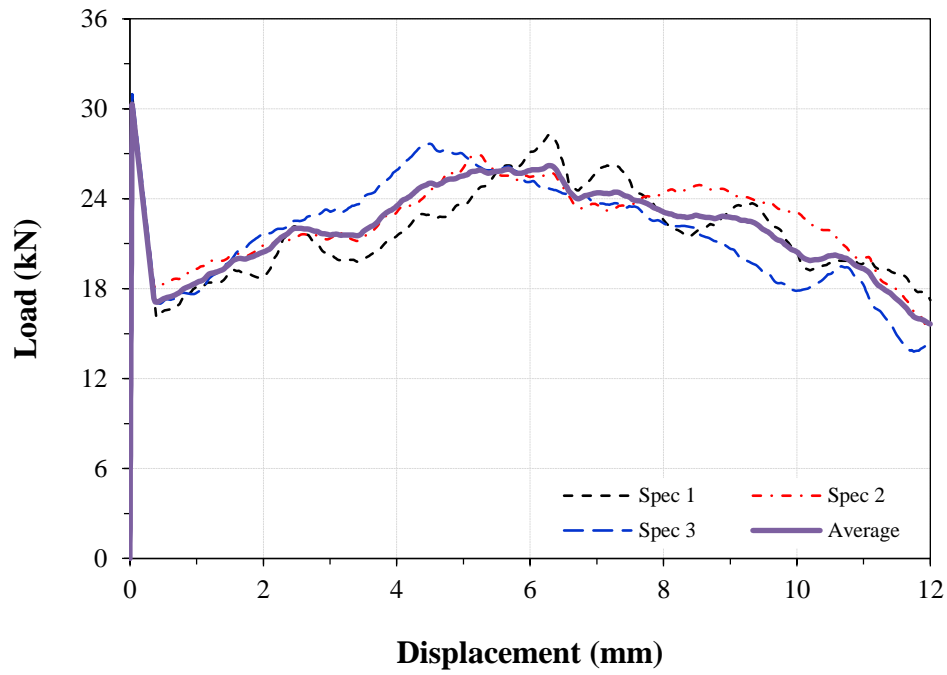


$f_m = 35$ MPa

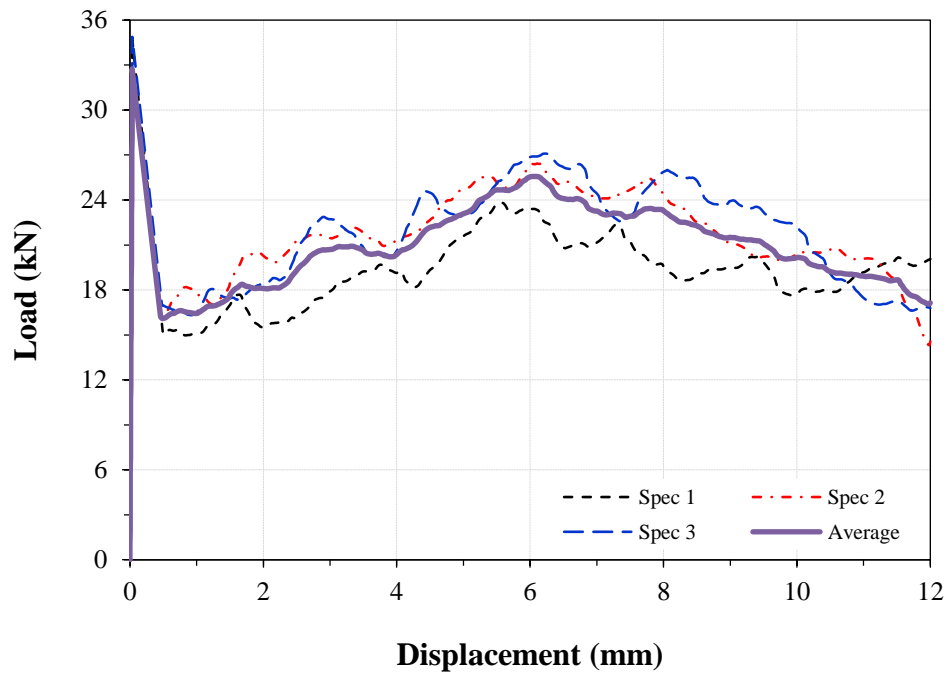


$f_m = 45$ MPa

Fig. 4.11. Individual and average flexural responses of SFRC containing 0.2% of the new fibre (ASTM C1609/C1609M - 12 2012).

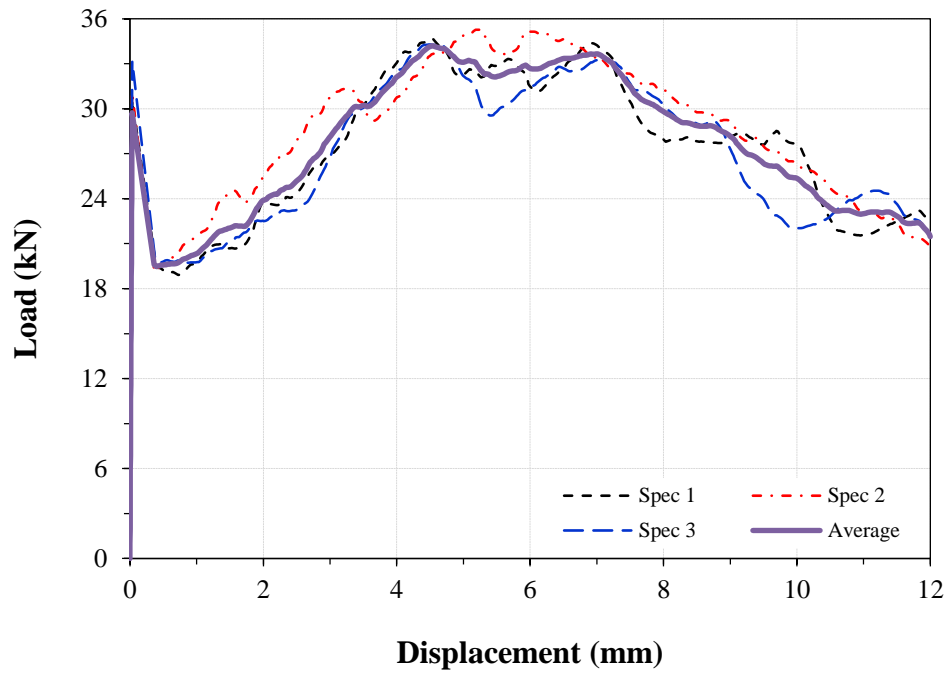


$f_m = 35$ MPa

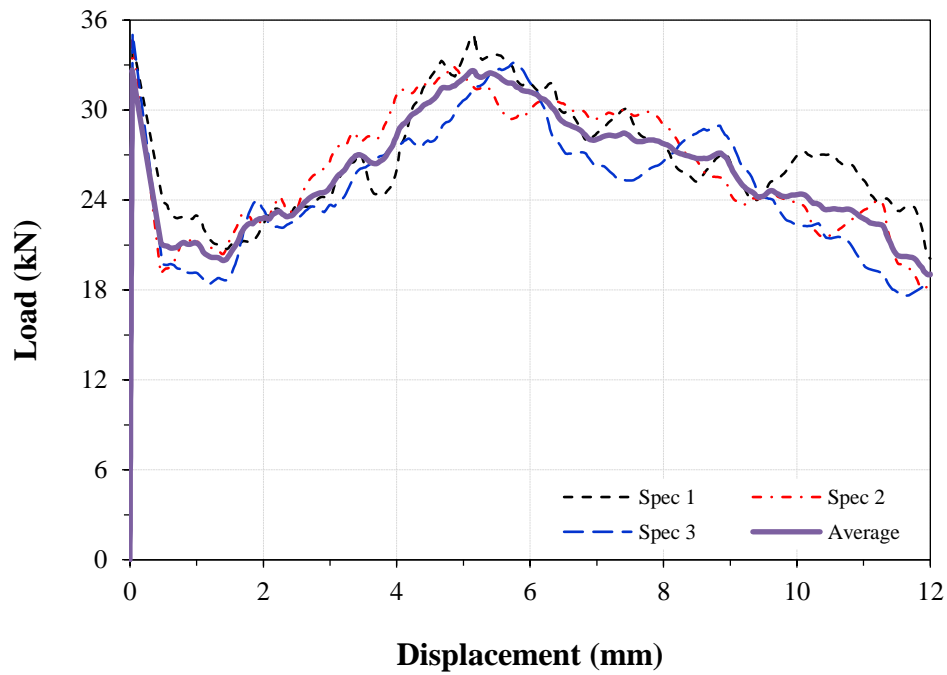


$f_m = 45$ MPa

Fig. 4.11 (Continued). Individual and average flexural responses of SFRC containing 0.35% of the new fibre (ASTM C1609/C1609M - 12 2012).

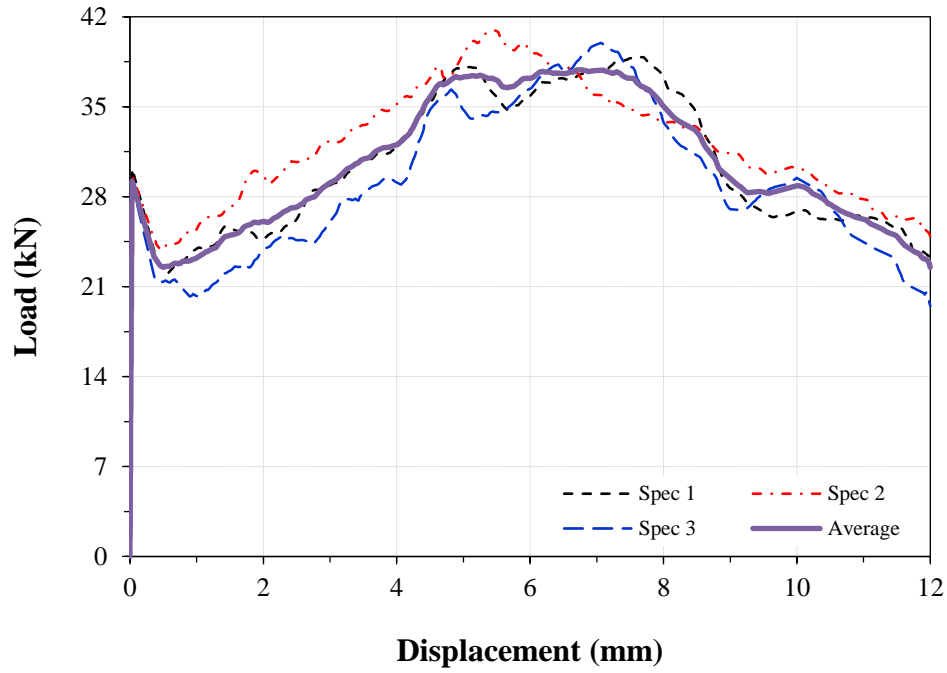


$f_m = 35 \text{ MPa}$



$f_m = 45 \text{ MPa}$

Fig. 4.11 (Continued). Individual and average flexural responses of SFRC containing 0.5% of the new fibre (ASTM C1609/C1609M - 12 2012).



$$f_m = 35 \text{ MPa}$$

Fig. 4.11 (Continued). Individual and average flexural responses of SFRC containing 0.65% of the new fibre (ASTM C1609/C1609M - 12 2012).

As seen in **Fig. 4.11**, the flexure response of SFRC specimens with the new fibre are characterised by a linear part up to the elastic limit load, followed by a sudden load decay to a certain load which depending on the fibre volume content continues with different behaviours (deflection-hardening or deflection-softening). The sudden load decay in the responses could be attributed to the low fibre volume contents used in this project so that wider cracks are needed to activate an effective overall fibre bridging action. From the figure, it is evident that increasing the fibre content improves the flexure performance of SFRC by:

1. decreasing the severity of the sudden load drop,
2. enhancing the post-cracking response.

In **Fig. 4.12**, the schematic response of SFRC specimens (with the new fibre) under bending is illustrated on which three distinctive points are shown.

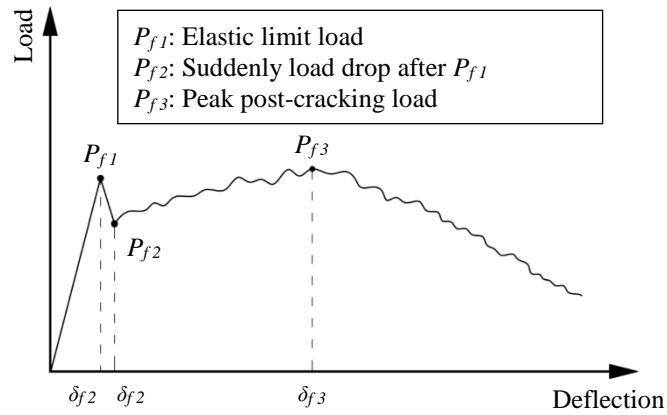
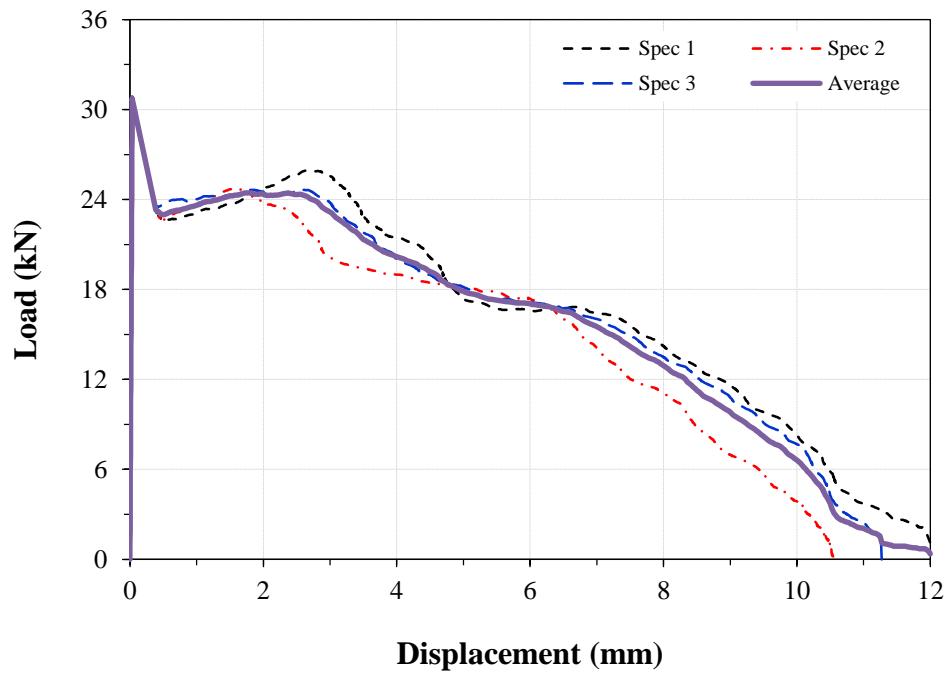


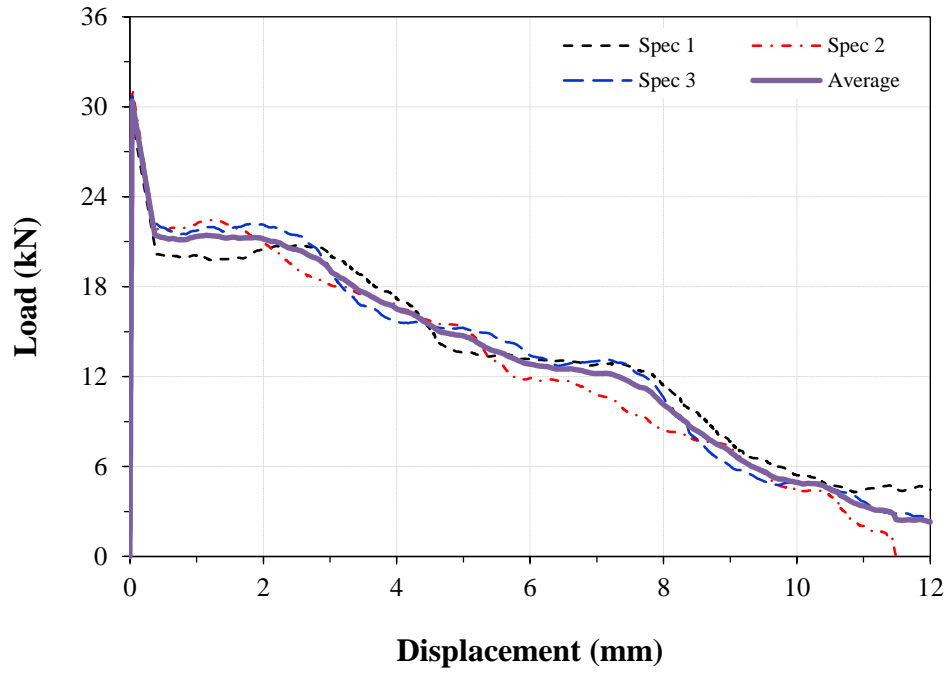
Fig. 4.12. Schematic load vs. deflection curve of SFRC with the new fibre.

The flexural response of SFRC with hooked-end and crimped steel fibres are provided in **Fig. 4.13**.



Hooked-end fibre, $f_m = 35$ MPa

Fig. 4.13. Individual and average flexural responses of SFRC containing 0.5% of the commercially available fibres (ASTM C1609/C1609M - 12 2012).



Crimped fibre, $f_m = 35$ MPa

Fig. 4.13 (Continued). Individual and average flexural responses of SFRC containing 0.5% of the commercially available fibres (ASTM C1609/C1609M - 12 2012).

The results of flexure tests are summarised in **Table 4.9**.

Table 4.9

Flexural tests results.

Mix ID	f_r (MPa)	P_{f1}^1 (kN)	P_{f2}^1 (kN)	P_{f3}^1 (kN)	f_{45}^D ² (MPa)	T_{45}^D ³ (kN.mm)	f_{150}^D (MPa)	T_{150}^D (kN.mm)	Response
P-35	4.06±0.11	30.42	-	-	-	-	-	-	-
P-45	4.56±0.18	34.17	-	-	-	-	-	-	-
N-0.2-35	4.15±0.19	31.14	14.07	18.17	2.20	165.4	2.24	47.7	Softening
N-0.2-45	4.65±0.04	34.90	13.86	17.37	2.18	163.5	2.15	48.3	Softening
N-0.35-35	4.09±0.07	30.29	17.35	26.20	2.72	228.0	2.88	61.6	Softening
N-0.35-45	4.57±0.14	32.75	16.20	25.57	2.69	214.8	2.76	57.2	Softening
N-0.5-35	4.21±0.21	29.72	19.59	34.20	3.38	286.0	3.76	69.8	Hardening
N-0.5-45	4.65±0.05	32.69	21.11	32.63	3.25	267.5	3.33	69.0	Softening
N-0.65-35	3.95±0.08	29.21	23.39	37.88	3.85	315.6	3.88	76.8	Hardening
H-0.5-35	4.10±0.07	30.74	23.30	23.30	0.80	168.8	3.08	73.3	Softening
C-0.5-35	4.05±0.12	30.36	19.70	19.70	0.61	136.6	2.53	65.3	Softening

¹ Refer to **Fig. 4.12**

² Residual strength at net deflection of 10 mm ($L/45$) calculated from the average load-deflection response

³ Toughness (area under the load vs. deflection curve from 0 to 10 mm calculated from the average response)

4.7.3. RESULTS ANALYSIS

From **Figs. 4.11** and **4.13** and **Table 4.9**, it is evident that the new fibre possesses superior performance compared with hooked-end and crimped steel fibres. The addition of 0.5% volume content of the new fibre results in favourable characteristics including deflection-hardening response, and considerable toughness and residual strengths at varying deflections. However, the effect of the new fibre is more pronounced at greater deflections. For instance, the addition of the new fibre enhances toughness and residual stress at the deflection of 10 mm, on average, by 87% and 380%, respectively compared with the existing fibres on the market, however, this increase is just 1% and 34% when the deflection is 3 mm. The comparison between SFRC with the new fibre and the other two commercially available steel fibres under flexure is shown in **Fig. 4.14**.

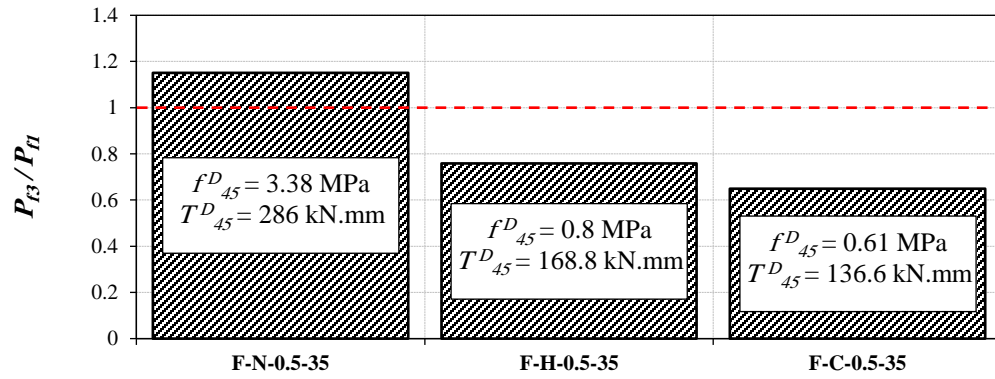


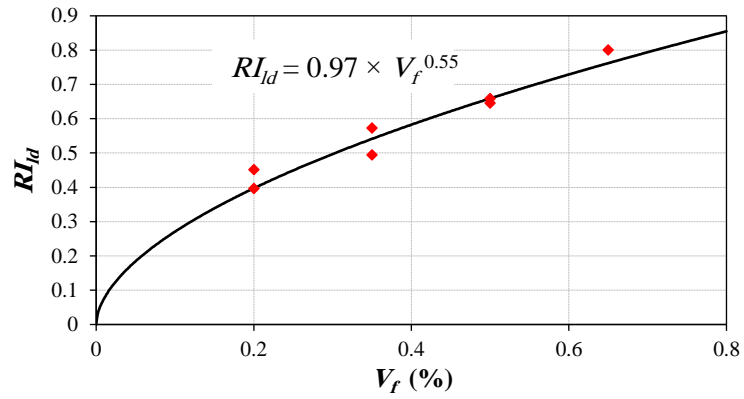
Fig. 4.14. SFRC specimens with different steel fibres under flexure.

RI_{ld} , i.e. ratio of the suddenly-decayed load (P_{f2}) to the peak elastic load (P_{fl}), and RI_p , i.e. the peak post-cracking load (P_{f3}) to the peak elastic load (P_{fl}), versus fibre volume content are shown in **Fig. 4.15**. GA optimisation algorithm is employed to predict RI_{ld} and RI_p based on V_f , as **Eqs. (4.5)** and **(4.6)**.

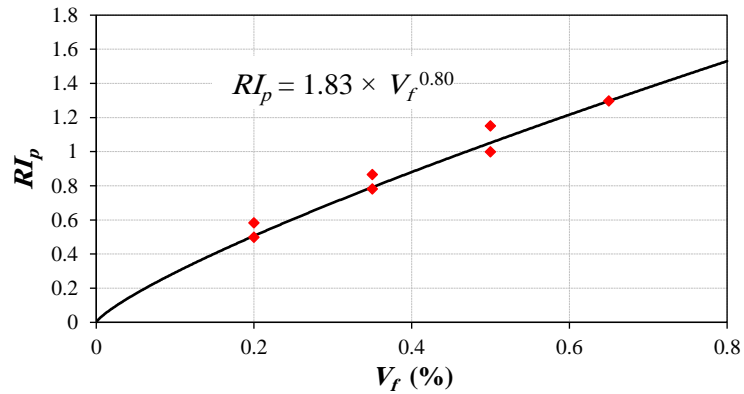
$$RI_{ld} = 0.97V_f^{.55} \quad (4.5)$$

$$RI_p = 1.83V_f^{0.80} \quad (4.6)$$

From the equations, 1% fibre volume content is needed to remove the sudden decay in the load-deflection response of SFRC with the new fibre. Moreover, with fibre content higher than 0.48%, deflection-hardening response ($RI_p \geq 1$) can be achieved.



(a) Suddenly-decayed load



(b) Post-peak response

Fig. 4.15. Effect of the new fibre volume content on the flexural characteristics.

Modulus of rupture (f_r) versus cylinder strength (f_{ck}) of SFRC specimens (see **Table 4.8** and **Table 4.9**) is plotted in **Fig. 4.16** which shows the close correlation between f_r and f_{ck} . Using GA algorithm, **Eq. (4.7)** is proposed to predict modulus of rupture (f_r) based on the concrete strength (f_{ck}).

$$f_r = 0.68 f_{ck}^{0.5} \quad (4.7)$$

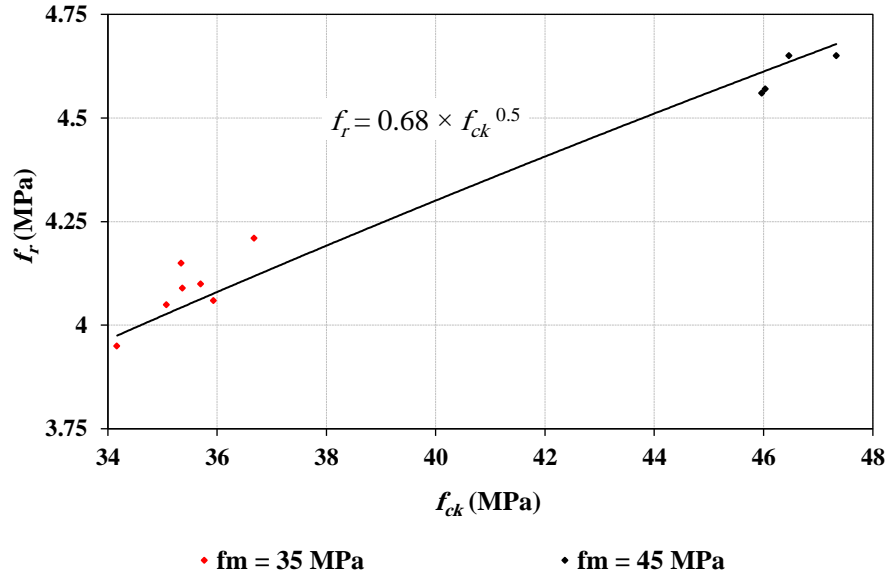


Fig. 4.16. Relationship of cylinder strength of concrete and modulus of rupture.

4.8. CONSTITUTIVE MATERIAL BEHAVIOURS

The stress-strain response of SFRC material dominates its performance under varying loading conditions and applications. As mentioned in **Section 2.3.3.1.3**, the flexural test is an alternative to the direct tension test whose results can be used to indirectly calculate the material response in tension (and also compression). A formulation is presented to back-calculate the material properties by fitting the experimental results with a closed form relationship of the load-deflection response using a non-linear constitutive material model.

The material response in compression and tension (stress-strain curves) can be employed for the numerical simulations and analytical designs of SFRC components and structures.

4.8.1. LOAD-DEFLECTION FORMULATION

The constitutive model consists of an elastic perfectly plastic model in compression and a tri-linear tensile response. The material parameters are described in terms of Young's modulus in tension (E), first cracking strain (ε_{cr}) and seven non-dimensional parameters to define post-peak tensile response, compressive yield strain and compressive strength, as well as ultimate strain levels in tension and compression (see **Fig. 4.17**). The model is capable of simulating strain softening and hardening behaviours (Mobasher, Bakhshi et al. 2014).

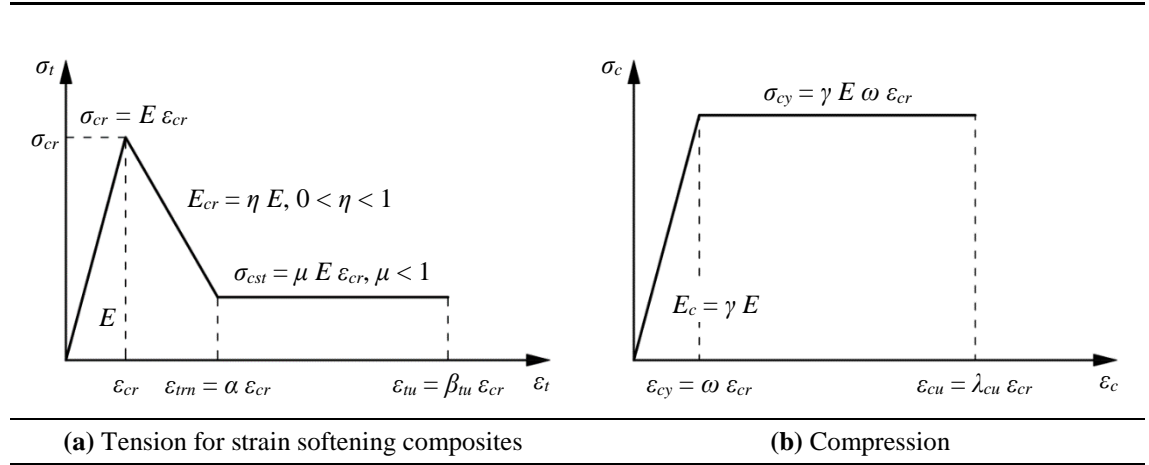


Fig. 4.17. Material models for FRC materials (Mobasher, Bakhshi et al. 2014).

The tri-linear response in tension, as shown in **Fig. 4.17(a)**, is described by a linear elastic region up to the first cracking point (ε_{cr} , $E \varepsilon_{cr}$), a post-cracking region with a modulus of $E_{cr} = \eta E$, and a range with a constant stress equals σ_{cst} . Parameter η can be assigned a negative or positive scalar value to respectively simulate either strain softening or hardening behaviours. Two other strain values, i.e. transition and ultimate tensile strains (ε_{trm} , ε_{tu}) define lower and upper bounds of the constant stress region.

As can be seen in **Fig. 4.17(b)**, the elastic linear part of the compressive response with a modulus of E_c terminates at the yield point (ε_{cy} , σ_{cy}). The response remains constant at a level of σ_{cy} (compressive yield stress) and finally terminates at the ultimate compressive strain (ε_{cu}). In order to convert this approach into a closed-form, two material

parameters, first cracking tensile strain (ε_{cr}) and tensile modulus of elasticity (E), are used to define seven normalised parameters as seen in **Fig. 4.17** and **Eq. 4.8**.

$$\omega = \frac{\varepsilon_{cy}}{\varepsilon_{cr}}; \alpha = \frac{\varepsilon_{tm}}{\varepsilon_{cr}}; \beta_{tu} = \frac{\varepsilon_{tu}}{\varepsilon_{cr}}; \lambda_{cu} = \frac{\varepsilon_{cu}}{\varepsilon_{cr}}; \gamma = \frac{E_c}{E}; \eta = \frac{E_{cr}}{E} = \frac{1-\mu}{\alpha-1}; \mu = \frac{\sigma_{cst}}{E\varepsilon_{cr}} \quad (4.8)$$

Using the normalised parameters, calculation of moment-curvature responses are expressed in a closed-form solution. In a flexural test, for a rectangular cross-section with a width of b and depth of d , the moment-curvature diagram is derived with the assumption that plane sections remain plane.

The tensile strain at the bottom fibre (ε_{tbot}) and the compressive strain at the top fibre (ε_{ctop}) are normalised with the first cracking strain (ε_{cr}) where the normalised strains, i.e. β and λ , are linearly related to the neutral axis depth ratio, k , as seen in **Eq. 4.9**.

$$\begin{aligned} \beta &= \frac{\varepsilon_{tbot}}{\varepsilon_{cr}}; \lambda = \frac{\varepsilon_{ctop}}{\varepsilon_{cr}} \\ \frac{\lambda \varepsilon_{cr}}{kd} &= \frac{\beta \varepsilon_{cr}}{d - kd} \text{ or } \lambda = \frac{k}{1-k} \beta \end{aligned} \quad (4.9)$$

The compressive and tensile stresses, σ_c and σ_t , are calculated using the normalised parameters in **Eq. 4.8** and **Eq. 4.9** as presented in **Eq. 4.10**.

$$\begin{aligned} \frac{\sigma_c(\lambda)}{E\varepsilon_{cr}} &= \begin{cases} \gamma\lambda & 0 \leq \lambda \leq \omega \\ \gamma\omega & \omega \leq \lambda \leq \lambda_{cu} \\ 0 & \lambda_{cu} < \lambda \end{cases} \\ \frac{\sigma_t(\beta)}{E\varepsilon_{cr}} &= \begin{cases} \beta & 0 \leq \beta \leq \omega \\ 1 + \eta(\beta - 1) & 1 \leq \beta \leq \alpha \\ \mu & \alpha < \beta \leq \beta_{tu} \\ 0 & \lambda_{cu} < \lambda \end{cases} \end{aligned} \quad (4.10)$$

Stress distribution across the cross-section is derived in a closed-form at three stages of the normalised tensile strain, $0 \leq \beta \leq 1$, $1 < \beta \leq \alpha$, and $\alpha < \beta \leq \beta_{tu}$, by assuming linear strain distribution across the depth and ignoring shear deformations. The strain and stress distribution across the cross-section at three stages are shown in **Fig. 4.18**.

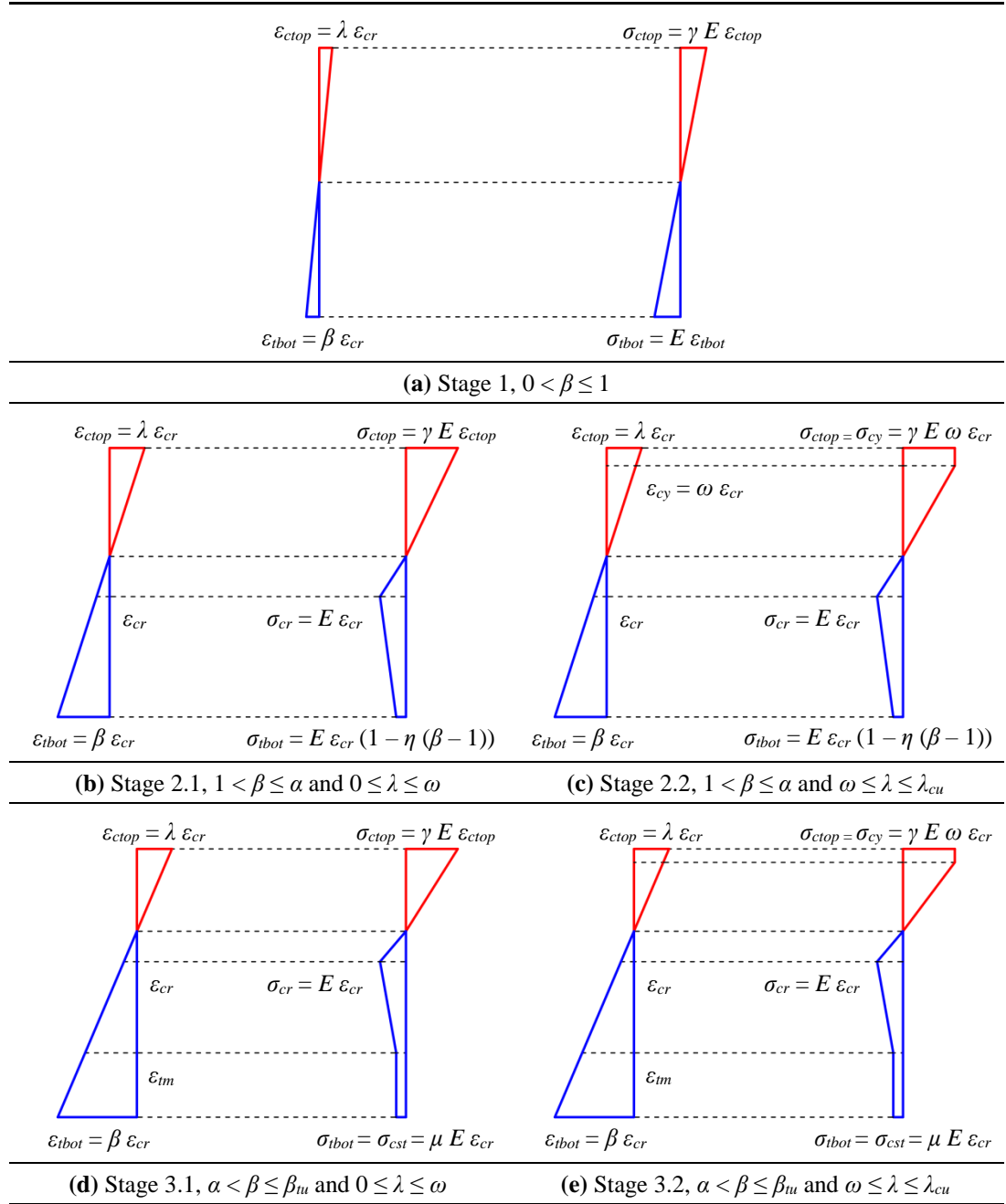


Fig. 4.18. Strain and stress diagrams at pre-cracking and post-cracking stages.

The area under the stress diagram in each sub-compression and tension zone represents the respective internal force. Using the force components and respective distances from the neutral axis (moment-arm), the internal moment of the section is obtained. The curvature (ϕ) is the ratio of the compressive strain at the top fibre ($\varepsilon_{ctop} = \lambda \varepsilon_{cr}$) to the neutral axis depth, kd (k is the neutral axis depth ratio). The internal bending moment and curvature at each stage i , (M_i and ϕ_i), are normalised with respect to the first cracking moment and curvature (M_{cr} and ϕ_{cr}) as presented in **Eq. 4.11** and **Eq. 4.12**:

$$M'_i = M_i / M_{cr} ; M_{cr} = \frac{1}{6} b d^2 E \varepsilon_{cr} \quad (4.11)$$

$$\phi'_i = \phi_i / \phi_{cr} ; \phi_{cr} = \frac{2 \varepsilon_{cr}}{d} \quad (4.12)$$

Critical normalised post-peak tensile stress (μ_{crit}) which defines the transition from deflection-softening behaviour to hardening behaviour is obtained using **Eq. 4.13**.

$$\mu_{crit} = \frac{\omega}{3\omega - 1} \quad (4.13)$$

Calculation of k , M'_i , and ϕ'_i values for the five stages of governing strain is presented in **Table 4.10**. As seen in **Fig. 4.18(a)** during stage 1, both tensile and compressive zones are linear elastic which continues until reaching the first cracking point. When tensile cracking starts there are two potential cases (stage 2), the compression side may or may not enter the plastic zone which are respectively denoted as stage 2.1 and stage 2.2 (see **Figs. 4.18(b)** and **4.18(c)**). Following stage 2, there are two potential transition cases, elastic and plastic responses in compression which are respectively denoted as stage 3.1 and stage 3.2, as shown in **Figs. 4.18(d)** and **4.18(e)**. It is worth mentioning that depending on the material parameters, any of the stages 2.1, and 2.2, or 3.1, and 3.2 are potentially possible in succession.

Table 4.10Governing equations for calculating k , M' and ϕ' for each stage specified by strains at the bottom and top fibres.

Stage	Parameters	k	$M' = M / M_{cr}$	$\phi' = \phi / \phi_{cr}$
1	$0 \leq \beta \leq 1$	$k_1 = \begin{cases} \frac{1}{2} & \text{for } \gamma = 1 \\ \frac{-1 + \sqrt{\gamma}}{-1 + \gamma} & \text{for } \gamma \neq 1 \end{cases}$	$M'_1 = \frac{2\beta[(\gamma - 1)k_1^3 + 3k_1^2 - 3k_1 + 1]}{1 - k_1}$	$\phi'_1 = \frac{\beta}{2(1 - k_1)}$
2.1	$1 < \beta \leq \alpha$ $0 \leq \lambda \leq \omega$	$k_{21} = \frac{D_{21} - \sqrt{D_{21}\gamma\beta^2}}{D_{21} - \gamma\beta^2}$ $D_{21} = \eta(\beta^2 - 2\beta + 1) + 2\beta - 1$	$M'_{21} = \frac{(2\gamma\beta - C_{21})k_{21}^3 + 3C_{21}k_{21}^2 - 3C_{21}k_{21} + C_{21}}{1 - k_{21}}$ $C_{21} = \frac{(2\beta^3 - 3\beta^2 + 1)\eta + 3\beta^2 - 1}{\beta^2}$	$\phi'_{21} = \frac{\beta}{2(1 - k_{21})}$
2.2	$1 < \beta \leq \alpha$ $\omega < \lambda \leq \lambda_{cu}$	$k_{22} = \frac{D_{22}}{D_{22} + 2\omega\gamma\beta}$ $D_{22} = D_{21} + \gamma\omega^2$	$M'_{22} = (3\gamma\omega + C_{22})k_{22}^2 - 2C_{22}k_{22} + C_{22}$ $C_{22} = C_{21} - \frac{\gamma\omega^3}{\beta^2}$	$\phi'_{22} = \frac{\beta}{2(1 - k_{22})}$
3.1	$\alpha < \beta \leq \beta_{tu}$ $0 \leq \lambda \leq \omega$	$k_{31} = \frac{D_{31} - \sqrt{D_{31}\gamma\beta^2}}{D_{31} - \gamma\beta^2}$ $D_{31} = \eta(\alpha^2 - 2\alpha + 1) + 2\mu(\beta - \alpha) + 2\alpha - 1$	$M'_{31} = \frac{(2\gamma\beta - C_{31})k_{31}^3 + 3C_{31}k_{31}^2 - 3C_{31}k_{31} + C_{31}}{1 - k_{31}}$ $C_{31} = \frac{(2\alpha^3 - 3\alpha^2 + 1)\eta - 3\mu(\alpha^2 - \beta^2) + 3\alpha^2 - 1}{\beta^2}$	$\phi'_{31} = \frac{\beta}{2(1 - k_{31})}$
3.2	$\alpha < \beta \leq \beta_{tu}$ $\omega < \lambda \leq \lambda_{cu}$	$k_{32} = \frac{D_{32}}{D_{32} + 2\omega\gamma\beta}$ $D_{32} = D_{31} + \gamma\omega^2$	$M'_{32} = (3\gamma\omega + C_{32})k_{32}^2 - 2C_{32}k_{32} + C_{32}$ $C_{32} = C_{31} - \frac{\gamma\omega^3}{\beta^2}$	$\phi'_{32} = \frac{\beta}{2(1 - k_{32})}$

By applying the moment-area method to the moment-curvature responses, mid-span deflection of bending tests can be derived explicitly. The three patterns of curvature distribution for three- and four-point bending tests are shown in **Fig. 4.19**.

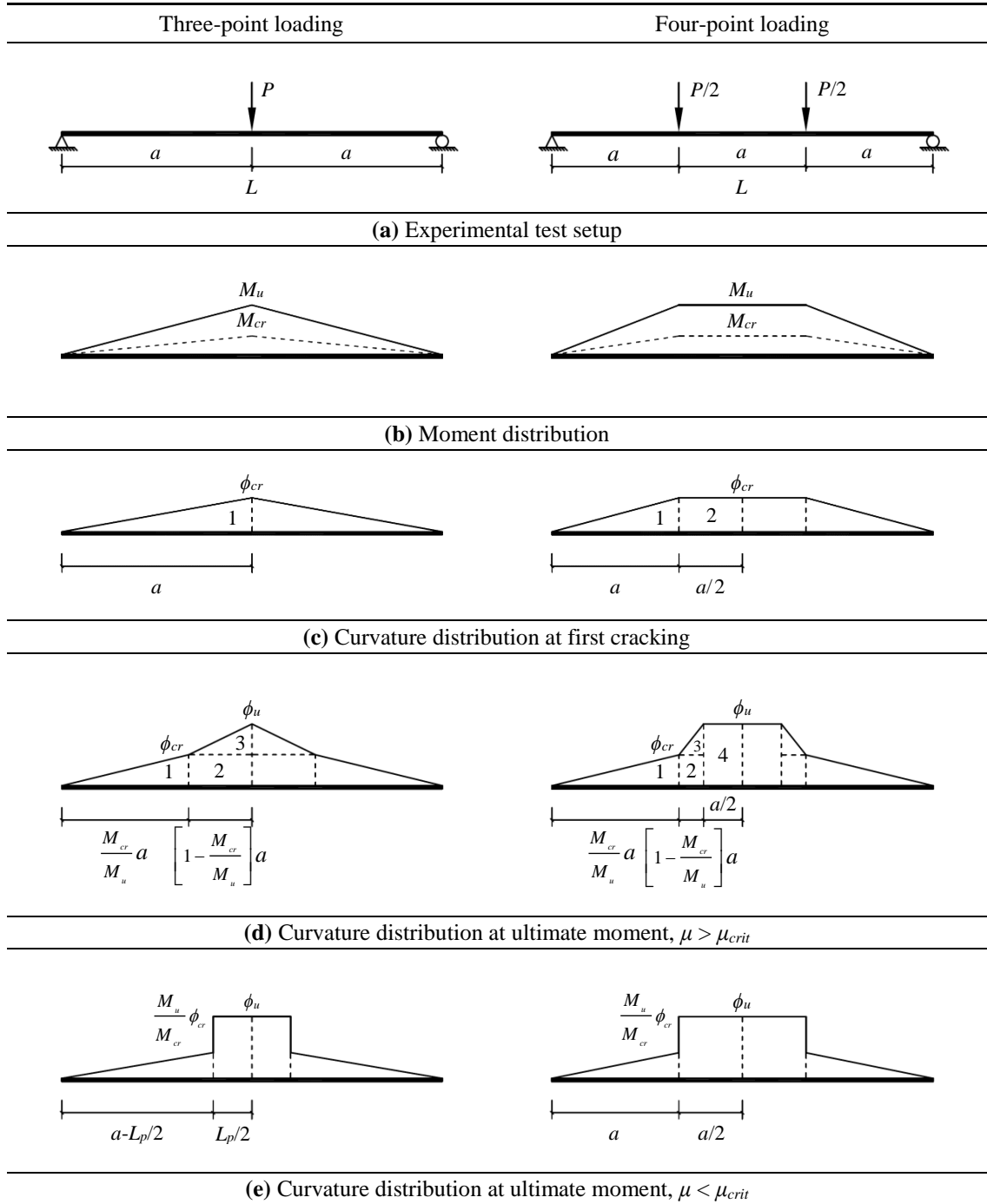


Fig. 4.19. Bending test.

The curvature diagram of a half-model (**Figs. 4.19(c), 4.19(d), and 4.19(e)**) is divided into several areas. The mid-span deflection of three-point bending tests is obtained by taking the moment of the areas around the left support. The maximum deflection during the elastic stage of loading (stage 1) is calculated from the curvature at cracking (ϕ_{cr}) using **Eq. 4.14**. When the first crack initiates, the curvature distribution depends on the critical normalised post-peak tensile stress (μ_{crit}). If $\mu > \mu_{crit}$, as the post-crack curvature increases, the moment continues to increase (deflection-hardening behaviour) where the deflection determined by **Eq. 4.15**. On the other hand, if $\mu < \mu_{crit}$, with an increase in the post-crack curvature, the moment either increases or decreases, however at the levels below the cracking moment, M_{cr} , (deflection-softening behaviour). The corresponding deflection is determined by **Eq. 4.16** where L_p is the length of crack localisation zone.

$$\delta_{cr} = \frac{1}{12} L^2 \phi_{cr} \quad (4.14)$$

$$\delta_u = \frac{L^2}{24M_u^2} \left[(2M_u^2 - M_u M_{cr} - M_{cr}^2) \phi_u + (M_u^2 + M_u M_{cr}) \phi_{cr} \right] ; \quad \mu > \mu_{crit} \quad (4.15)$$

$$\delta_u = \frac{\phi_u L_p}{8} (2L - L_p) + \frac{M_u \phi_{cr} L}{12M_{cr}} (L - 2L_p) ; \quad \mu < \mu_{crit} \quad (4.16)$$

Likewise, a set of equations for the four-point bending test can be derived as:

$$\delta_{cr} = \frac{23}{216} L^2 \phi_{cr} \quad (4.17)$$

$$\delta_u = \frac{L^2}{216M_u^2} \left[(23M_u^2 - M_u M_{cr} - 4M_{cr}^2) \phi_u + (4M_u^2 + 4M_u M_{cr}) \phi_{cr} \right] ; \quad \mu > \mu_{crit} \quad (4.18)$$

$$\delta_u = \frac{5\phi_u L^2}{72} + \frac{M_u L^2 \phi_{cr}}{27M_{cr}} ; \quad \mu < \mu_{crit} \quad (4.19)$$

The total load P_i at a given point i , is calculated by **Eq. 4.20**.

$$P_i = \frac{2M_i}{\frac{L}{3}} \quad (4.20)$$

4.8.2. SIMULATION PROCEDURE

To back-calculate the constitutive model of SFRC in tension and compression from the flexural testing result, a spreadsheet is developed based on the presented model to reduce the analysis time. The constitutive models are manipulated by the material parameters in order to best fit the simulated load-deflection diagram to its experimental counterpart. In the iterative process, following tips are helpful:

1. The slope of the linear part in the load-deflection response is adjusted by Young's modulus (E). SFRC generally has a Young's modulus in the range of 18 GPa to 35 GPa.
2. First cracking tensile strain (ε_{cr}) adjusts the approximate point where the linear elastic behaviour ceases and non-linear behaviour begins. This parameter depends on the cement performance, and fibre type and dosage, which all contribute to the point where cracking is observed.
3. The post-cracking slope of the response is adjusted by parameter η which is dependent on the values of α and μ through **Eq. (4.8)**. By manipulating α and μ , the post-cracking slope can be fitted to the experimental load-deflection response.
4. For conventional SFRC material, the normalised compressive yield strain, ω , is in the range of 6 to 12, hence critical normalised post-peak tensile stress, μ_{crit} , varies within a narrow range (between 0.353 and 0.343). This indicates if the post-peak tensile stress in a material is greater than 35% of its tensile strength, the material can exhibit deflection hardening behaviour under bending moment (Soranakom and Mobasher 2007 (a)).

5. For typical SFRC material, the effect of the compressive strength, σ_{cy} , on the flexural behaviour is marginal (Soranakom and Mobasher 2007 (a), Soranakom and Mobasher 2007 (b)).
6. In the three-point loading test, the length of the crack localisation zone affects the rate of load decay beyond the ultimate strength. The smaller the L_p value, the steeper the post-peak load decay (Soranakom and Mobasher 2007 (b)).
7. Normalised ultimate tensile strain (β_{tu}) is used to determine the ending point of the simulated load-deflection curve.

4.8.3. MATERIAL BEHAVIOUR (TENSION AND COMPRESSION)

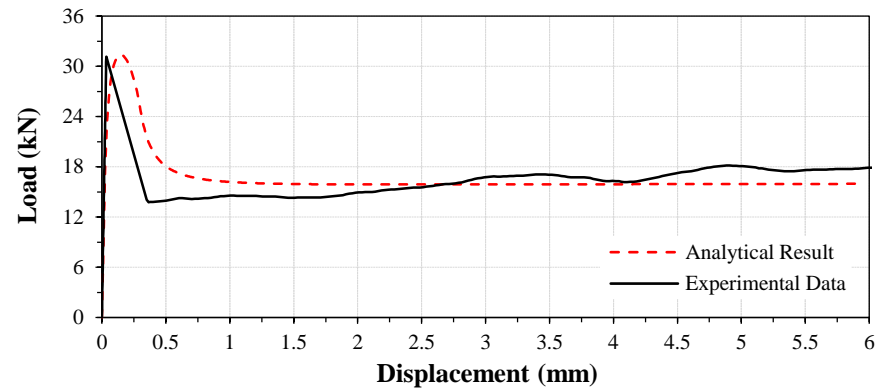
The preliminary curves fitting process reveals that the proposed constitutive material model cannot properly simulate the load-deflection response beyond net deflection 6 mm. Therefore, the process for all the results is performed up to 6 mm deflection.

The constitutive material parameters and tensile and compressive stress-strain curves of the SFRC (see **Table 4.7**) are provided in **Table 4.11** and **Fig. 4.20**.

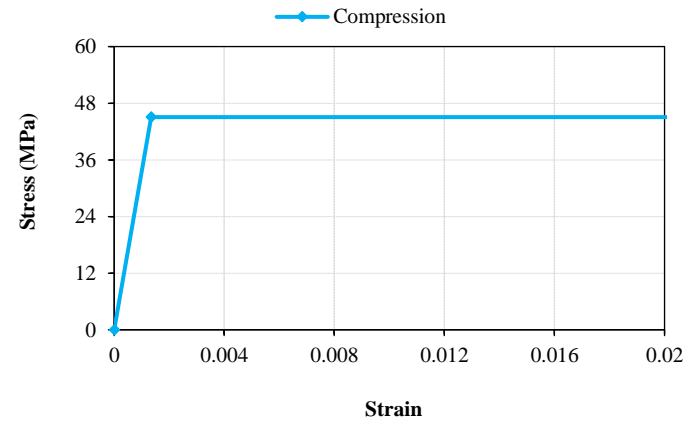
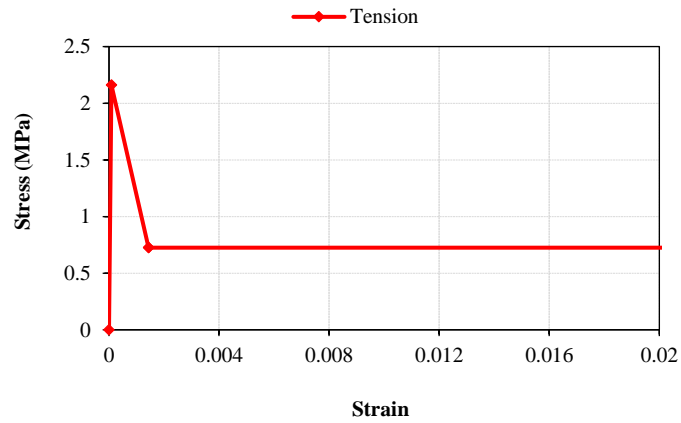
Table 4.11

The parameters used for simulating the load-deflection response of SFRC.

Mix ID	Adjusted Parameters							
	E (MPa)	ε_{cr}	μ	α	β_{tu}	γ	ω	λ_{cu}
Newly-designed fibre								
N-0.2-35	24000	0.000090	0.340	16	600	1.4	14.9	400
N-0.2-45	26800	0.000090	0.290	16	600	1.4	16.3	400
N-0.35-35	22800	0.000088	0.465	18	800	1.4	16.0	400
N-0.35-45	24800	0.000088	0.430	18	800	1.4	18.0	400
N-0.5-35	22000	0.000087	0.610	20	1000	1.4	16.8	400
N-0.5-45	23800	0.000087	0.580	20	1000	1.4	19.0	400
N-0.65-35	21000	0.000085	0.780	22	1200	1.4	18.0	400
Hooked-end fibre								
H-0.5-35	23000	0.000088	0.450	20	1000	1.4	16.0	400
Crimped fibre								
C-0.5-35	23000	0.000088	0.380	20	1000	1.4	16.0	400



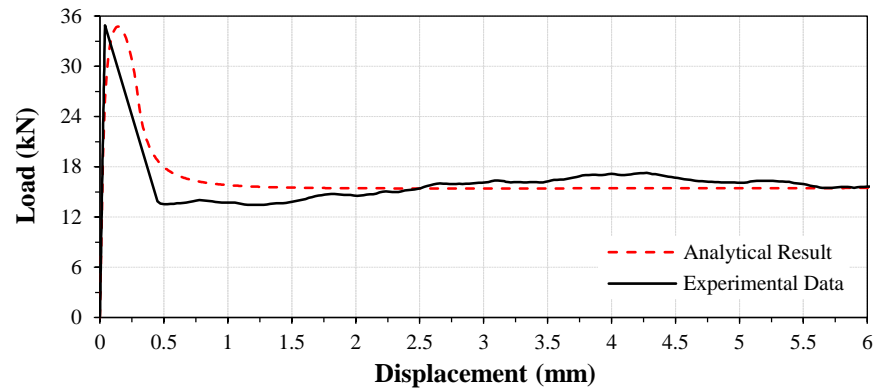
Predicted load-deflection curve



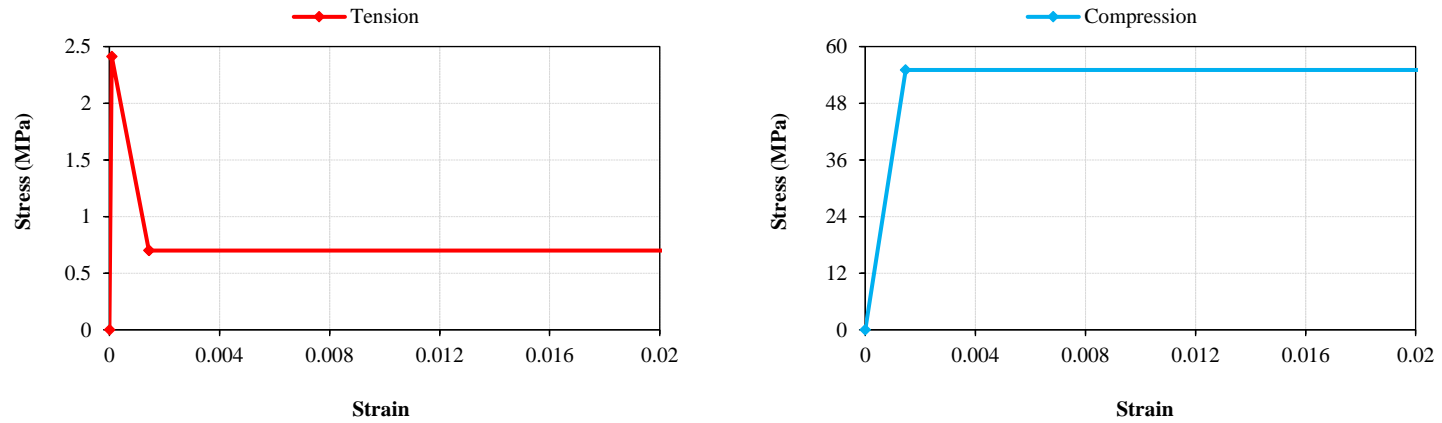
Material behaviour

N-0.2-35

Fig. 4.20. Predicted constitutive models from load-deflection curves fitting.



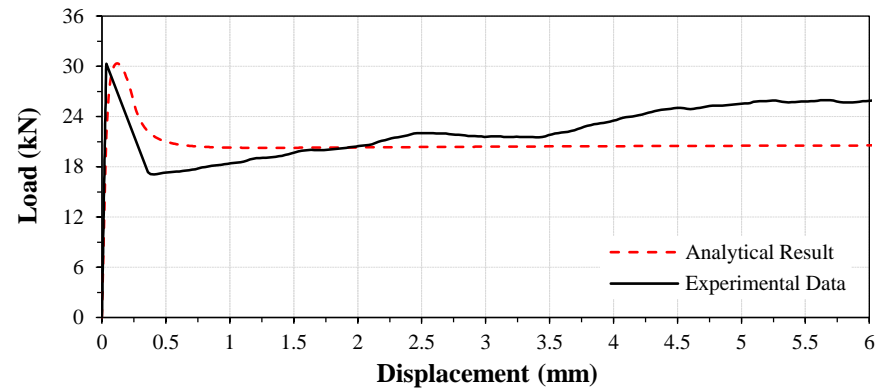
Predicted load-deflection curve



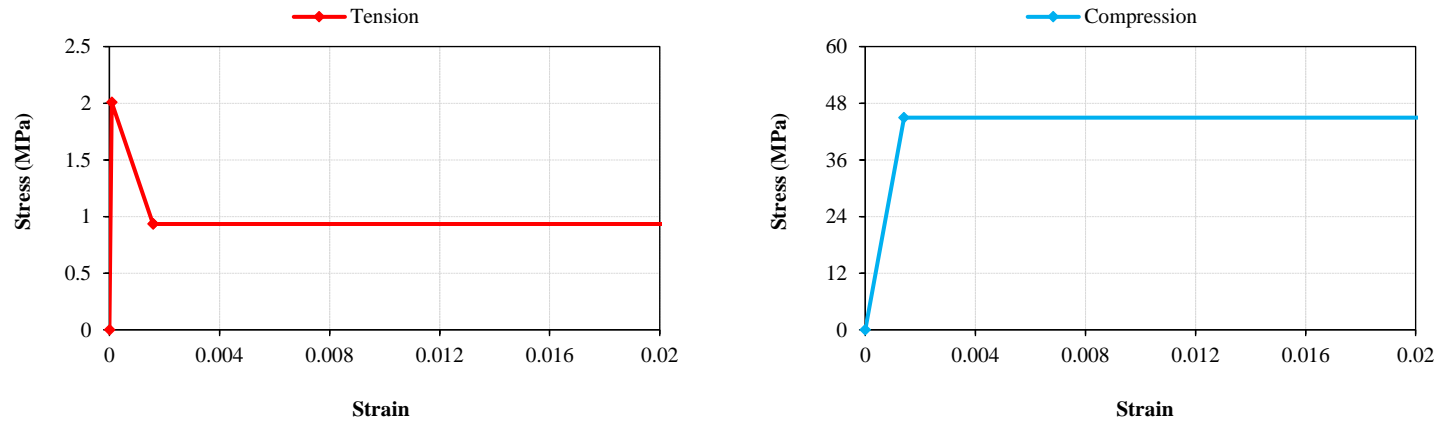
Material behaviour

N-0.2-45

Fig. 4.20 (Continued). Predicted constitutive models from load-deflection curves fitting.



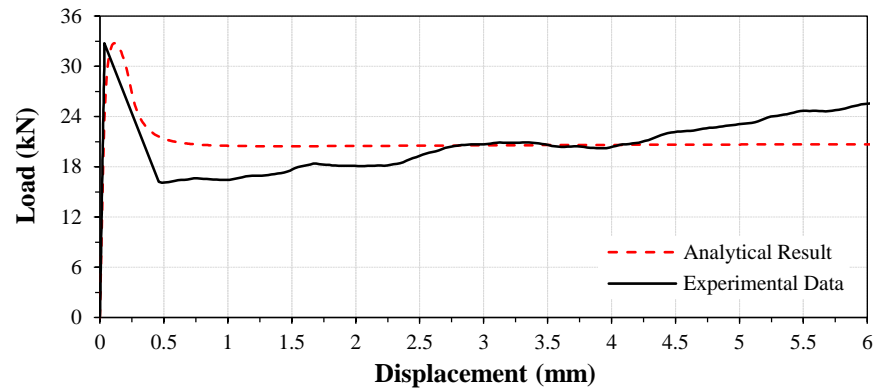
Predicted load-deflection curve



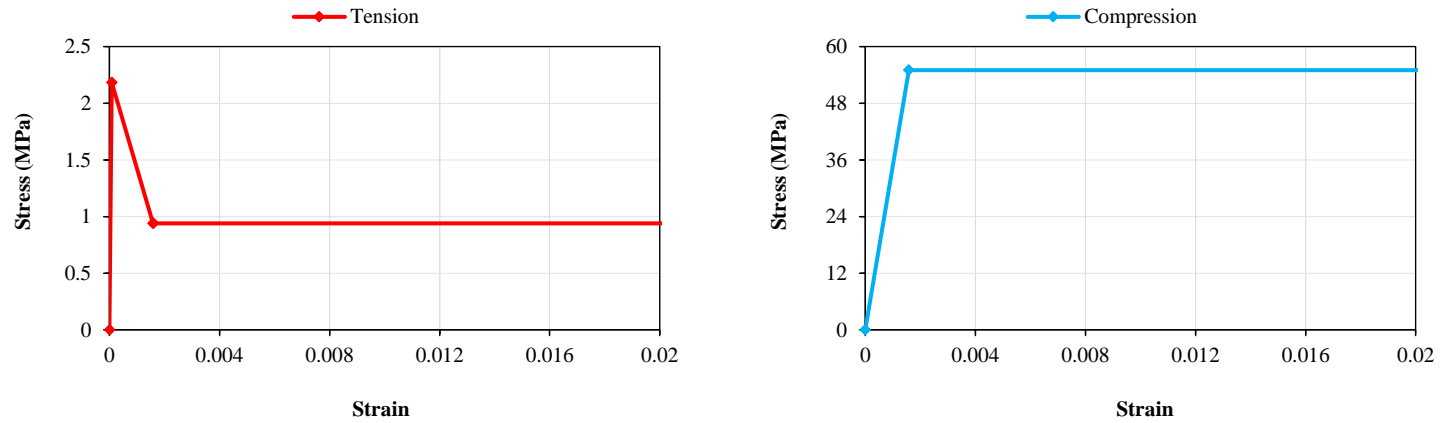
Material behaviour

N-0.35-35

Fig. 4.20 (Continued). Predicted constitutive models from load-deflection curves fitting.



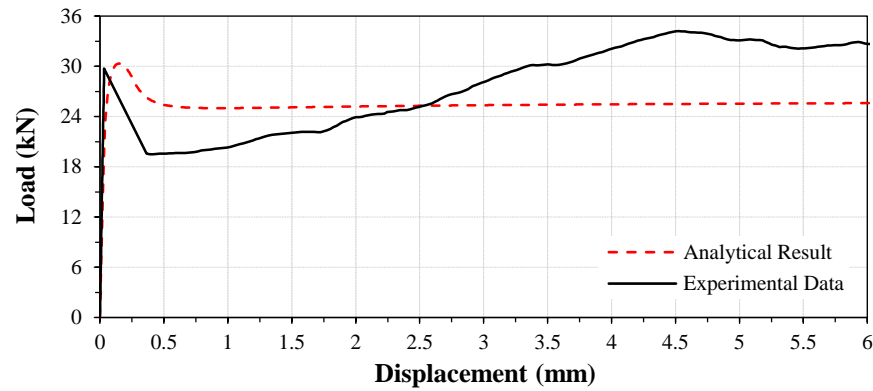
Predicted load-deflection curve



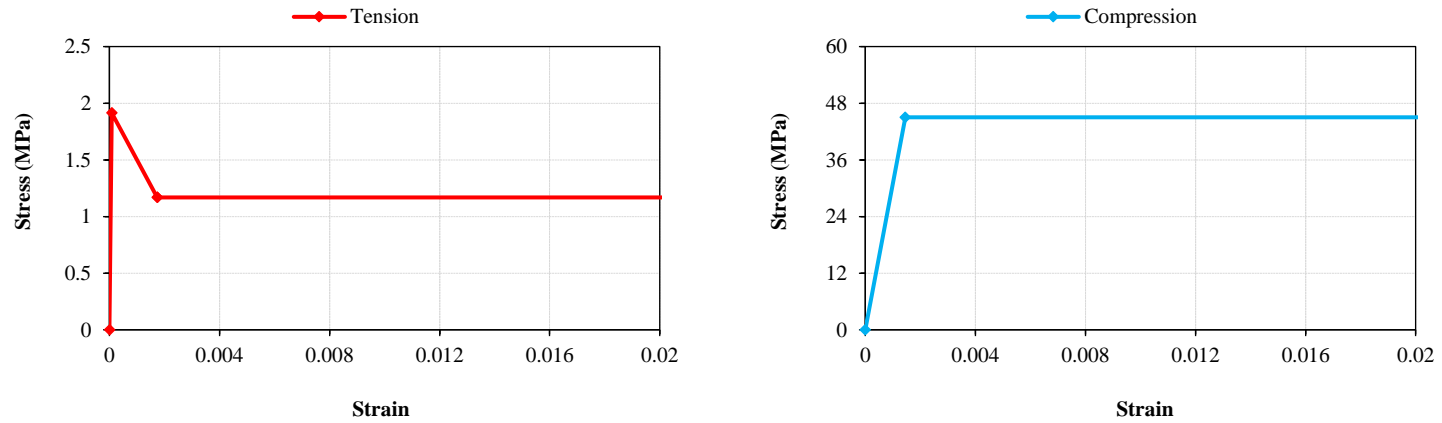
Material behaviour

N-0.35-45

Fig. 4.20 (Continued). Predicted constitutive models from load-deflection curves fitting.



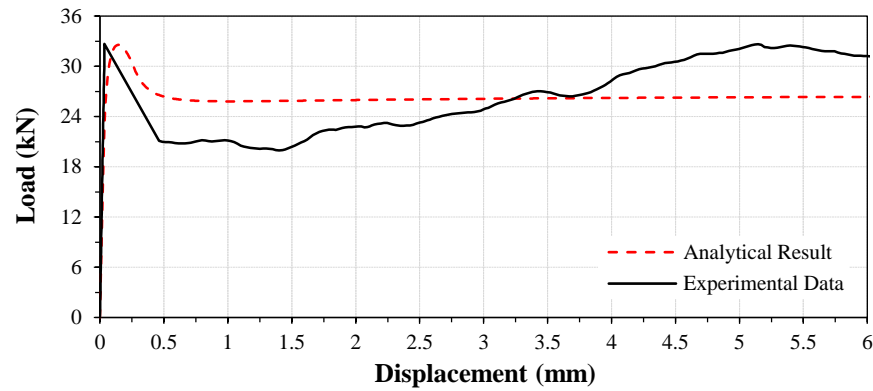
Predicted load-deflection curve



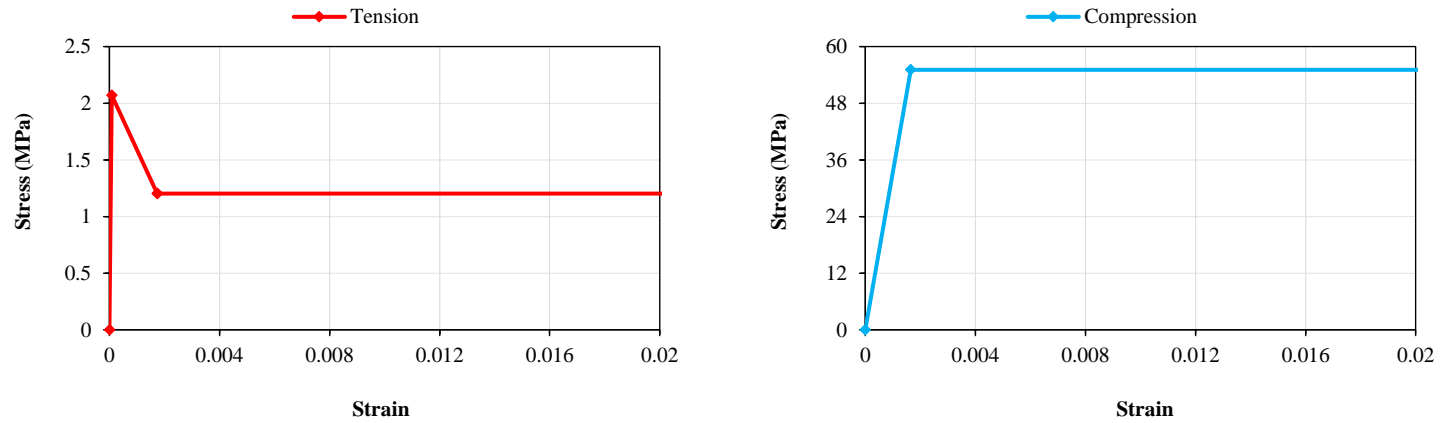
Material behaviour

N-0.5-35

Fig. 4.20 (Continued). Predicted constitutive models from load-deflection curves fitting.



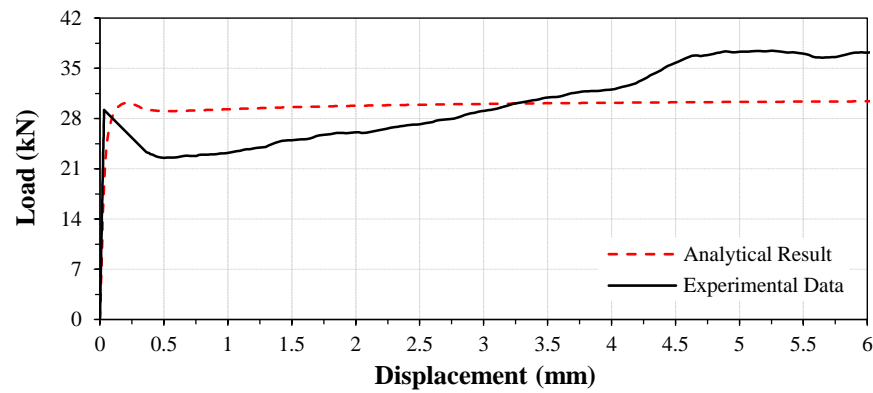
Predicted load-deflection curve



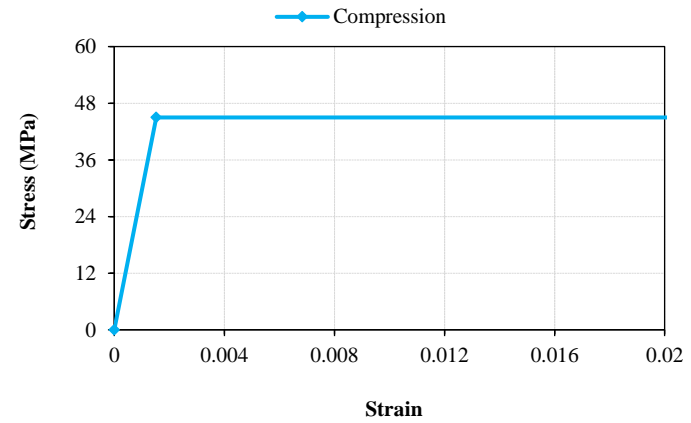
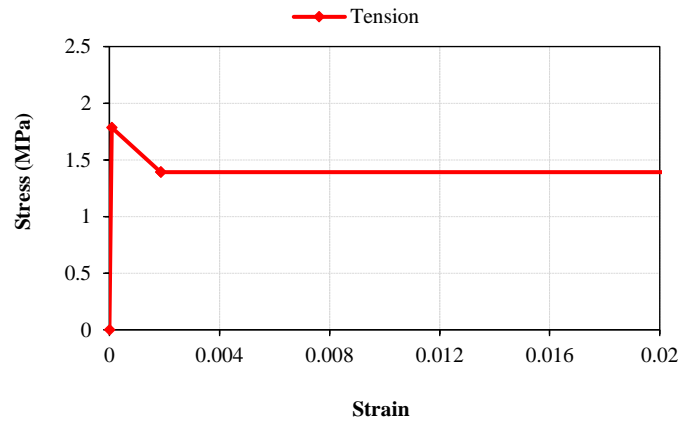
Material behaviour

N-0.5-45

Fig. 4.20 (Continued). Predicted constitutive models from load-deflection curves fitting.



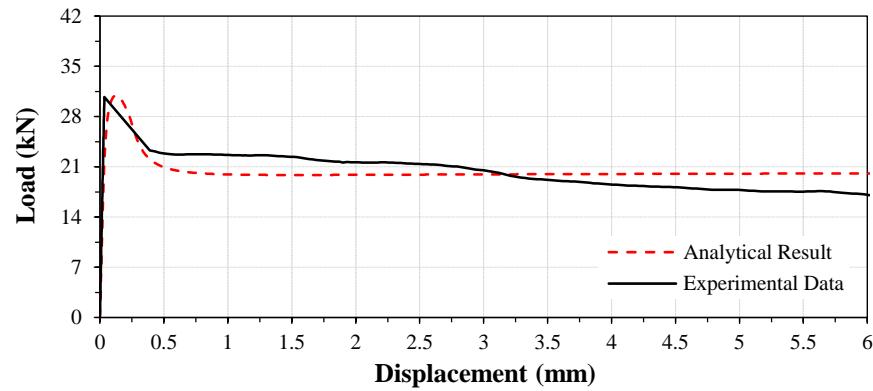
Predicted load-deflection curve



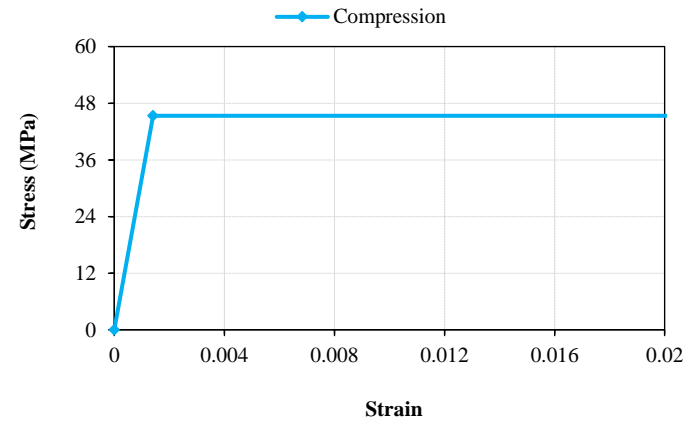
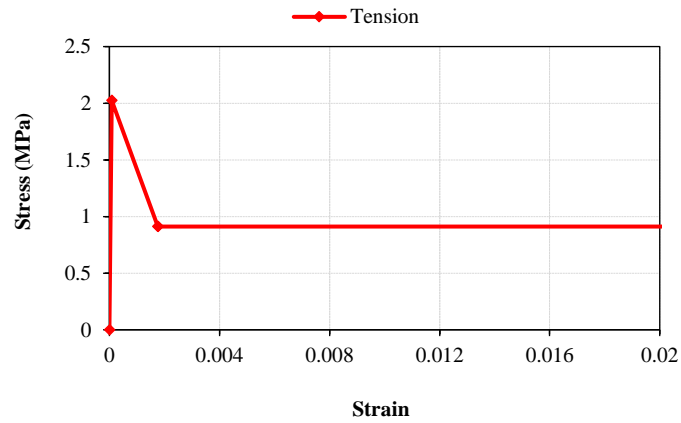
Material behaviour

N-0.65-35

Fig. 4.20 (Continued). Predicted constitutive models from load-deflection curves fitting.



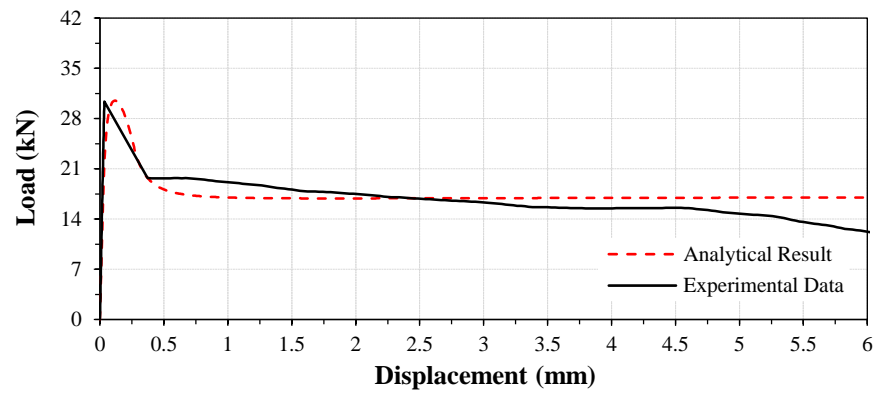
Predicted load-deflection curve



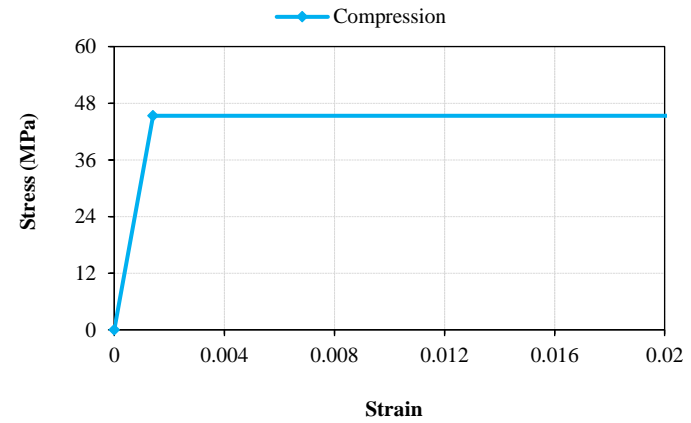
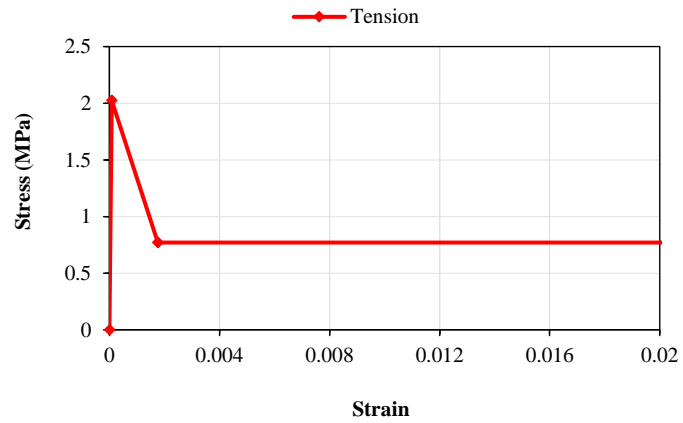
Material behaviour

H-0.5-35

Fig. 4.20 (Continued). Predicted constitutive models from load-deflection curves fitting.



Predicted load-deflection curve



Material behaviour

C-0.5-35

Fig. 4.20 (Continued). Predicted constitutive models from load-deflection curves fitting.

The post-peak tensile stresses of SFRC are shown in **Fig. 4.21**. As seen in the figure, increasing of the volume content of the new fibre leads to the increase in the post-peak tensile stress. As the fibre content increases from 0.2% to 0.35% and from 0.35% to 0.5%, on average for concrete with different compressive stresses, the tensile stress increases from 0.71 MPa to 0.93 MPa and from 0.93 MPa to 1.19 MPa, respectively.

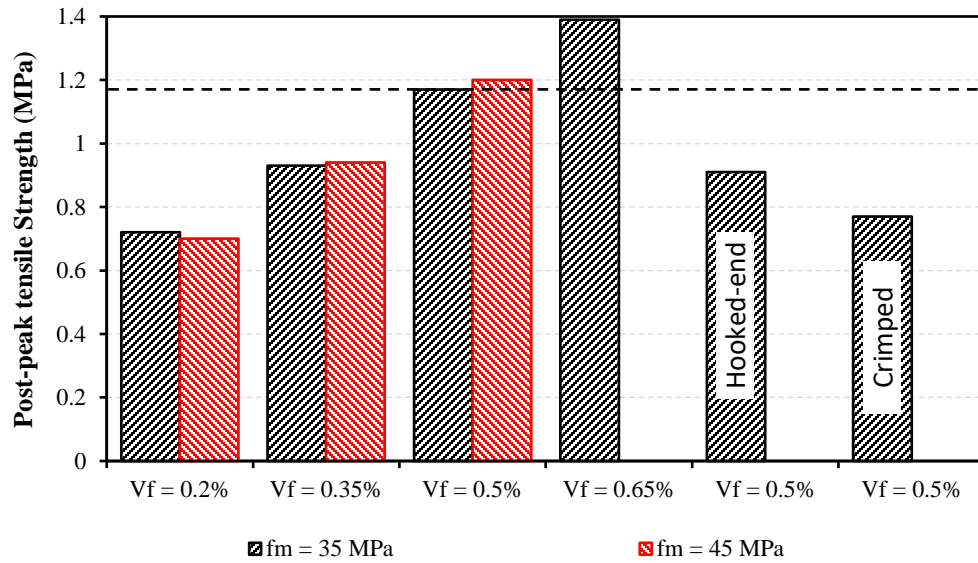


Fig. 4.21. Effect of fibre volume content on the post-peak tensile stress.

Moreover, with the same fibre volume content (0.5%), the addition of the new fibre to concrete with the compressive stress (f_m) of 35 MPa, results in the tensile stress of 1.17 MPa. However, with the employment of the existing fibres on the market, the post-peak tensile stress of 0.84 MPa is achieved, on average.

4.9. SUMMARY

In this chapter, an experimental programme including compression and flexure tests is performed to investigate the effect of the newly-designed steel fibre (SD-9-1.45-0.4-40) inclusion on the concrete material behaviour where fibre volume content and concrete strength are considered as the experiment parameters.

CHAPTER 5

STRUCTURAL TESTING

5.1. INTRODUCTION

The capability of steel fibres in stress transferring across the cracked sections (bridging effect) is employed to enhance the concrete role (especially in tension zones) in the overall load bearing capacity of RC members. However, as mentioned in **Section 2.4**, the structural applications of SFRC is limited mainly due to the poor performance of the fibres available on the market at the cracking levels expected at the ultimate state of the members. After the early stage of the fibre pullout process (peak pullout load), as the fibres are pulled out from concrete, their resistance decreases with the slippage known as slip-softening behaviour. The continuous pullout load decay cannot result in a major contribution of fibres to the ultimate load bearing capacity of RC members (Noghabai 2000, Richardson and Landless 2009).

As the main objective of this research project, the first generation of high-performing steel fibres in normal concrete is developed to overcome the shortcomings of the commercially available fibres for structural applications. Following the fibre development and material testing of concrete with the fibre, a structural testing programme was designed and performed to examine the contribution of the new steel fibre to the structural performance of RC beams. The testing programme consists of two sets of RC beams, i.e. shear-critical and flexure-critical, which was designed such that

the shear and flexural contribution of the fibre can be assessed individually. Varying experiment parameters are considered in the testing programme.

5.2. STRUCTURAL TESTING PROGRAMME

The preparation and casting of RC beams were simultaneously performed with the material testing specimens; hence the obtained material properties can be used for the structural response analysis of the beams. The concrete mixing, casting, and curing procedure and the SFRC characteristics are provided in **Sections 4.3** and **4.5**. The structural testing programme is undertaken on shear-critical and flexure-critical RC beam specimens. The dimensions of the specimens, respectively width, height, and length, are 130 mm, 165 mm, 1200 mm with a span length of 1100 mm. The effective depth of sections for all the specimens is 140 mm. The beams are statically loaded in a displacement-controlled manner with the loading rate of 0.6 mm/min (Adhikary, Li et al. 2014, Kim, Kim et al. 2016) using the closed-loop control UTM with the capacity of 300 kN used for the material testing (see **Fig. 5.1**). Regulations provided in **Appendix 4.4** are strictly followed during the tests.

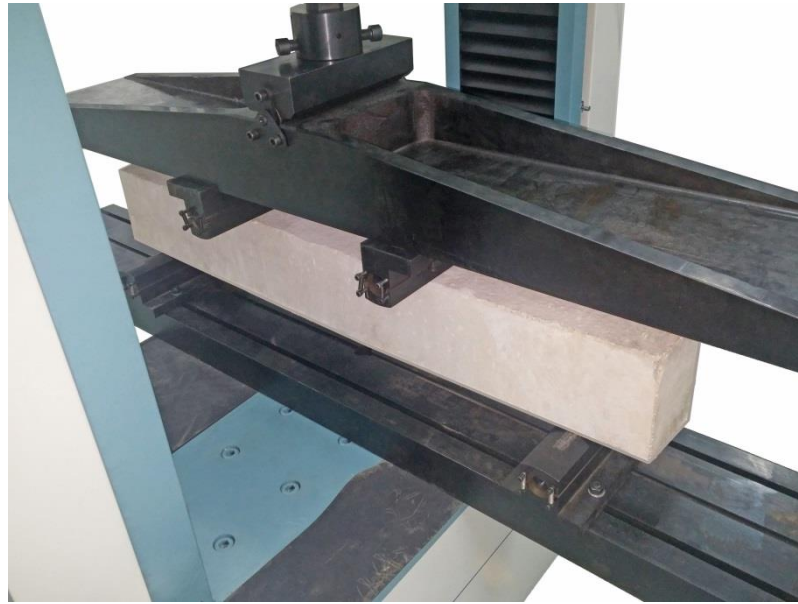


Fig. 5.1. Universal Testing Machine (300 kN) with the beam testing setup.

Non-fibrous RC beams are included in the programme as the reference. Furthermore, a number of fibrous RC beams with commercially available steel fibres (hooked-end and crimped) are also tested for the comparison of the fibres' performance.

5.2.1. REINFORCEMENT PROPERTIES

In this project, steel reinforcing bars with three different diameters (6 mm, 8 mm, and 10 mm) are used. Tensile coupon tests (ASTM E8/E8M - 13a 2013) are performed on three samples for each category of steel bars where the material characteristics, i.e. Young's modulus and yield and ultimate stresses, are calculated from the average stress-strain curves.

The tensile coupon test setup is shown in **Fig. 5.2**. An extensometer with a total stroke of ± 5 mm and precision of ± 0.001 mm is employed for measuring the samples extension.

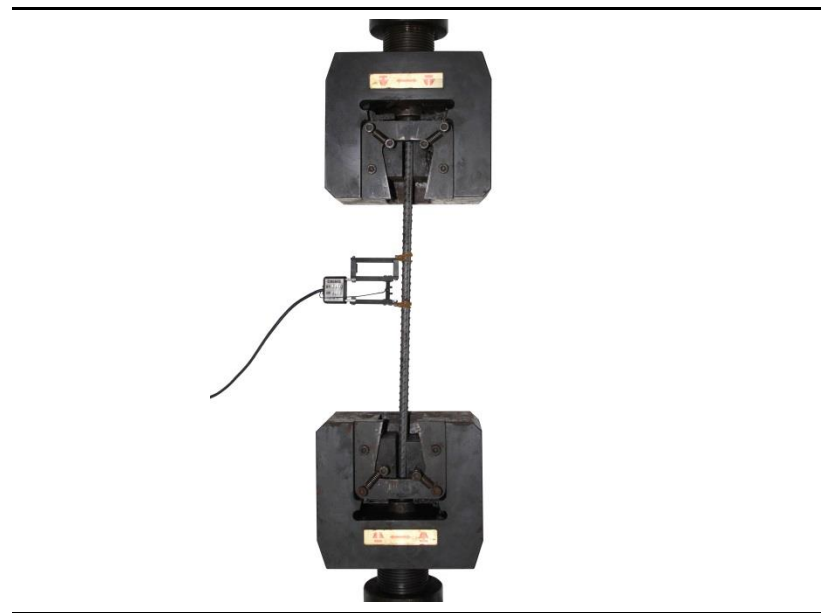


Fig. 5.2. Coupon testing setup.

The average stress-strain curves of the reinforcement are provided in **Fig. 5.3**. The material properties of steel reinforcing bars are summarised in **Table 5.1**.

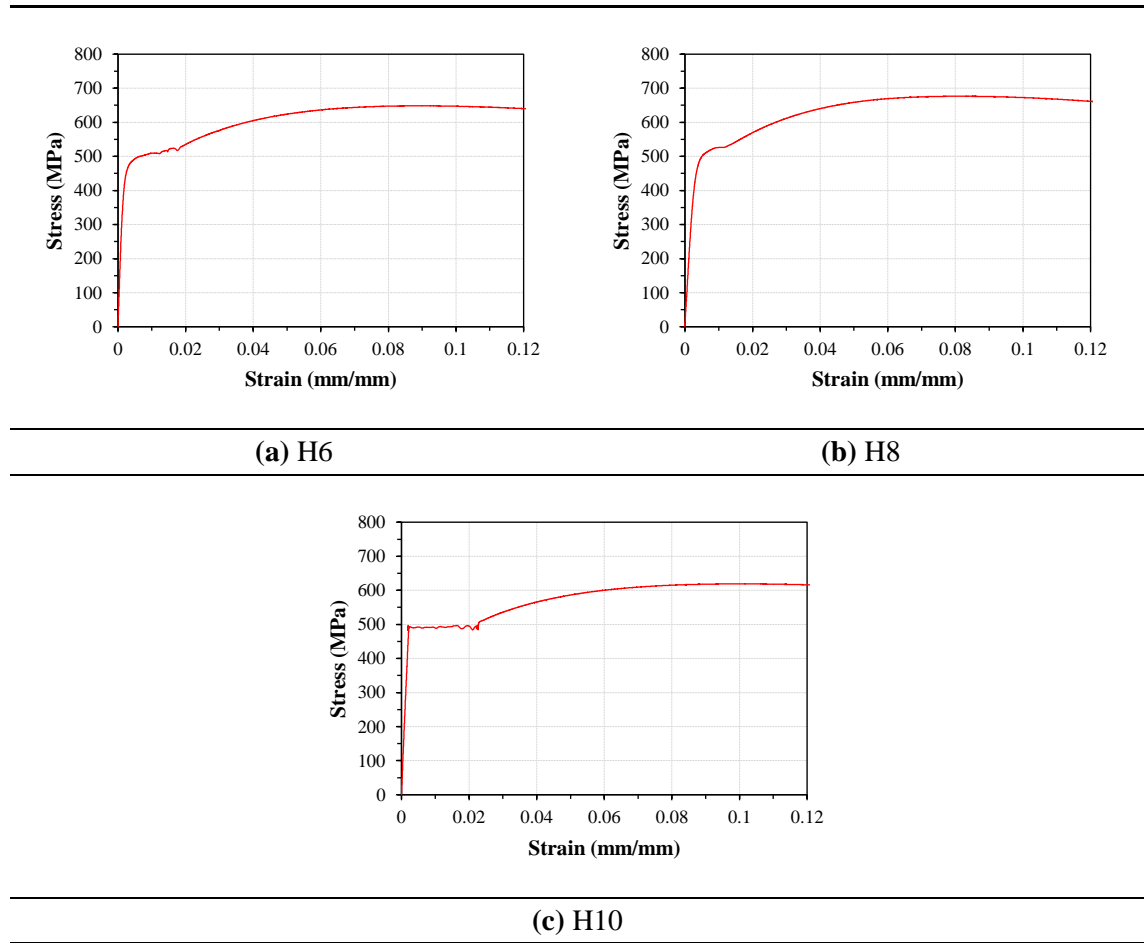


Fig. 5.3. Average coupon testing results of steel reinforcement bars.

Table 5.1
Coupon test results of reinforcing bars.

Bar No. Bar diameter, d_b (mm)	Modulus of elasticity, E_s (GPa)	Yield stress, f_y (MPa)	Ultimate stress, f_u (MPa)
6	230	500	650
8	210	520	670
10	225	490	620

5.2.2. SHEAR RESISTANCE CONTRIBUTION OF NEW FIBRE

Fibre volume content (V_f), concrete strength (f_{ck}), longitudinal reinforcement ratio (ρ), and shear span to effective depth (a/d) are considered as the experiment parameters for the shear-critical category. The aim of this phase is to investigate the effectiveness of the new fibre in the shear bearing capacity of RC beams. All the specimens do not have shear links where the shear action is intended to be carried by the overall contribution of concrete, longitudinal reinforcement, and the fibres. The number and specifications of the specimens are summarised in **Table 5.2**.

Table 5.2

Number and specifications of the shear-critical beams with the new fibre.

Fibre	f_m (MPa)	ρ (%)	V_f (%)	a/d (-)	No. of specimens
Newly-designed	35, 45	0.55 ^a , 0.86 ^b	0 ^c , 0.2, 0.35, 0.5, 0.65 ^d	1.5, 3	36

^a 2H8 as longitudinal reinforcement

^b 2H10 as longitudinal reinforcement

^c Non-fibrous RC beams as the reference

^d $f_m = 35$ MPa

The beams are labelled such that their specifications can be identified by the corresponding labels. For instance, “SC-0.55-1.5-N-0.2-35” indicates that the beam is shear-critical, having a reinforcement ratio of 0.55%, which is tested with a shear span to the effective depth of 1.5. The remaining parts of the label indicate the SFRC characteristics (fibrous concrete with 0.2% of the new fibre and the target compressive strength of 35 MPa) as mentioned in **Section 4.5**.

The testing setup and the cross-section layouts are shown in **Fig. 5.4**. The mid-deflection is measured using a high-precision pair of LVDTs, mounted underneath the beams’ sides and the average result is considered as the mid-span deflection. The intended shear span is adjusted using the moveable roller supports of the loading beam (see **Fig. 5.4(a)**).

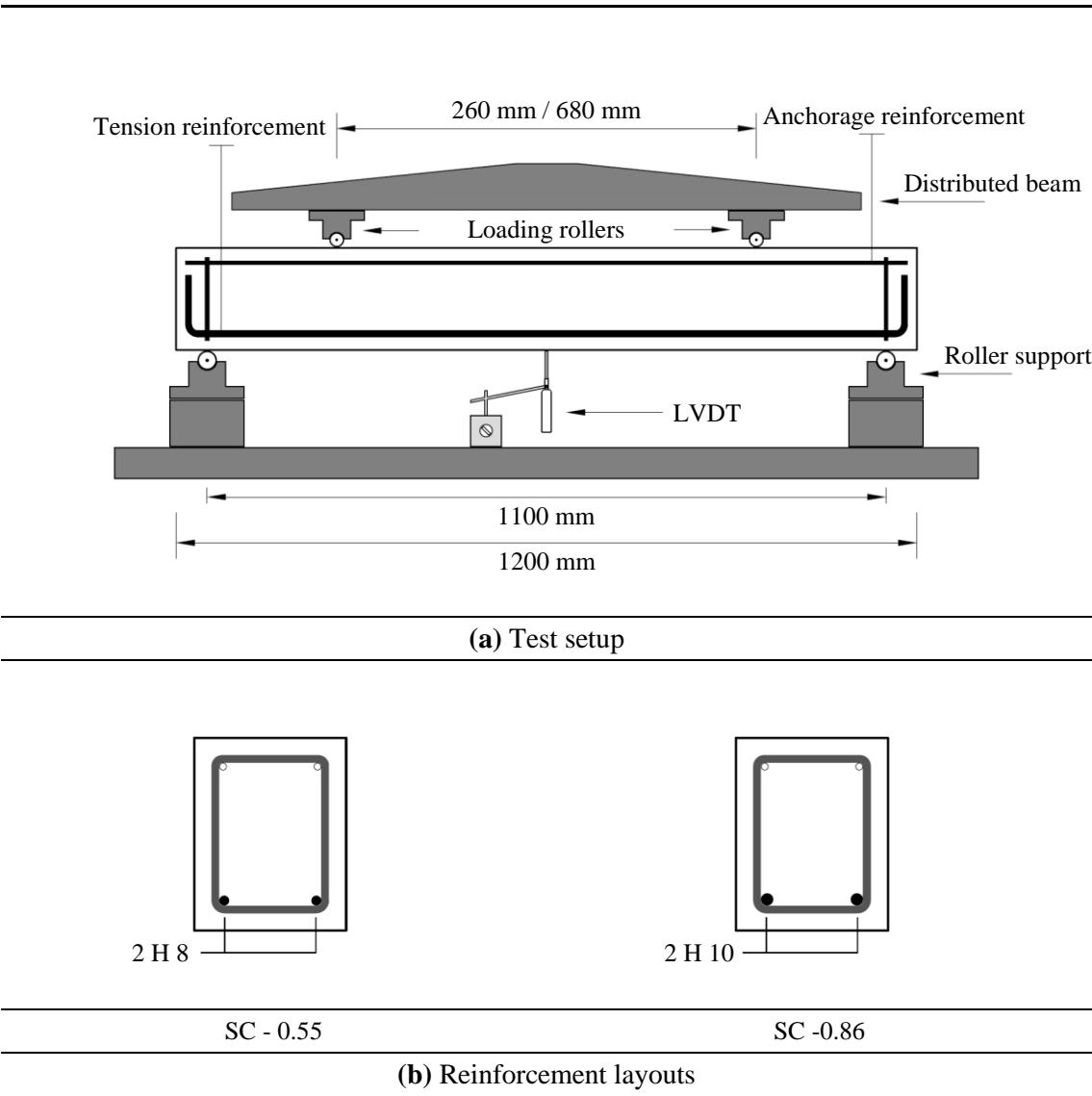
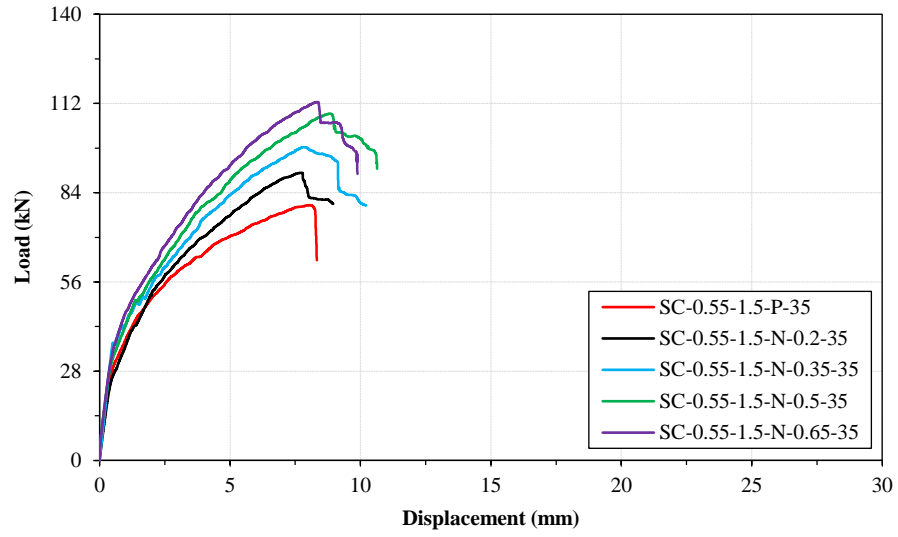
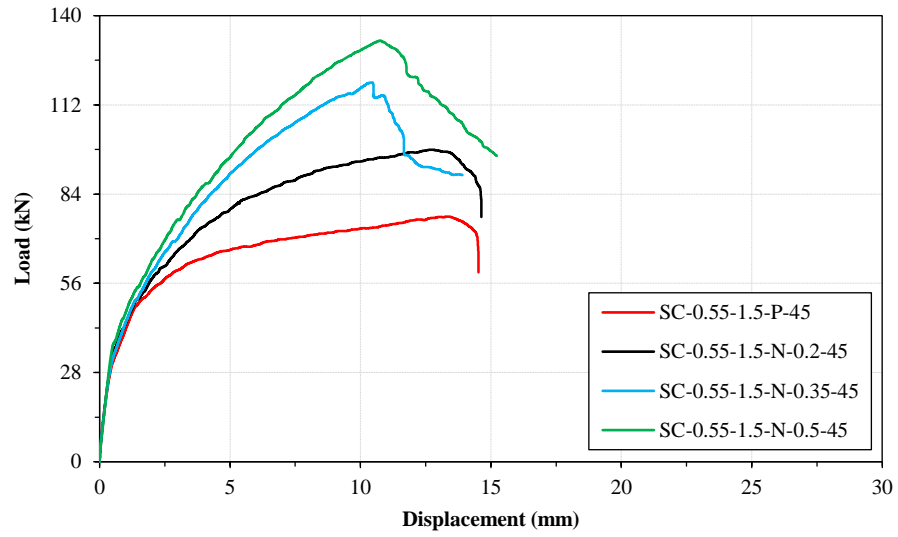


Fig. 5.4. Shear-critical SFRC beams testing.

The load-deflection response of the shear-critical RC beams, non-fibrous and fibrous with the newly-designed, is provided in **Fig. 5.5** such that the contribution of the new fibre and the effect of fibre dosages can be assessed. The responses are smoothed in order to remove the graphs noises. The capacity of the beams and corresponding failure modes are summarised in **Table 5.3**.

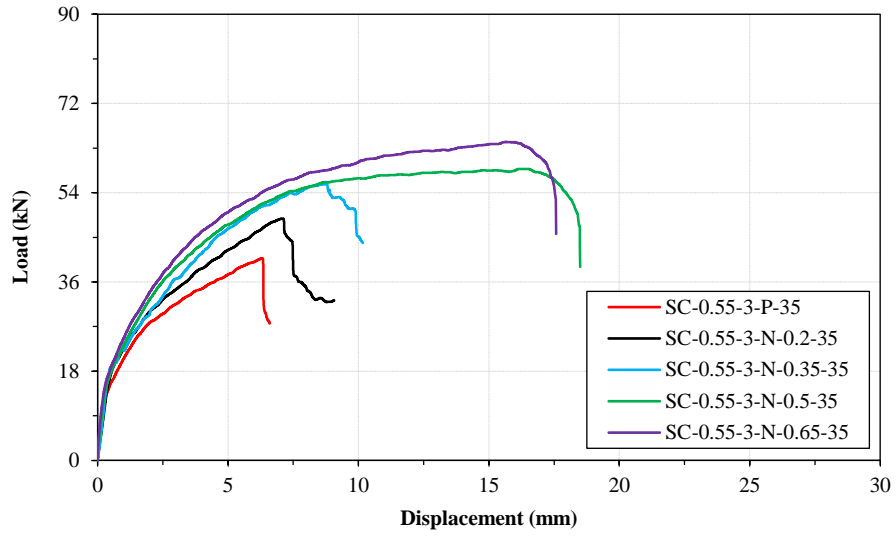


(a) $f_m = 35$ MPa

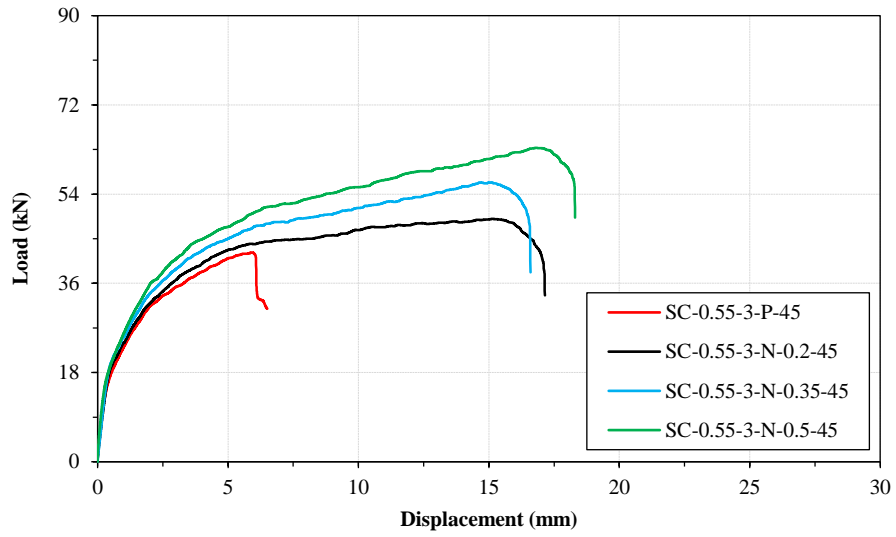


(b) $f_m = 45$ MPa

Fig. 5.5. Response of shear-critical RC beams, $\rho = 0.55\%$ and $a/d = 1.5$.

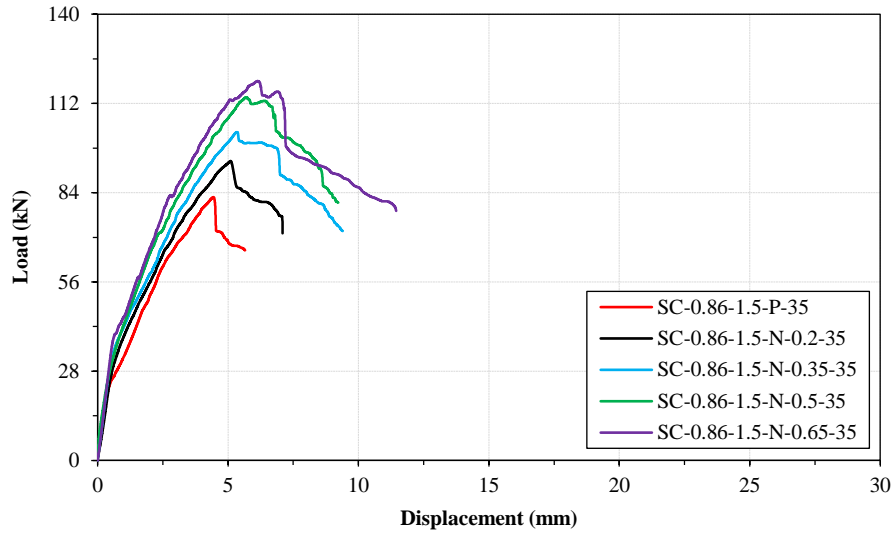


(a) $f_m = 35$ MPa

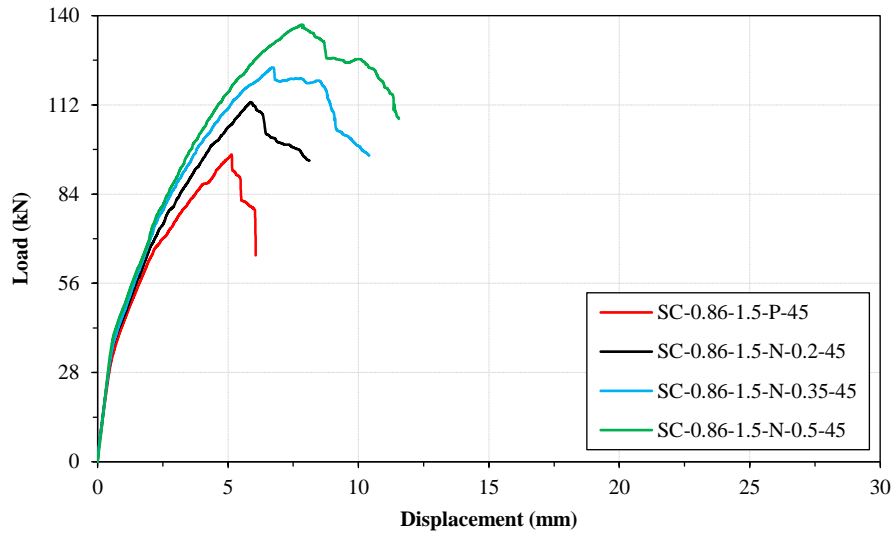


(b) $f_m = 45$ MPa

Fig. 5.5 (Continued). Response of shear-critical RC beams, $\rho = 0.55\%$ and $a/d = 3$.

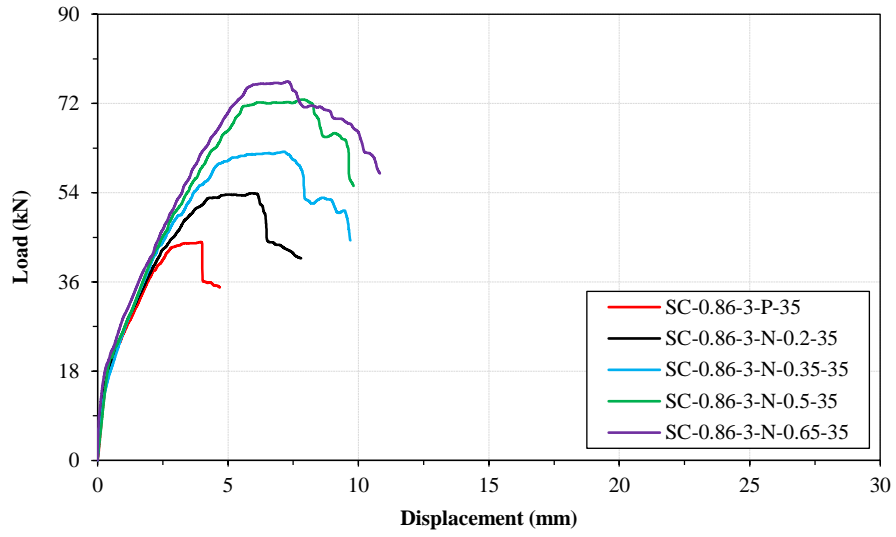


(a) $f_m = 35$ MPa

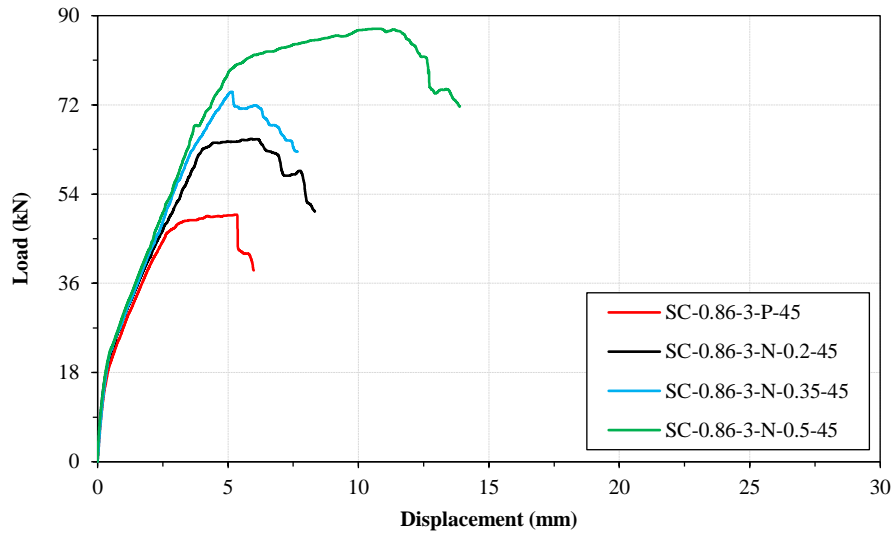


(b) $f_m = 45$ MPa

Fig. 5.5 (Continued). Response of shear-critical RC beams, $\rho = 0.86\%$ and $a/d = 1.5$.



(a) $f_m = 35$ MPa



(b) $f_m = 45$ MPa

Fig. 5.5 (Continued). Response of shear-critical RC beams, $\rho = 0.86\%$ and $a/d = 3$.

Table 5.3
Shear-critical beams results.

Beam ID	a/d	f_{ck}	V_f	ρ	Failure Mode	$V_{fc,exp.}^1$ (MPa)	$V_{fc,pre.}^2$ (MPa)	$V_{fc,pre.}^3$ (MPa)
SC-0.55-1.5-P-35	1.5	35.9	0	0.55	Shear	2.20	-	2.15
SC-0.86-1.5-P-35	1.5	35.9	0	0.86	Shear	2.27	-	2.28
SC-0.55-1.5-N-0.2-35	1.5	35.3	0.2	0.55	Shear	2.48	1.41	2.49
SC-0.86-1.5-N-0.2-35	1.5	35.3	0.2	0.86	Shear	2.58	1.48	2.62
SC-0.55-1.5-N-0.35-35	1.5	35.4	0.35	0.55	Shear	2.70	1.63	2.73
SC-0.86-1.5-N-0.35-35	1.5	35.4	0.35	0.86	Shear	2.83	1.71	2.86
SC-0.55-1.5-N-0.5-35	1.5	36.7	0.5	0.55	Shear	2.99	1.83	3.01
SC-0.86-1.5-N-0.5-35	1.5	36.7	0.5	0.86	Shear	3.13	1.92	3.14
SC-0.55-1.5-N-0.65-35	1.5	34.2	0.65	0.55	Shear	3.09	1.86	3.12
SC-0.86-1.5-N-0.65-35	1.5	34.2	0.65	0.86	Shear	3.27	1.96	3.26
SC-0.55-1.5-P-45	1.5	46.0	0	0.55	Flexure	-	-	2.55
SC-0.86-1.5-P-45	1.5	46.0	0	0.86	Shear	2.65	-	2.68
SC-0.55-1.5-N-0.2-45	1.5	46.5	0.2	0.55	Flexure	-	1.7	2.94
SC-0.86-1.5-N-0.2-45	1.5	46.5	0.2	0.86	Shear	3.10	1.79	3.07
SC-0.55-1.5-N-0.35-45	1.5	46.0	0.35	0.55	Shear	3.27	1.95	3.16
SC-0.86-1.5-N-0.35-45	1.5	46.0	0.35	0.86	Shear	3.40	2.05	3.29
SC-0.55-1.5-N-0.5-45	1.5	47.3	0.5	0.55	Shear	3.63	2.18	3.43
SC-0.86-1.5-N-0.5-45	1.5	47.3	0.5	0.86	Shear	3.77	2.29	3.56
SC-0.55-3-P-35	3	35.9	0	0.55	Shear	1.12	-	0.98
SC-0.86-3-P-35	3	35.9	0	0.86	Shear	1.21	-	1.12
SC-0.55-3-N-0.2-35	3	35.3	0.2	0.55	Shear	1.34	1.41	1.33
SC-0.86-3-N-0.2-35	3	35.3	0.2	0.86	Shear	1.48	1.48	1.46
SC-0.55-3-N-0.35-35	3	35.4	0.35	0.55	Flexure-Shear	1.53	1.63	1.57
SC-0.86-3-N-0.35-35	3	35.4	0.35	0.86	Shear	1.71	1.71	1.7
SC-0.55-3-N-0.5-35	3	36.7	0.5	0.55	Shear-Flexure	-	1.83	1.85
SC-0.86-3-N-0.5-35	3	36.7	0.5	0.86	Shear	2.00	1.92	1.98
SC-0.55-3-N-0.65-35	3	34.2	0.65	0.55	Shear-Flexure	-	1.86	1.96
SC-0.86-3-N-0.65-35	3	34.2	0.65	0.86	Shear	2.10	1.96	2.09
SC-0.55-3-P-45	3	46.0	0	0.55	Flexure-Shear	1.16	-	1.39
SC-0.86-3-P-45	3	46.0	0	0.86	Shear	1.37	-	1.52
SC-0.55-3-N-0.2-45	3	46.5	0.2	0.55	Flexure	-	1.7	1.77
SC-0.86-3-N-0.2-45	3	46.5	0.2	0.86	Shear	1.79	1.79	1.91
SC-0.55-3-N-0.35-45	3	46.0	0.35	0.55	Flexure	-	1.95	1.99
SC-0.86-3-N-0.35-45	3	46.0	0.35	0.86	Shear	2.05	2.05	2.12
SC-0.55-3-N-0.5-45	3	47.3	0.5	0.55	Flexure	-	2.18	2.27
SC-0.86-3-N-0.5-45	3	47.3	0.5	0.86	Shear	2.40	2.29	2.4

¹ Experimental shear strength

² Predicted shear strength using Eq. (5.1)

³ Predicted shear strength using Eq. (5.2)

The failure patterns for selected beams ($V_f = 0\%$, 0.5% , and 0.65%) are shown in **Figs. 5.6** and **5.7**.

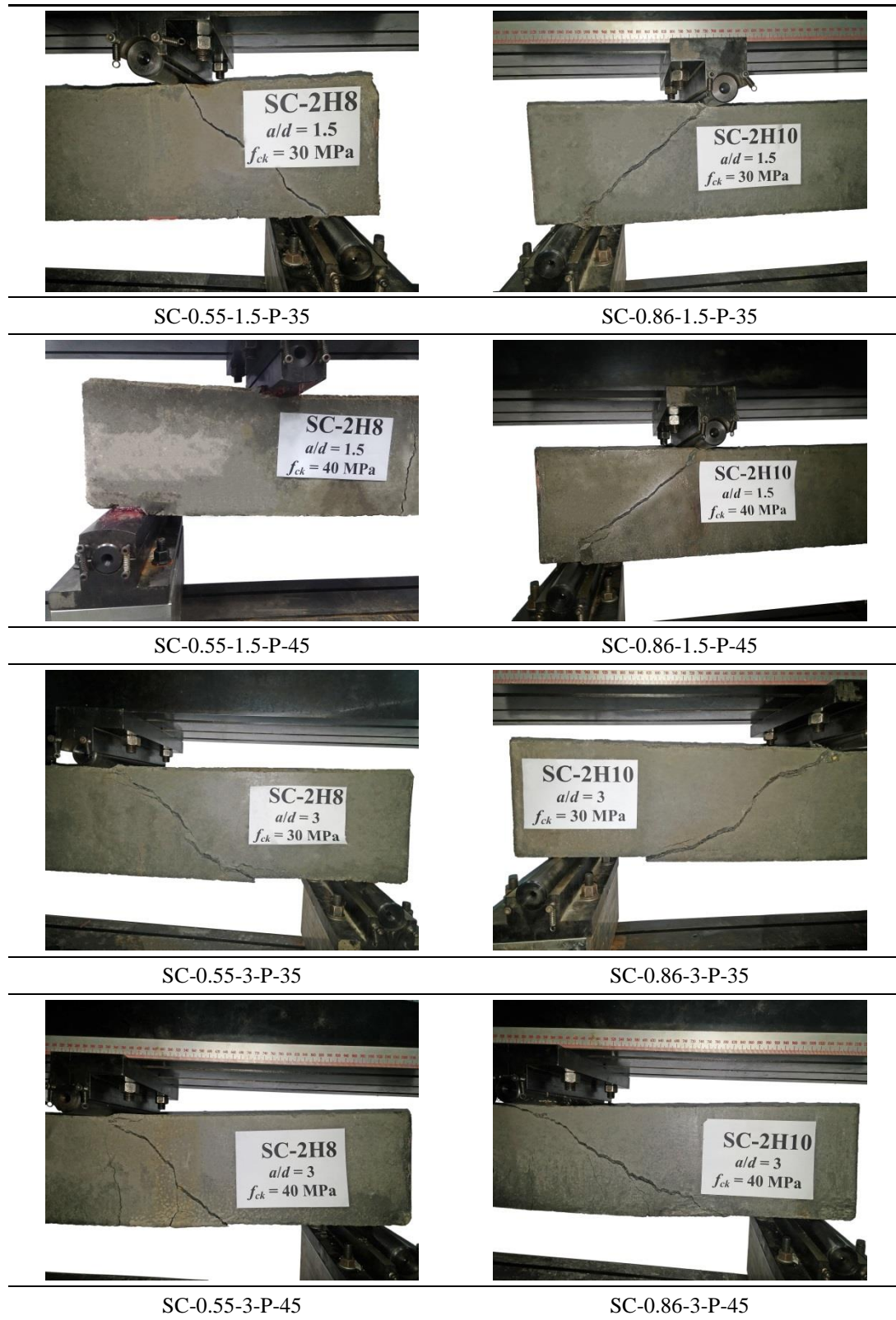


Fig. 5.6. Failure of shear-critical non-fibrous RC beams.

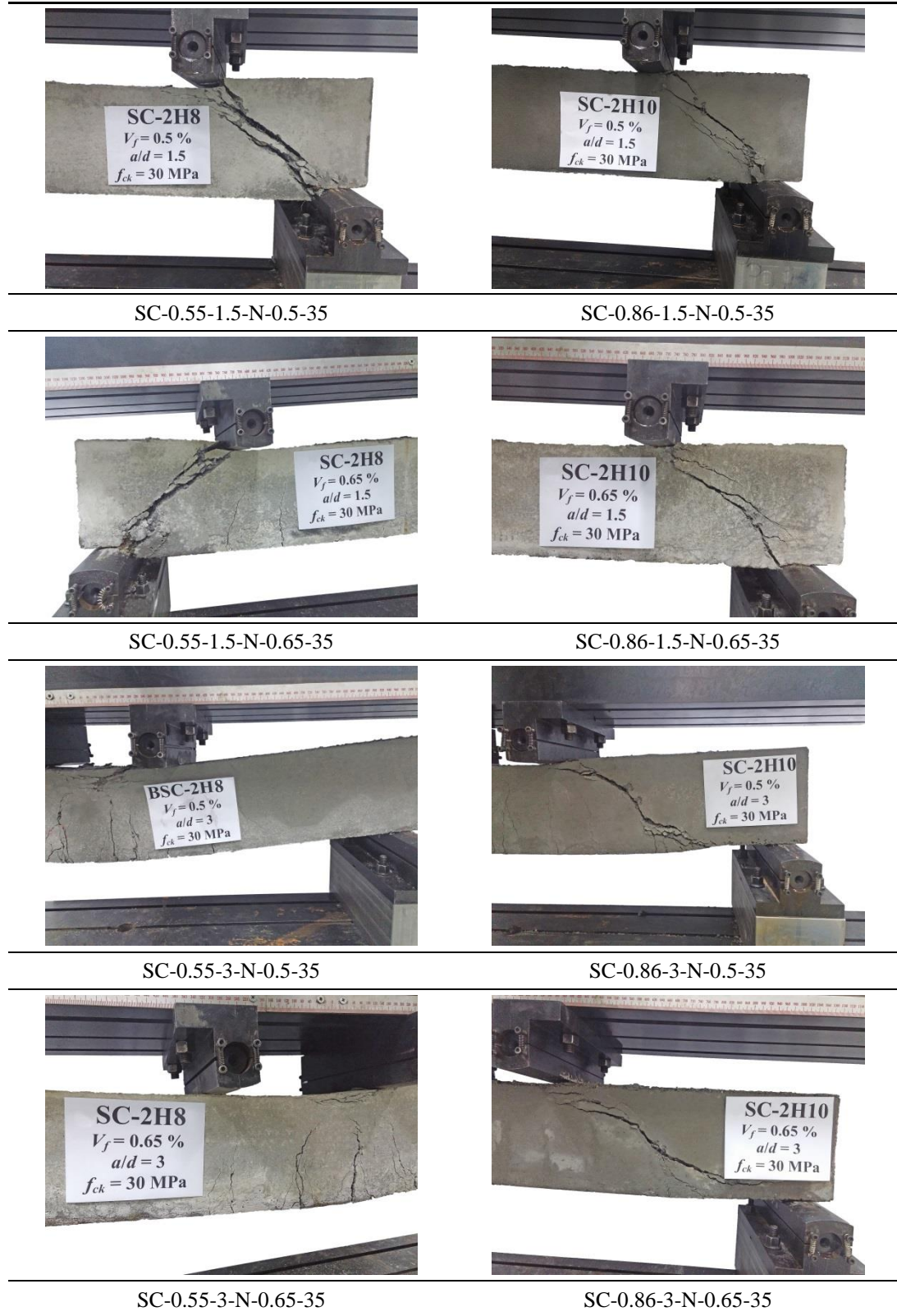


Fig. 5.7. Failure of shear-critical RC beams with the newly-designed fibre.

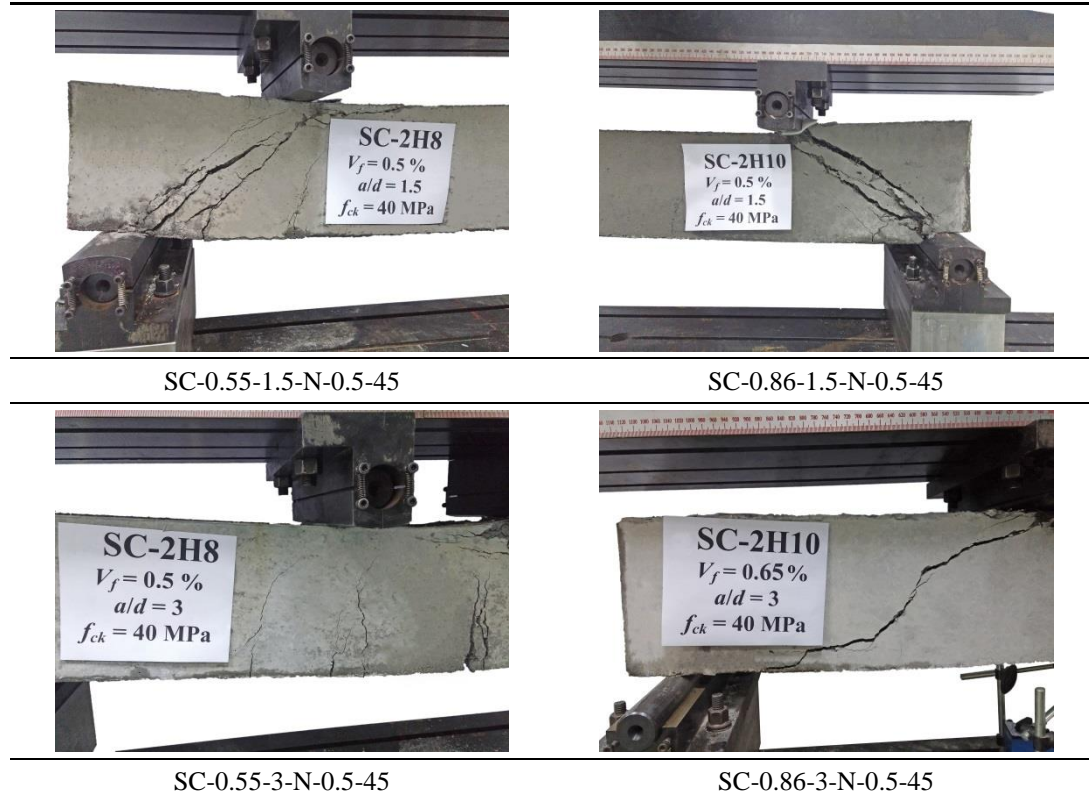


Fig. 5.7 (Continued). Failure of shear-critical RC beams with the newly-designed fibre.

Fig. 5.8 shows the scatter plots of the shear strength of the beams with shear and flexure-shear failures versus the experiment parameters including a/d , f_{ck} , V_f , and ρ .

The contribution of each parameter on the shear strength of SFRC beams is discussed as follows:

1. Shear span to effective depth (a/d) is one of the most influential parameters on the shear strength of SFRC beams (v_{fc}) as seen in **Fig. 5.8**. As a/d increases, the v_{fc} decreases drastically which is confirmed by the literature (Narayanan and Darwish 1988). In an overall analysis, the results indicate that v_{fc} of the SFRC beams decreases by 45% (from 2.96 MPa to 1.64 MPa) as a/d increases from 1.5 to 3. It is attributed to the arch action which is the transfer process of the compressive force through the path created along the loading points and the supports of the beams. As the shear span decreases, the arch action improves the shear strength.

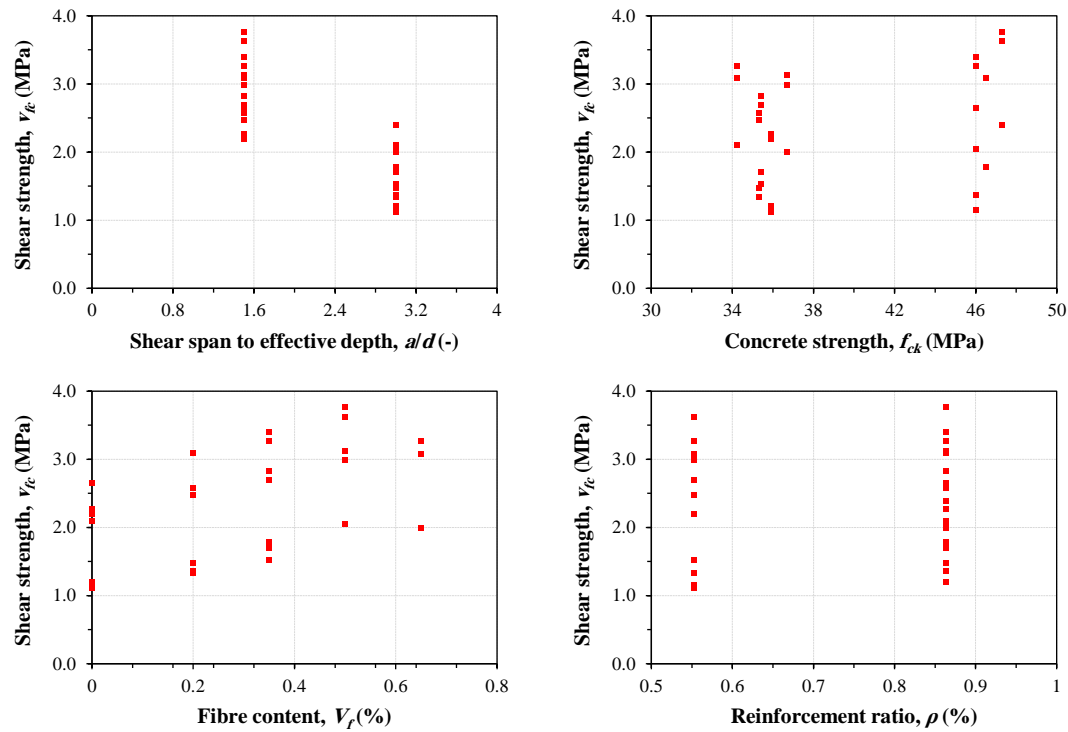


Fig. 5.8. Contribution of the experiment parameters on the shear strength of SFRC beams.

2. Concrete effectively contributes to the shear capacity of SFRC beams, as the concrete compressive strength increases, shear strength increases (Shahnewaz and Shahria Alam 2014). From the test results, by increasing of the target mean cylinder strength of concrete (f_m) from 35 MPa to 45 MPa, v_{fc} increases from 2.22 MPa to 2.6 MPa, on average.
3. The longitudinal tension reinforcement contributes to enhancing the shear strength of SFRC beams. As the tension reinforcement ratio (ρ) increases from 0.55% to 0.86%, v_{fc} increases 2.32 MPa to 2.40 MPa.
4. The fibres act as the crack growth arrestors, transfer tensile stresses across the cracked sections and leads to the improvement of the shear capacity of the beams. The addition of 0.5% the new fibre results in the shear strength increases from 1.71 MPa to 2.99 MPa, on average. As provided in **Table 5.3**, with the addition of the newly-designed fibre, it is possible to increase the shear capacity of the beams and alter the failure mode from shear to flexure (those highlighted in red).

5. It is evident that the addition of the new fibre not only increases the capacity of RC members but also enhances the ductility of the members (ratio of the deflection corresponding to 80% of the peak load to the deflection at elastic limit) and guarantees a desirable and gradual failure and. As the fibre dosage increases, the load decay rate (after the peak load) decreases. The addition of the new fibre with dosages $V_f = 0.2\%$, 0.35% , 0.5% , and 0.65% , on average, enhances the ductility by 15.1%, 29.4%, 35.1%, and 21.4%, respectively. Besides, the fibres effectiveness is more pronounced at the greater shear span to effective depth ratio ($a/d=3$).

5.2.2.1. EMPIRICAL SHEAR DESIGN EQUATION

To propose shear design equations for SFRC beams with the newly-designed steel fibre, the Genetic algorithm (GA) (Goldberg 1989) is proposed as a robust optimisation tool. This is employed over the obtained experimental database (capacity of beams with shear failure) as seen in **Table 5.3** to determine the coefficients and exponents of the considered general forms for the equation (**Eq. (5.1)** and **Eq. (5.2)**). The first form of the equation, i.e. **Eq. (5.1)**, is intended just for fibrous RC beams ($V_f \neq 0$) while the second form is for both non-fibrous and fibrous RC beams. The coefficients and exponents values of the equations are constrained to vary between -10 and 10.

$$v_{fc,pre.} = a_0 f_{ck}^{a_1} \rho^{a_2} (a/d)^{a_3} V_f^{a_4} \quad (5.1)$$

$$v_{fc,pre.} = b_0 + b_1 f_{ck}^{b_2} + b_3 \rho^{b_4} + b_5 (a/d)^{b_6} + b_7 V_f^{b_8} \quad (5.2)$$

To initiate the iterative optimisation process using the GA, 1000 sets of the coefficients and exponents are randomly generated known as the initial populations where each set (combination) is a member of the population.

The mean absolute error (MAE) as the fitness function is employed to measure and score how close the predicted shear strengths ($v_{fc,pre.}$) are to the respective experimental strengths ($v_{fc,exp.}$). From the current population, 60% of the members which possess a lower MAE are chosen as elite and passed to the next population. Using crossover

(combining pairs of members in the current population) and mutation (randomly changing the variables of individual members) techniques, the rest of the next generation (40%) is produced (Goldberg 1989).

The iterative process (scoring members and producing new populations) is stopped manually when the target MAE is achieved.

To this end, a GA code was written in MATLAB version 8.5.1 (2015).

The proposed empirical shear design equations are **Eq. (5.3)** and **Eq. (5.4)** which respectively result in MAEs of 6% and 5%.

$$v_{fc,pre.} = 0.43f_{ck}^{0.69}\rho^{0.11}(a/d)^{-0.73}V_f^{0.25} \quad (5.3)$$

$$v_{fc,pre.} = 0.77 + 0.31f_{ck}^{0.59} + 0.37\rho^{1.25} - 0.95(a/d)^{0.89} + 1.54V_f^{0.89} \quad (5.4)$$

The predicted shear strengths using **Eq. (5.3)** and **Eq. (5.4)** are provided in **Table 5.3**. As seen in **Eq. (5.3)** and **Eq. (5.4)**, a/d and $v_{fc,pre.}$ have a negative correlation while as f_{ck} , ρ , and V_f increase, $v_{fc,pre.}$ increases (positive correlation) which confirms findings of previous research.

5.2.3. FLEXURAL CONTRIBUTION OF NEW FIBRE

This Phase is intended to examine the contribution of the new fibre on the overall flexural performance of RC members. To this end, a set of RC beams were designed, cast, and tested where two different concrete strengths (f_m) and longitudinal reinforcement ratios (ρ) were incorporated into the programme. The number and specifications of the specimens are summarised in **Table 5.4**. The specimens are identified as the generic format of the shear-critical RC beams, except for the first part of the labels which is “FC” (indicative of flexure-critical behaviour) and the third section (a/d) is omitted. The testing setup and the reinforcement arrangements of the specimens are shown in **Fig. 5.9**. Adequate shear reinforcement is provided for all the beams to ensure the failure mode is flexure. The shear span is set to be 300 mm.

The load-deflection responses of the beams are shown in **Fig. 5.10**. As seen in the figure, the addition of the new fibre enhances the capacity of the beams considerably

which implies the effective contribution of the fibre to the tensile strength of concrete. The flexural capacity of the non-fibrous beams reinforced with 0.31% and 0.55% longitudinal tension steel bars are 4.67 kN and 7.48 kN (for $f_m=35$ MPa) and 4.95 kN and 7.80 kN (for $f_m=45$ MPa). The beams capacities are increased with the addition of 0.5% of the new steel fibre to 9.37 kN and 12.29 kN (for $f_m=35$ MPa) and 10.24 kN and 13.33 kN (for $f_m=45$ MPa).

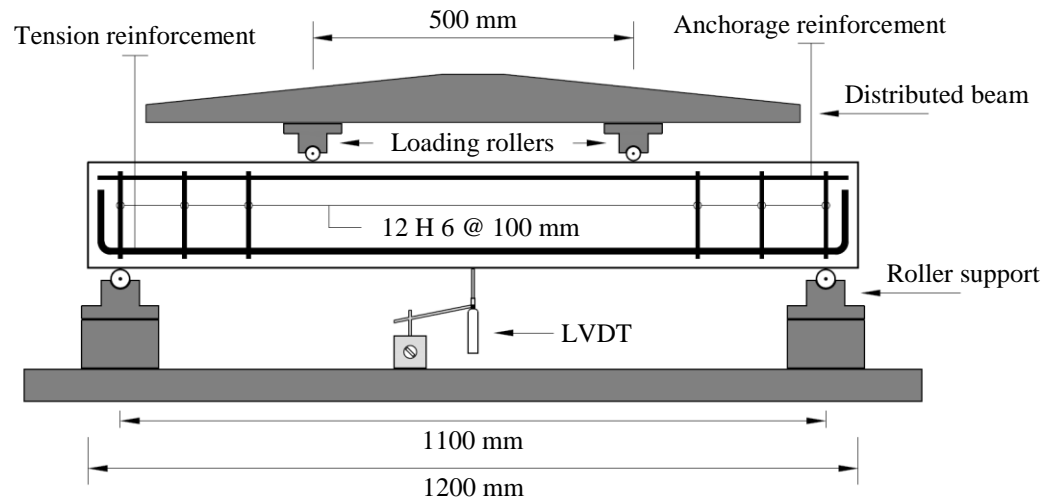
Table 5.4

Number and specifications of the flexure-critical beams with the new fibre.

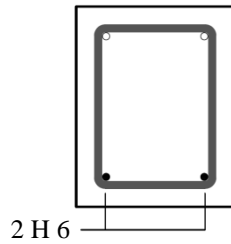
Fibre	f_m (MPa)	ρ (%)	V_f (%)	No. of specimens
Newly-designed	35, 45	0.31 ^a , 0.55 ^b	0.5	8

^a 2H6 as longitudinal reinforcement

^b 2H8 as longitudinal reinforcement



(a) Test setup



FC - 0.31

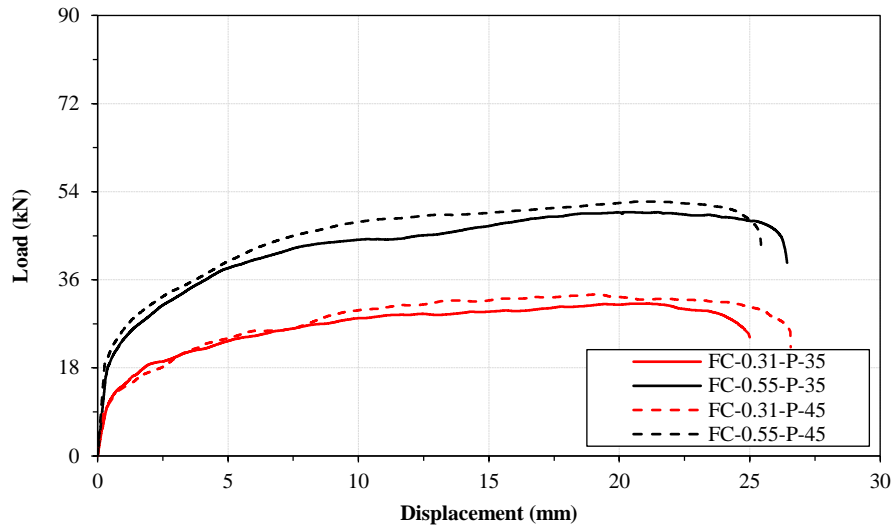
2 H 8

FC - 0.55

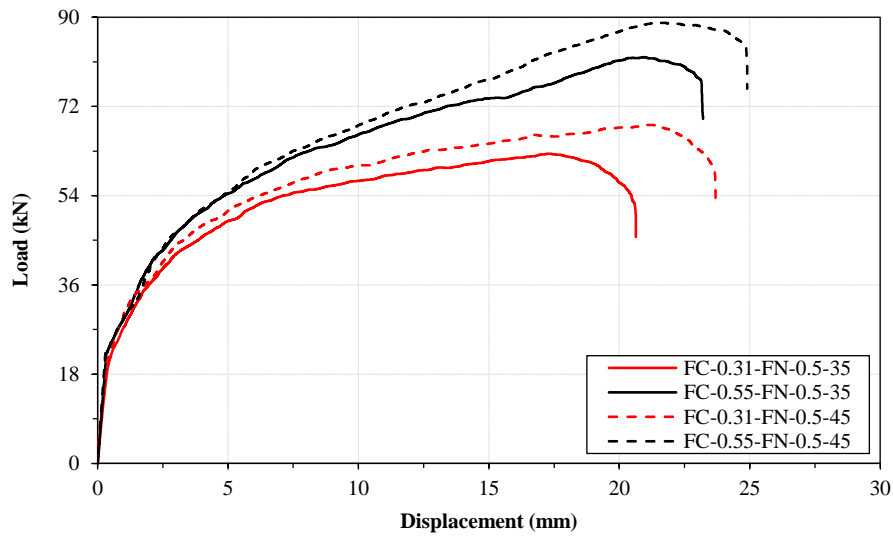
(b) Reinforcement layouts

Fig. 5.9. Flexure-critical SFRC beams testing.

From the results, it is evident that by increasing of the concrete compressive strength, the contribution of the fibre to the flexural capacity of fibrous RC beams is more pronounced. At the ultimate state, as the concrete strength increases, the neutral axis depth decreases which leads to a greater tensile area and consequently fibres contribute more effectively to the capacity.



(a) Non-fibrous concrete



(b) Fibrous concrete with newly-designed steel fibres

Fig. 5.10. Response of flexure-critical RC beams.

The failure patterns for selected beams ($f_m=45$ MPa and $V_f=0\%$ and 0.5%) are shown in **Figs. 5.11**.

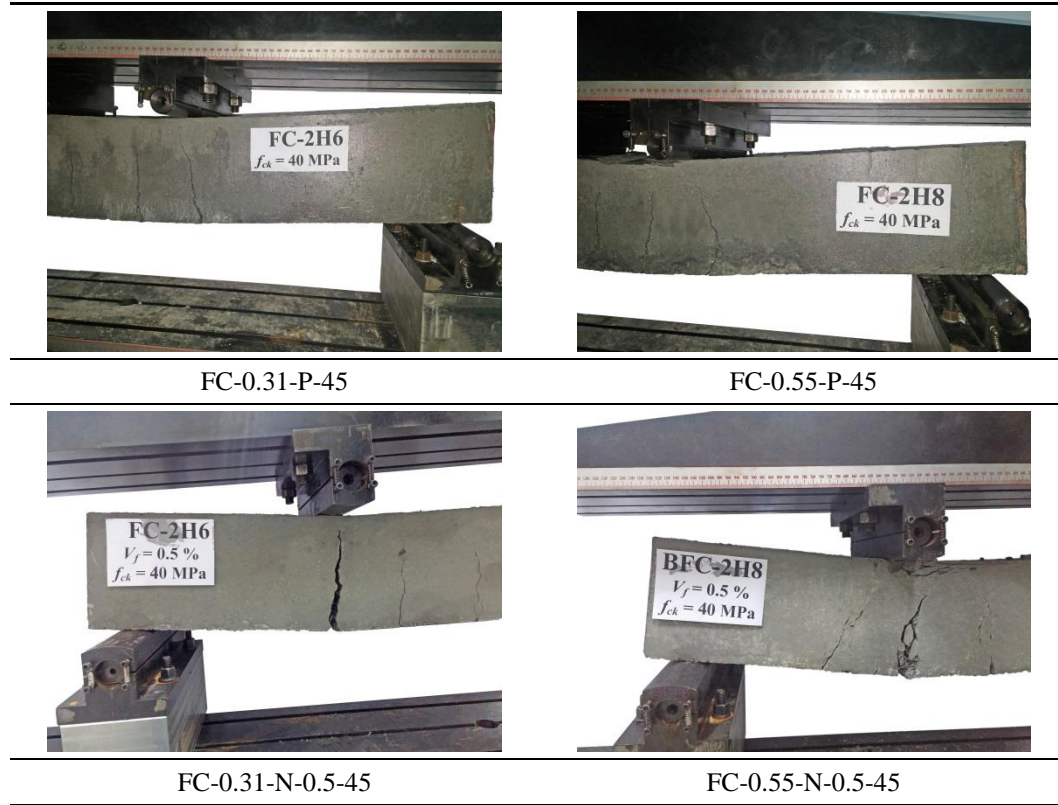


Fig. 5.11. Failure of flexure-critical RC beams with the newly-designed fibre.

5.2.4. FIBRES PERFORMANCE COMPARISON

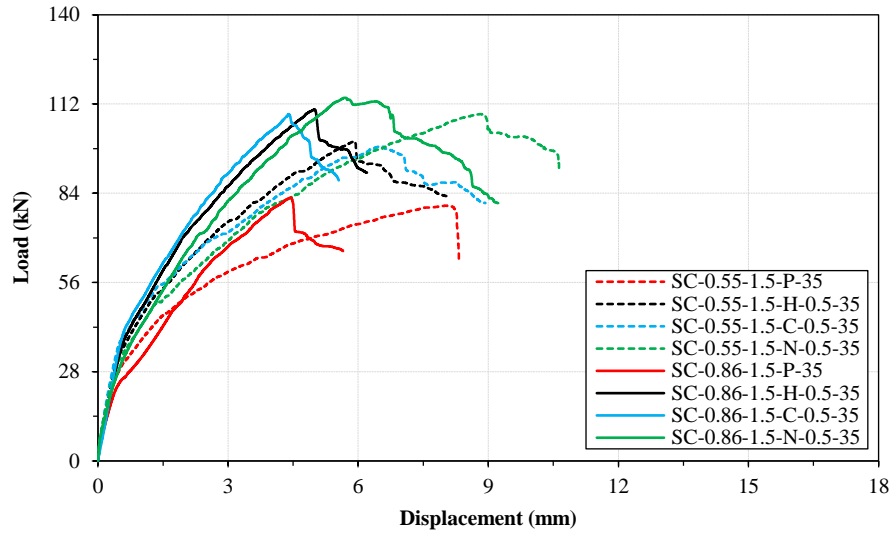
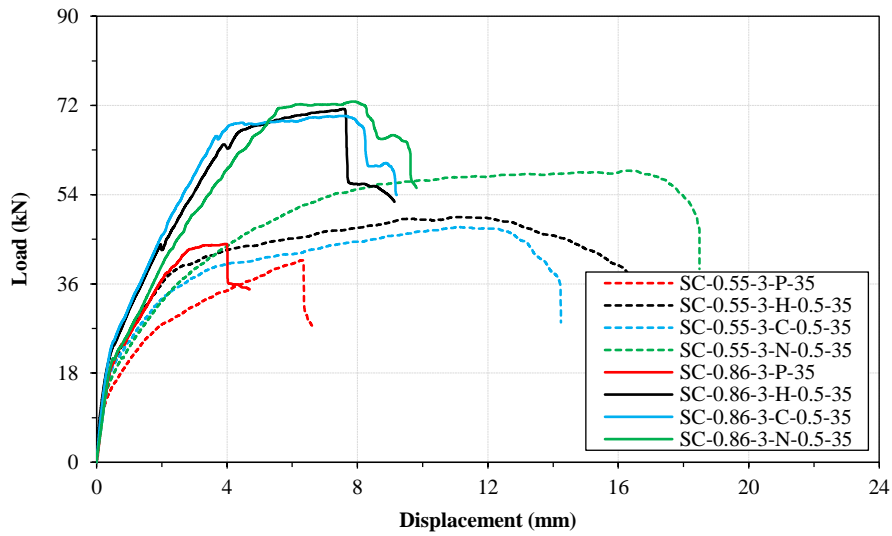
In this section, the structural performance of the newly-designed fibre and those available on the market (hooked-end and crimped steel fibres) are compared. To this end, a set of shear-critical and flexure-critical beams are designed, cast, and tested with fibrous concrete containing hooked-end and crimped steel fibres. The number and specifications of the beams are listed in **Table 5.5**.

The load-deflection response of the beams is shown in **Fig. 5.12** where the response of the corresponding beams with the newly-designed fibre (beams having identical characteristics except for the fibre type) and non-fibrous beams is included for the comparison purposes.

Table 5.5

Number and specifications of the beams with commercially available fibres.

Beam type	Fibre	f_m (MPa)	ρ (%)	V_f (%)	a/d (-)	No. of specimens
shear-critical	Hooked-end Crimped	35	0.55, 0.86	0.5	1.5, 3	8
flexure-critical	Hooked-end Crimped	35	0.31, 0.55	0.5	-	4

**(a)** $a/d = 1.5$ **(b)** $a/d = 3$ **Fig. 5.12.** Response of shear-critical RC beams with commercially available steel fibres.

As expected, the addition of hooked-end and crimped fibres increases the shear capacity of the beams and also in some cases it can alter the failure mode from shear to flexure. There is a negligible difference in the fibres performance, however the results indicate that hooked-end fibre possesses slightly higher performance. The results of the beams are summarised in **Table 5.6**.

Table 5.6

Results summary of the shear-critical beams with commercially available fibres.

Beam ID	Failure mode	Capacity (kN)	Improvement (%)
SC-0.55-1.5-P-35	Shear	80.1	-
SC-0.55-1.5-H-0.5-35	Shear	100.3	25
SC-0.55-1.5-C-0.5-35	Shear	98.7	23
SC-0.55-1.5-N-0.5-35	Shear	108.8	36
SC-0.86-1.5-P-35	Shear	82.6	-
SC-0.86-1.5-H-0.5-35	Shear	110.3	33
SC-0.86-1.5-C-0.5-35	Shear	108.8	32
SC-0.86-1.5-N-0.5-35	Shear	113.9	38
SC-0.55-3-P-35	Shear	40.8	-
SC-0.55-3-H-0.5-35	Flexure	49.5	-
SC-0.55-3-C-0.5-35	Flexure	47.5	-
SC-0.55-3-N-0.5-35	Flexure	58.8	-
SC-0.86-3-P-35	Shear	44.0	-
SC-0.86-3-H-0.5-35	Shear	71.3	62
SC-0.86-3-C-0.5-35	Shear	69.9	59
SC-0.86-3-N-0.5-35	Shear	72.8	65

As the reinforcement ratio increases, the fibres (hooked-end, crimped, newly-designed) more effectively contribute to the load bearing capacity; however the effect of fibre type decreases.

The failure patterns for selected shear-critical RC beams with commercially available fibres are shown in **Figs. 5.13**.

As expected, the addition of hooked-end and crimped steel fibre enhances the overall performance of RC beams including ductility through bridging mechanism and transferring stresses across the cracks. Specifically regarding the ductility (as seen in **Fig. 5.12**), the fibres effectiveness is more pronounced at the greater shear span to effective depth ratio ($a/d=3$).

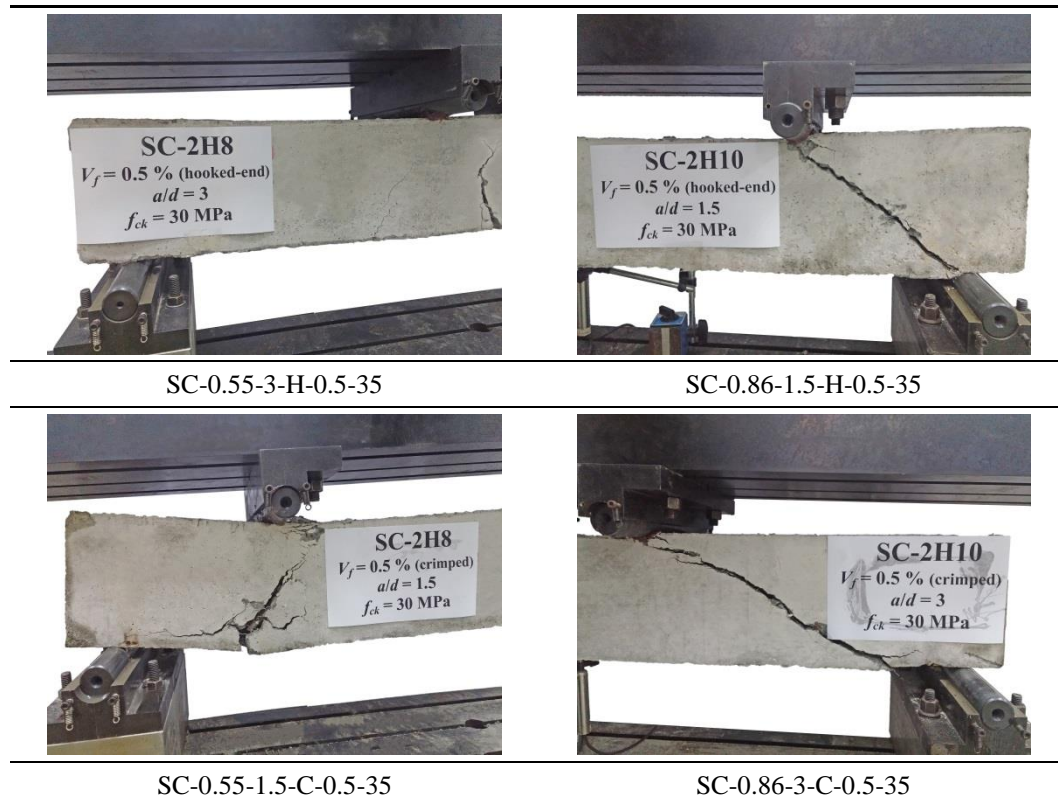
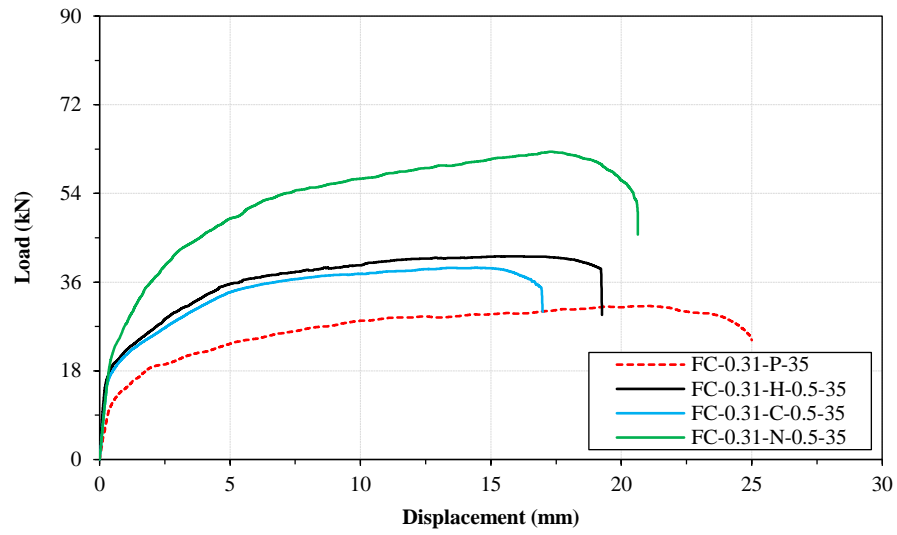


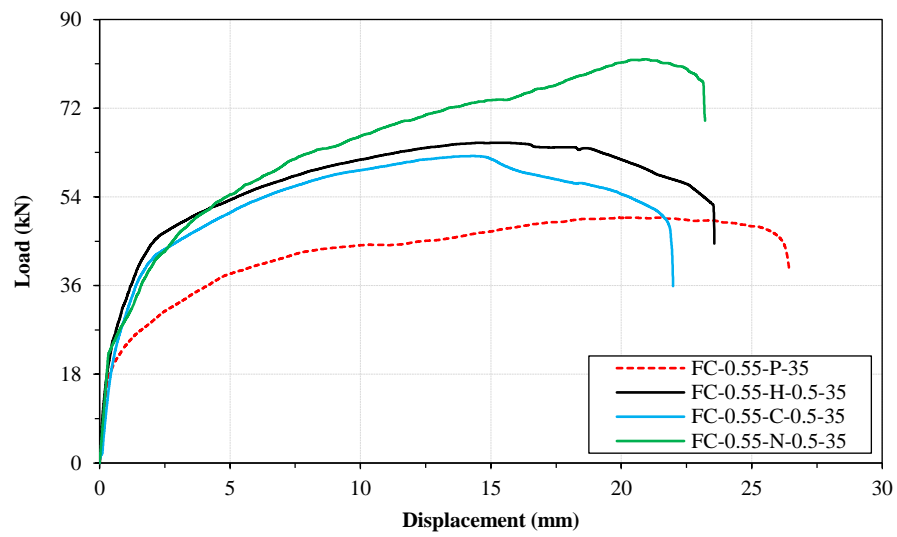
Fig. 5.13. Failure of shear-critical RC beams with commercially available fibres.

The load-deflection curves of the flexure-critical beams with hooked-end and crimped steel fibres are shown in **Fig. 5.14**. The responses of the corresponding beams with the new steel fibre (beams having identical characteristics except for the fibre type) and non-fibrous beams are included for comparison purposes. The flexural capacity of the SFRC beams and capacity enhancement relative to the capacity of the corresponding non-fibrous RC beams are summarised in **Table 5.7**.

From the results, it is evident that the addition of fibres generally enhances the flexural capacity of the beams. Furthermore, there is no considerable difference between hooked-end and crimped fibres, however the capacity enhancement is further pronounced for the new steel fibre.



(a) $\rho = 0.31\%$



(b) $\rho = 0.55\%$

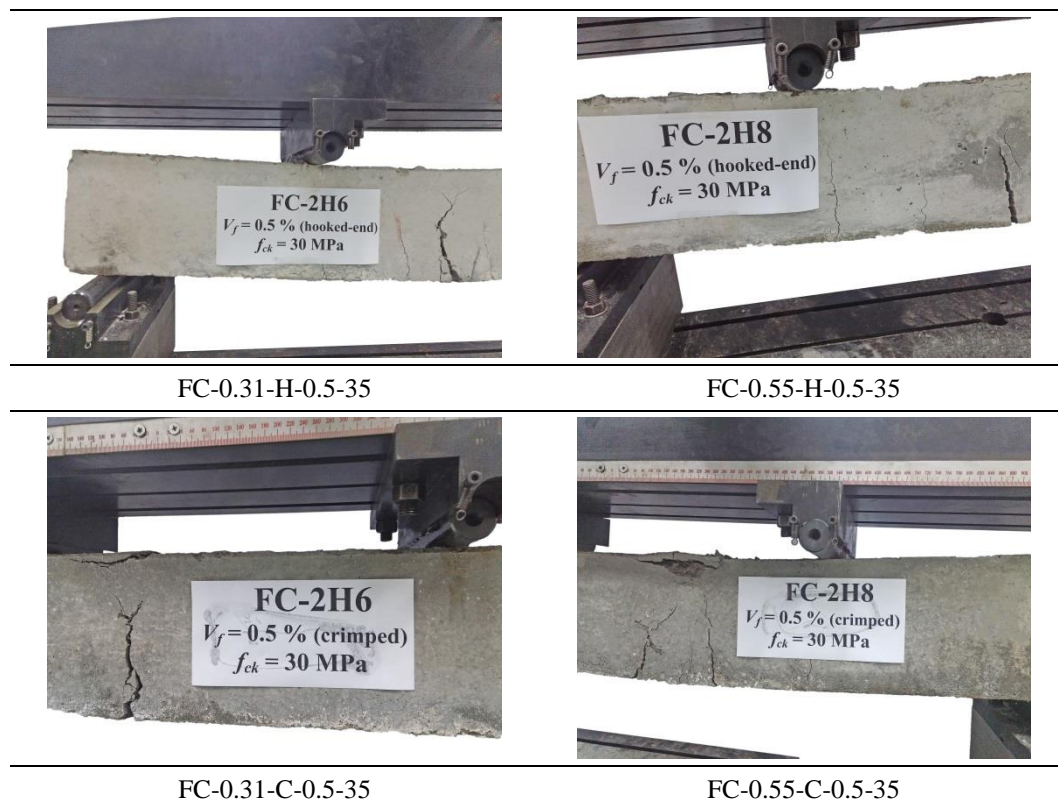
Fig. 5.14. Response of flexure-critical RC beams with commercially available steel fibres.

Table 5.7

Results summary of the flexure-critical beams with commercially available fibres.

Beam ID	Capacity (kN)	Improvement (%)
FC-0.31-P-35	31.1	-
FC-0.31-H-0.5-35	41.3	33
FC-0.31-C-0.5-35	38.9	25
FC-0.31-N-0.5-35	62.5	100
FC-0.55-P-35	49.8	-
FC-0.55-H-0.5-35	65.0	31
FC-0.55-C-0.5-35	62.3	25
FC-0.55-N-0.5-35	81.9	65

The failure patterns of flexure-critical RC beams with commercially available fibres are shown in **Figs. 5.15**.

**Fig. 5.14.** Failure of flexure-critical RC beams.

5.3. SUMMARY

To assess the structural performance of the newly-designed fibre, an experimental programme is conducted on shear- and flexure-critical RC beams. Moreover, in order to compare the effectiveness of the fibre compared with those available on the market, a series of RC beams with hooked-end and crimped fibres are tested.

In general, it was observed that the SFRC beams containing the spiral fibre experience multiple cracking especially developed adjacent to the critical sections thanks to the hardening behaviour the fibre. Hence, the post-peak load decay is more gradual leading to the increase in the members' ductility. In contrary, hooked-end and crimped steel fibres cannot lead to such level of increase in the ductility as spiral fibres due to the softening response. In an overall analysis, the results of this study indicate that the ductility of the SFRC beams containing the spiral and commercially available fibres increases by respective 27.1% and 19.2%, on average. Furthermore, the results reveal that the new fibre possesses more favourable contribution to the capacity of the beams compared with hooked-end and crimped fibres.

CHAPTER 6

DESIGN OF REINFORCED CONCRETE BEAMS WITH THE NEW FIBRE

6.1. INTRODUCTION

There are codes, regulations, and technical recommendations developed by the relevant institutes and societies (RILEM TC 162-TDF 2003, CEB-fib Model Code for Concrete Structures 2011, ACI Committee 544 2014) for SFRC members design with available fibres on the market. However, these regulations cannot be adopted for the design purpose of members containing the new fibre. Therefore, an experimental programme was conducted to propose relevant design equations and procedures for the new fibre (**Chapters 5 and 6**). In this chapter, the empirical equation proposed for the shear design of RC beams with the new fibre (**Section 5.2.2.1**) is employed for the design example. The flexural contribution of the fibre is back-calculated from the flexure-critical beams results using stress block analysis.

To compare the advantageous aspects of the employment of the newly-designed fibre, a reinforced concrete beam is designed with plain concrete and fibrous concrete with hooked-end and the new fibre. Then, the steel weight used for the different design schemes are compared.

6.2. ANALYSIS OF SECTION

The cross-section of a typical SFRC beam under bending with stress distribution is shown in **Fig. 6.1**. The contribution of the concrete in compression is estimated from the Whitney stress block (Mosley, Bungey et al. 2007, TR34 Concrete Society 2016). In addition, a uniform stress distribution over the fibrous concrete in tension zone is considered. It is evident that the inclusion of the newly-designed fibre enhances the concrete material properties in compression (in particular toughness and post-cracking response). However, in order to determine the accurate contribution of concrete in compression and tension, compression and direct tension tests are required. The formulation provided in TR34 Concrete Society (2016) are based on the existing steel fibres on the market. Hence, conservatively the response of concrete in compression is considered as plain concrete.

For equilibrium of the section:

$$F_{cc} = F_{ct} + F_{st} \quad (6.1)$$

where, F_{cc} is the compressive force in the concrete and F_{ct} and F_{st} are the tensile forces in the concrete and the steel bars, respectively and are calculated using **Eq. (6.2)**.

$$\begin{aligned} F_{cc} &= 0.85f_c / \gamma_c \times 0.8x \times b \\ F_{ct} &= f_{ctm,pc} \times (h - x) \times b \\ F_{st} &= \sigma_{st} A_s = \frac{E_s \varepsilon_{st}}{\gamma_s} A_s \end{aligned} \quad (6.2)$$

Moreover, for equilibrium, the ultimate moment, M , must be balanced by the moment of resistance of the section, as **Eq. (6.3)**.

$$M = F_{cc} \times 0.6x + F_{st} (d - x) + F_{ct} (h - x) / 2 \quad (6.3)$$

Using the section analysis, the tensile stresses in the fibrous concrete (with hooked-end and new fibres) for flexure-critical RC beams (see Section 5.2.3) are estimated. The results are summarised in **Table 6.1**.

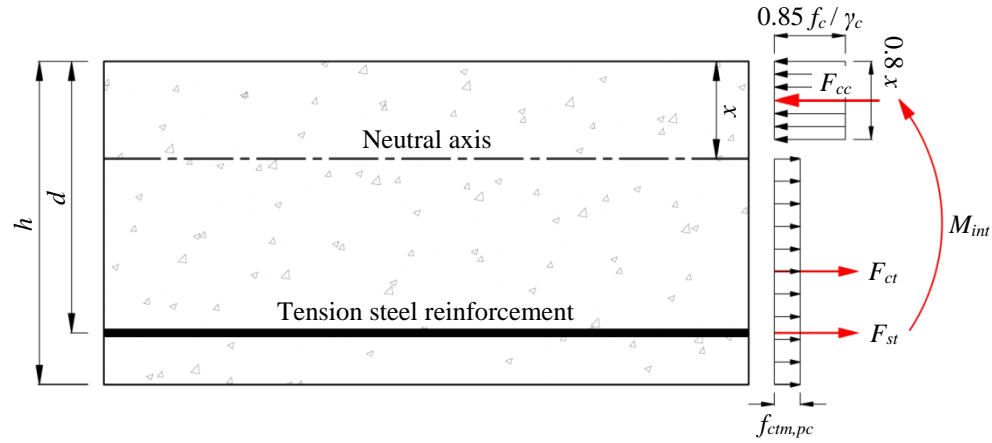


Fig. 6.1. Stress block of RC section with steel fibre.

Table 6.1

Tensile contribution of fibrous concrete to the flexural performance of RC beams.

Beam ID	Ultimate flexural capacity (kN.m)	Concrete tensile stress ($f_{ctm,pc}$) (MPa)
Spirally deformed fibre (SD-9-1.45-0.4-40)		
FC-0.31-N-0.5-35	9.37	3.81
FC-0.55-N-0.5-35	12.29	3.98
FC-0.31-N-0.5-45	10.24	4.25
FC-0.55-N-0.5-45	13.33	4.46
Commercially available fibres (hooked-end and crimped)		
FC-0.31-H-0.5-35	6.19	1.5
FC-0.55-H-0.5-35	9.75	1.96
FC-0.31-C-0.5-35	5.84	1.27
FC-0.55-C-0.5-35	9.34	1.65

6.3. DESIGN EXAMPLE FOR BEAMS WITH THE NEW STEEL FIBRE

A simply supported rectangular concrete beam carries a two-point load of 500 kN over a clear span (L) of 5000 mm where the shear span (a , distance between a reaction and the nearest load point) is 1400 mm. The dimensions of the beam cross-section, respectively width (b), height (h), and effective depth (d) are 350 mm, 600 mm, and 550 mm (as seen in Fig. 6.2).

It is desired to design the singly reinforced section (reinforcement layout) of the concrete beam with:

1. Plain concrete (non-fibrous concrete).
2. Fibre reinforced concrete with hooked-end and the newly-designed steel fibre and volume content (V_f) of 0.5%.

The specified characteristic cylinder strength of concrete (f_c) and yield strength of steel (f_y) are 50 MPa and 500 MPa, respectively. The maximum tension reinforcement ratio is 1.25%. Consider the partial factors of safety for concrete and steel (γ_c and γ_s) 1.5 and 1.15, respectively.

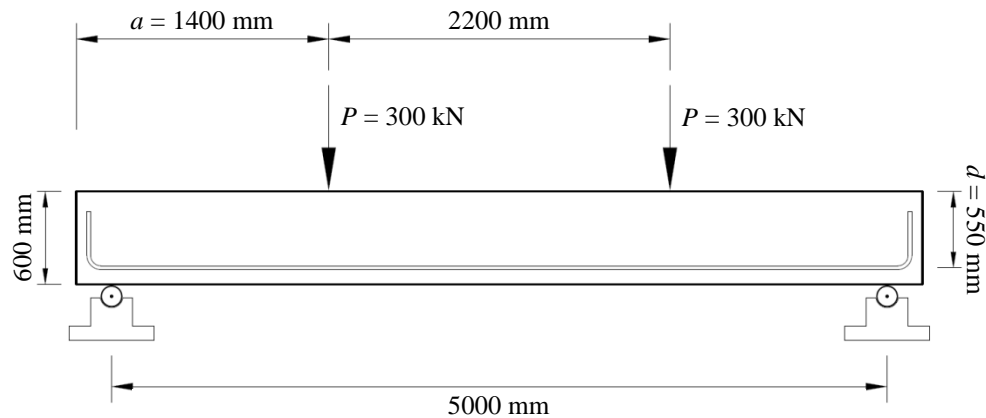


Fig. 6.2. Dimensions of the RC beam for three different design schemes.

At the end, compare the weight of steel used for the different schemes.

Reinforced Concrete Beam with Plain Concrete

FLEXURAL DESIGN

External bending moment (M): $M = P \times a = 300 \text{ kN} \times 1.4 \text{ m} = 420 \text{ kN.m}$

Yield strain of steel (ϵ_y): $\epsilon_y = f_y / (\gamma_c \times E_s) = 500 / (1.15 \times 200000) = 0.00217$

An iterative process is performed as follows:

1. Assuming neutral axis depth (x) and reinforcement ratio (ρ).
2. According to the assumed values for x and ρ , the internal forces (concrete compressive and tensile steel forces, respectively F_{cc} and F_{st}) are calculated.
3. The process continues until:
 - The section equilibrium is satisfied; $F_{cc} = F_{st}$
 - The moment of resistance of the section ($M_{int.}$) equals or greater than M ; $M_{int.} \geq M$,

It is found that $x = 105.5 \text{ mm}$ and $\rho = 1\%$ ($A_s = 1925 \text{ mm}^2$), as below:

Strain and stress of tension steel reinforcement (ϵ_{st} and σ_{st}):

$$\epsilon_{st} = \epsilon_{cu} \times (d - x) / x = 0.0035 \times (550 - 105.5) / 105.5 = 0.0147 \geq 0.00217; \text{Yielded}$$

$$\sigma_{st} = f_{yd} = f_y / \gamma_s = 500 / 1.15 = 434.78 \text{ MPa}$$

Tensile force in steel:

$$F_{st} = f_{yd} A_s = 434.78 \times 1925 = 836.95 \text{ kN}$$

Compressive force in concrete:

$$F_{cc} = 0.85 f_c / \gamma_c \times 0.8 x \times b = 0.85 \times 50 / 1.5 \times 0.8 \times 105.5 \times 350 = 836.97 \text{ kN}$$

$F_{cc} = F_{st} \rightarrow$ The section equilibrium is satisfied.

$M_{int.} = F_{cc} z = 836.97 \times (550 - 42.2) = 425 \text{ kN.m} \geq M \rightarrow$ Provided reinforcement is sufficient.

SHEAR DESIGN

Maximum shear force (V_{Ed}): $V_{Ed} = 300 \text{ kN}$

Shear capacity of concrete ($V_{Rd,c}$):

$$V_{Rd,c} = \left[12\kappa (100\rho f_c)^{1/3} \right] b d \geq \left[0.035\kappa^3 f_c^{1/2} \right] b d = 136.42 \text{ kN}$$

$$\kappa = \left(1 + \sqrt{200/d} \right) \leq 2$$

$V_{Rd,c} \leq V_{Ed} \rightarrow$ Shear reinforcement is required.

Angle of diagonal concrete strut (θ): $22^\circ \leq \theta \leq 45^\circ$

Maximum design value of the shear which can be resisted by the concrete strut ($V_{Rd,max}$):

$$V_{Rd,max} = \frac{0.36 b d (1 - f_c / 250) f_{ck}}{(\cot \theta + \tan \theta)}$$

$$\left. \begin{array}{l} V_{Rd,max(22)} = 962.8 \text{ kN} \\ V_{Rd,max(45)} = 1386.0 \text{ kN} \end{array} \right\} \rightarrow V_{Ed} \leq V_{Rd,max(22)} \rightarrow \theta = 22^\circ$$

Required shear reinforcement (A_{sw} / S):

$$\left. \begin{array}{l} \frac{A_{sw}}{S} = \frac{V_{Ed}}{0.78 d f_y \cot \theta} = 0.56 \\ \frac{A_{sw,min}}{S} = \frac{0.08 f_c^{0.5} b}{f_y} = 0.396 \end{array} \right\} \rightarrow \text{H10 @ 280 mm}$$

Steel Fibre-Reinforced Concrete Beam with Hooked-end Fibre

FLEXURAL DESIGN

The tensile contribution of fibrous concrete with hooked-end fibre ($f_{ctm,pc}$) can be taken from **Table 6.1**.

Determine A_s and x which satisfy the section equilibrium and result in the moment of resistance of the section ($M_{int.}$) equals 420 kN.m.

$$F_{cc} = F_{st} + F_{ct}$$

$$0.85 f_c / \gamma_c \times 0.8 x \times b = \sigma_{st} A_s + f_{ctm,pc} \times (h - x) \times b$$

$$M_{int.} = F_{cc} \times 0.6 x + F_{st} (d - 0.4 x) + f_{ctm,pc} \times (h - x)^2 \times b / 2$$

$$M_{int.} = 0.85 f_c / \gamma_c \times 0.8 x \times b \times 0.6 x + \sigma_{st} A_s (d - 0.4 x) + f_{ctm,pc} \times (h - x)^2 \times b / 2$$

It is found that $x = 121.5$ mm and $A_s = 1462$ mm², as below:

SHEAR DESIGN

The shear contribution of fibrous concrete with hooked-end fibre is estimated to be $v_{fc,pre.} = 1.18$ MPa by shear design equation proposed by Shahnewaz and Shahria Alam (2014). The excess of shear is resisted by shear link.

$$V_{Ed} - v_{fc,pre.} \times bd = 300 - 227 = 73 \text{ kN}$$

$$V_{Rd,max} = \frac{0.36 b d (1 - f_{ck} / 250) f_{ck}}{(\cot \theta + \tan \theta)}$$

$$\left. \begin{array}{l} V_{Rd,max(22)} = 962.8 \text{ kN} \\ V_{Rd,max(45)} = 1386.0 \text{ kN} \end{array} \right\} \rightarrow 73 \leq V_{Rd,max(22)} \rightarrow \theta = 22^\circ$$

Required shear reinforcement (A_{sw} / S):

$$\frac{A_{sw}}{S} = \frac{V_{Ed}}{0.78 d f_y \cot \theta} = 0.14 \rightarrow \text{H 6 @ 400 mm}$$

Steel Fibre-Reinforced Concrete Beam with the Newly-designed Fibre

FLEXURAL DESIGN

The tensile contribution of fibrous concrete with the newly-designed fibre ($f_{ctm,pc}$) can be taken from **Table 6.1**.

Determine A_s and x which satisfy the section equilibrium and result in the moment of resistance of the section ($M_{int.}$) equals 420 kN.m.

$$F_{cc} = F_{st} + F_{ct}$$

$$0.85 f_c / \gamma_c \times 0.8 x \times b = \sigma_{st} A_s + f_{ctm,pc} \times (h - x) \times b$$

$$M_{int.} = F_{cc} \times 0.6 x + F_{st} (d - 0.4 x) + f_{ctm,pc} \times (h - x)^2 \times b / 2$$

$$M_{int.} = 0.85 f_c / \gamma_c \times 0.8 x \times b \times 0.6 x + \sigma_{st} A_s (d - 0.4 x) + f_{ctm,pc} \times (h - x)^2 \times b / 2$$

It is found that $x = 136.5$ mm and $A_s = 1006$ mm², as below:

SHEAR DESIGN

The shear contribution of fibrous concrete with hooked-end fibre is estimated to be $v_{fc,pre.} = 2.72$ MPa by **Eq. (5.4)**.

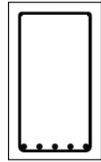
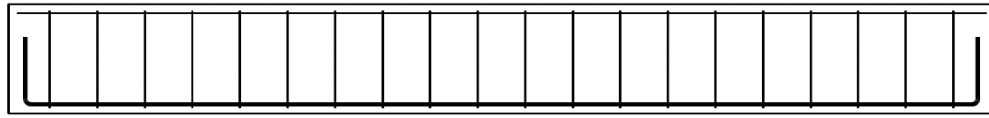
$v_{fc,pre.} \geq v_{Ed} \rightarrow$ No shear links is required.

The shear and longitudinal reinforcement layouts of the three different design schemes are shown in **Fig. 6.3**. The steel weight used for the schemes are summarised in **Table 6.2**.

Table 6.2
Steel weight used for the RC beam design.

Reinforcement type		Shear link (kg)	Longitudinal (kg)	Fibre (kg)	Sum (kg)
Concrete type	Plain	22.1	94.8	-	116.9
	Hooked-end	5.5	72.0	51.7	129.2
	Fibrous Newly-designed	-	49.6	51.7	101.3

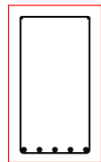
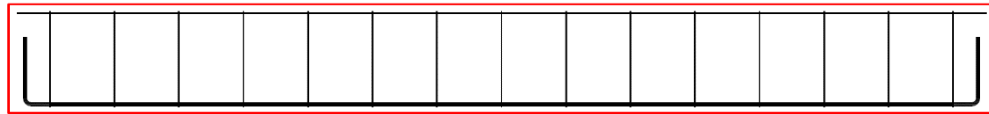
As seen, the employment of the new fibre reduces the total weight steel required.



Tension reinforcement:
 $A_s = 1925 \text{ mm}^2$
 5 H 22

Shear reinforcement:
 $A_{sw} / S = 0.56$
 H 10 @ 280 mm

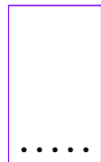
(a) Non-fibrous RC beam



Tension reinforcement:
 $A_s = 1462 \text{ mm}^2$
 5 H 20

Shear reinforcement:
 $A_{sw} / S = 0.56$
 H 6 @ 400 mm

(b) Steel fibre-reinforced concrete beam with 0.5% hooked-end fibre



Tension reinforcement:
 $A_s = 1006 \text{ mm}^2$
 5 H 16

Shear reinforcement:
Not required

(c) Steel fibre-reinforced concrete beam with 0.5% new fibre

Fig. 6.3. Reinforcement schemes.

6.4. SUMMARY

From the flexure-critical RC beams, the contribution of the fibrous concrete is estimated using a stress block analysis. Using the proposed shear equations for the newly-designed fibre (**Eq. (5.4)**) and hooked-end fibre (Shahnewaz and Shahria Alam 2014), a reinforced concrete beam is designed with three different schemes (non-fibrous concrete and fibrous concrete with hooked-end and the new fibres). The results indicate that, it is possible to fully replace the shear links and considerably reduce the demand for longitudinal reinforcement (about 50%).

CHAPTER 7

CONCLUSIONS AND RECOMMENDATIONS

7.1. CONCLUSIONS

The main objective of this project is to develop a new generation of steel fibres with a high-performance response in normal concrete to advance structural applications of such discontinuous fibres in the design of Reinforced Concrete (RC) members. For this purpose, a numerical Finite Element (FE) model for the single fibre pullout problem is proposed and validated which is employed to develop and optimise the new steel fibre. The newly-designed steel fibre possesses favourable pullout characteristics including slip-hardening response in normal concrete. A material testing programme (including compression and flexural tests) is designed and undertaken to assess the effectiveness of the newly-designed steel fibre to the enhancement of the concrete material properties. Following the fibre development and material testing phase, a structural testing programme is performed to examine the contribution of the new fibre to the shear and flexural response of RC beams. Finally, shear and flexural design procedures for RC beams with the new fibre are proposed.

Findings of the structural testing programme reveal that the newly-designed fibres effectively contribute to capacities of SFRC members which reduce the total steel reinforcement required and results in more viable designs.

From this research programme, the following conclusions are drawn:

1. The proposed FE model can accurately predict the fibre pullout performance. Considering the comparative advantages of simulations over experimental test, the model can be used as an efficient tool to examine the fibres performance.
2. Contrary to the commercially available steel fibres such as hooked-end and crimped fibres, the fully-deformed steel fibres with a spiral configuration show slip-hardening response in normal concrete. The pullout mechanism of such fibres is significantly influenced by the spiral geometrical properties (number of turns, and outer diameter and length of the spirals).
3. Considering the diameter and strength of the steel wire, the pullout load of a given spirally deformed fibre can be estimated by **Eq. (3.13)** which is an empirical equation.
4. The optimised spirally deformed steel fibre (SD-9-1.45-0.4-40) possesses favourable pullout characteristics including high pullout stiffness and fibre efficiency.
5. The flexure test results of fibrous concrete prisms indicate that the new fibre more effectively contributes to the flexural characteristics of the concrete specimens compared with those reinforced with hooked-end and crimped steel fibres. For example, the flexural toughness (up to 10 mm deflection) of SFRC prisms with $f_m = 35$ MPa having 0.5% of the new fibre is 1.7 and 2.1 times of those containing hooked-end and crimped fibres, respectively. It is shown that with the addition of 0.5% newly-designed fibre, the deflection-hardening response can be achieved.
6. Findings of the structural testing phase reveal that the new fibre effectively contributes to the shear bearing capacity of fibrous RC members. The fibre shows superior contribution to the flexural capacity of the members compared with hooked-end and crimped fibres where large deformations and wide cracks are expected owing to its slip-hardening characteristics. Overall, the new fibre simultaneously enhances the shear and flexural capacities of the members; hence it can eliminate/reduce the demand for conventional reinforcement. Regarding

the example provided in **Section 6.3**, the new fibre reduces the total steel weight required (steel fibre and conventional reinforcement) by 15% compared with the layout with conventional reinforcement.

7.2. RECOMMENDATIONS FOR FUTURE WORKS

The following recommendations for future works are made:

1. An investigation on the effect of coating and embossment of the fibre surface could be undertaken to further improve the performance of the fibre.
2. The fibre production process affects the material strength of the fibre. A study should be performed to characterise the effects and propose methods to avoid material strength reduction.
3. To fully quantify the effect of the new fibre on the concrete behaviour in pure compression and tension using displacement-controlled equipment and testing fixtures.
4. In material and structural testing, wider ranges for the experiment parameters including cylinder strength of concrete (f_m), fibre volume content (V_f), longitudinal reinforcement ratio (ρ), and shear span to effective depth (a/d) should be investigated to further assess the effectiveness of the fibre in the enhancement of the concrete properties and structural performance of RC members.
5. The tension stiffening effect in the presence of both rebar and the new fibre is suggested to be investigated.
6. In order to examine the scale effects in the fibrous RC beams, specimens with various dimensions should be tested. In the programme, half-scale and full-scale beams are suggested for the investigation.
7. In order to examine the scale effects in the fibrous RC beams, specimens with various dimensions should be tested. In the programme, half-scale and full-scale beams are suggested for the investigation.

8. SFRC components subjected to dynamic and cyclic loading should be investigated to assess the effect of the new fibre on the seismic response of structures.
9. It is recommended to compare the results of different design approaches from the available codes with the procedure adopted in this thesis.

REFERENCES

(!!! INVALID CITATION !!! (Wang, Backer et al. 1987, Bernard 2002, ACI Committee 544 2014)).

Abbas, A. A., S. M. Syed Mohsin and D. M. Cotsovos (2016). "A simplified finite element model for assessing steel fibre reinforced concrete structural performance." Computers & Structures **173**: 31-49.

Abu-Lebdeh, T., S. Hamoush and B. Zornig (2010). "Rate Effect on Pullout Behavior of Steel Fibers Embedded in Very-High Strength Concrete." American Journal of Engineering and Applied Sciences **3**(2): 454-463.

ACI 318-08 (2008). Building Code Requirements for Structural (ACI 318-08) and Commentary. ACI Committee 318. Farmington Hills, MI, American Concrete Institute.

ACI Committee 544 (2014). Fiber Reinforced Concrete. Design and Construction of Steel Fiber-Reinforced Precast Concrete Tunnel Segments. Detroit, USA, American Concrete Institute.

Adamantia, A. and P.-M. Gustavo (2013). "Experimental Study on the Seismic Behavior of High- Performance Fiber-Reinforced Concrete Low-Rise Walls." ACI Structural Journal **110**(5): 767-778.

Adhikary, S. D., B. Li and K. Fujikake (2014). "Effects of High Loading Rate on Reinforced Concrete Beams (with Appendix)." ACI Structural Journal **111**(3): 651-660.

Álvarez, A. B. (2013). Characterisation and modelling of SFRC elements. Ph.D. Dissertation, Polytechnic University of Catalonia.

Alwan, J. M., A. E. Naaman and P. Guerrero (1999). "Effect of mechanical clamping on the pull-out response of hooked steel fibers embedded in cementitious matrices." Concrete Science and Engineering **1**: 15-25.

ANSYS® Academic Research (2015). Release 16.1, Help System, ANSYS Inc. Canonsburg (PA, USA).

Aoude, H., M. Belghiti, W. D. Cook and D. Mitchell (2012). "Response of Steel Fiber-Reinforced Concrete Beams with and without Stirrups." ACI Structural Journal **109**(3): 359-368.

Armelin, S. H. and N. Banthia (1997). "Predicting the Flexural Postcracking Performance of Steel Fiber Reinforced Concrete from the Pullout of Single Fibers." ACI Materials Journal **94**(1): 14.

Ashour, S. A., G. S. Hasanain and F. F. Wafa (1992). "Shear Behavior of High-Strength Fiber-Reinforced Concrete Beams." ACI Structural Journal **89**(2): 176-184.

ASTM C127 - 15 (2015). Standard Test Method for Relative Density (Specific Gravity) and Absorption of Coarse Aggregate. West Conshohocken, PA, ASTM International.

ASTM C128 - 15 (2015). Standard Test Method for Relative Density (Specific Gravity) and Absorption of Fine Aggregate. West Conshohocken, PA, ASTM International.

ASTM C143/C143M - 15a (2015). Standard Test Method for Slump of Hydraulic-Cement Concrete. West Conshohocken, PA, American Society for Testing and Materials (ASTM) International.

ASTM C192/C192M - 16a (2016). Standard Practice for Making and Curing Concrete Test Specimens in the Laboratory. West Conshohocken, PA, American Society for Testing and Materials (ASTM) International.

ASTM C566 - 13 (2013). Standard Test Method for Total Evaporable Moisture Content of Aggregate by Drying. West Conshohocken, PA, ASTM International.

ASTM C1609/C1609M - 12 (2012). Standard test method for flexural performance of fiber-reinforced concrete (using beam with third-point loading). West Conshohocken, PA, American Society for Testing and Materials (ASTM) International.

ASTM E8/E8M - 13a (2013). Standard Test Methods for Tension Testing of Metallic Materials. West Conshohocken, PA, American Society for Testing and Materials (ASTM) International.

Banthia, N., M. Azabi and M. Pigeon (1993). "Restrained shrinkage cracking in fibre reinforced cementitious composites." Materials and Structures **26**(7): 405-413.

Banthia, N., V. Bindiganavile and J. N. John Jones (2012). "Fiber-reinforced concrete in precast concrete applications: Research leads to innovative products." PCI Journal **57**(3): 33-46.

Banthia, N. and J.-F. Trottier (1994). "Concrete Reinforced with Deformed Steel Fibers, Part I: Bond-Slip Mechanisms." ACI Materials Journal **91-M43**(5): 435-446.

Banthia, N. and J.-F. Trottier (1995). "Test Methods for Flexural Toughness Characterization of Fiber Reinforced Concrete: Some Concerns and a Proposition." ACI Materials Journal **no. 92-M06**: 10.

Bathe, K. J. (1996). Finite element procedures. Englewood Cliffs, New Jersey, Prentice-Hall.

Batson, G. (1976). "Steel Fiber Reinforced Concrete." Materials Science and Engineering **25**: 53-58.

- Behbahani, H. (2011). Steel Fiber Reinforced Concrete: A Review. Proceedings of the International Conference on Structural Engineering Construction and Management. Kandy, Sri Lanka.
- Belytschko, T. and I. S. Yeh (1993). "The splitting pinball method for contact-impact problems." Computer Methods in Applied Mechanics and Engineering **105**(3): 375-393.
- Blanco, A., S. Cavalaro, A. de la Fuente, S. Grünwald, C. B. M. Blom and J. C. Walraven (2014). "Application of FRC constitutive models to modelling of slabs." Materials and Structures **48**(9): 2943-2959.
- Blanco, A., P. Pujadas, S. Cavalaro, A. de la Fuente and A. Aguado (2014). "Constitutive model for fibre reinforced concrete based on the Barcelona test." Cement and Concrete Composites **53**: 327-340.
- Boshoff, W. P., V. Mechtcherine and G. P. A. G. van Zijl (2009). "Characterising the time-dependant behaviour on the single fibre level of SHCC: Part 2: The rate effects on fibre pull-out tests." Cement and Concrete Research **39**(9): 787-797.
- Brandt, A. M. (2008). "Fibre reinforced cement-based (FRC) composites after over 40 years of development in building and civil engineering." Composite Structures **86**(1-3): 3-9.
- BS EN 12390-1 (2012). Testing hardened concrete; Part 1: Shape, dimensions and other requirements for specimens and moulds, British Standards (BS) Publication.
- BS EN 12390-3 (2009). Testing hardened concrete; Part 3: Compressive strength of test specimens, British Standards (BS) Publication.
- BS EN 12620 (2013). Aggregates for concrete, British Standards (BS) Publication.
- Building Research Establishment (1997). Design of normal concrete mixes, second edition, BRE Press Publications.
- Carnovale, D. J. (2013). Behaviour and Analysis of Steel and Macro-Synthetic Fibre Reinforced Concrete Subjected to Reversed Cyclic Loading: A Pilot Investigation. Master's of Applied Science Thesis, University of Toronto.
- CEB-fib Model Code for Concrete Structures (2011). Lausanne, International Federation for Structural Concrete (fib).
- CEN Eurocode 2 (2004). Design of concrete structures - Part 1-1: General rules and rules for buildings, EN1992-1-1:2004:E.
- Chanvillard, G. (1999). "Modeling the pullout of wire-drawn steel fibers." Cement and Concrete Research **29**(7): 1027-1037.

Chao, S.-H., J.-S. Cho, N. B. Karki, D. R. Sahoo and N. Yazdani (2011). "FRC Performance Comparison: Uniaxial Direct Tensile Test, Third-Point Bending Test, and Round Panel Test." ACI Special Publication **276**: 1-20.

Chao, S.-H., W.-C. Liao, T. Wongtanakitcharoen and A. E. Naaman (2007). Large Scale Tensile Tests of High Performance Fiber Reinforced Cement Composites. Fifth International RILEM Workshop on High Performance Fiber Reinforced Cement Composites (HPFRCC5). H. W. Reinhardt and A. E. Naaman. Paris: 77-86.

Chin, C. S. and R. Y. Xiao (2012). Experimental and Nonlinear Finite Element Analysis of Fiber-Cementitious Matrix Bond-Slip Mechanism. High Performance Fiber Reinforced Cement Composites 6. G. Parra-Montesinos, H. Reinhardt and A. E. Naaman. Netherlands, Springer. **2**: 145-152.

Cook, R. D., D. S. Malkus and M. E. Plesha (1989). Concept and applications of finite element analysis. 3rd edition. New York, John Wiley.

Curiger, P. (1995). Glassfibre reinforced concrete: Practical design and structural analysis. Düsseldorf: Germany, Beton-Verlag.

Dupont, D. and L. Vandewalle (2003). "Shear Capacity of Concrete Beams Containing Longitudinal Reinforcement and Steel Fibers." ACI Special Publication **216**: 79-94.

Fanella, D. A. and A. E. Naaman (1985). "Stress-Strain Properties of Fiber Reinforced Mortar in Compression." ACI Journal **82**(4): 475-483.

Ferrara, L. and A. Meda (2006). "Relationships between fibre distribution, workability and the mechanical properties of SFRC applied to precast roof elements." Materials and Structures/Materiaux et Constructions **39**(288): 411-420.

Filiatrault, A., S. Pineau and H. Jules (1995). "Seismic Behavior of Steel-Fiber Reinforced Concrete Interior Beam-Column Joints." ACI Structural Journal **92**(5): 543-552.

GB 175 (2007). Common portland cement, Chinese Standard Publication.

Georgiadi-Stefanidi, K., E. Mistakidis, D. Pantousa and M. Zygomas (2010). "Numerical modelling of the pull-out of hooked steel fibres from high-strength cementitious matrix, supplemented by experimental results." Construction and Building Materials **24**(12): 2489-2506.

Goldberg, D. E. (1989). Genetic Algorithms in Search, Optimization, and Machine Learning. USA, Addison-Wesley Professional.

Grzybowski, M. and S. P. Shah (1990). "Shrinkage Cracking on Fiber Reinforced Concrete." ACI Materials Journal **87**(2): 138-148.

Gu, R. J., P. Murty and Q. Zheng (2002). "Use of penalty variable in finite element analysis of contacting objects." Computers & Structures **80**(31): 2449-2459.

Hallquist, J. O. (1998). LS-DYNA Theoretical Manual.

Imam, M., L. Vandewalle and F. Mortelmans (1995). "Shear-moment analysis of reinforced high strength concrete beams containing steel fibres." Canadian Journal of Civil Engineering **22**: 462-470.

Jamee, M. (2013). Effect of hooked-end fibers pull-out behavior on the mechanical properties of fiber reinforced concrete. M.Sc. Thesis, Shahrood University of Technology.

Khaloo, A. R. and N. Kim (1997). "Influence of Concrete and Fiber Characteristics on Behavior of Steel Fiber-Reinforced Concrete under Direct Shear." ACI Materials Journal **94**(6): 592-600.

Khuntia, M., B. Stojadinovic and S. Goel (1999). "Shear Strength of Normal and High-Strength Fiber-Reinforced Concrete Beams without Stirrups." ACI Structural Journal **96**(2): 282-290.

Kim, D.-J., A. E. Naaman and S. El-Tawil (2009). "High Performance Fiber Reinforced Cement Composites with Innovative Slip Hardening Twisted Steel Fibers." International Journal of Concrete Structures and Materials **3**(2): 119-126.

Kim, W., J. Kim and Y.-K. Kwak (2016). "Evaluation of flexural strength prediction of reinforced concrete beams with steel fibres." Journal of Structural Integrity and Maintenance **1**(4): 156-166.

Kwak, Y., M. O. Eberhard, W. Kim and J. Kim (2002). "Shear Strength of Steel Fiber-Reinforced Concrete Beams without Stirrups." ACI Structural Journal **99**(4): 530-538.

Laranjeira, F., C. Molins and A. Aguado (2010). "Predicting the pullout response of inclined hooked steel fibers." Cement and Concrete Research **40**(10): 1471-1487.

Laursen, T. A. and J. C. Simo (1993). "Algorithmic Symmetrization of Coulomb Frictional Problems Using Augmented Lagrangians." Computers Methods in Applied Mechanics and Engineering **108**(1&2): 133-146.

Lee, S.-C., J.-Y. Cho and F. J. Vecchio (2013). Constitutive model for steel fibre reinforced concrete in tension. 8th International Conference on Fracture Mechanics of Concrete and Concrete Structures. J. G. M. V. Mier, G. Ruiz, C. Andrade, R. C. Yu and X. X. Zhang. Toledo-Spain, University of Castilla La-Mancha.

Lee, S.-C., J.-Y. Cho and F. J. Vecchio (2013). "Simplified Diverse Embedment Model for Steel Fiber Reinforced Concrete Elements in Tension." ACI Materials Journal **110-M36**: 403-412.

- Lee, Y., S.-T. Kang and J.-K. Kim (2010). "Pullout behavior of inclined steel fiber in an ultra-high strength cementitious matrix." Construction and Building Materials **24**(10): 2030-2041.
- Li, C. Y. and B. Mobasher (1998). "Finite Element Simulations of Fiber Pullout Toughening in Fiber Reinforced Cement Based Composites." Advanced Cement Based Materials **7**(3-4): 123-132.
- Li, V. C., R. Ward and A. M. Hamza (1992). "Steel and Synthetic Fibers as Shear Reinforcement." ACI Materials Journal **89**(5): 499-508.
- Lin, W. J. V. and S. T. Quek (2007). Tensile Behavior of Twisted Steel Fiber Reinforced Cementitious Composite. 32nd Conference on Our World in Concrete & Structures. Singapore.
- Luo, J. W. (2014). Behaviour and Analysis of Steel Fibre-Reinforced Concrete under Reversed Cyclic Loading. Master of Applied Science Thesis, University of Toronto.
- MacGregor, J. G. (1992). Reinforced Concrete Mechanics and Design. Englewood Cliffs, NJ, Prentice-Hall, Inc.
- Mansour, A., J. Srebric and B. J. Burley (2007). "Development of straw-cement composite sustainable building material for low-cost housing in Egypt." Applied Sciences Research **3**(11): 1571-1580.
- Mansur, M. A., K. C. G. Ong and P. Paramasivam (1986). "Shear Strength of Fibrous Concrete Beams Without Stirrups." Journal of Structural Engineering **112**(9): 2066-2079.
- MATLAB version 8.5.1 (2015). Natick, Massachusetts, The MathWorks Inc.
- Mechtcherine, V. (2013). "Novel cement-based composites for the strengthening and repair of concrete structures." Construction and Building Materials **41**: 365-373.
- Michels, J., D. Waldmann, S. Maas and A. Zürbes (2012). "Steel fibers as only reinforcement for flat slab construction – Experimental investigation and design." Construction and Building Materials **26**(1): 145-155.
- Mobasher, B., M. Bakhshi and C. Barsby (2014). "Backcalculation of residual tensile strength of regular and high performance fiber reinforced concrete from flexural tests." Construction and Building Materials **70**: 243-253.
- Mohamed, N. and M. L. Nehdi (2016). "Rational finite element assisted design of precast steel fibre reinforced concrete pipes." Engineering Structures **124**: 196-206.
- Mosley, B., J. Bungey and R. Hulse (2007). Reinforced Concrete Design to Eurocode 2, Palgrave macmillan.

- Naaman, A. E. (1985). "Fiber Reinforcement for Concrete." Concrete International **7**(3): 21-25.
- Naaman, A. E. (1987). High Performance Fiber Reinforced Cement Composites. International Association for Bridge and Structural Engineering (IABSE) Symposium on Concrete Structures for the Future. Paris - Versailles: 371-376.
- Naaman, A. E. (2003). "Engineered Steel Fibers with Optimal Properties for Reinforcement of Cement Composites." Journal of Advanced Concrete Technology **1**(3): 241-252.
- Naaman, A. E. (2007). "Deflection-Softening and Deflection-Hardening FRC Composites: Characterization and Modeling." Special Publication **248**: 53-66.
- Naaman, A. E. and H. Najm (1991). "Bond-Slip Mechanisms of Steel Fibers in Concrete." ACI Materials Journal **88-M17**: 135-145.
- Naaman, A. E., G. G. Namur, J. M. Ahvan and H. S. Najm (1991 a). "Fiber pullout and bond slip. II: Experimental validation." Journal of Structural Engineering **117**(9): 2791-2800.
- Naaman, A. E., G. G. Namur, J. M. Alwan and H. S. Najm (1991 b). "Fiber pullout and bond slip. I: Analytical study." Journal of Structural Engineering **117**(9): 2769-2790.
- Naaman, A. E. and H. W. Reinhardt (2003). Setting the stage: Toward performance based classification of frc composites. high performance fiber reinforced cement composites (HPFRCC-4). R. H. Naaman AE, RILEM Publications, Pro.: 1-4.
- Naaman, A. E. and H. W. Reinhardt (2006). "Proposed classification of HPFRC composites based on their tensile response." Materials and Structures **39**(5): 547-555.
- Narayanan, R. and I. Y. S. Darwish (1988). "Fiber Concrete Beams in Shear." ACI Structural Journal **85**(2): 141-149.
- Neves, R. D. and J. C. O. F. d. Almeida (2005). "Compressive behaviour of steel fibre reinforced concrete." Structural Concrete **6**(1): 1-8.
- Noghabai, K. (2000). "Beams of fibrous concrete in shear and bending: experiment and model." Journal of Structural Engineering **126**(2): 243-251.
- Özcan, D. M., A. Bayraktar, A. Şahin, T. Haktanir and T. Türker (2009). "Experimental and finite element analysis on the steel fiber-reinforced concrete (SFRC) beams ultimate behavior." Construction and Building Materials **23**(2): 1064-1077.
- Parra-Montesinos, G. J. (2006). "Shear Strength of Beams with Deformed Steel Fibers." ACI Concrete International **28**(11): 57-66.

- Richardson, A. E. and S. Landless (2009). "Synthetic fibres and steel fibres in concrete with regard to bond strength and toughness." Built Environment Research Papers **2**(2): 128-140.
- RILEM TC 162-TDF (2003). Test and design methods for steel fibre reinforced concrete, sigma-epsilon-design method, RILEM Publications SARL.
- Romualdi, J. P. and G. B. Batson (1963). "Mechanics of Crack Arrest in Concrete." Journal of the Engineering Mechanics Division, ASCE **89**(3): 147-168.
- Romualdi, J. P. and J. A. Mandel (1964). "Tensile strength of concrete affected by uniformly dispersed and closely spaced short lengths of wire reinforcement." Journal of the American Concrete Institute **61**: 657-672.
- Sarmiento, E. V., M. A. N. Hendriks, M. R. Geiker and T. Kanstad (2016). "Modelling the influence of the fibre structure on the structural behaviour of flowable fibre-reinforced concrete." Engineering Structures **124**: 186-195.
- Setkit, M. (2012). Seismic Behaviour of Slender Coupling Beams Constructed With High-Performance Fibre-Reinforced Concrete. Ph.D. Dissertation, University of Michigan.
- Shah, S. P. and B. V. Rangan (1971). "Fiber Reinforced Concrete Properties." ACI Journal Proceedings **68**(2): 126-137.
- Shahnewaz, M. d. and M. Shahria Alam (2014). "Improved Shear Equations for Steel Fiber-Reinforced Concrete Deep and Slender Beams." ACI Structural Journal **111-S71**: 851-871.
- Sharma, A. K. (1986). "Shear Strength of Steel Fiber Reinforced Concrete Beams." ACI Journal **83**(4): 624-628.
- Shin, S. W., J. G. Oh and S. K. Ghosh (1994). Shear Behavior of Laboratory-Sized High-Strength Concrete Beams Reinforced with Bars and Steel Fibers. Fiber Reinforced Concrete: Developments and Innovations, SP-142. J. I. Daniel and S. P. Shah, American Concrete Institute, Farmington Hills, MI: 181-200.
- Singh, H. (2015). "Flexural Modeling of Steel Fiber-Reinforced Concrete Members: Analytical Investigations." Practice Periodical on Structural Design and Construction **20**(4): 1-10.
- Soranakom, C. and B. Mobasher (2007 (a)). "Closed-Form Solutions for Flexural Response of Fiber-Reinforced Concrete Beams." Journal of Engineering Mechanics **133**(8): 931-941.
- Soranakom, C. and B. Mobasher (2007 (b)). "Closed-Form Moment-Curvature Expressions for Homogenized Fiber-Reinforced Concrete." ACI Materials Journal **104-M39**: 351-359.

Sujivorakul, C., A. M. Waas and A. E. Naaman (2000). "Pullout Response of a Smooth Fiber with an End Anchorage." Journal of Engineering Mechanics **126**(9): 986-993.

Swamy, R. N. and H. M. Bahia (1985). "The Effectiveness of Steel Fibers as Shear Reinforcement." ACI Concrete International **7**(3): 35-40.

Swamy, R. N., R. Jones and A. T. P. Chiam (1993). "Influence of Steel fibers on the Shear Resistance of Lightweight Concrete I-Beams." ACI Structural Journal **90**(1): 103-114.

TR34 Concrete Society (2016). Concrete industrial ground floors: a guide to design and construction. 3rd Edition. Technical Report.

Tsai, J. H., A. Patra and R. Wetherhold (2005). "Finite element simulation of shaped ductile fiber pullout using a mixed cohesive zone/friction interface model." Composites Part A: Applied Science and Manufacturing **36**(6): 827-838.

Vandewalle, L. (1999). Influence of Tensile Strength of Steel Fiber on Toughness of High Strength Concrete. Proceedings of the Third International Workshop on High-Performance Cement Composites, Mainz, Germany, RILEM Publications, Bagneux, France.

Wang, Y., S. Backer and V. C. Li (1987). "An experimental study of synthetic fibre reinforced cementitious composites." Journal of Materials Science **22**(12): 4281-4291.

Willam, K. J. and E. P. Warnke (1975). Constitutive models for the triaxial behavior of concrete. Proceedings of the International Assoc. for Bridge and Structural Engineering, Bergamo, Italy.

Wille, K., S. El-Tawil and A. E. Naaman (2014). "Properties of Strain Hardening Ultra High Performance Fiber Reinforced Concrete (UHP-FRC) under Direct Tensile Loading." Cement and Concrete Composites.

Wille, K. and A. E. Naaman (2012). "Pullout Behavior of High-Strength Steel Fibers Embedded in Ultra-High-Performance Concrete." ACI Materials Journal **109-M46**: 479-488.

Wille, K. and A. E. Naaman (2013). "Effect of Ultra-High-Performance Concrete on Pullout Behavior of High-Strength Brass-Coated Straight Steel Fibers." ACI Materials Journal **No. 110-M41**: 451-462.

Wriggers, P., T. Vu Van and E. Stein (1990). "Finite element formulation of large deformation impact-contact problems with friction." Computers and Structures **37**(3): 319-331.

Yang, Q. S., Q. H. Qin and X. R. Peng (2003). "Size effects in the fiber pullout test." Composite Structures **61**(3): 193-198.

Zile, E. and O. Zile (2013). "Effect of the fiber geometry on the pullout response of mechanically deformed steel fibers." Cement and Concrete Research **44**: 18-24.

Zollo, R. F. (1997). "Fiber-reinforced concrete - an overview after 30 years of development." Cement and Concrete Composites **19**(2): 16.

APPENDICES

APPENDIX 3.1

CODE FOR SIMULATION OF SPIRALLY DEFORMED STEEL FIBRE

!-----
! ENTRIES AND CONSTANTS
!-----

! GEOMETRY

! Concrete Cylinder (Matrix)

*ASK,RM,Radius of the Concrete Cylinder (Matrix),
*ASK,HM,Height of the Concrete Cylinder (Matrix),
*ASK,II,Initial Imperfection of the Concrete Tunnel,

! Steel Fibre

*ASK,DSF,Diameter of the Steel Fibre,
*ASK,DSPSF,Diameter of the Spiral Path of the Steel Fibre,
*ASK,NTSF,Number of Turns of the Steel Fibre,

! MATERIAL PROPERTIES

! Concrete (Matrix)

*ASK,fc,Unconfined Strength of Concrete (Matrix) (MPa),
*ASK,ft,Tensile Strength of Concrete (Matrix) (MPa),
*ASK,Ec,Elastic Modulus of Concrete (Matrix) (GPa),
*ASK,vc,Poisson s Ratio of Concrete (Matrix),
*ASK,OST,Open Shear Transfer Coefficient (Matrix),
*ASK,CST, Closed Shear Transfer Coefficient (Matrix),

! Steel (Reinforcement)

*ASK,fy,Yield Strength of Steel (Fibre) (MPa),
*ASK,Es,Elastic Modulus of Steel (Fibre) (GPa),
*ASK,fu,Ultimate Strength of Steel (Fibre) (MPa),
*ASK,eus,Ultimate Strain of Steel (Fibre),
*ASK,ff,Fracture Strength of Steel (Fibre) (MPa),
*ASK,ef,Fracture Strain of Steel (Fibre),
*ASK,vs,Poisson s Ratio of Steel (Fibre),

! CONTACT PROPERTIES

*ASK,MU,Friction Coefficient,
*ASK,C,Contact Cohesion,

*ASK,NPS,Normal Penalty Stiffness (Constant),
 *ASK,PT,Penetration Tolerance (Constant),
 *ASK,MFS,Maximum Friction Stress,
 *ASK,SDR,Static to Dynamic Friction Ratio,
 *ASK,EDC,Exponential Decay Coefficient,
 *ASK,CA,If the Contact Algorithm is Augmented Method Enter 1 and If It is Penalty Method Enter 2,2

! MESHING SIZE

! Steel (Fibre)

*ASK,MSFR,Division Number of Steel Fibre Radius,
 *ASK,MSFC,Division Number of Steel Fibre Circumference (A Quarter of Fibre Circumference),
 *ASK,NDWSP,Division Number of a Whole Spiral Path (Even Number),
 *ASK,MEPSP,Division Number of Each Part of Spiral Path,

! Concrete Matrix

*ASK,MCC,Division Number of Concrete Matrix Circumference (A Quarter of Concrete Cylinder Circumference),

! MATERIAL CONSTANTS

$E_c = E_c * 1000$

$E_s = E_s * 1000$

$e_0 = (2 * f_c) / E_c$

$e_1 = (0.3 * f_c) / E_c$

$e_2 = (e_0 - e_1) / 9$

*DIM,fc1,ARRAY,9,1,1, , ,

*DIM,ec1,ARRAY,9,1,1, , ,

*DO,i,1,9,1

$ec1(i) = e_1 + i * e_2$

$fc1(i) = (E_c * ec1(i)) / (1 + (ec1(i) / e_0) * (ec1(i) / e_0))$

*ENDDO

!-----

! ARRAY AND CONSTANT

!-----

*DIM,X,ARRAY,NDWSP+1,1,1, , ,

*DIM,Y,ARRAY,NDWSP+1,1,1, , ,

*DIM,Z,ARRAY,NDWSP+1,1,1, , ,

!-----

! CONFIGURATIONS

!-----

*AFUN,DEG

/PMETH,OFF,0

KEYW,PR_SET,1

KEYW,PR_STRUC,1

KEYW,PR_FLUID,0

KEYW,PR_MULT,0

/GO

! /COM,
! /COM,Preferences for GUI filtering have been set to display:
! /COM, Structural

!-----
! PRE-PROCESSOR
!-----

/PREP7

! SELECTING ELEMENTS & KEY-OPTION AND DEGREES OF FREEDOM

ET,1,SOLID65
ET,2,SOLID185

KEYOPT,1,1,0
KEYOPT,1,3,0
KEYOPT,1,5,0
KEYOPT,1,6,0
KEYOPT,1,7,0
KEYOPT,1,8,0

KEYOPT,2,2,0
KEYOPT,2,3,0
KEYOPT,2,6,0
KEYOPT,2,10,0

! REAL CONSTANT

! for Non-Element

R,1, , ,
R,2, , ,

! MATERIAL PROPERTY

! Concrete

MPTEMP,,,,,,,,
MPTEMP,1,0
MPDATA,EX,1,,Ec
MPDATA,PRXY,1,,vc
TB,MISO,1,1,10,0
TBTEMP,0
TBPT,,0,0
TBPT,,e1,(0.3*fc)
TBPT,,ec1(1),fc1(1)
TBPT,,ec1(2),fc1(2)
TBPT,,ec1(3),fc1(3)
TBPT,,ec1(4),fc1(4)
TBPT,,ec1(5),fc1(5)
TBPT,,ec1(6),fc1(6)
TBPT,,ec1(7),fc1(7)
TBPT,,ec1(8),fc1(8)

TBPT,,ec1(9),fc1(9)

TB,CONC,1,1,9,
TBTEMP,0
TBDATA,,OST,CST,ft,fc,,
TBDATA,,,,,,,,
! Steel

MPTEMP,,,,,,,,
MPTEMP,1,0
MPDATA,EX,2,,Es
MPDATA,PRXY,2,,vs

TB,KINH,2,1,3,0
TBTEMP,0
TBPT,,fy/Es,fy
TBPT,,eus,fu
TBPT,,ef,ff

! MODELLING

! The Steel Fibre
! Spiral Path

! Key points

*DO,i,1,NDWSP+1,1
 $X(i) = (DSPSF/2) * \cos(((NTSF*360)/NDWSP)*(i-1))$
 $Y(i) = (DSPSF/2) * \sin(((NTSF*360)/NDWSP)*(i-1))$
*ENDDO

*DO,i,1,NDWSP+1,1

$Z(i) = ((i-1)/NDWSP) * HM$
*ENDDO

*Do,i,1,NDWSP+1,1

K, ,X(i),Y(i),Z(i), ,

*ENDDO

! Work Plane Configuration

wpoff,(DSPSF/2),0,0
CSYS,4

! Bottom Area of the Steel Fibre

! Key points

K, ,DSF/2, ,z(1),
K, , ,DSF/2,z(1),

! Radius and Circumference

```

LSTR,1,(NDWSP+2)
LSTR,1,(NDWSP+3)
LARC,(NDWSP+2),(NDWSP+3),1,DSF/2,

```

! Mesh Size

```

FLST,5,2,4,ORDE,2
FITEM,5,1
FITEM,5,2
CM,_Y,LINE
LSEL,, , ,P51X
CM,_Y1,LINE
CMSEL,,_Y
LESIZE,_Y1, , ,MSFR, , , ,0

```

```

FLST,5,1,4,ORDE,1
FITEM,5,3
CM,_Y,LINE
LSEL,, , ,P51X
CM,_Y1,LINE
CMSEL,,_Y
LESIZE,_Y1, , ,MSFC, , , ,0

```

! Area

```

FLST,2,3,4
FITEM,2,1
FITEM,2,3
FITEM,2,2
AL,P51X

```

! Reflection

```

FLST,3,1,5,ORDE,1
FITEM,3,1
ARSYM,X,P51X, , , ,0,0
FLST,3,2,5,ORDE,2
FITEM,3,1
FITEM,3,-2
ARSYM,Y,P51X, , , ,0,0

```

! Extrusion of the Steel Fibre

```

FLST,2,4,5,ORDE,4
FITEM,2,1
FITEM,2,2
FITEM,2,3
FITEM,2,4
VEXT,P51X, , ,X(2)-X(1),Y(2)-Y(1),Z(2)-Z(1),,,,

```

*DO,i,1,(NDWSP-1),1

```

FLST,2,4,5,ORDE,4
FITEM,2,5+(i-1)*16

```



```

FITEM,2,9+(i-1)*16
FITEM,2,13+(i-1)*16
FITEM,2,17+(i-1)*16
VEXT,P51X, , ,X(i+2)-X(i+1),Y(i+2)-Y(i+1),Z(i+2)-Z(i+1),,,,

*ENDDO
! No. of Volumes

*Get,NVSF,VOLU,0,NUM,MAXD

! Material Attributes of the Steel Fibre

VATT,2,2,2,0

! Mesh

*DO,i,1,NDWSP+1,1

ALLSEL,ALL
LSEL,S,LOC,Z,(HM/NDWSP)*(i-(1-II)),(HM/NDWSP)*(i-(2-II))
LESIZE,ALL, , ,MEPSP, , , ,0

*ENDDO

ALLSEL,ALL

! No. of Areas

*Get,NASF,VOLU,0,NUM,MAXD

! The Concrete Matrix
! Spiral Path

! Work Plane Configuration

wpoff,HM,0,0
CSYS,4

! Key points

K, , ,
K, ,(DSF/2)-II*DSF, ,Z(1),
K, , ,(DSF/2)-II*DSF,Z(1),

! Radius and Circumference

LSTR,NDWSP+2+9+(NDWSP*12)+2,NDWSP+2+9+(NDWSP*12)+3
LSTR,NDWSP+2+9+(NDWSP*12)+2,NDWSP+2+9+(NDWSP*12)+4
LARC,NDWSP+2+9+(NDWSP*12)+3,NDWSP+2+9+(NDWSP*12)+4,NDWSP+2+9+(NDWSP*12)+2,
(DSF/2)-II*DSF,

! Mesh Size

FLST,5,2,4,ORDE,2
FITEM,5,NDWSP*12+(NDWSP+1)*12+1
FITEM,5,NDWSP*12+(NDWSP+1)*12+2

```

```

CM,_Y,LINE
LSEL, , , P51X
CM,_Y1,LINE
CMSEL,,_Y
LESIZE,_Y1, , MSFR, , , , 0

```

```

FLST,5,1,4,ORDE,1
FITEM,5,NDWSP*12+(NDWSP+1)*12+3
CM,_Y,LINE
LSEL, , , P51X
CM,_Y1,LINE
CMSEL,,_Y
LESIZE,_Y1, , MSFC, , , , 0

```

! Bottom Area

```

FLST,2,3,4
FITEM,2,NDWSP*12+(NDWSP+1)*12+1
FITEM,2,NDWSP*12+(NDWSP+1)*12+2
FITEM,2,NDWSP*12+(NDWSP+1)*12+3
AL,P51X

```

! Reflection

```

ASEL,S,LOC,X,-DSF,2*DSF

```

```

ARSYM,X,ALL, , , 0,0

```

```

ARSYM,Y,ALL, , , 0,0

```

```

ALLSEL,ALL

```

! Extrusion

```

ASEL,S,LOC,X,(-DSPSF-DSF)/2-DSF,(DSPSF+DSF)/2+DSF

```

```

VEXT,ALL, , , X(2)-X(1),Y(2)-Y(1),Z(2)-Z(1),,,,

```

```

*DO,i,1,(NDWSP-1),1

```

```

ALLSEL,ALL

```

```

ASEL,S,LOC,X,(-DSPSF-DSF)/2-2.5*DSF,(DSPSF+DSF)/2+2.5*DSF

```

```

ASEL,R,LOC,Z,(HM/NDWSP)*i-II,(HM/NDWSP)*i+II

```

```

VEXT,ALL, , , X(i+2)-X(i+1),Y(i+2)-Y(i+1),Z(i+2)-Z(i+1),,,,

```

```

*ENDDO

```

```

ALLSEL,ALL

```

! Material Attributes

```

VSEL,S,LOC,X,(-DSPSF-DSF)/2-DSF,(DSPSF+DSF)/2+DSF
VATT,1,1,1,0

```

! The Spiral Concrete Tunnel Group

VSEL,R, , ,ALL
CM,SCT,VOLU
CMSEL,A,SCT
! Mesh

*DO,i,1,NDWSP+1,1

ALLSEL,ALL
LSEL,S,LOC,X,(-DSPSF-DSF)/2-DSF,(DSPSF+DSF)/2+DSF
LSEL,R,LOC,Z,(HM/NDWSP)*(i-(1-II)),(HM/NDWSP)*(i-(2-II))
LESIZE,ALL, , ,MEPSP, , , ,0

*ENDDO

! Unselect Volume

ALLSEL,ALL
VSEL,U, , ,ALL

! Concrete Cylinder

CYL4, , ,RM, , , ,HM/2-(HM/NDWSP)
wpoff,0,0,HM/2
CYL4, , ,RM, , , ,HM/2

! Material Attributes

VATT,1,1,1,0

! Group the Concrete Cylinder

VSEL,R, , ,ALL
CM,CC,VOLU
CMSEL,A,CC

! Mesh Sizes

! Work Plane Configuration

wpoff,0,0,-(HM/2)
CSYS,4

! Cross-Sections

LSEL,R,LOC,Z,-II,+II
LESIZE,ALL, , ,MCC, , , ,0
ALLSEL,ALL
CMSEL,S,CC
ASLV,S
LSLA,S
LSEL,R,LOC,Z,(HM/2)-(HM/NDWSP)-II,(HM/2)+II
LESIZE,ALL, , ,MCC, , , ,0
ALLSEL,ALL

```

CMSEL,S,CC
ASLV,S
LSLA,S
LSEL,R,LOC,Z,HM-II,HM+II
LESIZE,ALL,,MCC,,,,0

! Heights

ALLSEL,ALL
CMSEL,S,CC

ASLV,S
LSLA,S

LSEL,R,LOC,X,RM-II,RM+II
LSEL,R,LOC,Z,-II,(HM/2)-(HM/NDWSP)+II

LESIZE,ALL,,(NDWSP*MEPSP)/2-MEPSP,,,,0

ALLSEL,ALL
CMSEL,S,CC

ASLV,S
LSLA,S

LSEL,R,LOC,X,-RM-II,-RM+II
LSEL,R,LOC,Z,-II,(HM/2)-(HM/NDWSP)+II

LESIZE,ALL,,(NDWSP*MEPSP)/2-MEPSP,,,,0

ALLSEL,ALL
CMSEL,S,CC

ASLV,S
LSLA,S

LSEL,R,LOC,X,RM-II,RM+II
LSEL,R,LOC,Z,(HM/2)-II,HM+II

LESIZE,ALL,,(NDWSP*MEPSP)/2,,,,0

ALLSEL,ALL
CMSEL,S,CC

ASLV,S
LSLA,S

LSEL,R,LOC,X,-RM-II,-RM+II
LSEL,R,LOC,Z,(HM/2)-II,HM+II

LESIZE,ALL,,(NDWSP*MEPSP)/2,,,,0

ALLSEL,ALL

```

! Subtract Spiral Concrete Tunnel From Concrete Cylinders

FLST,2,2,6,ORDE,2
FITEM,2,(NVSF*2)+1
FITEM,2,(NVSF*2)+2
FLST,3,NVSF,6,ORDE,2
FITEM,3,NVSF+1
FITEM,3,-(NVSF*2)

VSBV,P51X,P51X, ,DELETE,DELETE

! Mesh Sizes
! Spiral Path

LSEL,S,LOC,X,-DSF/2-II,DSF/2+II
LSEL,R,LOC,Z,-II,II
LESIZE,ALL, , ,MSFC, , , ,0
ALLSEL,ALL

*DO,i,1,NDWSP,1

wpoff,X(i+1)-X(i),Y(i+1)-Y(i),Z(i+1)-Z(i)
LSEL,S,LOC,X,-DSF/2-II,DSF/2+II
LSEL,R,LOC,Z,-II,II
LESIZE,ALL, , ,MSFC, , , ,0
ALLSEL,ALL

*ENDDO

! Mesh

ALLSEL,ALL
CM,_Y1,VOLU
CHKMSH,'VOLU'
CMSEL,S,_Y
VSWEEP,ALL

! Merge Coincident Nodes

ESEL,S,MAT,,1
VSEL,S,MAT,,1
ASLV,S
LSLA,S
KSLI,S
NSLE,S
NSLV,R,1
NUMMRG,NODE,II/2, , ,LOW

ALLSEL,ALL

ESEL,S,MAT,,2
VSEL,S,MAT,,2
ASLV,S
LSLA,S
KSLI,S

NSLE,S
NSLV,R,1
NUMMRG,NODE,II/2, , ,LOW
ALLSEL,ALL
EPLOT

! Contact Configuration

wpoff,0,0,-HM

/COM, CONTACT PAIR CREATION - START
CM,_NODECM,NODE
CM,_ELEMCM,ELEM
CM,_KPCM,KP
CM,_LINECM,LINE
CM,_AREACM,AREA
CM,_VOLUCM,VOLU

/GSAV,cwz,gsav,,temp

TB,FRIC,3,,18,ISO,,

TBFIELD,SLDI,0
TBDATA,1,0.1475

TBFIELD,SLDI,9
TBDATA,1,0.1475

TBFIELD,SLDI,22.5
TBDATA,1,0.725

MAT,3
MP,EMIS,3,0

R,3
REAL,3
ET,3,170
ET,4,174

R,3,,,-NPS,-PT,0,
RMORE,,,MFS,0.0,1.0,
RMORE,C,0,1.0,,1.0,0.5
RMORE,0,1.0,SDR,EDC,,1.0

KEYOPT,4,4,0
KEYOPT,4,5,0
KEYOPT,4,7,0
KEYOPT,4,8,0
KEYOPT,4,9,0
KEYOPT,4,10,2
KEYOPT,4,11,0
KEYOPT,4,12,0

*IF,CA,EQ,1,THEN

KEYOPT,4,2,0

```

*else

KEYOPT,4,2,1

*ENDIF
KEYOPT,3,5,0

! Generate the target surface

ASEL,S,LOC,X,-DSF-DSPSF-II,DSF+II
ASEL,U,LOC,Z,-II,II
ASEL,U,LOC,Z,(HM/2)-(HM/NDWSP)-II,(HM/2)-(HM/NDWSP)+II
ASEL,U,LOC,Z,(HM/2)-II,(HM/2)+II
ASEL,U,LOC,Z,HM-II,HM+II
ASEL,R,LOC,Y,-DSF-DSPSF-II,DSF+DSPSF+II

ASEL,R, , ,ALL
CM,TARGET,AREA
CMSEL,A,TARGET

CM,_TARGET,AREA

TYPE,3
NSLA,S,1
ESLN,S,0
ESLL,U
ESEL,U,ENAME,,188,189
NSLE,A,CT2 ! CZMESH patch (fsk qt-40109 8/2008)
ESURF
CMSEL,S,_ELEMCM

! Generate the contact surface

ALLSEL,ALL
ASEL,U, , ,ALL

*DO,i,1,NDWSP+1,1

ASEL,A, , ,7+(i-1)*16
ASEL,A, , ,11+(i-1)*16
ASEL,A, , ,15+(i-1)*16
ASEL,A, , ,19+(i-1)*16

*ENDDO

ASEL,R, , ,ALL
CM,CONTACT,AREA
CMSEL,A,CONTACT

CM,_CONTACT,AREA

TYPE,4
NSLA,S,1
ESLN,S,0
NSLE,A,CT2 ! CZMESH patch (fsk qt-40109 8/2008)

```

```

ESURF
ALLSEL

ESEL,ALL
ESEL,S,TYPE,,3
ESEL,A,TYPE,,4
ESEL,R,REAL,,3
/PSYMB,ESYS,1
/PNUM,TYPE,1
/NUM,1
EPLOT
ESEL,ALL
ESEL,S,TYPE,,3
ESEL,A,TYPE,,4
ESEL,R,REAL,,3
CMSEL,A,_NODECM
CMDEL,_NODECM
CMSEL,A,_ELEMCM
CMDEL,_ELEMCM
CMSEL,S,_KPCM
CMDEL,_KPCM
CMSEL,S,_LINECM
CMDEL,_LINECM
CMSEL,S,_AREACM
CMDEL,_AREACM
CMSEL,S,_VOLUCM
CMDEL,_VOLUCM
/GRES,cwz,gsav
CMDEL,_TARGET
CMDEL,_CONTACT
/COM, CONTACT PAIR CREATION - END
/MREP,EPLOT

! Superpose the Steel Fibre and the Concrete Matrix

VSEL,S,LOC,X,-1.25*RM,1.25*RM

VGEN, ,ALL, , , -HM, , , , 1

ALLSEL,ALL

WPCSYS,-1,0

!-----
!PROCESSING
!-----

!SOLUTION

/SOL
NSUBST,100,200,20
OUTRES,ERASE
OUTRES,ALL,-2
LNSRCH,1
NEQIT,1000
RESCONTRL,DEFINE,ALL,ALL,1

```



```

NLGEOM,1
NROPT,FULL, ,ON
STAOPT,DEFA
LUMPM,0
EQLV,SPAR, ,0, ,DELE
PRECISION,0
MSAVE,0
PCGOPT,0, ,AUTO, , ,AUTO
PIVCHECK,1
SSTIF
PSTRES

```

! Loading

```

ALLSEL,ALL
ESEL,S,MAT,,1
NSLE,S
NSEL,R,LOC,Z,-(HM/(NDWSP*MEPSP))/2,(HM/(NDWSP*MEPSP))/2

```

```

D,ALL, , , , ,ALL, , , ,

```

! Coupling

```

ALLSEL,ALL
ESEL,S,MAT,,1
NSLE,S
NSEL,R,LOC,Z,HM-(HM/(NDWSP*MEPSP))/2,HM+(HM/(NDWSP*MEPSP))/2

```

```

CP,BC,ALL,ALL

```

```

ALLSEL,ALL

```

APPENDIX 4.1

CONCRETE MIX DESIGN ($f_m = 35$ MPa)

Stage	Item	Reference or Calculation	Values
1	1.1 Characteristic Strength	Specified	37 N/mm ² at 28 days Proportion Defective: 5 %
	1.2 Standard Deviation	Fig. 3 ^a	---- N/mm ² or No Data: 5 N/mm ²
	1.3 Margin	C1 or Specified	($k = 1.64$) 1.64 \times 5 ~ 8 N/mm ² ---- N/mm ²
	1.4 Target Mean Cube Strength	C2	37 + 8 = 45 N/mm ²
	1.5 Cement Strength Class	Specified	42.5 / 52.5
	1.6 Aggregate Type: Coarse Aggregate Type: Fine		Crushed / Uncrushed Crushed / Uncrushed
	1.7 Free-Water / Cement Ratio, i.e. W/C	Table 2 ^a , Fig. 4 ^a	0.538
	1.8 Maximum W/C	Specified	---- Use the Lower Value [-]
2	2.1 Slump or Vebe Time	Specified	Slump 10-30 mm or Vebe Time - s
	2.2 Maximum Aggregate Size	Specified	10 mm
	2.3 Free-Water Content	Table 3 ^a	(2 / 3) \times 180 + (1 / 3) \times 205 ~ 188.3 kg/m ³
3	3.1 Cement Content	Specified	188.3 \div 0.538 ~ 350.0 kg/m ³
	3.2 Maximum Cement Content	Specified	---- mm
	3.3 Minimum Cement Content	Table 3 ^a	---- kg/m ³ Use 3.1 if \leq 3.2 Use 3.3 if $>$ 3.1
	3.4 Modified Free-Water / Cement Ratio		----
4	4.1 Relative Density of Aggregate (SSD)		2.656 Known / Assumed
	4.2 Concrete Density	Fig. 5 ^a	~ 2405.7 kg/m ³
	4.3 Total Aggregate Content	C4	2405.7 - 350.0 - 188.3 = 1867.4 kg/m ³
5	5.1 Grading of Fine Aggregate	Percentage Passing 600 μ m Sieve	42.41 % (~ 40 %)
	5.2 Proportion of Fine Aggregate	Fig. 6 ^a	47.11 %
	5.3 Fine Aggregate Content	} C5	1867.4 \times 0.4711 ~ 879.73 kg/m ³
	5.4 Coarse Aggregate Content		1867.4 - 879.73 = 987.67 kg/m ³

Aggregate Condition	Quantities	Cement (kg)	Water (kg or Litres)	Fine Aggregate (kg)	Coarse Aggregate (kg)
SSD	Per m ³ (to nearest 5 kg)	350.0	188.3	879.73	987.67

a (Building Research Establishment 1997)

CONCRETE MIX DESIGN ($f_m = 45$ MPa)

Stage	Item	Reference or Calculation	Values
1	1.1 Characteristic Strength	Specified	50 N/mm ² at 28 days Proportion Defective: 5 %
	1.2 Standard Deviation	Fig. 3 ^a	---- N/mm ² or No Data: 3 N/mm ²
	1.3 Margin	C1 or Specified	($k = 1.64$) $1.64 \times 3 \sim 5$ N/mm ² ---- N/mm ²
	1.4 Target Mean Cube Strength	C2	$37 + 5 = 55$ N/mm ²
	1.5 Cement Strength Class	Specified	42.5 / 52.5
	1.6 Aggregate Type: Coarse Aggregate Type: Fine		Crushed / Uncrushed Crushed / Uncrushed
	1.7 Free-Water / Cement Ratio, i.e. W/C	Table 2 ^a , Fig. 4 ^a	0.445
	1.8 Maximum W/C	Specified	---- Use the Lower Value [-]
2	2.1 Slump or Vebe Time	Specified	Slump 10-30 mm or Vebe Time - s
	2.2 Maximum Aggregate Size	Specified	10 mm
	2.3 Free-Water Content	Table 3 ^a	$(2 / 3) \times 180 + (1 / 3) \times 205 \sim 188.3$ kg/m ³
3	3.1 Cement Content	Specified	$188.3 \div 0.445 \sim 423.1$ kg/m ³
	3.2 Maximum Cement Content	Specified	---- mm
	3.3 Minimum Cement Content	Table 3 ^a	---- kg/m ³ Use 3.1 if ≤ 3.2 Use 3.3 if > 3.1
	3.4 Modified Free-Water / Cement Ratio		----
	4.1 Relative Density of Aggregate (SSD)		2.656 Known / Assumed
4	4.2 Concrete Density	Fig. 5 ^a	~ 2405.7 kg/m ³
	4.3 Total Aggregate Content	C4	$2405.7 - 423.1 - 188.3 = 1794.3$ kg/m ³
5	5.1 Grading of Fine Aggregate	Percentage Passing 600 μ m Sieve	42.41 % (~ 40 %)
	5.2 Proportion of Fine Aggregate	Fig. 6 ^a	44.67 %
	5.3 Fine Aggregate Content	}C5	$1794.3 \times 0.4467 \sim 801.5$ kg/m ³
	5.4 Coarse Aggregate Content		$1794.3 - 801.5 = 992.8$ kg/m ³

Aggregate Condition	Quantities	Cement (kg)	Water (kg or Litres)	Fine Aggregate (kg)	Coarse Aggregate (kg)
SSD	Per m ³ (to nearest 5 kg)	423.1	188.3	801.5	992.8

a (Building Research Establishment 1997)

APPENDIX 4.2

RISK ASSESSMENT

Job Description: General Considerations

Special risks not fully covered by these regulations and Main Risks of the job	Precautions required
--	----------------------

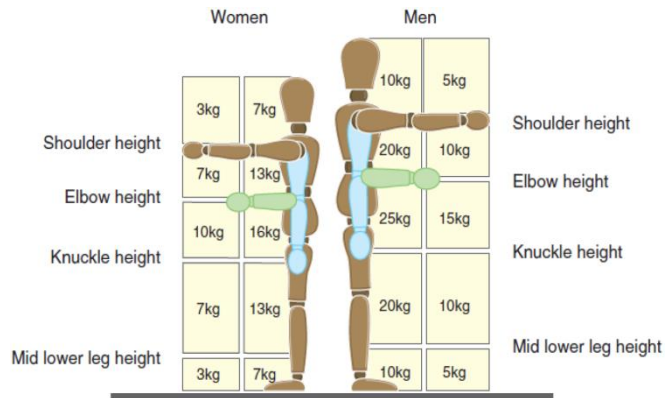
<p style="text-align: center;">General Requirements</p> <p>Potential for:</p> <ul style="list-style-type: none"> • Workplace accident caused by human carelessness, negligence, impulsive, irresponsible behaviour, etc. 	<ol style="list-style-type: none"> 1. The correct clothing must be worn at all times. Adequate footwear is mandatory for all laboratory works. Shorts and open-toed footwear are prohibited. 2. No smoking, eating, drinking or use of mobile phones, MP3 players etc. allowed in the laboratory. Jewellery, watches, and rings must be removed. 3. When working in the laboratory everyone is responsible for maintaining adequate levels of cleanliness and tidiness so as not to create hazards for other users. 4. Any tool or equipment damage must be immediately reported to the supervising member of staff. 5. Any tools used in the laboratory must be used in the correct manner and returned to their correct place of storage. 6. When in the laboratory, students must not run or participate in horseplay of any nature. It is the responsibility protocols, if in doubt please STOP and ASK. Any accident caused by such irresponsible behaviour will be dealt with severely! 7. All students must acquaint themselves with the laboratory layout, personnel, emergency action, and equipment associated with first aid, firefighting and machinery emergency stop and subsequent reporting procedures. Fire escape routes are identified and must be kept clear of any obstructions at all times. 8. Any injuries, however, small must be immediately reported to the supervising staff member.
--	--

Manual Handling of Specimens

Potential for:

- Back injuries when lifting heavy objects.
- Arm, hand, leg, or foot injuries if the heavy specimen falls.
- Serious cuts/injuries caused by sharp objects.

1. Lab coats, protective gloves, goggles and safety boots must be worn at all times.
2. Anything including concrete specimens and moulds weigh more than 8 kg each should be handled carefully without letting them to drop.
3. Restriction of tasks to the weights, shown below, gives a reasonable level of protection to prevent injury from lifting weights. Use a trolley or gantry crane to move weights which goes beyond individual capacity. Gantry crane must be operated by a licensed driver.



APPENDIX 4.3

RISK ASSESSMENT

Job Description: Concrete Mixing and Casting, and Cylinder Grinding

Special risks not fully covered by these regulations and Main Risks of the job	Precautions required
<p>Mixing, Vibration, and Casting of Concrete Specimens</p> <p>Potential for:</p> <ul style="list-style-type: none">• Serious cuts/injuries caused by sharp objects.• Eyes and skin injuries due to the handling of cement and mould oil.• Injuries when moving heavy objects.	<ol style="list-style-type: none">1. All personal protective equipment (i.e. lab coats, protective gloves, goggles, and safety boots) must be worn.2. Ensure all the mixer guards are in place before use.3. Ensure all cables are intact and away from conductive objects.4. Ensure hands are dry before grabbing any cords to plug or unplug them.5. Ensure the emergency stop button works before use.6. Ensure hands and arms are out of the mixer at all times.7. Turn the mixer off before moving or cleaning it.8. If cement comes or moulds oil in contact with your skin, wash it off straight away using the soap provided in the laboratory.9. The concrete moulds, particularly when full of concrete are very heavy. Palette lifter should be used to avoid unnecessary injury.
<p>Concrete Specimens Grinding</p> <p>Potential for:</p> <ul style="list-style-type: none">• Physical hurting of someone's finger.• Electric shock.• Silica dust hurting eyes or skins of the operator.	<ol style="list-style-type: none">1. Never put your hands or fingers inside the grinding area during the operation of the grinder.2. Ensure all cables are intact and away from conductive objects.3. Never operate the machine when hands are wet.4. Operate in a well-circulated environment.5. Wear appropriate protective equipment.

APPENDIX 4.4

RISK ASSESSMENT

Job Description: Operating Testing Equipment

Special risks not fully covered by these regulations and Main Risks of the work/project	Precautions required
<p>A. Working with the Compression Testing Machine (300 Tonne)</p> <p>Potential for:</p> <ul style="list-style-type: none">• Arm, hand, leg, or foot injuries when dealing with machinery.• Damage to the testing machine/equipment due to abuse or misuse.	<ol style="list-style-type: none">1. The specimens should be handled with care as they could be very sharp in places and can cause serious puncture wounds.2. Extreme care should be taken when dealing with machinery as it may cause physical harm to the operator or to other people.3. Do not touch any moving parts and always keep hands and feet away when the machine is in operation.4. Do not attempt to replace or move the specimens while the machine is operating.5. At all stages of the experiments, the protective cover of the machine should be closed in order to prevent crushed particles of the specimens from falling into the surrounding area.
<p>B. Working with the Universal Testing Machine (UTM - 30 Tonne)</p> <p>Potential for:</p> <ul style="list-style-type: none">• Arm, hand, leg, or foot injuries when dealing with machinery.• Damage to the testing machine/equipment due to abuse or misuse.	<ol style="list-style-type: none">1. The specimens should be handled with care as they could be very sharp in places and can cause serious puncture wounds.2. The machine operator must have suitable training and a full understanding of its operation.3. Extreme care should be taken when dealing with machinery as it may cause physical harm to the operator or to other people.4. Do not touch any moving parts and always keep hands and feet away when the machine is in operation.